

## AN ABSTRACT OF THE THESIS OF

Gregory A. Peterson for the degree of Doctor of Philosophy in Chemistry  
presented on 10 June 1999.

Title: Studies on New Inorganic Solid-State Borates  
and Oxoanion Fluorides.

Abstract Approved: Redacted for Privacy

Douglas A. Keszler

High-temperature solution growth and structural characterization of  $\text{CeSc}_3(\text{BO}_3)_4$  (CSB) are described. This material is the first example of a stoichiometric scandium borate that exhibits both a wide transparency range and the trigonal, noncentrosymmetric structure of the mineral huntite. Interest in the borate huntites stems from their potential as optical frequency converters and self-frequency doubling lasers.

The crystal structure of  $\text{NaLiB}_4\text{O}_7$  and results of its equilibrium interactions with  $\text{Li}_2\text{B}_4\text{O}_7$  are described. Crystal-growth experiments corroborate the peritectic behavior of the compound as well as the existence of intermediate compositions, which may provide a mechanism for tuning linear and nonlinear properties in this noncentrosymmetric crystal.

From an investigation of the Plasma Display Panel (PDP) phosphor  $\text{Eu:}(\text{Y,Gd})\text{BO}_3$  and development of new  $\text{Eu}^{3+}$ -containing phosphors, a simple model has been formulated for correlating the excitation maxima of  $\text{BO}_3$  groups with the average cation electronegativity per formula unit. Correlation between site symmetry and the nature of the  $\text{Eu}^{3+}$  emission, and between structural

coordination and the efficiency of energy transfer from the host to the  $\text{Eu}^{3+}$ -activator are made from analysis of excitation and emission spectra.

$\text{YMgB}_5\text{O}_{10}$  was synthesized during a search for new ternary phases in the system  $\text{Y}_2\text{O}_3\text{-B}_2\text{O}_3\text{-MgO}$ ; it provides a rare example of a structure containing a ten-coordinate Y atom.  $\text{Y}_4\text{BO}_7\text{F}$  was discovered during an investigation of the ternary system  $\text{Y}_2\text{O}_3\text{-B}_2\text{O}_3\text{-YF}_3$ . Structure analysis and a subsequent synthesis effort led to the development of a new family of borate fluorides  $\text{Ln}_4\text{BO}_7\text{F}$  ( $\text{Ln} = \text{Y, Dy, Ho, Er, Tm, and Yb.}$ )

The new materials  $\text{Li}_2\text{Ca}_6(\text{MO}_4)\text{F}_2$  ( $\text{M} = \text{Si, Ge}$ ) have been synthesized and structurally characterized, and a convenient synthesis method has been developed for the compound  $\text{Sr}_4\text{Ge}_2\text{O}_7\text{F}_2$ . Such materials are of interest for the production of highly anisotropic crystal fields and the production of unusual luminescence characteristics.

**Studies on New Inorganic Solid-State Borates  
and Oxoanion Fluorides.**

**by**

**Gregory A. Peterson**

**A THESIS  
submitted to  
Oregon State University**

**In partial fulfillment of  
the requirements for the  
degree of**

**Doctor of Philosophy**

**Completed June 10, 1999  
Commencement June 2000**

Doctor of Philosophy thesis of Gregory A. Peterson presented on 10 June, 1999

APPROVED:

Redacted for Privacy

Major Professor, representing Chemistry

Redacted for Privacy

Department Chair, Department of Chemistry

Redacted for Privacy

Dean of Graduate School

I understand that my thesis will become part of the permanent collection of Oregon State University libraries. My signature below authorizes release of my thesis to any reader upon request.

Redacted for Privacy

Gregory A. Peterson, Author

## ACKNOWLEDGMENTS

I am thankful for all of the people who have enriched my life with acts of kindness, encouragement, and support during my graduate work at Oregon State University.

Dr. Douglas Keszler has been an inspiration during my graduate studies at OSU. His endless patience, encouraging support, and friendship have made my experience at OSU personally and intellectually rewarding.

I would like to extend my appreciation to my PhD committee members: Dr. Carroll DeKock, Dr. Victor Hsu, Dr. Mike Lerner, Dr. Joseph Nibler and Dr. Michael Schuyler for their time and commitment to my program.

I would like to extend my sincere appreciation to all of the Chemistry support staff at OSU who helped to make the day-to-day necessities of being a graduate student manageable. I want to especially thank Ted Hinke for all of his help building experimental apparatus. Ted's expertise in design and manufacturing was instrumental to the success of these projects.

The Keszler Group, which currently consists of Dr. Judith Kissick, Ben Clark, Sangmoon Park, Candice Pike, and Jennifer Stone have been a tremendous source of helpful discussion, encouragement, and friendship. Judith has been especially helpful with several of my projects, and has been the source of endless goodies. I am grateful to the previous members of the Keszler group for all of the instructive and helpful discussions, and friendship. They include Dr. Jun-Ming Tu, Dr. Annapoorna Akella, Dr. Anthony Diaz, Dr. Ki-Seog Chang, Dr. Dong Li, M.S. Ken Vandenberghe, M.S. Steve Crossno, and Melissa Harrington.

I have had the pleasure of working with Dr. Thomas Reynolds of ReyTech Corporation, and former member of the Keszler Group on many occasions. He has provided many hours of instructive discussion and some financial resources for which I am grateful.

Dr. Alexandre Yokochi has been very helpful with the crystal structure solutions, and has spent much time helping to maintain X-ray equipment vital to my research. He is also a good friend and I appreciate his support and encouragement while at OSU.

Dr. Larry Thomas is responsible for my decision to come to Oregon State University. I want to thank Larry for all that he has done to support me in my undergraduate education at Seattle University, and my continued education at OSU. Larry is a good friend and mentor.

I know that my friend Walt Wiechmann who passed away in the summer of 1992, would be proud of my accomplishment. Walt was a kind, gentle friend whose love for Chemistry and for Life will always be an inspiration to me. I thought about Walt throughout my program at OSU, and wish that I could have shared my experiences with him.

I want to thank three very special people whom make my life complete. Annie, my beautiful wife and best friend, has always been a source of encouragement, support, and has made my lengthy stay at OSU possible. My son Joshua Michael, and my daughter Karen Elizabeth are my most cherished blessings.

I wish to acknowledge my mother, Jean Peterson, and my father Wallace Peterson for their encouragement to continue my education. They have always realized the importance of education and have made personal sacrifices to insure that my siblings and myself have had educational opportunities. I appreciate the support of my family members, particularly my sisters, Stephanie and Angela, and my Brothers, Chris and Eric for all of their encouragement in my progress toward this degree.

I would like to acknowledge Ann's family who has been supportive and encouraging of our educational endeavors and family struggles.

## CONTRIBUTION OF AUTHORS

The data presented in Chapter 2 resulted from a collaboration of Dr. Thomas Reynolds, Dr. Douglas Keszler, and myself. Dr. Reynolds provided resourceful insight regarding the spectroscopic studies of Nd:CeSc<sub>3</sub>(BO<sub>3</sub>)<sub>4</sub>. Dr. Jun-Ming Tu is responsible for the structure characterization of NaLiB<sub>4</sub>O<sub>7</sub> and the solid-solution data found in Chapter 3. Professor Richard Meltzer, Delena Bell Gatch, and Kiwan Jiang are responsible for collecting the VUV spectra of the Eu-doped phosphors discussed in Chapter 4. Professor Richard Meltzer collaborated and reviewed the manuscript found in Chapter 4. Dr. Alexandre Yokochi assisted with the structural refinements found in Chapters 2, 5, and 7. Dr. Judith Kissick was responsible for collecting the X-ray data, and worked with Dr. Yokochi on the structural refinement of Li<sub>2</sub>Ca<sub>6</sub>(GeO<sub>4</sub>)<sub>3</sub>F<sub>2</sub> (Chapter 7.) Dr. Kissick performed the fluoride analysis on Li<sub>2</sub>Ca<sub>6</sub>(GeO<sub>4</sub>)<sub>3</sub>F<sub>2</sub> to corroborate the F-content. Annapoorna Akella was responsible for the initial discovery of Li<sub>2</sub>Ca<sub>6</sub>(GeO<sub>4</sub>)<sub>3</sub>F<sub>2</sub>, and the structural refinement of Sr<sub>4</sub>Ge<sub>2</sub>O<sub>7</sub>F<sub>2</sub>.

## TABLE OF CONTENTS

	<u>Page</u>
<b>CHAPTER 1: INTRODUCTION.....</b>	<b>1</b>
Nonlinear Optical Materials.....	2
Structure-Property Relationships of VUV-excited phosphors, and luminescence.....	7
Oxoanion Fluorides.....	10
References.....	12
 <b>CHAPTER 2: TRIGONAL HUNTITE BORATE <math>\text{CeSc}_3(\text{BO}_3)_4</math> (CSB).....</b>	 <b>14</b>
Abstract.....	15
Introduction.....	15
Materials and Methods.....	16
Results and Discussion.....	18
Spectroscopic Studies.....	25
Summary.....	31
Acknowledgments.....	31
References.....	31
 <b>CHAPTER 3: THE NONCENTROSYMMETRIC ALKALI METAL BORATE     <math>\text{NaLiB}_4\text{O}_7</math>.....</b>	 <b>33</b>
Abstract.....	34
Introduction.....	34
Materials and Methods .....	35
Results and Discussion.....	37
Acknowledgments.....	52
References.....	52
 <b>CHAPTER 4: STRUCTURE-PROPERTY RELATIONSHIPS OF VUV-     EXCITED PHOSPHORS.....</b>	 <b>54</b>
Abstract.....	55



## TABLE OF CONTENTS (Continued)

	<u>Page</u>
Introduction.....	55
Results and Discussion.....	56
Chromaticity.....	64
Summary.....	66
Acknowledgments.....	66
References.....	67
<b>CHAPTER 5: THE STRUCTURE AND LUMINESCENCE PROPERTIES OF YTTRIUM MAGNESIUM PENTABORATE <math>\text{YMgB}_5\text{O}_{10}</math>.....</b>	<b>68</b>
Abstract.....	69
Introduction.....	69
Materials and Methods.....	70
Results and Discussion.....	73
$\text{Eu}^{3+}$ Luminescence.....	77
Acknowledgments.....	85
References.....	85
<b>CHAPTER 6: <math>\text{Ln}_4\text{BO}_7\text{F}</math>, (<math>\text{Ln} = \text{Y}, \text{Dy}, \text{Ho}, \text{Er}, \text{Tm}, \text{and Yb}</math>); STRUCTURE AND SELECTED OPTICAL PROPERTIES.....</b>	<b>86</b>
Abstract.....	87
Introduction.....	87
Materials and Methods.....	88
Results and Discussion.....	90
Spectroscopic Properties.....	97
Summary.....	105
Acknowledgments.....	105
References.....	106

## TABLE OF CONTENTS (Continued)

	<u>Page</u>
<b>CHAPTER 7: SYNTHESIS, CHARACTERIZATION AND LUMINESCENCE PROPERTIES OF <math>\text{Li}_2\text{Ca}_6(\text{MO}_4)_3\text{F}_2</math> (M = Si, Ge).....</b>	<b>107</b>
Abstract.....	108
Introduction.....	108
Materials and Methods.....	109
$\text{Li}_x\text{Ca}_2\text{SiO}_4\text{F}_x$ .....	109
$\text{Li}_x\text{Ca}_2\text{GeO}_4\text{F}_x$ .....	110
Doped Samples of $\text{Li}_x\text{Ca}_2\text{GeO}_4\text{F}_x$ .....	112
Results and Discussion.....	118
Crystal Structure of $\text{Li}_2\text{Ca}_6(\text{GeO}_4)_3\text{F}_2$ .....	118
Optical Properties of $\text{Nd}^{3+}$ and $\text{Yb}^{3+}$ doped $\text{Li}_2\text{Ca}_6(\text{GeO}_4)_3\text{F}_2$ .....	131
Summary.....	136
Acknowledgments.....	136
References.....	136
 <b>CHAPTER 8: STRUCTURE OF <math>\text{Sr}_4\text{Ge}_2\text{O}_7\text{F}_2</math> AND SELECTED LUMINESCENCE PROPERTIES.....</b>	 <b>138</b>
Abstract.....	139
Introduction.....	139
Materials and Methods.....	140
Results and Discussion.....	144
$\text{Pb}^{2+}$ Luminescence.....	149
$\text{Eu}^{3+}$ Luminescence.....	150
$\text{Tb}^{3+}$ Luminescence.....	151
Summary.....	151
Acknowledgments.....	155
References.....	155
 <b>CHAPTER 9: CONCLUSION.....</b>	 <b>157</b>

## TABLE OF CONTENTS (Continued)

	<u>Page</u>
BIBLIOGRAPHY.....	160
CURRICULUM VITAE.....	167

## LIST OF FIGURES

<u>Figure</u>	<u>Page</u>
1.1 Photoluminescent Processes in a Phosphor Grain.....	8
2.1. Unit-cell contents of $\text{CeSc}_3(\text{BO}_3)_4$ viewed down the $c$ axis.....	22
2.2. Borate polyhedra: a) viewed down $[001]$ b) viewed down $[010]$ .....	23
2.3. a) Columnar Sc-centered octahedra spiraling along the $c$ axis. b) Sc-centered polyhedra viewed down the $c$ axis.....	24
2.4. Ce excitation (left) and emission (right) energy spectrum for $\text{CeSc}_3(\text{BO}_3)_4$ at 78 K.....	27
2.5. Ce excitation (left) and emission (right) energy spectrum for $\text{CeSc}_3(\text{BO}_3)_4$ at 300 K.....	28
2.6. Energy spectrum of $\text{Nd}_{0.02}\text{Ce}_{0.98}\text{Sc}_3(\text{BO}_3)_4$ .....	29
2.7. Energy level diagram for $\text{Nd}_{0.02}\text{Ce}_{0.98}\text{Sc}_3(\text{BO}_3)_4$ .....	30
3.1. Labeled drawing of the unit-cell of $\text{NaLiB}_4\text{O}_7$ viewed along the $c$ axis.	42
3.2. Drawing of $\text{NaLiB}_4\text{O}_7$ viewed down the $a$ axis.....	43
3.3. Drawing of $\text{NaLiB}_4\text{O}_7$ viewed down the $b$ axis.....	44
3.4. Drawing of the $\text{B}_4\text{O}_9$ rings; triangles are $\text{BO}_3$ groups, tetrahedra $\text{BO}_4$ groups.....	45
3.5. Environment and connectivity of the Na- and Li- centered polyhedra.	49
3.6. Unit-cell per formula unit for the solid-solution series $\text{Na}_x\text{Li}_{2-x}\text{B}_4\text{O}_7$ as a function of composition ( $0 \leq x \leq 1$ ).....	50
3.7. a) Phase diagram for the binary system $\text{Li}_2\text{B}_4\text{O}_7$ and $\text{Na}_2\text{B}_4\text{O}_7$ . b) crystal boule has approximate composition: $\text{Na}_{0.55}\text{Li}_{1.45}\text{B}_4\text{O}_7$ . Each square is 5mm.....	51
4.1. Excitation spectra from $\text{Eu}^{3+}:\text{Y}_2\text{O}_3$ and $\text{Eu}^{3+}:\text{Ca}_4\text{Gd}(\text{BO}_3)_3\text{O}$ .....	57

## LIST OF FIGURES (Continued)

<u>Figure</u>	<u>Page</u>
4.2. $\sigma$ -interaction model for energy transfer a) linear interaction b) orthogonal interaction.....	59
4.3. Relative transfer efficiency vs. cosine weighted average B-O-Eu angle.	60
4.4. Emission spectrum of $\text{ScBO}_3$ .....	62
4.5. Emission spectra from $\text{Eu}^{3+}$ -doped oxides.....	63
4.6. (a) Unit-cell drawing of $\text{Ca}_4\text{Gd}(\text{BO}_3)_3\text{O}$ , (b) left ) $\text{YO}_6$ octahedron in $\text{Y}_2\text{O}_3$ , right ) $\text{GdO}_6$ octahedron in $\text{Ca}_4\text{Gd}(\text{BO}_3)_3\text{O}$ .....	65
5.1. HKP Brightness Measuring Device. 1) mercury pen lamp used for excitation, 2) filter holder with 254 nm interference bandpass filter, 3) horizontally oriented powder-sample holder 4) filter holder with 500 nm cutoff filter and neutral-density filter, and 5) photomultiplier tube (PMT).....	72
5.2. Unit-cell contents for $\text{YMgB}_5\text{O}_{10}$ as viewed along [010].....	78
5.3. Two-dimensional borate layers as viewed along [010].....	79
5.4. Zigzag chains of Y atoms extending parallel to the $b$ axis. Inter-chain distance is 6.20 Å and intra-chain distances 3.95 Å.....	80
5.5. The luminescence spectrum of $\text{Y}_{0.95}\text{Eu}_{0.05}\text{MgB}_5\text{O}_{10}$ .....	83
5.6. Emission signal <u>vs.</u> $\text{Eu}^{3+}$ concentration in the series $\text{Y}_{1-x}\text{Eu}_x\text{MgB}_5\text{O}_{10}$ ( $0 < x < 1$ .).....	84
6.1. Unit-cell contents for $\text{Y}_4\text{BO}_7\text{F}$ .....	95
6.2. Y-centered Polyhedra.....	96
6.3. The relationship between the unit cell volume and the size of the atomic sphere.....	98
6.4. Excitation and emission spectra of $\text{Tb}_{0.1}\text{Y}_{3.9}\text{BO}_7\text{F}$ ; emission $\lambda_{\text{exc}} = 285 \text{ nm}$ excitation $\lambda_{\text{em}} = 546 \text{ nm}$ .....	100

## LIST OF FIGURES (Continued)

<u>Figure</u>	<u>Page</u>
6.5. Excitation and emission spectra of $\text{Eu}_{0.1}\text{Y}_{3.9}\text{BO}_7\text{F}$ emission $\lambda_{\text{exc}} = 276 \text{ nm}$ excitation $\lambda_{\text{em}} = 612 \text{ nm}$ .....	101
6.6. Concentration quenching of $\text{Y}_{4-x}\text{Eu}_x\text{BO}_7\text{F}$ and $\text{Y}_{4-x}\text{Tb}_x\text{BO}_7\text{F}$ ( $x = 0.02, 0.05, 0.10, 0.20$ , and $0.50$ .).....	102
6.7. Temperature quenching in $\text{Y}_{3.9}\text{Eu}_{0.1}\text{BO}_7\text{F}$ .....	103
6.8. VUV excitation spectra for 1) $\text{Eu}:(\text{Y},\text{Gd})\text{BO}_3$ , 2) $\text{Eu}:\text{Y}_2\text{O}_3$ , and 3) $\text{Eu}:\text{Y}_4\text{BO}_7\text{F}$ .....	104
7.1. Unit-cell contents viewed along $c$ . (a) Ge-centered tetrahedra plotted, (b) F-centered octahedra plotted.....	120
7.2. Unit-cell contents viewed down the $c$ axis. a) $\text{GeO}_4$ tetrahedra plotted, b) F-centered octahedra plotted; $\text{FCa}_6 = \text{yellow}$ and $\text{FLi}_6 = \text{light blue}$ .....	121
7.3. Ca-centered pentagonal-bipyramid polyhedra.....	122
7.4. F3-centered, $\text{FLi}_6$ octahedron with surrounding $\text{GeO}_4$ tetrahedra. (a) viewed down $c$ . (b) Ge-centered tetrahedra which alternate directions in the $ab$ plane as they encompass the $\text{FLi}_6$ octahedron....	124
7.5. F-centered octahedral environments.....	125
7.6. Excitation and emission spectrum for $\text{Nd}_{0.02}\text{Li}_{0.67}\text{Ca}_{1.98}\text{GeO}_{4.02}\text{F}_{0.65}$ ....	133
7.7. Energy-diagram with stark levels for $\text{Nd}_{0.02}\text{Li}_{0.67}\text{Ca}_{1.98}\text{GeO}_{4.02}\text{F}_{0.65}$ .....	134
7.8. Emission spectrum for $\text{Yb}_{0.02}\text{Li}_{0.67}\text{Ca}_{1.98}\text{GeO}_{4.02}\text{F}_{0.65}$ .....	135
8.1. Unit-cell diagram of $\text{Sr}_4\text{Ge}_2\text{O}_7\text{F}_2$ ; view is along the $b$ axis.....	145
8.2. Framework resulting from condensation of Sr Polyhedra. Small circles represent Ge atoms.....	146
8.3. Excitation and emission spectrum of $\text{Sr}_{3.95}\text{Pb}_{0.05}\text{Ge}_2\text{O}_7\text{F}_2$ at 298 K. ( $\lambda_{\text{exc}} = 294 \text{ nm}$ for emission and $\lambda_{\text{em}} = 368 \text{ nm}$ for excitation).....	152

## LIST OF FIGURES (Continued)

<u>Figure</u>	<u>Page</u>
8.4.    Excitation and emission spectrum of $\text{Sr}_{3.95}\text{Eu}_{0.03}\text{Na}_{0.03}\text{Ge}_2\text{O}_7\text{F}_2$ at 298 K ( $\lambda_{\text{exc}}$ = 260 nm for emission and $\lambda_{\text{em}}$ = 611 nm for excitation).....	153
8.5.    Excitation and emission spectrum of $\text{Sr}_{3.90}\text{Tb}_{0.05}\text{Na}_{0.05}\text{Ge}_2\text{O}_7\text{F}_2$ at 298 K ( $\lambda_{\text{exc}}$ = 264 nm for emission and $\lambda_{\text{em}}$ = 548 nm for excitation).....	154

## LIST OF TABLES

<u>Table</u>	<u>Page</u>
1.1 NLO crystals used for frequency conversion into the UV.....	3
2.1. Crystal data and experimental conditions for $\text{CeSc}_3(\text{BO}_3)_4$ .....	20
2.2. Atom positions and $U_{\text{eq}}$ for $\text{CeSc}_3(\text{BO}_3)_4$ .....	20
2.3. Selected bond distances and angles for $\text{CeSc}_3(\text{BO}_3)_4$ .....	21
3.1. Crystallographic data for $\text{NaLiB}_4\text{O}_7$ .....	38
3.2. Atomic coordinates and equivalent displacement coefficients for $\text{NaLiB}_4\text{O}_7$ .....	39
3.3. Indexed X-ray powder pattern for $\text{NaLiB}_4\text{O}_7$ .....	40
3.4. Interatomic distances (Å) and angles (°) for $\text{NaLiB}_4\text{O}_7$ .....	46
4.1. Average cation electronegativities and excitation peak maxima for $\text{Eu}^{3+}$ -doped borates.....	57
5.1. Crystal data and experimental conditions for $\text{YMgB}_5\text{O}_{10}$ .....	74
5.2. Atom positions and $U_{\text{eq}}$ for $\text{YMgB}_5\text{O}_{10}$ .....	75
5.3. Selected bond distances and angles for $\text{YMgB}_5\text{O}_{10}$ .....	76
6.1. Crystal data and experimental conditions for $\text{Y}_4\text{BO}_7\text{F}$ .....	92
6.2. Atom parameters for $\text{Y}_4\text{BO}_7\text{F}$ .....	93
6.3. Bond valence calculations and results for $\text{Y}_4\text{BO}_7\text{F}$ .....	93
6.4. Selected interatomic distances (Å) and angles (°).....	94
6.5. Cell data for $\text{Ln}_4\text{BO}_7\text{F}$ .....	97
7.1. Crystal data and structural refinement parameters for $\text{Li}_2\text{Ca}_6(\text{GeO}_4)_3\text{F}_2$ and $\text{Li}_2\text{Ca}_6(\text{SiO}_4)_3\text{F}_2$ .....	113
7.2. Atomic coordinates and equivalent isotropic displacement parameters for $\text{Li}_2\text{Ca}_6(\text{SiO}_4)_3\text{F}_2$ .....	114



## LIST OF TABLES (Continued)

<u>Table</u>	<u>Page</u>
7.3. Anisotropic displacement coefficients for $\text{Li}_2\text{Ca}_6(\text{SiO}_4)_3\text{F}_2$ .....	115
7.4. Atomic coordinates and equivalent isotropic displacement parameters for $\text{Li}_2\text{Ca}_6(\text{GeO}_4)_3\text{F}_2$ .....	116
7.5. Anisotropic displacement coefficients for $\text{Li}_2\text{Ca}_6(\text{GeO}_4)_3\text{F}_2$ .....	117
7.6. Distances and angles for $\text{Li}_2\text{Ca}_6(\text{SiO}_4)_3\text{F}_2$ .....	127
7.7. Distances and angles for $\text{Li}_2\text{Ca}_6(\text{GeO}_4)_3\text{F}_2$ .....	129
8.1. Crystal data and experimental conditions for $\text{Sr}_4\text{Ge}_2\text{O}_7\text{F}_2$ .....	142
8.2. Atom positions and Beq for $\text{Sr}_4\text{Ge}_2\text{O}_7\text{F}_2$ .....	143
8.3. Selected interatomic distances (Å) and bond angles ( °).....	147

# STUDIES ON NEW SOLID-STATE INORGANIC BORATES AND OXOANION FLUORIDES

## CHAPTER 1

### INTRODUCTION

Lasers, acoustical sensors, and flat-panel emissive displays are just a few of the technologies that rely on materials research for the discovery and improvement of solid-state compounds required for the next generation of device. Developing a fundamental understanding of structure-property relationships from existing solid-state materials serves as a starting point in this effort. This contribution to the field of solid-state inorganic materials follows this approach, and it is divided into three distinct parts. In the first section, two new nonlinear optical materials,  $\text{CeSc}_3(\text{BO}_3)_4$  and  $\text{NaLiB}_4\text{O}_7$  are presented (Chapters 2 and 3, respectively.) These noncentrosymmetric borates have been structurally characterized, and crystal growth, optical properties, and potential applications are discussed for each. In the second section, structure-property relationships of (vacuum ultraviolet) VUV-excited phosphors are presented in Chapter 4, and two new materials  $\text{YMgB}_5\text{O}_{10}$  and  $\text{Ln}_4\text{BO}_7\text{F}$  ( $\text{Ln} = \text{Y, Dy, Ho, Er, Tm and Yb}$ ), which were discovered in a search for new plasma display panel (PDP) phosphors are described in Chapters 5 and 6, respectively. The third section (Chapters 7 and 8) includes structural and optical characterization of the new oxoanion fluorides  $\text{Li}_2\text{Ca}_6(\text{MeO}_4)_3\text{F}_2$  ( $\text{Me} = \text{Si and Ge}$ ) and  $\text{Sr}_4\text{Ge}_2\text{O}_7\text{F}_2$ .

## Nonlinear Optical Materials

The number of uses for laser radiation continues to increase, placing a constant demand on generation of specific wavelengths at higher output powers as well as extending wavelength limits of laser radiation into the VUV and FIR regions of the electromagnetic spectrum.<sup>1</sup> Currently, these wavelength issues are addressed by use of optical frequency converters or nonlinear optical (NLO) materials. Inorganic single crystals are used exclusively for applications involving the conversion of high power laser radiation from one frequency to another. Many elaborate laser/NLO configurations have been devised to convert the frequency of either one or two input laser beams to a higher frequency output as in the case of harmonic generation and sum frequency generation, or multiple lower frequency beams as in the case of difference frequency generation. A source of tunable wavelengths is made possible by a process known as optical parametric oscillation, involving NLO materials. Of the thousands of possible crystalline phases examined for their possible use as frequency converters, only a handful have met the severe demands required to compete successfully with existing materials. Some of the important physical properties required of a potential second-order NLO material include a crystalline phase that is noncentrosymmetric, highly transparent over a wide wavelength range, sufficient birefringence, high nonlinearity susceptibilities, and good chemical and mechanical stability. Also, single crystals of extremely high optical quality and sufficient size must be grown with relative ease. No single NLO crystal in use today is the best possible choice for every application, and often, laser systems use several different types of NLO crystals to achieve a desired result.

Interest in the potential uses of lasers capable of producing UV and VUV wavelengths has encouraged researchers to look for new materials with the properties necessary for optical frequency conversion into this range. Currently, the borate materials  $\beta$ -BaB<sub>2</sub>O<sub>4</sub> (BBO) and LiB<sub>3</sub>O<sub>5</sub> (LBO) have been

the most widely used NLO crystals. One important limiting characteristic for VUV-NLO crystals is the transparency range of the crystal. To operate efficiently, NLO crystals must not absorb in the wavelength region of the desired output. BBO has an absorption edge at 189 nm and second harmonic generation (SHG) output is limited to 205 nm.<sup>2</sup> LBO with an absorption edge at 160 nm is limited by its small birefringence, and it has a short wavelength limit of 276 nm for SHG.<sup>3</sup> CsLiB<sub>6</sub>O<sub>10</sub> (CLBO), discovered in the Keszler Lab at OSU<sup>4</sup> and later developed in Japan by Mori et.al.,<sup>5</sup> is a very promising NLO material with an absorption edge at 180 nm. Fifth harmonic generation (FiHG) of Nd:YAG laser beam produces an emission wavelength of 213 nm from CLBO. Lithium tetraborate, Li<sub>2</sub>B<sub>4</sub>O<sub>7</sub>, is one of the latest borate materials to be examined as a possible optical frequency converter into the VUV region by using sum-frequency mixing with femtosecond pulses.<sup>6</sup> Table 1.1 contains the properties of some of the more important borate crystals of interest for conversion of infrared laser beams into the UV. To this end, we have grown and structurally characterized crystals of two new noncentrosymmetric borates CeSc<sub>3</sub>(BO<sub>3</sub>)<sub>4</sub> and NaLiB<sub>4</sub>O<sub>7</sub>.

Table 1.1. NLO crystals used for frequency conversion into the UV.

Borate Crystal	*KH <sub>2</sub> PO <sub>4</sub> (KDP)	LiB <sub>3</sub> O <sub>5</sub> (LBO)	β-BaB <sub>2</sub> O <sub>4</sub> (BBO)	CsLiB <sub>6</sub> O <sub>10</sub> (CLBO)	Li <sub>2</sub> B <sub>4</sub> O <sub>7</sub>	YAl <sub>3</sub> (BO <sub>3</sub> ) <sub>4</sub> (YAB)
Melting Properties		Incong.	Incong.	Congruent	Congruent	Incong.
Crystal Growth	Aqueous solution	HTS growth	HTS and Czoch.	HTS and Czoch.	Bridgman	HTS growth
Transparency Range nm	180 1800	160 2300	180 - 2600	180 - 2750	160 - 3600	160 - 4500

The family of borate huntite materials,  $\text{LnM}_3(\text{BO}_3)_4$  ( $\text{Ln}$  = lanthanide and  $\text{M}$  = Al, Sc, Cr, Fe, and Ga) holds the promise of being a potential candidate for UV conversion.  $\text{Nd:YAl}_3(\text{BO}_3)_4$  (NYAB) crystals are one of a few NLO materials that are capable of self-frequency doubling. In this case, the  $\text{Nd}^{3+} {}^2\text{F}_{3/2} \rightarrow {}^4\text{I}_{11/2}$  emission transition, which has one of the larger known stimulated emission cross sections at 1064 nm,  $\sigma = 2 \times 10^{-19} \text{ cm}^2$ , is internally doubled producing green light at 532 nm.<sup>7</sup> NYAB is well suited for diode pumping because of the large absorption band at 808 nm. Nd atoms occupying trigonal prismatic sites in the huntite structure are isolated from each other, which allows very high concentrations of Nd to be incorporated into a crystal without concentration quenching effects. High Nd-dopant concentrations as well as efficient absorption result in the high optical gains from relatively small crystals. The optical slope efficiency for these materials has been shown to be close to the theoretically calculated values.

$\text{LaSc}_3(\text{BO}_3)_4$  and  $\text{CeSc}_3(\text{BO}_3)_4$  crystals have been grown directly from the melt, and they are reported to crystallize in the space group  $\text{C}2/\text{c}$ .<sup>10</sup> Crystals of the Sc huntite derivatives have been reported to grow more favorably, and  $\text{Ce}_{0.8}\text{Gd}_{0.2}\text{Sc}_3(\text{BO}_3)_4$  crystals with the trigonal huntite structure have been grown directly from the melt.<sup>8</sup> Crystals of the trigonal borate huntite  $\text{CeSc}_3(\text{BO}_3)_4$  have been grown in our lab by using a high-temperature solution growth incorporating a unique  $\text{LiBO}_2/\text{LiF}$  flux combination. DTA data indicated that a first order phase transformation  $\text{R}32 \rightarrow \text{C}2/\text{c}$  occurs at a temperature of 1224°C, and melting occurs at 1490°C, thus providing the possibility of pulling the stoichiometric borate huntite  $\text{CeSc}_3(\text{BO}_3)_4$  from a supercooled melt.

Crystal growth of  $\text{NaLiB}_4\text{O}_7$  from a stoichiometric melt resulted in a small crack-free cylindrical boule with the approximate dimensions  $1.6 \times 0.8 \text{ cm}$  and an approximate composition of  $\text{Na}_{0.55}\text{Li}_{1.45}\text{B}_4\text{O}_7$ . A phase diagram was constructed from DTA data (Chapter 3), and peritectic decomposition of  $\text{NaLiB}_4\text{O}_7$  is observed at 765°C. We predict that larger crystals of  $\text{NaLiB}_4\text{O}_7$

can be grown from a melt slightly rich in  $\text{Na}_2\text{B}_4\text{O}_7$ , and that a small amount of NaF would also be beneficial in reducing the viscosity of the melt.

Crystal growth is a very important part of the production of NLO materials because of the reproducibility and high quality required for these single crystals. The crystal growth method to be used for the production of an NLO single crystal is determined from the melting characteristics of its stoichiometric, microcrystalline solid phase. Two types of melting behavior are considered, congruent and incongruent melting. A congruently melting solid retains its stoichiometric composition when in the liquid phase, which allows crystals to be pulled directly from the melt. Noncongruently melting materials decompose or undergo a phase transformation on heating, and therefore require addition of a flux to reduce the melting temperature so that the desired composition or phase is stable in the liquid phase. This type of crystal growth incorporating one or more additional components to reduce the melting temperature is referred to as a high temperature solution growth.

Growth from the melt is generally limited to crystals that melt congruently. One method for pulling crystals from a melt is called the Czochralski method. Modern Czochralski crystal-pulling equipment incorporates redundant feedback systems that monitor crystal weight and melt/solution temperature to provide automatic diameter control. Nearly all crystals grown by the Czochralski method are "seeded growths," which use an oriented seed crystal attached to the pulling rod to initiate crystallization in the melt.<sup>9</sup> After a crystal-melt interface is established, techniques such as necking are used to eliminate defects from the growing crystal. Seeded growth eliminates the need for nucleation to occur, which suppresses the supercooling that is associated with self-nucleation. Melt growth techniques are not limited to the pulling of a crystal from the melt. The Bridgman method, a form of zone growth, is commonly used for the growth of  $\text{Li}_2\text{B}_4\text{O}_7$ ,<sup>10</sup> producing very high optical quality crystals.

High temperature top-seeded solution growth (TSSG) is another method for obtaining NLO single crystals. LBO, BBO, and NYAB are three examples of

crystals grown by high temperature solution methods. For compounds that decompose prior to melting, or undergo an undesirable phase change, this method is almost always essential. This method was necessary to obtain the trigonal phase of  $\text{CeSc}_3(\text{BO}_3)_4$ , since the high temperature C-centered monoclinic phase is present when crystals are pulled directly from the melt. Growth from solution is less desirable than growth from the melt, since the solvent in a solution growth can often be incorporated into the growing crystal. Crystal growers sometimes search for solid solution compositions that melt congruently, and that are close to the desired composition of an incongruently melting material,<sup>11,12</sup> so that crystals can be grown directly from the melt.

The NLO material  $\beta\text{-BaB}_2\text{O}_4$  (BBO) undergoes a first order phase transition from the  $\beta$ -phase to the  $\alpha$ -phase above 925°C. Recently a method has been developed for pulling BBO single crystals from a supercooled melt, which requires very high radial and vertical gradients. Initially crystals were grown with limited success,<sup>13</sup> however, under suitable conditions high quality large crystals can be produced by this method. This type of growth eliminates the possibility of flux inclusions found in the high temperature solution grown crystals.

Differential thermal analysis (DTA) can provide much of the information necessary to begin the crystal growth, since it is in fact a small-scale crystal growth experiment. A typical DTA device has a pair of thermocouples that are wired in series to monitor the difference in temperature between a sample and a reference. A third thermocouple is used for measuring and controlling the furnace temperature. The furnace chamber surrounding the sample-reference assembly is normally capable of atmospheric control. The DTA output is a plot of the differential temperature between the sample and the inert reference on the abscissa, as a function of temperature, the ordinate. During an endothermic reaction such as melting or a solid-solid phase transition, the temperature of the sample will lag behind the temperature of the reference. The differential temperature will be negative as the sample absorbs heat from

the environment, and it should go to zero when the temperature of the sample and reference are the same. The size of the sample and reference are kept small, and the linear rate at which the sample and standard are heated is low, so that the response to changes in the system is quite fast. Heat is dissipated to the environment during an exothermic reaction and the sample temperature is greater than the reference. This will occur as the sample relaxes from a higher temperature phase to a lower temperature phase, or as a liquid-to-solid phase transition occurs. The environment absorbs the heat of crystallization, and the differential temperature should go from a positive value to zero. In a properly calibrated DTA, a measurable change in the heat capacity of a sample results in a shift in the baseline. Thus, the DTA plot provides the information needed to do a proper crystal growth, such as the temperature at which the sample melts, and the amount of hysteresis between the melting point and the point of spontaneous nucleation. When a crystal of a low temperature phase is desired, DTA plots of a series of samples with increasing amounts of flux can be collected so that the minimum amount of flux is used in the scaled-up growth.

Structure-property relationships of VUV-excited phosphors, and luminescence.

The development of new inorganic phosphors for plasma-display panels (PDPs) requires the incorporation of several material properties into a single compound. The compound must strongly absorb vacuum ultraviolet (VUV) light near 147 nm, and it must exhibit efficient transfer of this energy to the luminescent center. The luminescent center itself must emit with high efficiency and provide a suitable chromaticity. And in current display designs, the phosphor must be stable both in the environment of the plasma and to the short-wavelength VUV exciting light. Figure 1.1a represents a solid state luminescent host containing impurity ions, A and S. The impurity A, also



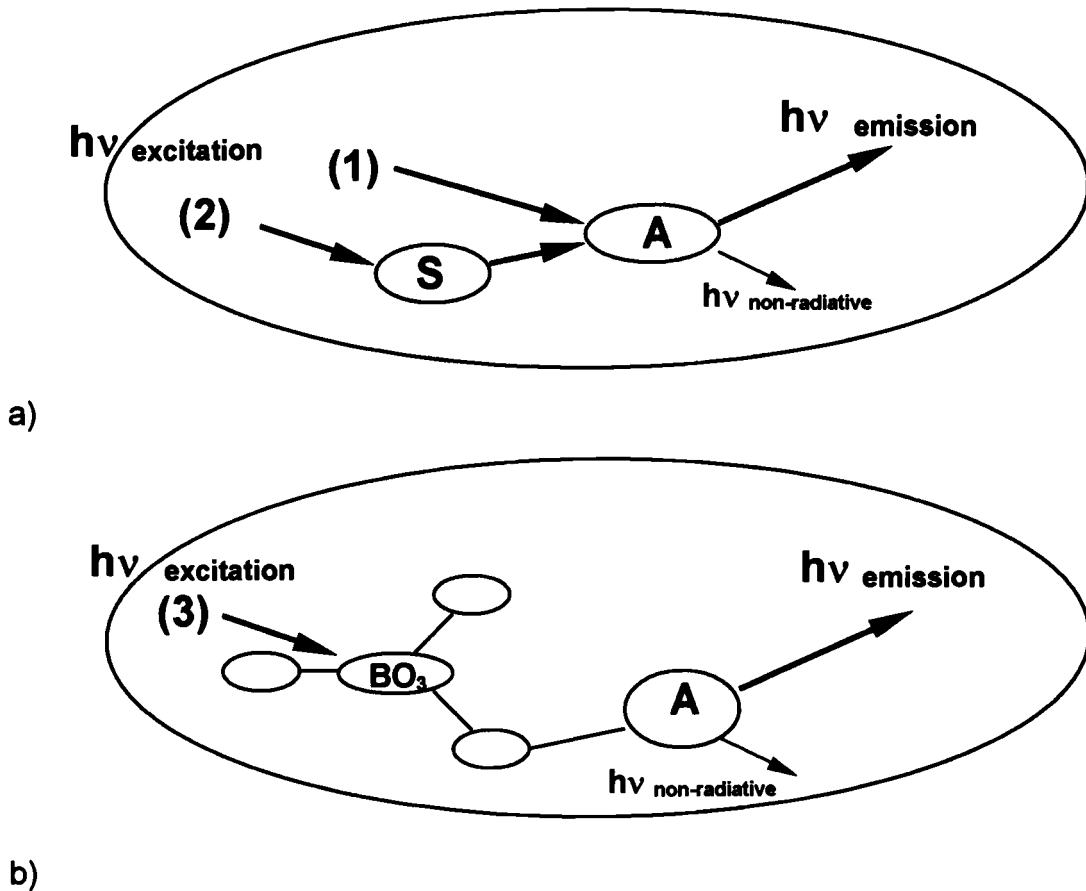


Figure 1.1. Photoluminescent Processes in a Phosphor Grain. A = activator ion, S = sensitizer ion,  $h\nu$ (excitation or emission) = a photon of UV or visible light, and  $h\nu$ (non-radiative) = vibrational heat in the phosphor grain. a)  $\text{Y}_2\text{O}_3:\text{Eu}^{3+}$ , and  $\text{GdMgB}_5\text{O}_{10}:\text{Ce}^{3+}$ ,  $\text{Tb}^{3+}$  are typical examples of a phosphor containing an activator, or both activator and sensitizer ions, respectively. Excitation energy is absorbed by the activator directly as in (1), or by the sensitizer with energy transfer to the activator as in (2). b)  $(\text{YGd})_1\text{BO}_3:\text{Eu}^{3+}$  is an example of a phosphor where the excitation energy is absorbed by the host (3), and this energy is transferred to the activator which acts as the emitting center. In a photoluminescent process, radiative and non-radiative processes are competitors, and efficient phosphors minimize the amount of non-radiative decay.

referred to as the activator ion, can be excited directly by an electromagnetic-radiation field if the frequency of the radiation is resonant with the energy levels of the activator. This process (1) is called spontaneous absorption of radiation, and it is termed a photoluminescent process when the absorbed radiation is a photon of light. Certain impurity ions have energy levels that lie higher in energy than the activator. When excited by electromagnetic energy, an impurity ion termed a sensitizer S can undergo spontaneous absorption (2), and it can be raised to an excited state. The excited state of the sensitizer will relax, a process that includes non-radiative energy losses to some lower excited state, at which point it can transfer its energy to the activator if energy levels in the activator have a resonant overlap with the relaxed excited state. The activator energy levels often sit slightly lower in energy preventing a back-transfer of the energy to the sensitizer. The compound  $\text{GdMgB}_5\text{O}_{10}:\text{Ce}^{3+}, \text{Tb}^{3+}$  is an example of a commercial phosphor that contains both an activator and a sensitizer. This material is isostructural to  $\text{YMgB}_5\text{O}_{10}$  found in Chapter 5, and it is used in deluxe fluorescent lamps.  $\text{Ce}^{3+}$  has a much stronger absorption cross-section in the UV where excited  $\text{Hg}^+$  ions emit. Energy absorbed by  $\text{Ce}^{3+}$  is transferred to  $\text{Tb}^{3+}$  with complete quenching of the  $\text{Ce}^{3+}$  emission when the number density of  $\text{Tb}^{3+}$  reaches a critical level, producing its characteristic green emission.

The plasma display panel (PDP) phosphor  $(\text{Y},\text{Gd})\text{BO}_3:\text{Eu}^{3+}$ , is an example of the process illustrated in Figure 1.1b, where absorption of an electromagnetic radiation field occurs in the phosphor host. The energy is absorbed by the host in a ligand-to-metal charge transfer (CT) of the  $\text{BO}_3$  group, and subsequently transferred to the  $\text{Eu}^{3+}$  activator. The absorption edges of borate materials (Table 1.1) are at slightly longer wavelengths in the VUV portion of the spectrum than where the Xe emission occurs (147 nm.) Crystal field splitting can cause a sufficient mixing of states to occur, broadening the absorption bands so that some borates, e.g.,  $(\text{Y},\text{Gd})\text{BO}_3:\text{Eu}^{3+}$  absorb efficiently over a wide region of the spectrum including at the Xe-

plasma emission. DV-SCM-X $\alpha$  calculations on the position of the absorption due to the CT transition place them, for an isolated anionic  $\text{BO}_3^{3-}$  group in which non-bonding O-orbitals are absent, at 150 – 160 nm.<sup>2</sup> Once absorbed, energy must be transferred to the activator. Blasse proposed that a linear interaction between absorbing group and activator ion, i.e., B – O – Eu, would increase the exchange interaction, because of the increased sigma overlap.<sup>14</sup> The efficiency, and the luminescence properties of the activator ion are related to the field that surrounds the dopant site. The relationship between the activator and the phosphor host has been investigated and the results are presented in Chapter 4. After consideration of these relationships, we proceeded to look for new materials in the ternary systems  $\text{Y}_2\text{O}_3 - \text{B}_2\text{O}_3 - \text{MgO}$  and  $\text{Y}_2\text{O}_3 - \text{B}_2\text{O}_3 - \text{YF}_3$ . From these systems we have identified and structurally and optically characterized the compounds  $\text{YMgB}_5\text{O}_{10}$  and  $\text{Y}_4\text{BO}_7\text{F}$ .

## Oxoanion Fluorides

Relatively few examples of oxoanion silicate and germanate fluoride materials have been structurally characterized. The compounds  $\text{Sr}_2\text{LiSiO}_4\text{F}$ ,<sup>15</sup>  $\text{Ca}_2\text{Mg}_5\text{Si}_8\text{O}_{22}\text{F}_2$ ,<sup>16</sup> and  $\text{Ca}_4\text{Si}_2\text{O}_7\text{F}_2$ <sup>17</sup> are a few examples of reported silicates, and  $\text{Ca}_{2.275}\text{GeO}_4(\text{O}_{0.45}\text{F}_{0.55})$ ,<sup>18</sup>  $\text{Mg}_{28}\text{Ge}_{7.55}\text{O}_{32}\text{F}_{15.04}$ ,<sup>19</sup> and  $\text{KMg}_{2.5}\text{Ge}_4\text{O}_{18}\text{F}_2$ <sup>20</sup> are the only reported examples of alkaline-earth germanate fluorides. To this list we add three new materials,  $\text{Li}_2\text{Ca}_6(\text{MeO}_4)_3\text{F}_2$  (Me = Si and Ge) and  $\text{Sr}_4\text{Ge}_2\text{O}_7\text{F}_2$ .

Our interest in finding new alkaline-earth silicate and germanate fluorides stems from the need for finding new phosphor and laser hosts. The commercial fluorescent lamp phosphor  $\text{Sb,Mn:Ca}_5(\text{PO}_4)_3\text{F}$  and the laser hosts  $\text{Yb:Ca}_5(\text{PO}_4)_3\text{F}$ <sup>21</sup> (Yb:FAP) and  $\text{Yb:Sr}_5(\text{PO}_4)_3\text{F}$ <sup>22</sup> (Yb:S-FAP) are examples of materials that possess similar chemical properties, and crystallographic features. The fluoroapatite  $\text{Ca}_5(\text{PO}_4)_3\text{F}$  structure has been investigated

extensively. Two Ca sites exist, and they are very different in their coordination. One Ca site has nine O atoms forming its coordination sphere, and the other is coordinated to six O and one F atom. It has been shown that lanthanide ions, for example  $\text{Nd}^{3+}$  and  $\text{Yb}^{3+}$ , substitute on the 7-coordinate Ca site by replacement of the F atom with O, resulting in a charge-balanced environment. This site provides a highly anisotropic crystal field that has a dramatic effect on the splitting of the energy levels for the dopant lanthanide ions and particularly for  $\text{Yb}^{3+}$ .

$\text{Ca}_5(\text{PO}_4)_3\text{F}$  (FAP) and  $\text{Y}_3\text{Al}_5\text{O}_{12}$  (YAG) with the garnet structure were the first two extensively studied materials for use as laser hosts for  $\text{Nd}^{3+}$ .  $\text{Nd:FAP}$  had roughly twice the emission cross section as  $\text{Nd:YAG}$ . The thermal and mechanical properties of YAG, however, are superior to FAP, and so  $\text{Nd:YAG}$  became the standard. The  $4f^{13}$  electronic configuration of  $\text{Yb}^{3+}$  is much different than the  $4f^3$  electronic configuration of  $\text{Nd}^{3+}$ .  $\text{Yb}^{3+}$  has only two accessible electronic states, the  $^2F_{7/2}$  ground state and the  $^2F_{5/2}$  excited state, with an energy separation of approximately  $10,000\text{ cm}^{-1}$ . There exists only a small window in the region of 925 nm in which to excite the  $\text{Yb}^{3+}$  ion, and this made initial laser experiments with Yb-doped lasers impractical, because only inefficient pumping schemes such as Xe flash lamps were available. Today it is possible to produce compact, all solid-state InGaAs diode pumps, providing efficient sources for excitation of Yb-doped laser crystals.

In all  $\text{Yb}^{3+}$  systems, thermal population of the ground-state levels occurs because of the relatively small energy separation of these levels. The highly anisotropic crystal fields that surround the  $\text{Yb}^{3+}$ -dopant site in FAP and S-FAP cause a larger splitting of the  $^2F_{7/2}$  ground, reducing the thermal population in the upper ground state levels, the same Stark levels for which laser emission terminates. This has the effect of lowering the saturation intensity by making population inversion easier to achieve, which reduces the thermal energy in the crystal, making the fluoroapatite structure a suitable choice for  $\text{Yb}^{3+}$ -doped laser crystals. The Ca and Sr sites in FAP and S-FAP are remarkably similar

to the two Ca sites in the compounds  $\text{Li}_2\text{Ca}_6(\text{MeO}_4)_3\text{F}_2$  (Me = Si, Ge), which are both seven coordinate and have O and F atoms in their coordination sphere, and to the four Sr sites ranging from six to eight coordinate and having O and F atoms coordination environments in  $\text{Sr}_4\text{Ge}_2\text{O}_7\text{F}_2$ . Thus, similar spectral results are expected for Yb in these hosts. The spectrum of  $\text{Yb}:\text{Li}_2\text{Ca}_6(\text{GeO}_4)_3\text{F}_2$  is presented in Chapter 8.

## References

1. Bordui P. F. and Fejer M. M., *Annu. Rev. Mater. Sci.*, 23, **1993**, 321.
2. Kato K., *IEEE J. Quantum Electron.* 22(7), **1986**, 1013.
3. Chen C., Wang Y., Xia Y., Wu B., Tang D., Wu K., Wenrong Z., Yu L. and Mei L., *J. Appl. Phys.*, 77(6), **1995**, 2268.
4. Tu J-M. and Keszler D. A., *Mater. Res. Bull.*, 30(2), **1995** 209.
5. Mori Y., Kuroda I., Nakajima S., Sasaki T. and Nakai S., *Appl. Phys. Lett.*, 67(13), **1995**, 1818.
6. Petrov V., Rotermund F., Noack F., R. Komatsu, Sugawara T., and Uda S., *J. Applied Physics*, 84(11), **1998**, 5887.
7. Aka G., Viegas N., Telsseire B., Kahn-Harari A. and Godard J., *J. Mater. Chem*, 5(4), **1995**, 583.
8. Ostroumov V., Petermann K., Huber G, Ageev A. A., Kutovoj S., Kuzmin O., Panyutin V., Pfeifer E. and Hinz A., *J. Luminescence*, 72-74, **1997**, 826.
10. Huber G., Jensen T., Meyn J. P., *IEEE J. Quantum Electronics*, 30, **1994**, 913.
11. Fan S-J., Shen G-S., Wang W., Li J-L. and Le X-H., *J. Crystal Growth*, 99, **1990**, 811.
12. Chani V. I., et. al., *J. Crystal Growth*, 133, **1993**, 173.

- 
13. Chani V. I., et. al., *J. Crystal Growth*, 133, **1993**, 181.
  13. Itoh K., Marumo F. and Kuwano Y., *J. Crystal Growth*, 106, **1990**, 728.
  14. Blasse G., *J. Chem. Phys.* 45, **1966**, 2356.
  15. Akella A., Keszler, D. A., *Chem. Mater.* 7, **1995**, 1299.
  16. Cameron M., Gibbs G. V., *Am. Mineral.* 58, **1973**, 879.
  17. Smirnova R. F., Rumanova I. M., Belov N. V., *Zap. Vsesoy. Mineralog. Obschch.* 84, **1955**, 159.
  18. Nishi F., Takeuchi Y., *Acta Crystallogr., Sect. C* 40, **1984**, 730.
  19. Bless P.W., Dreele R.B., von Kostiner E., Hughes R.E., *J. Solid State Chem.* 4, **1972**, 262.
  20. Toraya H., Iwai, S., Marumo F., Hirao M., *Z. Kristallogr.* 148, **1978**, 65.
  21. DeLoach L. D., Payne, S. A., Chase L. L., Smith L. K., Kway W.L., and Krupke W. F., *IEEE J. Quantum Electron.* 29, **1993**, 1179.
  22. Marshall C. D., Smith L. K., Beach R. J., Emanuel M. A., Schaffers K. I., Skidmore J., Payne S. A., Chai B. T., *IEEE J. Quantum Electron.* 32, **1996**, 650.

## CHAPTER 2

### TRIGONAL HUNTITE BORATE $\text{CeSc}_3(\text{BO}_3)_4$ (CSB)

Gregory A. Peterson, Thomas A. Reynolds, and Douglas A. Keszler

To be submitted to Journal of Solid-State Chemistry.

## Abstract

Crystals of trigonal, stoichiometric  $\text{CeSc}_3(\text{BO}_3)_4$  (CSB) have been grown from a high-temperature solution by employing an  $\text{LiBO}_2/\text{LiF}$  flux. The structure has been determined on the basis of X-ray diffraction measurements. The material crystallizes with three formula units in a cell dimensions  $a = 9.796(1)$  and  $c = 7.960(2)$ . Luminescence data have been used to derive energy levels schemes for Ce in CSB and Nd in Nd:CSB.

## Introduction

The compound  $\text{CeSc}_3(\text{BO}_3)_4$  (CSB) is one member of a large class of compounds  $\text{LnM}_3(\text{BO}_3)_4$  ( $\text{Ln}$  = lanthanide,  $\text{M}$  = Al, Sc, Cr, Fe, Ga) that crystallize in the structure of the mineral huntite,  $\text{CaMg}_3(\text{CO}_3)_4$ .<sup>1</sup> These materials generally adopt a noncentrosymmetric structure, trigonal space group  $R\bar{3}2$ , that affords relatively high second order optical nonlinearities.<sup>2</sup> Interest in the Sc borate derivatives derives from the exceptional slope efficiency of the laser crystal Nd:LaSc<sub>3</sub>(BO<sub>3</sub>)<sub>4</sub> (Nd:LSB)<sup>3</sup> and the potential to observe self-frequency doubling. Both LSB and CSB crystals have been grown directly from the melt by using the Czochralski technique. These crystals, however, form in the centrosymmetric space group  $C2/c$  as distorted versions of the trigonal huntite structure, and second-order nonlinear effects can not be observed. Trigonal forms of the Sc borate huntites have been produced by incorporating high concentrations of smaller lanthanides, e.g., Gd. Here trigonal crystals such as  $\text{La}_{0.8}\text{Gd}_{0.2}\text{Sc}_3(\text{BO}_3)_4$  and  $\text{Ce}_{0.8}\text{Gd}_{0.2}\text{Sc}_3(\text{BO}_3)_4$  can be grown directly from the melt. The quality of these crystals and their optical performance, however, have been poor, presumably because of the strain introduced from the size mismatch of the large (La, Ce) and small (Gd) lanthanides.



To circumvent these limitations and to produce a transparent, stoichiometric trigonal Sc borate huntite we have examined the phase formation of  $\text{CeSc}_3(\text{BO}_3)_4$  at temperatures well below its melting. We have been prompted to do so because of related high-temperature phase transformations  $\text{R}32 \rightarrow \text{C}2/c$  that have been reported for the Al huntite borate  $\text{YAl}_3(\text{BO}_3)_4$ .<sup>4</sup> In this contribution, we describe the crystal growth, structural characterization, and optical properties of the trigonal Sc borate huntite  $\text{CeSc}_3(\text{BO}_3)_4$ .

## Materials and Methods

Regular, block-shaped crystals of  $\text{CeSc}_3(\text{BO}_3)_4$  were obtained by melting the undoped powder in a 45-mm diameter, 50-mL Pt crucible with a  $\text{LiBO}_2$ -LiF flux. The melt composition in wt % was 55:5:40  $\text{LiBO}_2$ :LiF:CSB. The crystal-growth system consisted of a resistance-heated furnace, and a Mellen computer-controlled vertical pulling system. A series of mullite and alumina baffles were used to produce horizontal and vertical temperature gradients near 21 and 13 K/cm, respectively. The crucible was supported inside a closed alumina tube under a 4%  $\text{H}_2/\text{Ar}$  atmosphere. A Pt rod attached to an alumina shaft was employed to initiate crystallization. The rod was rotated at a rate of 9 rpm, and the furnace was cooled at 12 K/day. A polycrystalline boule 3 mm-thick with a 16 mm-diameter containing large optically clear crystals was removed from the melt after 7 days of crystal growth, then the melt and crystals were cooled at a rate of 20 K/hr to room temperature. The crystalline mass was placed in warm dilute  $\text{HNO}_3$  and heated for 24 h to aid in the separation of the crystals.

A crystal of approximate dimensions 0.3 x 0.25 x 0.15 mm was physically separated from the solidified boule and mounted on a glass fiber with epoxy for structure determination. All measurements were made on a Rigaku AFC6R diffractometer with graphite-monochromated  $\text{Mo K}\alpha$  radiation. Cell parameters and the orientation matrix for the data collection were obtained from a least-

squares refinement with 25 automatically-centered reflections in the range  $28 < 2\theta < 38^\circ$ . Intensity data were collected over the range of indices  $-7 < h < 15$ ,  $-15 < k < 15$ ,  $-6 < l < 12$  by using an  $\omega$ - $2\theta$  scan technique to a maximum  $2\theta$  value of  $70^\circ$ . A total of 2712 general reflections were collected, and 663 were observed ( $F_o^2 > 2\sigma(F_o^2)$ ) and unique. The structure was solved and refined by using SHELXS-97<sup>5</sup> and SHELXL-97.<sup>6</sup> The computer program Texsan<sup>6</sup> was used to apply Psi-scan corrections to the raw data prior to use of SHELXS. Final least-squares refinement on  $F_o^2$  resulted in the residuals  $R(F_o^2 > 2\sigma(F_o^2)) = 0.022$  and  $wR(F_o^2) = 0.056$ . The largest peak in the final difference electron-density map was 3.3% of a Ce atom.

Powder samples of CSB and  $\text{Ce}_{0.98}\text{Nd}_{0.02}\text{Sc}_3(\text{BO}_3)_4$  were made by combining stoichiometric quantities of  $\text{CeO}_2$  (Stanford Materials 99.999%),  $\text{Nd}_2(\text{C}_2\text{O}_4)_3 \cdot 10\text{H}_2\text{O}$  (Alfa-Aesar, 99.9%,)  $\text{Sc}_2\text{O}_3$  (Stanford Materials, 99.99%,) and (5 mol % excess)  $\text{B}_2\text{O}_3$  (Alfa-Aesar, 99.98%). A series of grinding and heating steps were executed prior to a final anneal at 1373 K for 12 h.

Luminescence data were collected in our laboratory. Excitation provided by an Oriel 300-W Xenon lamp was passed through a 50-cm water filter, focused onto the entrance slits of a Cary model-15 double prism monochromator, and subsequently directed onto the sample. Luminescence was collected at a right angle to the excitation beam through an Oriel 22500 1/8-m monochromator with interchangeable gratings. A ruled grating blazed at 500 nm was used for Ce emission, and one grazed at 1000 nm (spectral resolution ca. 0.2 nm) was used for collecting the  $\text{Nd}^{3+}$  emission. A Hamamatsu R636 photomultiplier tube (PMT) was used for detecting emission of CSB, and a Hamamatsu R1767 S-1 type PMT was cooled with dry ice for detection of the  $\text{Nd}^{3+}$  emission. The signal was collected and amplified with a Keithley model 486 picoammeter and converted to a digital signal for computer acquisition. Spectrometer control and data acquisition were achieved with computer programs written in this laboratory. The excitation spectra were corrected by using sodium salicylate and rhodamine B as quantum counters. The emission spectra were corrected with a tungsten lamp that has been calibrated at Eppley

Laboratories, Inc. Data were plotted as relative emitted energy per constant energy interval, and peak positions were determined by fitting the spectra with Gaussian profiles. Low temperature spectra were collected by using a Cryo Industries (Model CRG-102) cryostat. The sample was cooled to 78 K with  $N_2(l)$ , and a Conductus LTC-10 temperature controller was used to regulate the temperature for data collection.

## Results and Discussion

Crystal data and experimental conditions for the X-ray experiment are summarized in Table 2.1. Atomic coordinates and the isotropic displacement coefficients are listed in Table 2.2, and selected interatomic distances and angles are summarized in Table 2.3.

A *c*-axis view of the unit cell contents for  $CeSc_3(BO_3)_4$  is given in Figure 2.1. The Ce atom occupies a distorted trigonal prism, the Sc atom a distorted octahedron, and the B atoms triangles. The three-fold symmetry of the trigonal cell may be readily appreciated by passing rotation axes through atoms Ce and B2. The  $BO_3$  group formed by B2 and O3 is an equilateral triangle with  $D_3$  symmetry, its B2-O3 vertexes are directed along the cell edges and *ab* face diagonals. The Ce atom lies at the center of a slightly twisted, trigonal prism with six equivalent bonds to O1.  $D_3$  symmetry is clearly illustrated for the Ce atoms at positions  $(2/3, 1/3, 1/3)$  and  $(1/3, 2/3, 2/3)$  in Figure 2.1. The B1 atom is bonded to two O1 atoms and one O2 atom, and it occupies a site of  $C_2$  symmetry with the  $C_2$  axis parallel to the *ab* plane. As shown in Figures 2.2(a) and (b), the  $BO_3$  groups extend in layers parallel to the *ab* plane. The  $ScO_6$  distorted octahedra condense by sharing edges  $O2 \cdots O3$  to form helical columns that propagate along the *c* axis, (Figure 2.3(a).) Each Sc atom is bonded to two each of the atoms O1, O2, and O3. Each of the vertexes of the  $ScO_6$  octahedra is shared by a  $BO_3$  plane, which shares additional vertexes with the Ce-centered trigonal prism. With this connectivity, a set of six  $ScO_6$  octahedra

circumscribe each trigonal prism in the *ab* plane (Figure 2.3(b).) Each O atom has threefold coordination. Atom O1 is coordinated by Ce, Sc and B1; atom O2 by two Sc atoms and B1; and O3 by two Sc atoms and B2.

Interatomic distances and angles are listed in Table 2.3. All B-O distances and O-B-O angles are normal, and they compare well to those of ScBO<sub>3</sub>, B-O distance = 1.3752(5) Å, and the O-B-O angles are 120°. <sup>7</sup> Atom B1 binds to atoms O1 and O2 at the vertices of a triangle having C<sub>2</sub> symmetry, while atom B2 centers an equilateral triangle of O3 atoms.

The Ce atom is bound to six O1 atoms, each at a distance of 2.451(3) Å. This distance compares well to those reported for the lanthanide borosilicate mineral stillwellite, which has a nine-coordinate Ce-centered site with distances ranging from 2.341 to 2.729 Å. <sup>8</sup>

The average Sc-O distance is 2.102(3) Å, which compares well to the Sc-O distances of 2.1200(4) Å in ScBO<sub>3</sub>. There are two distorted ScO<sub>6</sub> octahedral sites in Sc<sub>2</sub>O<sub>3</sub>; <sup>9</sup> one site has six Sc-O distances at 2.120 Å, and the second has three Sc-O distances, two each at 2.080, 2.125, and 2.164 Å. The O-Sc-O angles around the less symmetrical Sc site in Sc<sub>2</sub>O<sub>3</sub> are similar to those of the CSB structure, ranging from 79.2 to 164.5° for the equatorial and axial angles.

Table 2.1. Crystal data and experimental conditions for  $\text{CeSc}_3(\text{BO}_3)_4$ .

Diffractometer	Rigaku AFC6R
Radiation	0.71703 Å graphite monochromated Mo K $\alpha$
Formula wt., amu	327.27
Unit cell	Trigonal (Hexagonal Axes)
a, Å	9.796(1)
c, Å	7.960(2)
V, Å <sup>3</sup>	661.5(2)
Space group	R32 (#155)
Z	3
D <sub>calc</sub> , g cm <sup>-3</sup>	3.842
F(000)	711
Absorption coeff., $\mu$ cm <sup>-1</sup>	7.345
No. of unique data with $F_o^2 > 2\sigma F_o^2$	663
$R[F_o^2 > 2\sigma F_o^2]^*$	0.022
$wR(F_o^2)^*$	0.056

$$^*R = \Sigma(|F_o^2| - |F_c^2|) / \Sigma|F_o^2|; R_w = [\Sigma w(|F_o^2| - |F_c^2|)^2 / \Sigma w|F_o^2|^2]^{1/2}$$

Table 2.2. Atom positions and  $U_{eq}$  for  $\text{CeSc}_3(\text{BO}_3)_4$ .

Atom	x	y	z	$U_{eq}^*$
Ce	0	0	0	0.0072(2)
Sc	0.11863(1)	1/3	1/3	0.0048(2)
O1	-0.1914(3)	0.0201(3)	-0.1813(3)	0.0087(4)
O2	0	0.4097(5)	1/2	0.0126(7)
O3	0.5092(3)	0.1408(4)	1/2	0.0065(5)
B1	0	0.5494(5)	1/2	0.0069(6)
B2	0	0	1/2	0.0062(9)

$$^*U_{eq} = (1/3)\Sigma_i\Sigma_j U_{ij}a_i a_j a_j.$$

Table 2.3. Selected bond distances and angles for CeSc<sub>3</sub>(BO<sub>3</sub>)<sub>4</sub>.

Atoms	Distance Å	Atoms	Degrees ( ° )
Ce – O1	2.451(3)	O(1) – Ce – O(1)	88.84(9)
		O(1) – Ce – O(1)	124.8(1)
Sc – O1	2.061(3)	O(1) – Ce – O(1)	140.0(1)
Sc – O2	2.131(3)	O(1) – Ce – O(1)	72.7(1)
Sc – O3	2.115(3)		
		O(1) – Sc – O(1)	101.1(1)
B1 – O1	1.374 (4)	O(1) – Sc – O(3)	94.9(9)
B1 – O2	1.368 (8)	O(1) – Sc – O(3)	92.7(1)
		O(1) – Sc – O(2)	86.6(7)
B2 – O3	1.380 (4)	O(1) – Sc – O(2)	167.5(1)
		O(2) – Sc – O(2)	87.7(4)
Ce – Ce	6.247(3)	O(3) – Sc – O(2)	76.7(1)
		O(3) – Sc – O(2)	94.7(1)
		O(1) – B1 – O(1)	123.5(4)
		O(1) – B1 – O(2)	118.3(2)
		O(3) – B2 – O(3)	120.000(1)

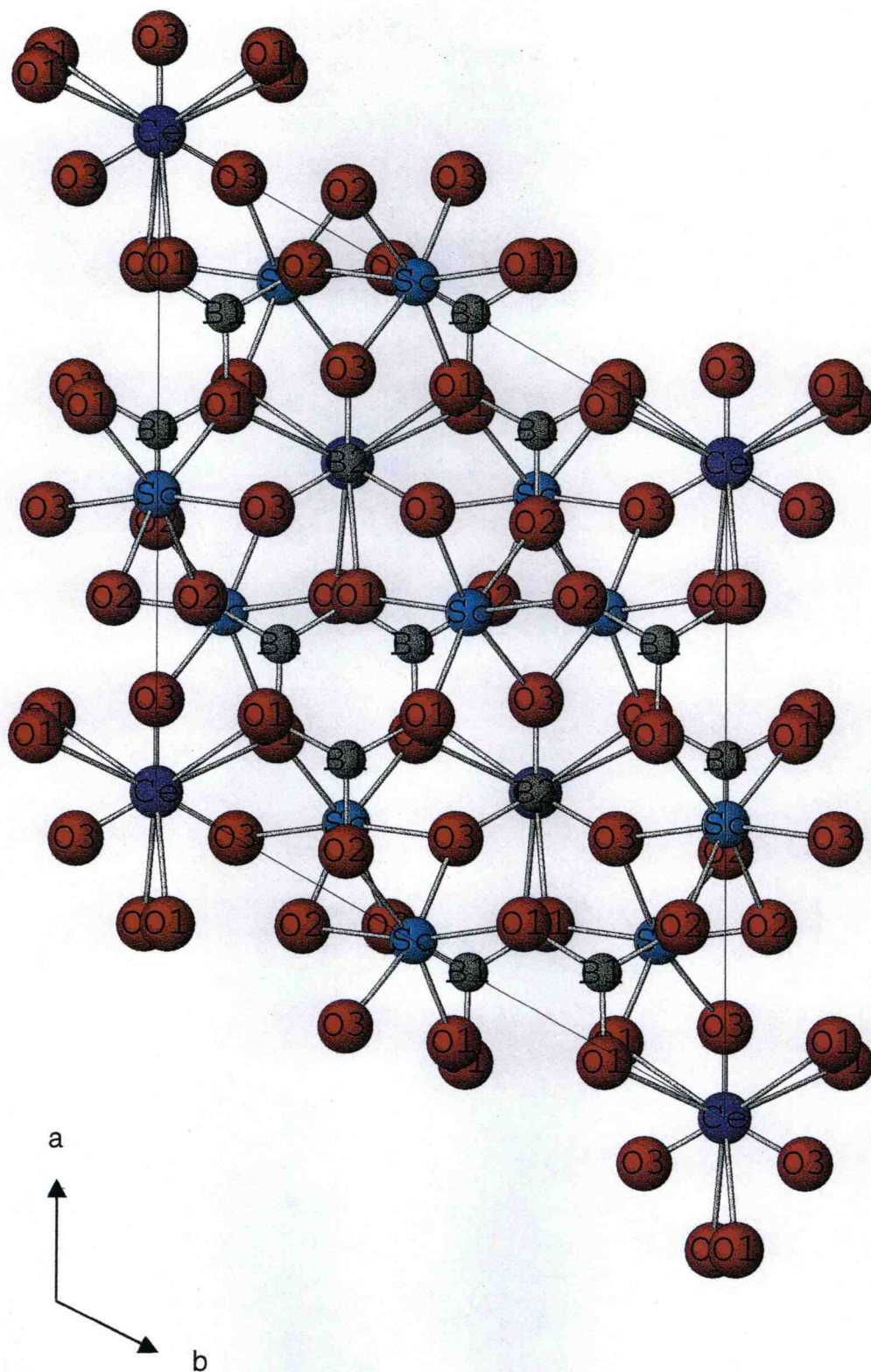
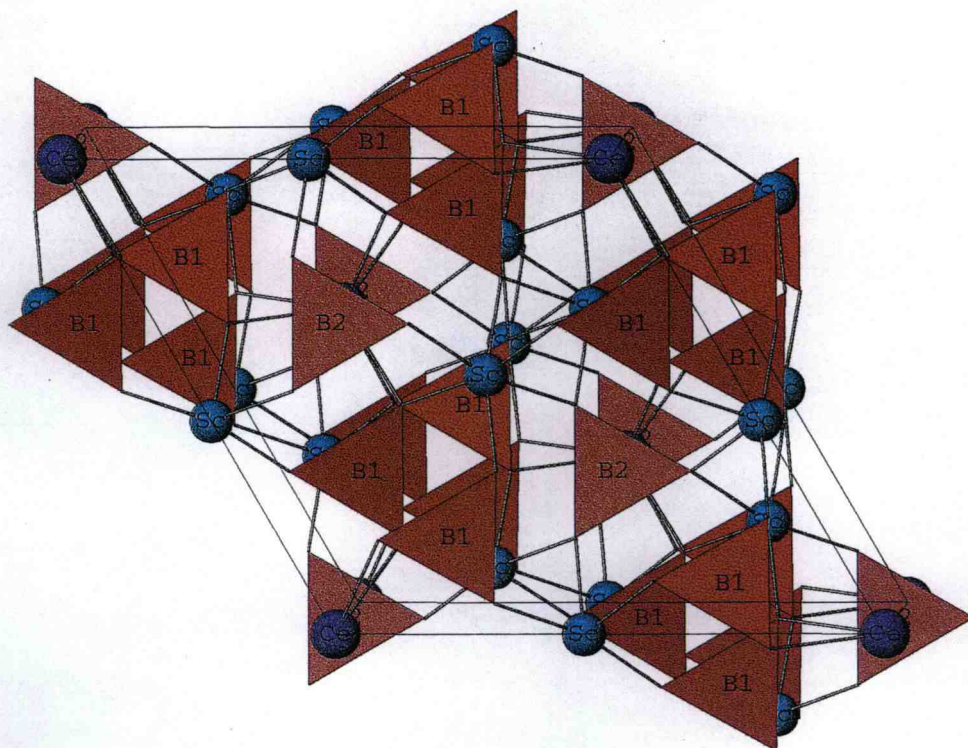
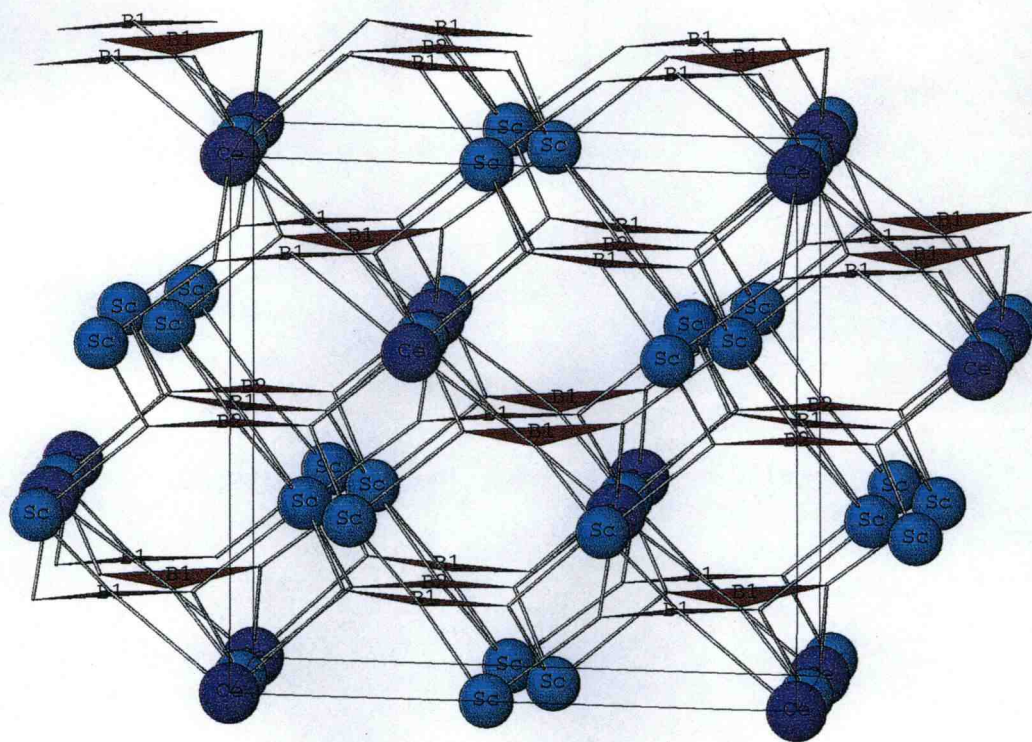


Figure 2.1. Unit-cell contents viewed down the  $c$  axis.





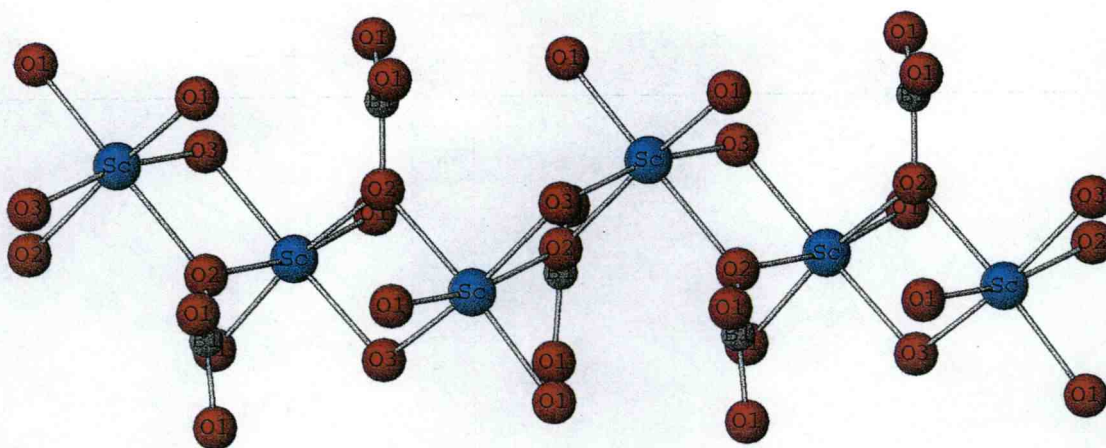
a)



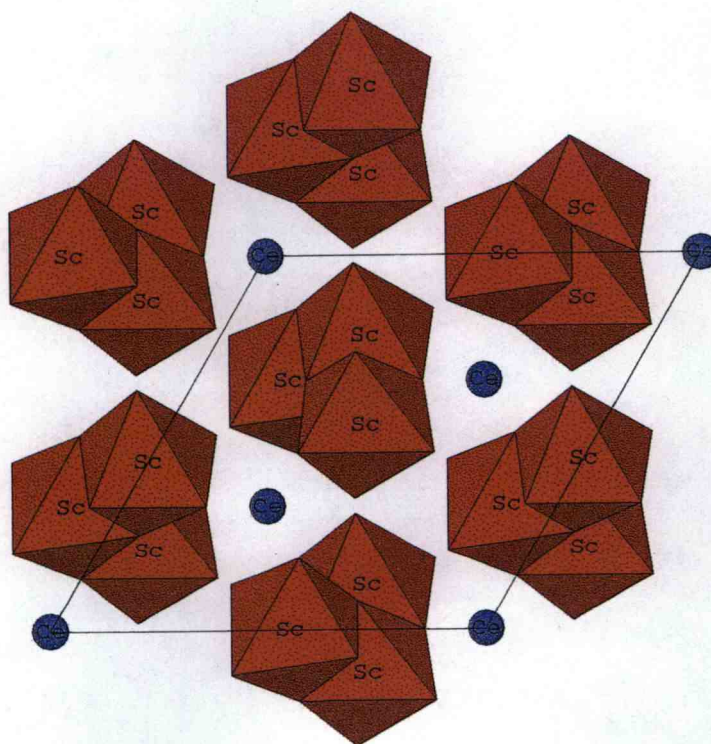
b)

Figure 2.2. Borate polyhedra: a) viewed down [001] b) viewed down [010].





a)



b)

Figure 2.3. a) Columnar Sc-centered octahedra spiraling along the  $c$  axis.  
b) Sc-centered polyhedra viewed down the  $c$  axis.

## Spectroscopic Studies

The ground-state,  $4f^1$  electron configuration of  $Ce^{3+}$  is split into two energy levels,  $^2F_{5/2}$  and  $^2F_{7/2}$ , by spin-orbit coupling. The splitting of these two levels is normally on the order of  $2000\text{ cm}^{-1}$ .<sup>10</sup> Excitation of  $Ce^{3+}$  is associated with a  $4f^1 \rightarrow 4f^0 5d^1$  electronic transition, which is parity allowed. The energetic position of this transition is strongly affected by the surroundings of the  $Ce^{3+}$  ion, resulting in broad excitation and emission bands. Because excited-state electrons can relax to  $^2F_{5/2}$  and  $^2F_{7/2}$ , emission is normally characterized by a broad overlapping double emission band falling in the near UV or blue regions of the spectrum.

Excitation and emission spectra are given in Figures 2.4, 2.5, and 2.6. Excitation profiles recorded at 78 and 300 K, Figures 2.4 and 2.5, respectively, exhibit bands with shoulders that represent excitation from both  $^2F_{5/2}$  and  $^2F_{7/2}$  levels to the crystal-field components of the excited state. The presence of three primary bands at 27180, 31890, and 35590  $\text{cm}^{-1}$  is consistent with the d-orbital splitting pattern for a trigonal prismatic environment,  $a + 2e$ . The shoulders are separated from the main peaks by approximately 2100 and 3100  $\text{cm}^{-1}$  at 78 and 300 K respectively, providing an estimate of the spin-orbit coupling of the ground state levels. These results are consistent with those reported for  $Ce:YAl_3(BO_3)_4$ .<sup>11</sup>

A splitting of  $\sim 2100\text{ cm}^{-1}$  between the  $^2F_{5/2}$  and  $^2F_{7/2}$  is calculated from the energy difference in the maxima of the two emission peaks at 78 K (Figure 2.4.) At 300 K, the splitting is closer to  $3000\text{ cm}^{-1}$  (Figure 2.5,) a result that is consistent with the slightly larger, and more symmetrical Ce site at higher temperatures.<sup>12</sup> These results are also consistent with those derived from the excitation spectra.

The 78-K emission spectrum of  $Nd:CSB$  is given in Figure 2.6. The spectrum is dominated by two main features, emission from  $^4F_{3/2} \rightarrow ^4I_{11/2}$  and  $^4F_{3/2} \rightarrow ^4I_{9/2}$ , with their most intense peaks at 9400 and 11260  $\text{cm}^{-1}$  respectively. Substitution of  $Nd^{3+}$  on the  $Ce^{3+}$  sites with  $D_3$  symmetry results in a lifting of the

degeneracy of the shielded multiplets of f-orbital parentage. The metastable  $^4F_{3/2}$  manifold with  $2J+1$  degeneracy is split into two doubly-degenerate levels (Kramers doublets.) Excited-state population from this manifold is channeled into the doubly-degenerate levels of the  $^4I_j$  multiplets. These transitions giving rise to luminescence can terminate on eight  $^4I_{15/2}$  levels with emission at ca. 1900 nm, seven  $^4I_{13/2}$  levels with emission at ca. 1300 nm, six  $^4I_{11/2}$  levels with emission at ca. 1060 nm, and five  $^4I_{9/2}$  levels containing the ground state near 890 nm.

Within the excited state at 78 K, thermal population of both levels of the split, metastable  $^4F_{3/2}$  will occur, giving rise to luminescence from both levels. The intensity of these transitions are dictated by dipole-selection rules, the fractional population of the excited state levels as determined by the partition function, and nonradiative pathways. Figure 2.6 is an energy-level diagram for  $\text{Nd}_{0.02}\text{Ce}_{0.98}\text{Sc}_3(\text{BO}_3)_4$  derived from the energy spectrum in Figure 2.5. The results are comparable to those of the stoichiometric compound  $\text{NdSc}_3(\text{BO}_3)_4$ .<sup>13</sup>

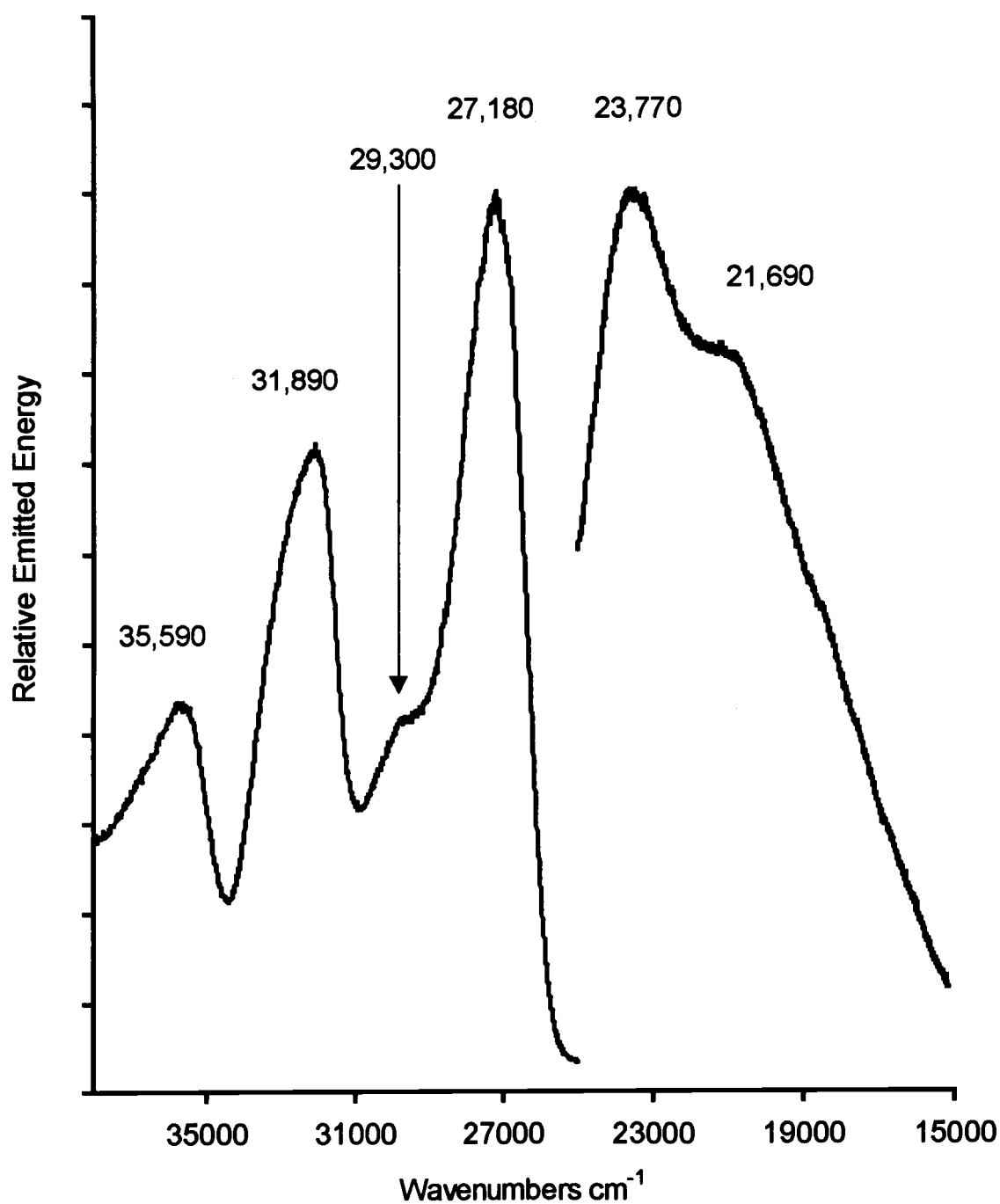


Figure 2.4. Ce excitation (left) and emission (right) energy spectrum for  $\text{CeSc}_3(\text{BO}_3)_4$  at 78 K.

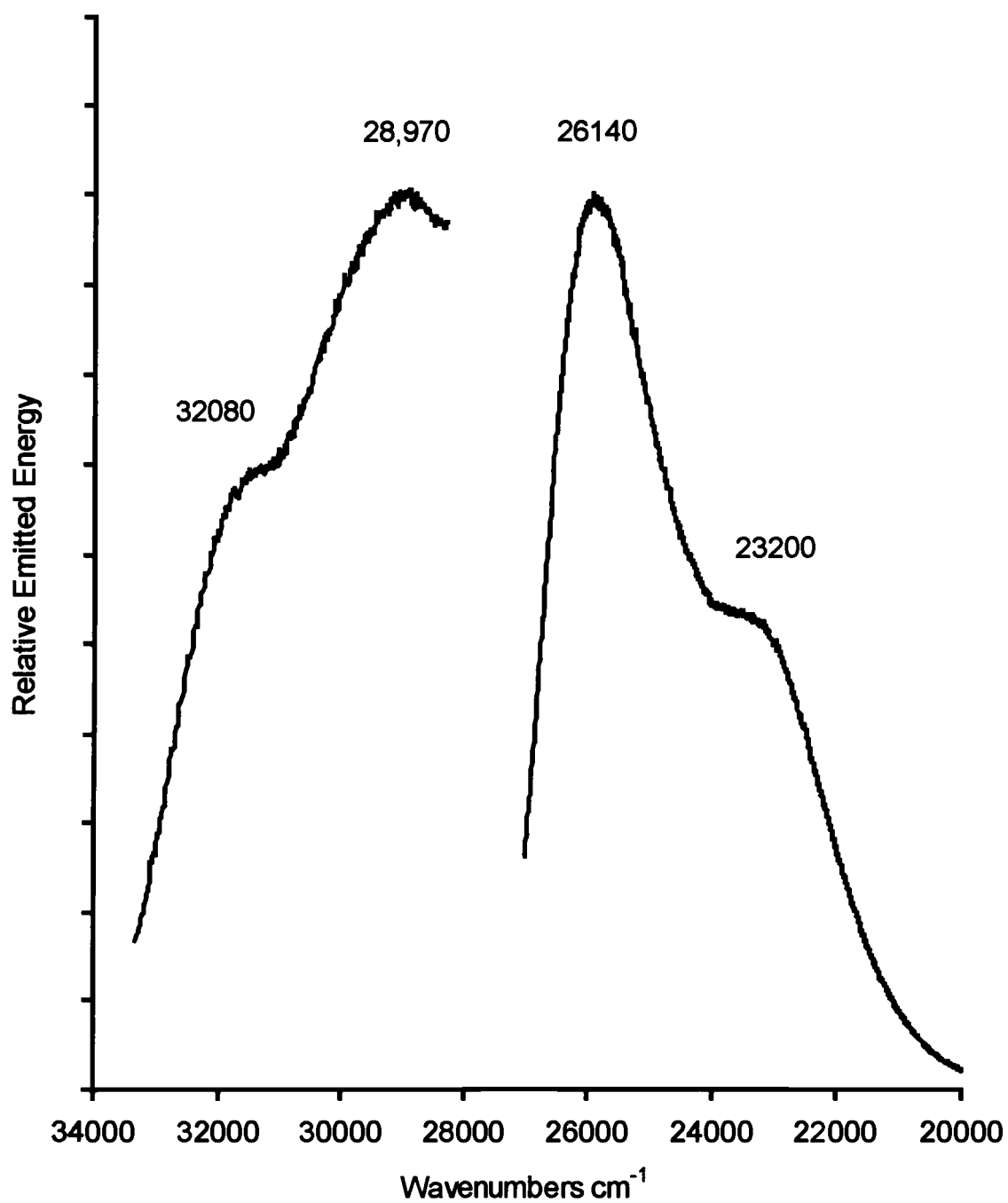


Figure 2.5. Ce excitation (left) and emission (right) energy spectrum for  $\text{CeSc}_3(\text{BO}_3)_4$  at 300 K.

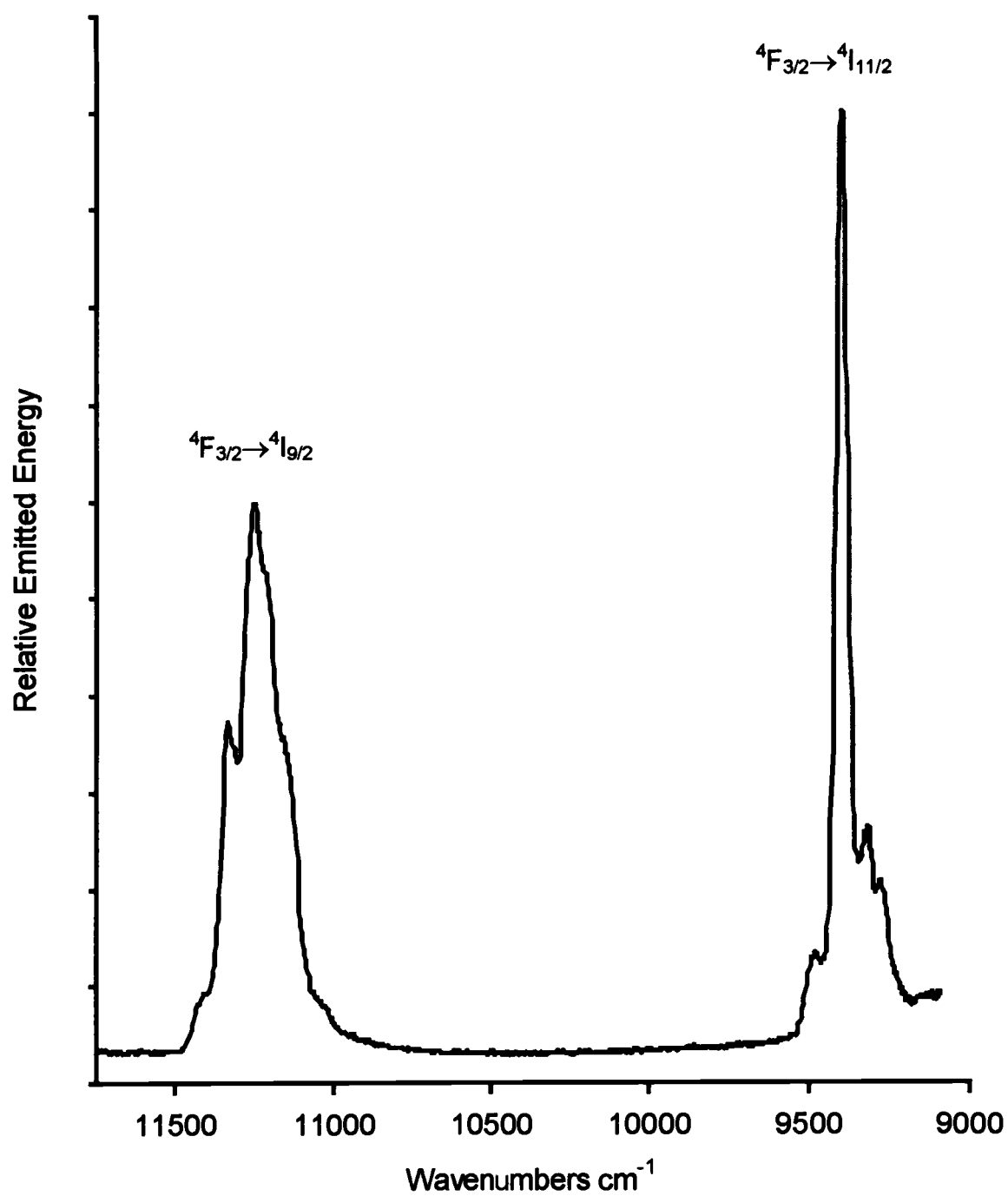


Figure 2.6. Energy spectrum of  $\text{Nd}_{0.02}\text{Ce}_{0.98}\text{Sc}_3(\text{BO}_3)_4$ .

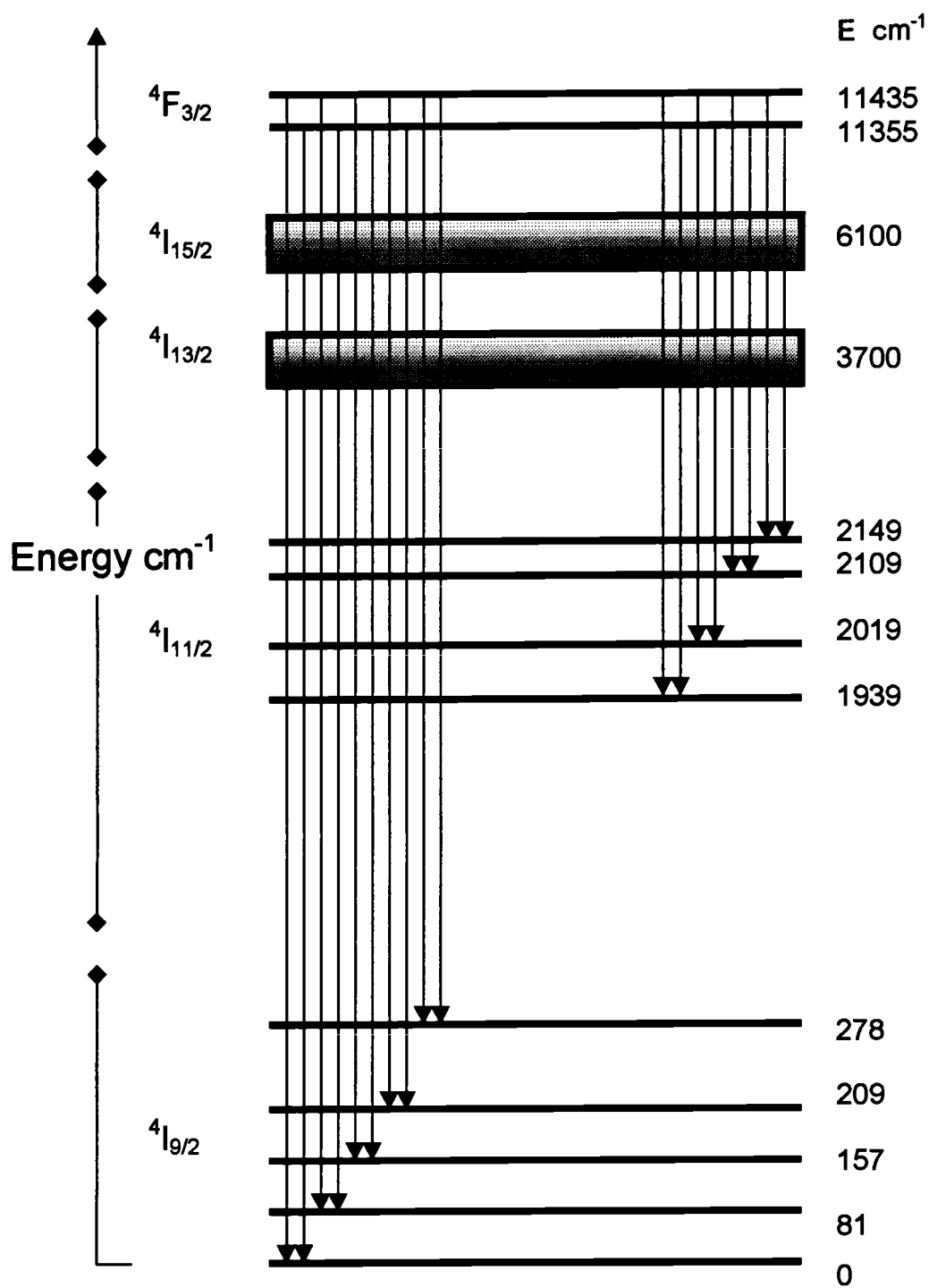


Figure 2.7. Energy level diagram for  $\text{Nd}_{0.02}\text{Ce}_{0.98}\text{Sc}_3(\text{BO}_3)_4$ .

## Summary

Crystals of the noncentrosymmetric, trigonal phase of  $\text{CeSc}_3(\text{BO}_3)_4$  have been grown by using a high-temperature solution method. An energy diagram has been constructed for  $\text{Ce}_{0.98}\text{Nd}_{0.02}\text{Sc}_3(\text{BO}_3)_4$ , and the results are similar to those reported for the stoichiometric compound  $\text{NdSc}_3(\text{BO}_3)_4$ .

## Acknowledgments

The authors thank the National Science Foundation, Solid State Chemistry Program, for supporting this research. We also wish to thank Scott Lovell and Alex Yokochi for assistance with the crystal-structure solution.



## References

---

1. Graf D. L., and Bradley W. F., *Acta Cryst.* 15, **1962**, 238.
2. Meyn J-P., Jensen T., Huber G., *IEEE J. Quantum Electron.* 30(4), **1994**, 913.
3. Ostroumov V., Petermann K., Huber G., Ageev A. A., Kutovoj S., Kuzmin O., Panyutin V., Pfeifer E., Hinz A., *J. Lumin.* 72-74., **1997**, 826.
4. Belokoneva E. L., and Timchenko T. I., *Sov. Phys. Crystallogr.* 28(6), **1983**, 658.
5. Sheldrick, G. M., Institut für Anorganische Chemie der Unniversitat, Gottingen, FRG.
6. *Texsan for Windows*, Version 1.0 (1997).  
Molecular Structure Corporation, 3200A Research Forest Drive,  
The Woodlands, TX 77381, USA.
7. Sun H., Keszler D. A., *Acta Cryst. Sect. C44*, **1988**, 1505.
8. Voronkov A. A., Pyatenko Y. A., *Kristallografiya* 12, **1967**, 258.
9. Norrestam R., *Arkiv foer Kemi*, 29, **1968**, 343.
10. Henderson B., and Imbush G. B., *Optical Spectroscopy of Inorganic Solids*, Clarendon Press, Oxford UK, **1989**.
11. Kellendonk F., van den Belt T., Blasse G., *J. Chem. Phys.*, 76(3), **1982**, 1194.
12. Blasse G., and Bril A., *J. Chem. Phys.*, 47(12), **1967**, 5139.
13. Reynolds T. A., Keszler D. A., Gruber J. B., Zhandi B., *Submitted to J. Lumin.*, **1999**.

## CHAPTER 3

### THE NONCENTROSYMMETRIC ALKALI METAL BORATE $\text{NaLiB}_4\text{O}_7$

Gregory A. Peterson, Jun-Ming Tu, and Douglas A. Keszler

In preparation for submission to Journal of Solid State Chemistry

## Abstract

The compound  $\text{NaLiB}_4\text{O}_7$  has been synthesized and its structure determined by single-crystal X-ray diffraction methods. It crystallizes in the orthorhombic space group  $Fdd2$  with  $Z = 16$ . The structure contains two interpenetrating, polyborate frameworks. Sites in channels extending along both the  $a$  and  $b$  axes are filled with either Na or Li atoms. A phase diagram of the binary system  $\text{Li}_2\text{B}_4\text{O}_7$ - $\text{Na}_2\text{B}_4\text{O}_7$  constructed from thermal-analysis data indicates that the title compound undergoes a peritectic decomposition at approximately 1045 K. Crystal growth from a stoichiometric melt of  $\text{NaLiB}_4\text{O}_7$  leads to a  $1.5 \times 1.0$  cm cylindrical boule of approximate composition  $\text{Na}_{0.5}\text{Li}_{1.5}\text{B}_4\text{O}_7$ . This result is consistent with the incongruent characteristics of the material and the immiscibility gap in the  $\text{NaLiB}_4\text{O}_7$ - $\text{Li}_2\text{B}_4\text{O}_7$  solid solution. An assessment of the nonlinear optical properties of the title compound is made on the basis of a Kurtz-Perry test and a consideration of the structure.

## Introduction

Lithium tetraborate,  $\text{Li}_2\text{B}_4\text{O}_7$ , has recently been examined as a possible nonlinear optical material for conversion into the vacuum ultraviolet by using sum-frequency mixing with femtosecond pulses.<sup>1</sup> The crystals are transparent from 170 to 3300 nm, and they can be grown by the Czochralski or Bridgman methods with few defects. They have also been extensively studied for applications in surface acoustic wave (SAW) and bulk acoustics wave (BAW) devices. The favorable characteristics of  $\text{Li}_2\text{B}_4\text{O}_7$  derive from a combination of high SAW coupling coefficient and small loss tangents as well as the relatively low density compared with  $\text{LiNbO}_3$  (LN) or  $\text{LiTaO}_3$  (LT).<sup>2</sup> It is believed that  $\text{Li}_2\text{B}_4\text{O}_7$  is very suitable for the design of SAW devices for high frequency applications requiring temperature compensation. As part of our interest in

synthesizing new noncentrosymmetric materials, we have identified the new compound  $\text{NaLiB}_4\text{O}_7$ , which exhibits a noncentrosymmetric structure similar to that of  $\text{Li}_2\text{B}_4\text{O}_7$ . In this contribution, we describe the structure and melting characteristics of this new polyborate. Commonly, the  $\text{B}_4\text{O}_7$  formulation results from the full condensation of  $\text{B}_4\text{O}_9$  rings. Examples of such polyborate structures are observed in the materials  $\text{Li}_2\text{B}_4\text{O}_7$ ,<sup>3</sup>  $\text{K}_2\text{B}_4\text{O}_7$ ,<sup>4</sup> and now the title compound.

## Material and Methods

Crystals of  $\text{NaLiB}_4\text{O}_7$  for single crystal X-ray diffraction were grown in a Pt crucible from a stoichiometric melt that was prepared from  $\text{NaNO}_3$  (JTB, ACS grade),  $\text{LiNO}_3$  (ALFA, reagent grade), and  $\text{B}_2\text{O}_3$  (ALFA, 99.98%). The melt was cooled from 1093 to 830 K at 6 K/h and then rapidly brought to room temperature by turning off the power to the furnace. A clear, block-shaped crystal of approximate dimensions 0.10 x 0.08 x 0.06 mm was mounted on a glass fiber with epoxy for X-ray structure analysis. Data were collected with Mo  $K\alpha$  radiation on a Rigaku AFC6R diffractometer. Unit-cell parameters were determined by automatic centering and least-squares refinement of the setting angles of 20 reflections in the range  $30 < 2\theta < 39^\circ$ . Laue symmetry was established as mmm on the diffractometer. The  $\omega$ -2 $\theta$  scan technique (scan speed =  $8^\circ / \text{min}$  in  $\theta$ ) was used to collect data covering the range of indices  $0 \leq h \leq 21$ ,  $0 \leq k \leq 22$ , and  $0 \leq l \leq 17$ . The space group Fdd2 was uniquely determined from the systematic absences  $hkl$ ,  $h+k$ ,  $k+l$ ,  $h+l = 2n+1$ ;  $0kl$ ,  $k+l = 4n$ ;  $h0l$ ,  $h+l = 4n$ . From the 998 measured reflections, 577 had  $F_o^2 \geq 3\sigma(F_o^2)$ . Three reflections, chosen as standards and measured after each block of 200 data, exhibited an overall average intensity decay of 1.7%. The structure was solved and refined with computer programs from the TEXSAN crystallographic software package.<sup>5</sup> The position of the Na atom was determined by using the

direct methods program SHELXS,<sup>6</sup> and the atomic positions of the remaining atoms were subsequently deduced by examination of difference electron density maps. After refinement with isotropic displacement coefficients on each atom, the data were corrected for absorption with the program DIFABS.<sup>7</sup> The refinement converged to  $R = 0.047$  and  $wR = 0.051$  with anisotropic displacement coefficients on each atom. The final difference electron-density map exhibited maximum and minimum peaks corresponding to 1.8 and 1.5%, respectively, of the height of the Na atom.

Differential thermal analysis (DTA) was used to determine the phase diagram for the binary system  $\text{Li}_2\text{B}_4\text{O}_7\text{-Na}_2\text{B}_4\text{O}_7$ . The samples were placed in covered platinum crucibles in a TA Instruments, Model 2920 Modulated DSC equipped with a 1873-K DTA module. A flow of  $\text{N}_2(\text{g})$  at 30 mL/min was used, and a heating rate of 5 K/min was employed after the furnace equilibrated at 823 K.

The crystal pulling system was comprised of a resistance heated furnace, and a Mellen, computer-controlled, vertical pulling system. The furnace was designed and constructed in our laboratory. A series of mullite and alumina baffles were used to produce horizontal and vertical temperature gradients near 21 and 13 K/cm, respectively. The melt was contained in a 57-mm diameter Pt crucible. The crucible was supported inside an alumina tube under a 4%  $\text{H}_2/\text{Ar}$  atmosphere. A Pt rod attached to an alumina shaft was employed to initiate crystallization. A rotation rate of 9 rpm was employed and the boule was pulled at 2.7 mm/day, while the furnace was cooled at 2 K/day.

A measurement of the efficiency of second-harmonic generation from a microcrystalline sample of  $\text{NaLiB}_4\text{O}_7$  was made by the Kurtz and Perry method.<sup>8</sup> A Q-switched  $\text{Nd}^{3+}:\text{YAG}$  laser was used to produce incident IR radiation at a wavelength of 1064 nm. The microcrystalline sample was placed on a fused silica plate, and the intensity of the second harmonic was monitored with a photomultiplier attached to a Tektronix 2457B oscilloscope. A microcrystalline sample of  $\text{KH}_2\text{PO}_4$  (KDP) served as the standard for the measurement.

## Results and Discussion

Crystallographic data are summarized in Table 3.1, and atomic parameters and equivalent displacement coefficients are listed in Table 3.2. The results of the structure determination were used to calculate an X-ray powder diffraction pattern with the program LAZY-PULVERIX.<sup>9</sup> Calculated and experimental results are listed in Table 3.3. A labeled drawing of the unit cell as viewed along the *c* axis is shown in Figure 3.1. The structure is characterized by two distinct, yet similar 3-dimensional borate frameworks, each containing 3- and 4-coordinate B atoms. The frameworks are connected by 7-coordinate Na atoms that occupy tunnels extending along the *a* axis (Figure 3.2) and 5-coordinate Li atoms that occupy tunnels extending along the *b* axis (Figure 3.3). The B<sub>4</sub>O<sub>9</sub> ring system is illustrated in Figure 3.4. Selected interatomic distances and angles are listed in Table 3.4. Environments and partial connectivity of the Na- and Li-centered polyhedra are presented in Figure 3.5. A unit cell Volume/*Z*-composition diagram for samples Na<sub>*x*</sub>Li<sub>2-*x*</sub>B<sub>4</sub>O<sub>7</sub> ( $1 < x \leq 2$ ) is illustrated in Figure 3.6. The approximate binary phase diagram for the system Li<sub>2</sub>B<sub>4</sub>O<sub>7</sub>-Na<sub>2</sub>B<sub>4</sub>O<sub>7</sub> is shown in Figure 3.7a. The crystal boule pictured in Figure 3.7b has the approximate composition Na<sub>0.55</sub>Li<sub>1.45</sub>B<sub>4</sub>O<sub>7</sub>.

Table 3.1. Crystallographic data for NaLiB<sub>4</sub>O<sub>7</sub>.

Diffractometer	Rigaku AFC6R
Radiation	$\lambda = 0.70926 \text{ \AA}$ (graphite monochromated Mo K $\alpha$ )
Formula wt., amu	185.17
Unit Cell	Orthorhombic
a, $\text{\AA}$	13.308(3)
b, $\text{\AA}$	14.098(2)
c, $\text{\AA}$	10.225(3)
Space group	(#43) Fdd2
Z	16
V $\text{\AA}^3$	1918.4(6)
Density <sub>calc</sub> g cm <sup>-3</sup>	2.564
F(000)	1440
Absorption coeff., $\mu \text{ cm}^{-1}$	2.94
T	298 K
R <sup>a</sup>	0.047
R <sub>w</sub> <sup>b</sup>	0.051
<sup>a</sup> $R = \sum   F_o  -  F_c   / \sum  F_o $ <sup>b</sup> $R_w = [\sum w( F_o  -  F_c )^2 / \sum w  F_o ^2]^{1/2}$	

Table 3.2. Atomic coordinates and equivalent displacement coefficients for NaLiB<sub>4</sub>O<sub>7</sub>.

Atom	x	y	z	B <sub>eq</sub>
Na	0.1005(2)	0.2611(2)	0.4418(4)	2.2(1)
Li	-0.004(1)	0.357(1)	0.194(1)	3.4(7)
B1	-0.0344(5)	0.4231(4)	0.4697(7)	0.7(2)
B2	0.0845(5)	0.0279(4)	0.4864(7)	0.6(2)
B3	0.1256(5)	0.4554(4)	0.3512(7)	0.7(2)
B4	-0.0442(5)	0.1208(4)	0.3689(7)	0.8(2)
O1	0.1197(3)	0.2962(3)	0.1528	0.8(1)
O2	-0.0446(3)	0.3329(3)	0.5381(5)	0.8(1)
O3	0.0405(3)	0.4024(3)	0.3646(5)	0.8(1)
O4	¼	¼	0.3022(6)	0.6(2)
O5	0.1354(3)	0.1960(3)	0.6496(5)	1.0(2)
O6	0.0538(3)	0.1091(3)	0.4025(5)	1.1(2)
O7	0	0	0.5699(6)	0.8(2) <sup>a</sup>
O8	-0.0725(3)	0.2012(3)	0.3072(5)	1.0(1)

$$B_{eq} = \left( \frac{8\pi^2}{3} \right) \sum_i \sum_j U_{ij} a_i^* a_j^* a_i a_j$$



Table 3.3. Indexed X-ray powder pattern for NaLiB<sub>4</sub>O<sub>7</sub>.

h k l	Calculated 2 $\theta$	Calculated Intensity	Observed 2 $\theta$	Observed Intensity
2 0 2	21.9	100	21.9	100
2 2 2	25.3	55	25.3	61
4 0 0	26.8	52	26.7	8
1 3 3	33.2	72	33.1	72
3 1 3	33.8	52	33.7	67
4 2 2	34.6	17	34.5	23
0 0 4	34.6	17	34.5	23
4 4 0	37.2	22	37.1	22
3 3 3	38.4	7	38.4	18
5 3 1	39.9	6	39.8	9
4 4 2	41.3	4	41.3	4
1 5 3	42.1	12	42.1	34
0 6 2	42.3	35	42.2	26
6 2 0	42.7	11	42.7	12
6 0 2	44.5	11	44.5	29
4 0 4	44.7	15	44.6	28
1 1 5	45.3	4	45.3	8
2 4 4	45.9	4	45.8	6
6 2 2	46.4	9	46.3	18
5 3 3	47.5	15	47.6	12
3 1 5	49.5	6	49.7	4
3 7 1	50.6	16	50.5	12
4 4 4	52.0	14	51.8	11
7 3 1	52.7	15	52.6	12
5 5 3	54.5	1	54.6	8

A labeled drawing of the unit cell as viewed along the *c* axis is shown in Figure 3.1. The structure is characterized by two distinct, yet similar 3-dimensional borate frameworks, each containing 3- and 4-coordinate B atoms. The frameworks are connected by 7-coordinate Na atoms that occupy tunnels extending along the *a* axis (Figure 3.2) and 5-coordinate Li atoms that occupy tunnels extending along the *b* axis (Figure 3.3).

The borate framework is built from  $B_4O_9$  rings, which contain two  $BO_3$  triangular and two  $BO_4$  tetrahedral groups (Figure 3.4). To produce the three dimensional framework, each  $B_4O_9$  ring links to four neighboring rings by sharing a single bonded, terminal O atom between a triangle and a distorted tetrahedron (Figure 3.1). The  $B_4O_7$  formulation is then simply generated by considering the condensation  $B_4O_{5+4/2} = B_4O_7$ . One framework contains atoms B1, B3, O1, O2, O3, and O4, and the other B2, B4, O5, O6, O7, and O8. With respect to average interatomic distances, the two frameworks are statistically equivalent. The two networks look like twins, when viewed from the *c* axis, as shown in Figure 3.1. This polyborate structure network is known to exist in the compound  $Li_2B_4O_7$ , which crystallizes in the tetragonal space group  $I4_1cd$ , and in  $K_2B_4O_7$ , which forms in the triclinic space group P1. Although the compound  $Na_2B_4O_7$  has a similar formula, it crystallizes in a layer type structure composed of  $B_5O_{11}$  groups and  $B_3O_7$  rings.

Selected interatomic distances and angles are listed in Table 3.4. Environments and partial connectives of the Na- and Li-centered polyhedra are presented in Figure 3.5. The Na atom is surrounded by seven O atoms in a distorted tetragonal base-trigonal base geometry. Five of the Na-O distances range from 2.266(5) to 2.393(5) Å, the other two are unusually long at 2.811(5) and 2.860(5) Å. Therefore, the Na environment is best described as 5+2. The mean distance of Na-O is  $2.490 \pm 0.244$  Å, which compares to a calculated value of 2.53 Å for a 7-coordinate Na atom.<sup>10</sup> The observed distance also compares to the separation of  $2.505 \pm 0.112$  Å for the 7-coordinate

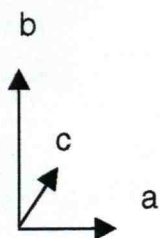
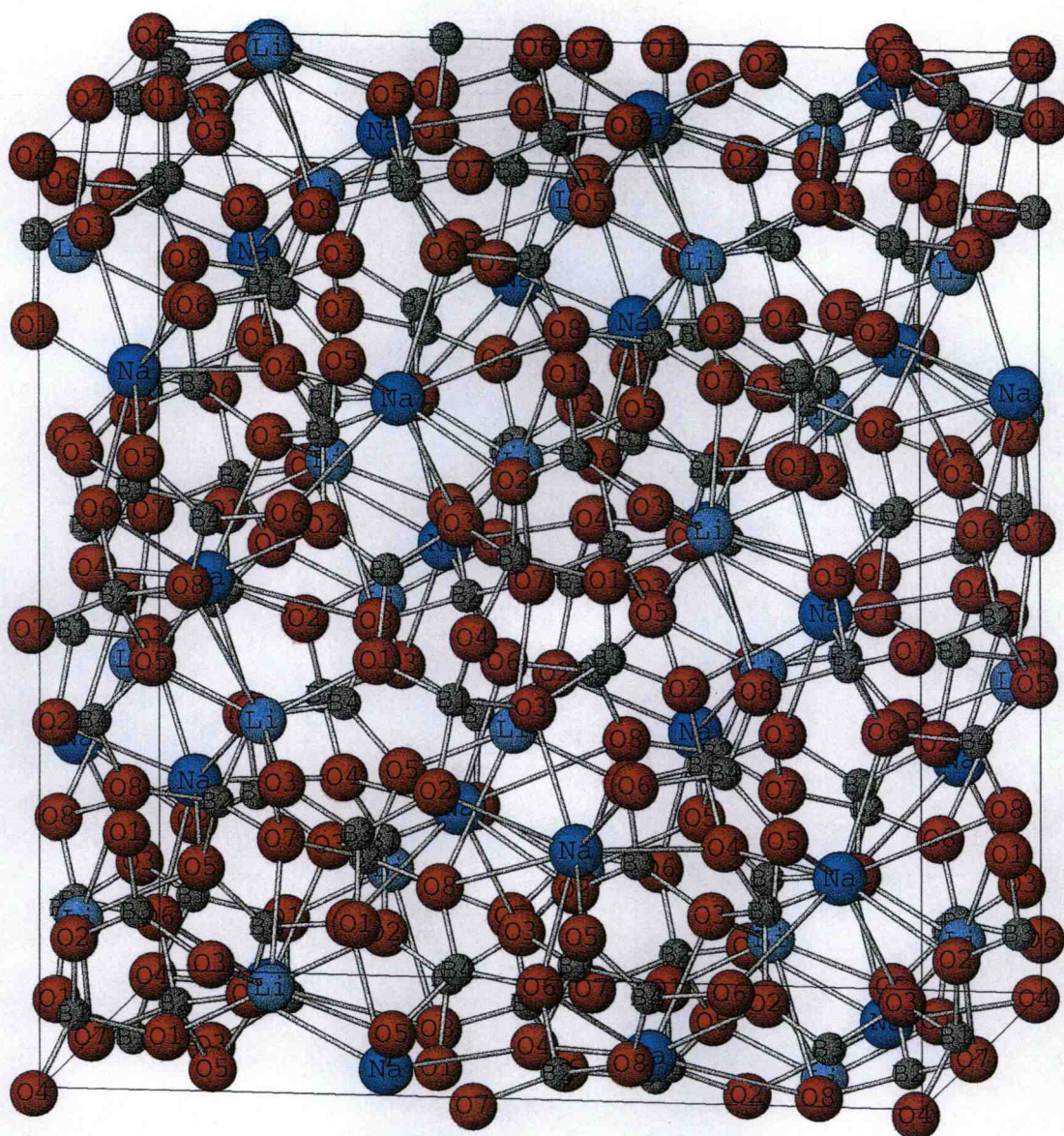


Figure 3.1. Labeled drawing of the unit cell of  $\text{NaLiB}_4\text{O}_7$  viewed along the  $c$  axis.



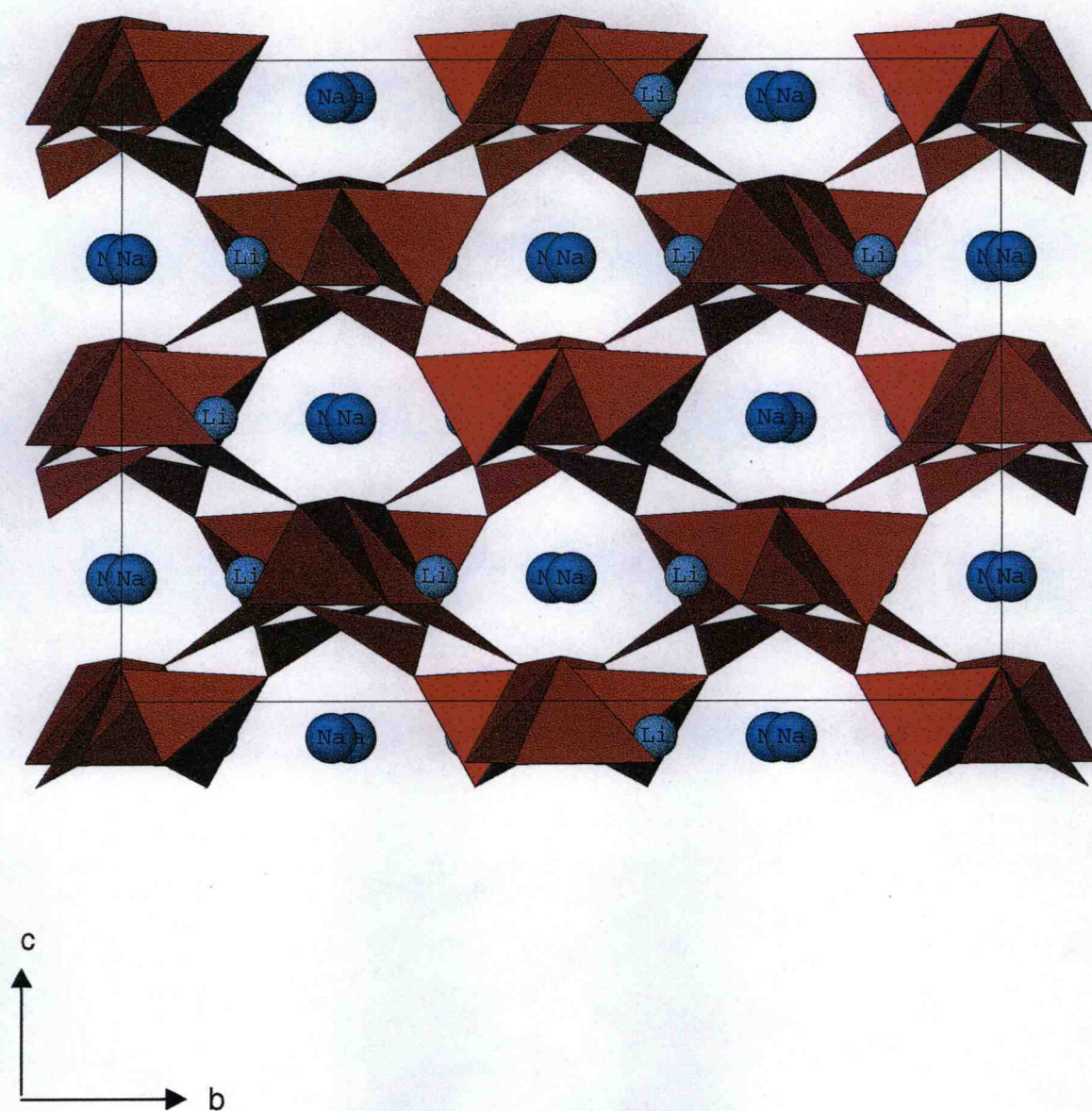


Figure 3.2. Drawing of  $\text{NaLiB}_4\text{O}_7$  viewed down the  $a$  axis.

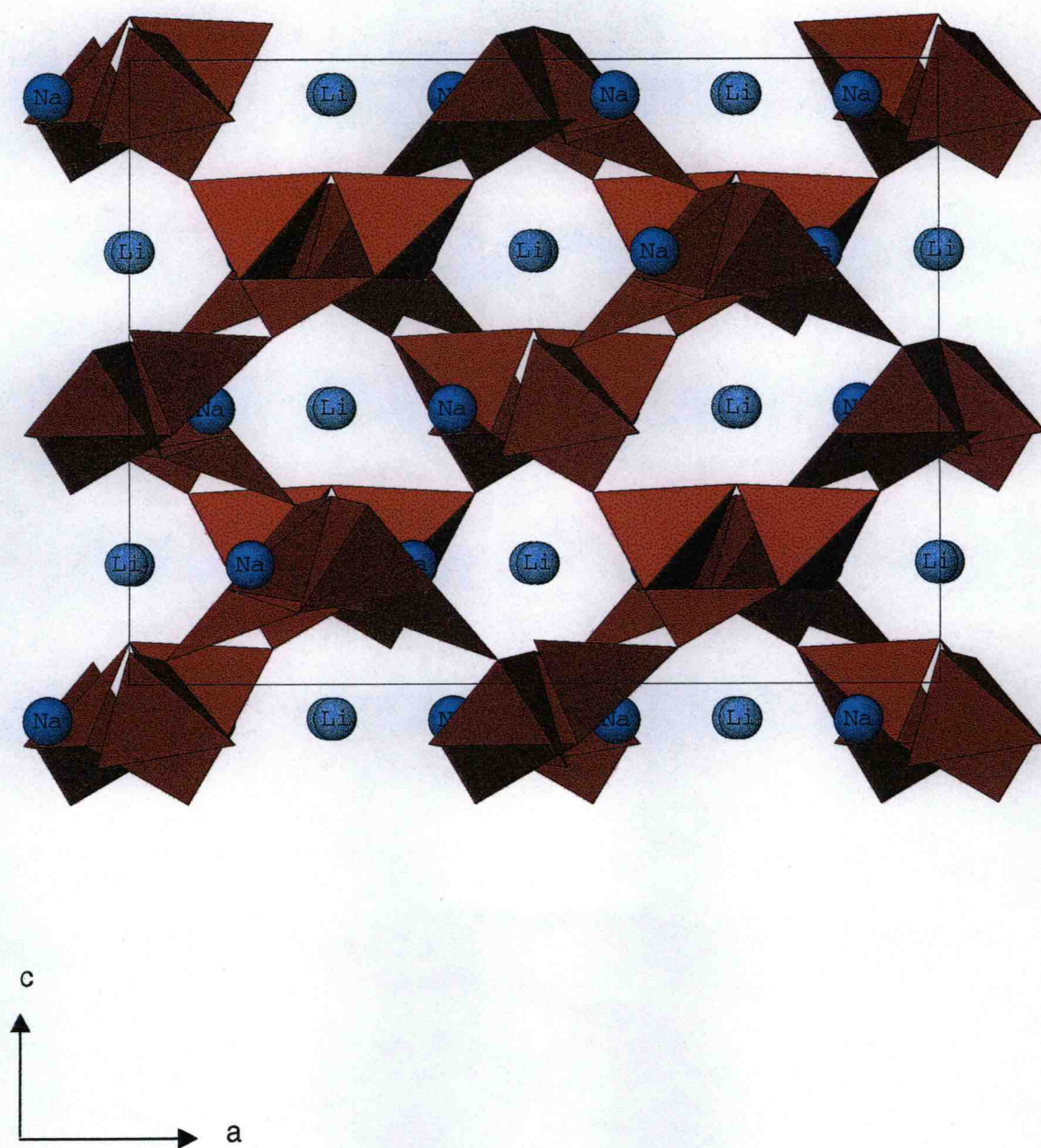


Figure 3.3. Drawing of NaLiB<sub>4</sub>O<sub>7</sub> viewed down the *b* axis.



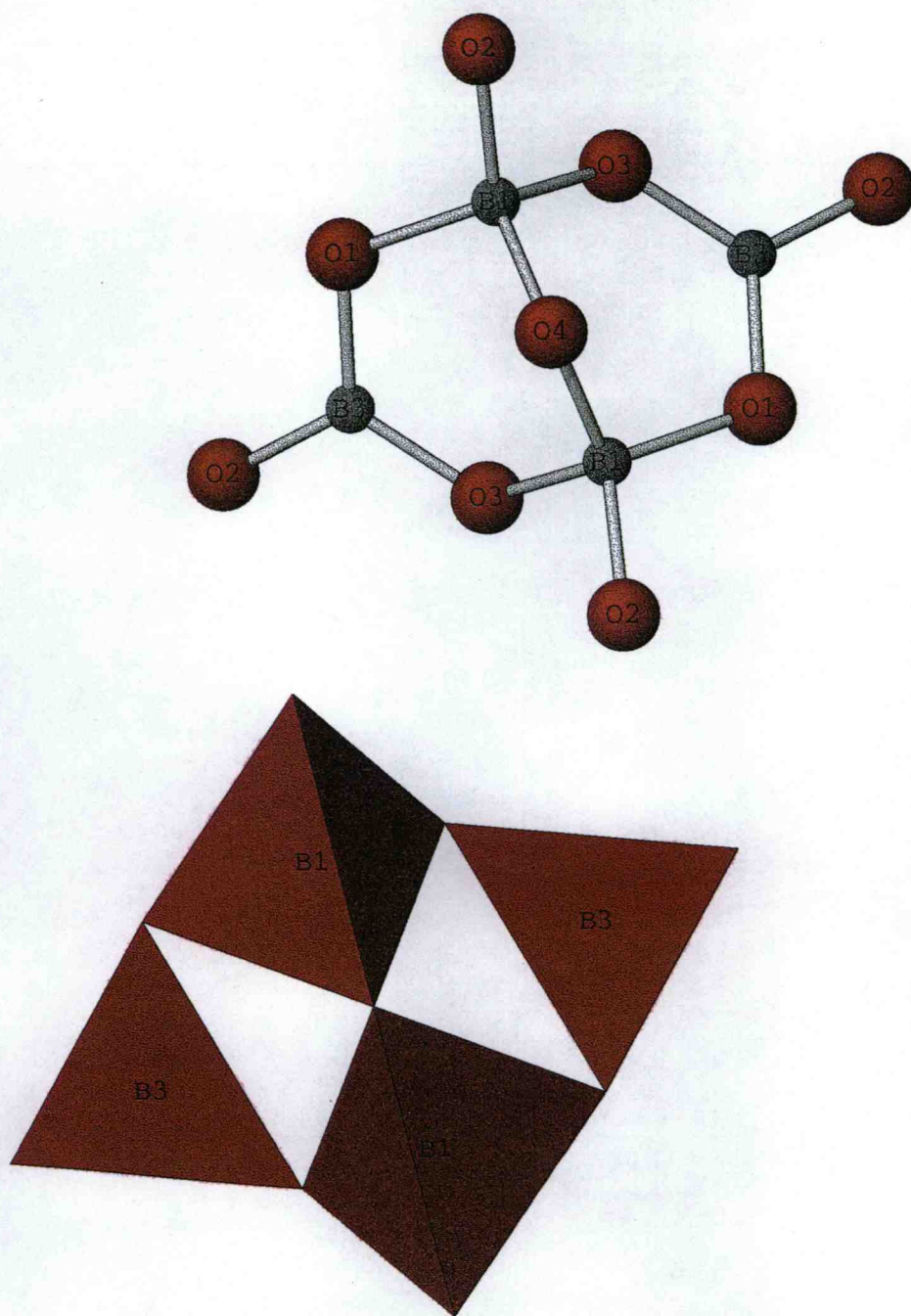


Figure 3.4. Drawing of the  $B_4O_9$  rings; triangles are  $BO_3$  groups, tetrahedra  $BO_4$  groups.

Table 3.4. Interatomic distances (Å) and angles (°) for NaLiB<sub>4</sub>O<sub>7</sub>.

Atoms	Length Å	Atoms	Length Å	Bonds	Degrees
Na-O2	2.393(5)	B3-O3	1.364(8)	O3-Li-O8	89..2(6)
Na-O3	2.287(5)	B4-O5	1.366(8)	O5-Li-O7	102.5(7)
Na-O4	2.454(4)	B4-O6	1.358(8)	O5-Li-O8	58.3(5)
Na-O5	2.361(5)	B4-O8	1.351(8)	O7-Li-O8	160.4(7)
Na-O6	2.266(5)			O1-B1-O2	112.9(5)
Na-O6	2.860(5)			O1-B1-O3	107.1(4)
Na-O8	2.811(5)	<b><u>Bonds</u></b>	<b><u>Degrees</u></b>	O1-B1-O4	108.4(4)
Li-O1	1.90(2)	O2-Na-O3	59.4(2)	O2-B1-O3	103.7(4)
Li-O3	1.95(1)	O2-NaO4	157.0(2)	O2-B1-O4	113.7(4)
Li-O5	1.96(2)	O2-NaO08	70.6(2)	O3-B1-O4	110.7(5)
Li-O7	2.38(2)	O3-Na-O5	135.9(2)	O5-B2-O6	108.8(4)
Li-O8	2.65(2)	O3-Na-O6	131.9(2)	O5-B2-O7	109.9(4)
B1-O1	1.511(7)	O4-Na-O5	109.8(2)	O5-B2-O8	102.7(4)
B1-O3	1.494(7)	O5-Na-O6	81.1(2)	O6-B2-O7	109.3(5)
B1-O2	1.458(7)	O5-Na-O6	135.4(2)	O6-B2-O8	111.3(5)
B1-O4	1.448(7)	O6-Na-O8	53.5(2)	O7-B2-O8	114.4(4)
B2-O5	1.510(7)	O1-Li-O3	95.0(7)	O1-B3-O2	120.9(6)
B2-O6	1.487(7)	O1-Li-O5	123.2(8)	O1-B3-O3	120.4(5)
B2-O7	1.466(7)	O1-Li-O7	104.3(7)	O2-B3-O3	118.7(5)
B2-O8	1.464(7)	O1-Li-O8	91.2(7)	O5-B4-O6	121.1(5)
B3-O1	1.385(7)	O3-Li-O5	127.1(8)	O5-B4-O8	119.6(6)
B3-O2	1.355(8)	O3-Li-O7	101.2(7)	O6-B4-O8	119.2(5)

Na atom in  $\text{Cs}_2\text{Na}_2\text{B}_{10}\text{O}_{17}$ .<sup>11</sup> A bond valence-calculation reveals atom O6 at 2.860 Å from the Na atom contributes only 7% to the Na valence.<sup>12</sup>

The Li atom binds three O atoms at distances shorter than 2 Å (Table 3.4), and two additional O atoms at distances of 2.38(2) and 2.65(2) Å; thus, the Li environment may be described as 3+2. Atom O1 (bond distance of O1-Li=1.90(2) Å) makes a contribution of 28%, while atom O4 (bond distance of O4-Li =2.65(1) Å) only makes a contribution of 5% to the Li valence. In the structure of  $\text{Li}_2\text{B}_4\text{O}_7$ , the Li atom is surrounded by four O atoms at distances ranging from 1.97 - 2.14 Å and 3 more O atoms at distances longer than 2.6 Å.

All O atoms bind two B atoms. In addition, atoms O4 and O6 bind two Na atoms; atom O7 hitches two Li atoms; atoms O3, O5, and O8 grip one Na and one Li atom; atom O2 bonds to the Na atom, and O1 connects one Li atom. Figures 3.2 and 3.5 show the Na-O and Li-O connectivity.

The extent of solubility of Li in the  $\text{NaLiB}_4\text{O}_7$  was examined by studying the system  $\text{Li}_{2-x}\text{Na}_x\text{B}_4\text{O}_7$  ( $0 \leq x \leq 1$ .) Volume/Z-composition plots are shown in Figure 3.6. The systematic increase in volume as x varies from 0 to 1 indicates that the larger Na atoms substitutes for smaller Li atoms. Obviously, there are two types of structures in the range seen in Figure 3.6 as evidenced by two different slopes. The body-centered tetragonal structure of  $\text{Li}_2\text{B}_4\text{O}_7$  appears in the range of  $0 \leq x \leq 0.55$ , and the face-centered orthorhombic structure of  $\text{NaLiB}_4\text{O}_7$  exists in the range of  $0.55 \leq x \leq 1$ . These two different structures types overlap for compositions near  $\text{Na}_{0.55}\text{Li}_{1.45}\text{B}_4\text{O}_7$ .

The binary phase diagram for the system  $\text{Li}_2\text{B}_4\text{O}_7$  -  $\text{Na}_2\text{B}_4\text{O}_7$  is shown in Figure 3.7a. The eutectic point, liquidus curves, and the  $\text{NaLiB}_4\text{O}_7$  decomposition were all readily deduced from the DTA data. The obvious feature in the diagram is the peritectic decomposition of  $\text{NaLiB}_4\text{O}_7$ . The approximate solidus curve has been constructed for the  $\text{NaLiB}_4\text{O}_7$  -  $\text{Li}_2\text{B}_4\text{O}_7$  solid solution by noting the immiscibility gap revealed by the X-ray studies and the approximate stoichiometry of the boule from the melt of  $\text{NaLiB}_4\text{O}_7$ . The boule shown in Figure 3.7b was pulled from the stoichiometric melt of



composition  $\text{NaLiB}_4\text{O}_7$ . As expected, the boule composition is representative of a  $\text{NaLiB}_4\text{O}_7$  -  $\text{Li}_2\text{B}_4\text{O}_7$  solid solution formulation.

Four crystals were extracted from the boule and mounted on glass fibers for determination of cell parameters on the Rigaku AFC6R diffractometer. The crystals were taken from a position close to the nucleation site near the Pt rod, the outer rim of the boule, the bottom of the boule, and from the center of the boule. In each case, cells were determined to be orthorhombic, with edge lengths  $a = 9.584(1) \text{ \AA}$ ,  $b = 9.561(1) \text{ \AA}$ , and  $c = 10.307(1) \text{ \AA}$ . This corresponds to a volume of  $944.5 \text{ \AA}^3$  and a Volume/Z number =  $118.1 \text{ \AA}^3$ . By comparing this value to those in Figure 3.6, an approximate composition of  $\text{Na}_{0.55}\text{Li}_{1.45}\text{B}_4\text{O}_7$  can be deduced. Hence, growth results in the production of the orthorhombic form near the Li solubility limit and the immiscibility gap with the tetragonal modification. Of course,  $\text{NaLiB}_4\text{O}_7$  crystal growth is possible by using a melt composition covering the approximate range  $\text{Na}_{1+x}\text{Li}_{1-x}\text{B}_4\text{O}_7$  ( $0.2 < x \leq 0.6$ .)

Many materials containing a noncentrosymmetric borate framework possess favorable properties for nonlinear optical frequency conversion. Among them, the chromophores  $\text{BO}_3$ ,  $\text{B}_3\text{O}_6$  and  $\text{B}_3\text{O}_7$  have been reported to have large nonlinear coefficients;<sup>13</sup> typical examples are  $\text{YAl}_3(\text{BO}_3)_4$  (YAB),  $\text{LiB}_3\text{O}_5$  (LBO), and  $\beta\text{-BaB}_2\text{O}_4$  (BBO). Anion group theory calculations have shown that  $\text{B}_4\text{O}_9$  has small nonlinear coefficients. The magnitude of the second harmonic signal of  $\text{NaLiB}_4\text{O}_7$ , relative to  $\text{KH}_2\text{PO}_4$  (KDP) has been obtained by the Kurtz-Perry method. The resulting signal from a 1064-nm fundamental of Nd:YAG corresponds to 10% of that observed for KDP. Inspection of the B-O framework reveals the existence of a pseudo-inversion center. The presence of this approximate center of symmetry affords the small second-harmonic generation signal.

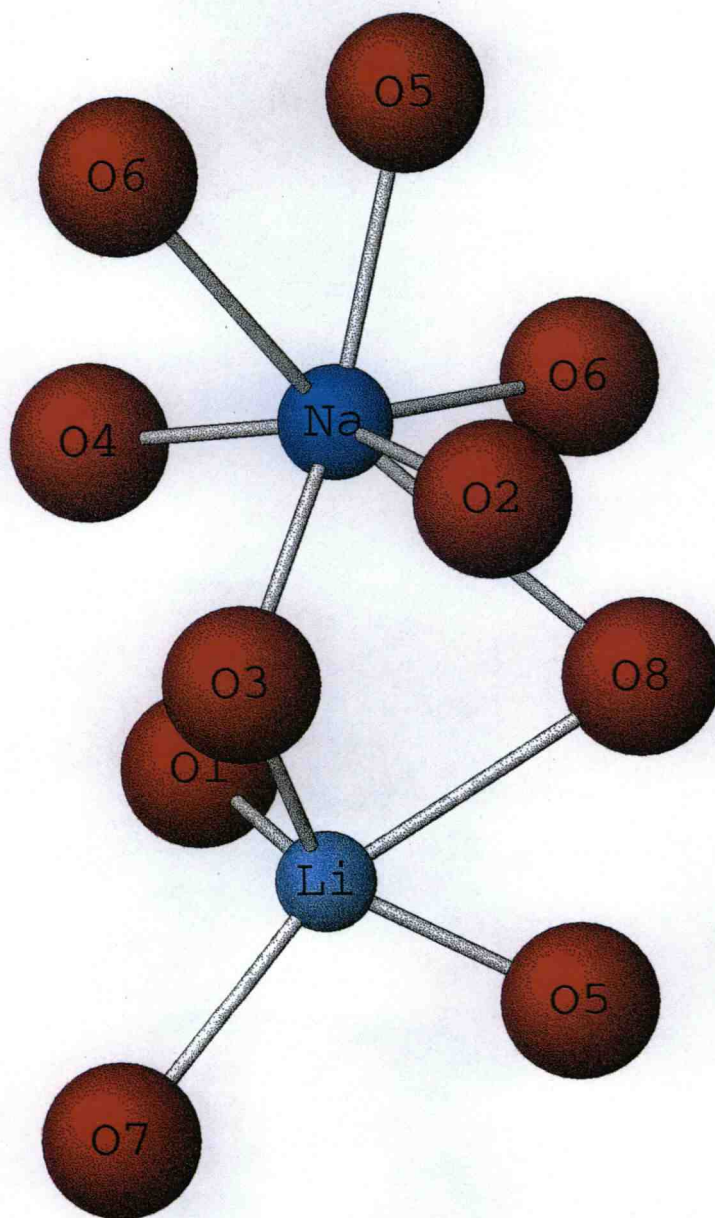


Figure 3.5. Environment and connectivity of the Na- and Li- centered polyhedra.

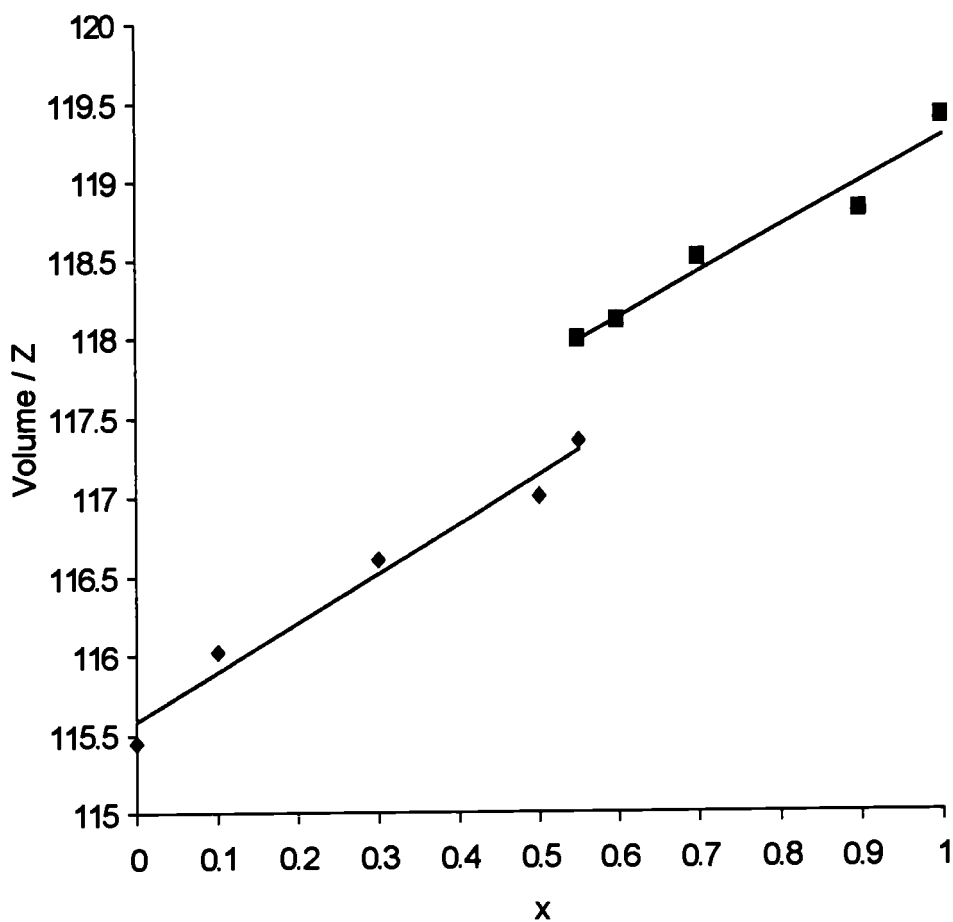


Figure 3.6. Unit cell per formula unit for the solid-solution series  $\text{Na}_x\text{Li}_{2-x}\text{B}_4\text{O}_7$  as a function of composition ( $0 \leq x \leq 1$ .)

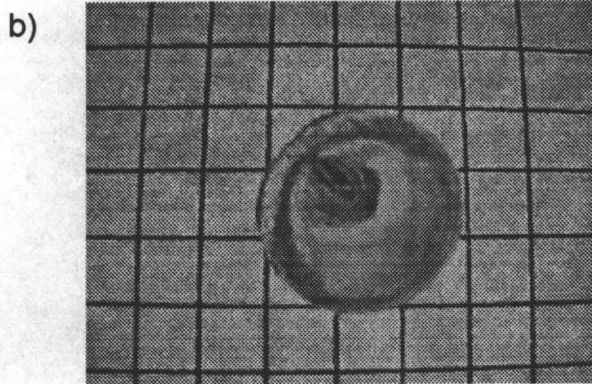
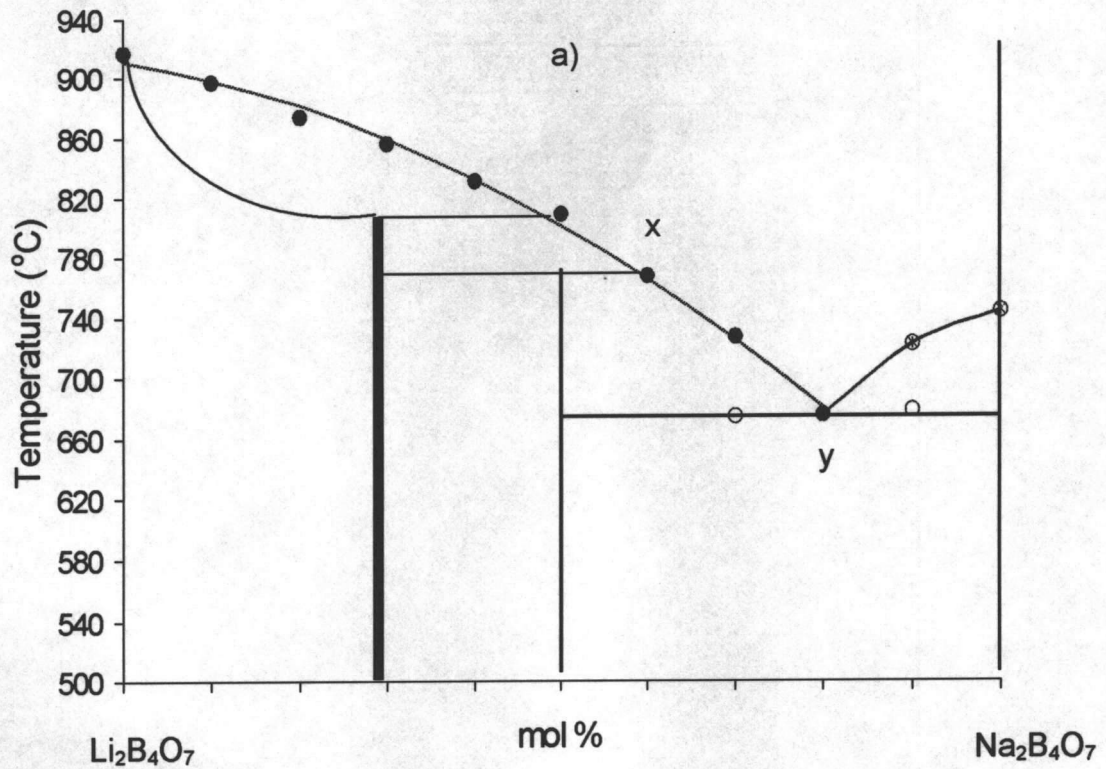


Figure 3.7. a) Phase diagram for the binary system  $\text{Li}_2\text{B}_4\text{O}_7$  and  $\text{Na}_2\text{B}_4\text{O}_7$ . b) crystal boule has approximate composition:  $\text{Na}_{0.55}\text{Li}_{1.45}\text{B}_4\text{O}_7$ . Each square is 5mm.

## **Acknowledgments**

This research was supported by the National Science Foundation (DMR-9221372). Acknowledgement is also made to the Donors of The Petroleum Fund, administered by the American Chemical Association, for partial support of the work. We thank Anthony Diaz for assistance in performing the SHG measurement.

## References

- 
1. Petrov V., Rotermund F., Noack F., R. Komatsu, Sugawara T., and Uda S., *J. Applied Physics*, 84(11), **1998**, 5887.
  2. Fan S., Shen G., Wang W., Li J., Le X., *J. Crystal Growth* 99, **1990**, 811.
  3. Krogh-Moe, *Acta Crystallogr. Sect. B*, 24, **1968**, 179.
  4. Krogh-Moe, *Acta Crystallogr. Sect. B*, 28, **1972**, 3089.
  5. TEXSAN, Structure Analysis Package, Molecular Structure Corp., MSC (3200A, Research Forest Drive, The Woodlands, TX 77381) International Tables for X-ray Crystallography, Vol. IV. Birmingham: Kynoch Press, **1974**.
  6. Sheldrick, G. M., In crystallographic Computing 3; Sheldrick G.M., Kruger C., and Goddard R., Eds.; Oxford Univ Press, Oxford U.K., 1985, 175.
  7. Walker N., Stuart D., *Acta Crystallogr. Sect. A* 39, **1983**, 158.
  8. Kurtz S. W., Perry T. T., *J. Appl. Phys.* 39, **1968**, 3798.
  9. Yvon K., Jeitschko W., Parthe E., *J. Appl. Crystallogr.* 10, **1977**, 73.
  10. Shannon R.D., *Acta Crystallogr. Sect. A* 32, **1976**, 751.
  11. Tu J., Keszler D. A., *Inorganic Chem.*, 35, **1996**, 463.
  12. Brese N. E., O'Keeffe M., *Acta Crystallogr. Sect. B* 47, **1991**, 192.
  13. Chen C., Wu Y., Li R., *J. Crystal Growth*, 99, **1990**, 790.

## **CHAPTER 4**

# **STRUCTURE-PROPERTY RELATIONSHIPS OF VUV-EXCITED PHOSPHORS**

**Gregory A. Peterson, Douglas A. Keszler, and Steven K. Crossno**

**To be submitted to SIDs**

## Abstract

To identify new phosphors for plasma display applications, due consideration must be given to several properties of the phosphor, including the quantum efficiency of the luminescent center, the energetic position of the host absorption band, and the host-luminescent transfer efficiency. A simple correlation between  $\text{BO}_3$ -group excitation maxima and average cation electronegativities per formula unit has been established. A qualitative model accounting for the transfer efficiency in host-sensitized luminescence base on angles involving the activator site and the absorbing group has been studied for a number of borate materials, and the results are presented.

## Introduction

The development of new inorganic phosphors for plasma-display panels (PDPs) requires the incorporation of several materials properties into a single compound. The compound must strongly absorb vacuum ultraviolet (VUV) light near 147 nm and exhibit efficient transfer of this energy to the luminescent center. The luminescent center itself must emit with high efficiency and provide a suitable chromaticity. And in current display designs, the phosphor must be stable both in the environment of the plasma and to the short-wavelength VUV exciting light. In present PDPs, the red component of the display is produced by the phosphor  $\text{Eu}^{3+}:(\text{Y,Gd})\text{BO}_3$ . This material exhibits a bright orange-red emission having an unexceptional chromaticity:  $x = 0.639$  and  $y = 0.360$ . These values compare to  $x = 0.654$  and  $y = 0.346$  for a sample of the common red phosphor  $\text{Eu}^{3+}:\text{Y}_2\text{O}_3$  from Osram-Sylvania.

In this contribution we highlight results from our studies aimed at identifying an improved red-emitting phosphor for application in PDPs. As part of this work, we have sought to distinguish both crystal and electronic features that may contribute to improved efficiencies. Because of their strong absorption



features in the VUV portion of the spectrum, established high quantum efficiencies, and demonstrated applicability in PDPs, we have concentrated on the study of simple orthoborates containing triangular, planar,  $\text{BO}_3$  units. In this contribution we will consider selected host characteristics that contribute to the energetic positions of excitation bands, energy transfer efficiencies, chromaticities, and brightness.

## Results and Discussion

VUV excitation spectra for several  $\text{Eu}^{3+}$ -doped materials have been measured with a VUV spectrometer at the University of Georgia; examples for the commercial material  $\text{Eu}^{3+}:(\text{Y,Gd})\text{BO}_3$  and the compound  $\text{Eu}^{3+}:\text{Ca}_4\text{Gd}(\text{BO}_3)_3\text{O}$  are given in Figure 4.1. Each spectrum exhibits two broad excitation bands. The bands centered near 220 nm for  $(\text{Y,Gd})\text{BO}_3$  and near 235 nm for  $\text{Ca}_4\text{Gd}(\text{BO}_3)_3\text{O}$  are attributable to direct excitation of the  $\text{Eu}^{3+}$  ion.<sup>1</sup> From comparison to single-crystal absorption measurements,<sup>2</sup> the bands peaking at 166 nm for  $(\text{Y,Gd})\text{BO}_3$  and 185 nm for  $\text{Ca}_4\text{Gd}(\text{BO}_3)_3\text{O}$  are associated with absorption into the  $\text{BO}_3$  groups. It is clearly evident from these two examples that the position of the  $\text{BO}_3$ -group absorption is dependent on the nature of the associated cations; additional data are given in Table 4.1. Here, it can be seen that the peak in the excitation spectrum associated with  $\text{BO}_3$ -group absorption can be shifted by approximately 25 nm. The energetic position of the peak largely correlates with a simple weighted average of the electronegativities of the cations in a given material. In general, as the average cation electronegativity increases, the peak in the excitation spectrum shifts to shorter wavelengths. This is consistent with a simple molecular orbital description in which the O atoms of the  $\text{BO}_3$  groups in those compounds containing electropositive cations (low average electronegativity) exhibit substantial lone electron-pair character.

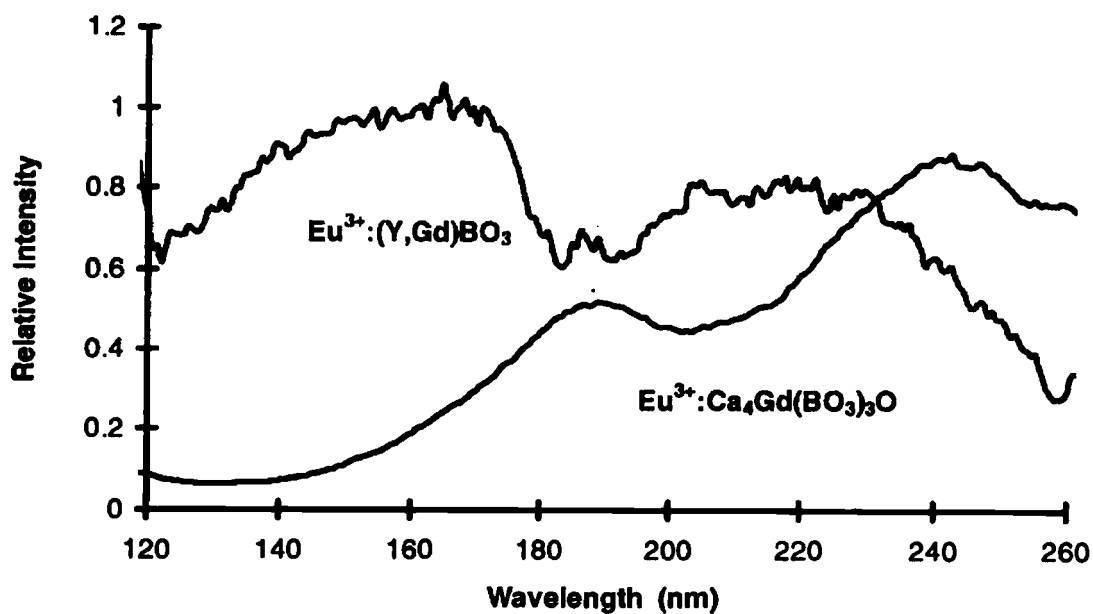


Figure 4.1. Excitation spectra from  $\text{Eu}^{3+}:\text{Y}_2\text{O}_3$  and  $\text{Eu}^{3+}:\text{Ca}_4\text{Gd}(\text{BO}_3)_3\text{O}$ .

Table 4.1. Average cation electronegativities and excitation peak maxima for  $\text{Eu}^{3+}$ -doped borates.

Phosphor	Average Cation Electronegativity per Formula Unit	$\text{BO}_3$ group absorption $\lambda_{\text{max}}$ (nm)
$\text{Ca}_4\text{Gd}(\text{BO}_3)_3\text{O}$	1.42	183
$\text{CaY}(\text{BO}_3)\text{O}$	1.42	185
$\text{Ca}_3(\text{BO}_3)_2$	1.42	185
$\text{Sr}_3\text{Sc}(\text{BO}_3)_3$	1.48	158
$(\text{YGd})\text{BO}_3$	1.63	166
$\text{BaZn}_2(\text{BO}_3)_2$	1.65	165
$\text{YAl}_3(\text{BO}_3)_4$	1.78	160
$\text{SrLiB}_9\text{O}_{15}$	1.84	166
$\text{YMgB}_5\text{O}_{10}$	1.82	160

In contrast, the valence electrons of the O atoms in those compounds having higher average electronegativities are tightly bound in interactions with the more highly electronegative cations. Lone-pair type electron density rises in energy relative to the density involved in stronger bonding, so the excitation energy shifts to lower energies, longer wavelengths. The host  $\text{Sr}_3\text{Sc}(\text{BO}_3)_3$  is an exception to the simple correlation. Here, the Sc-O interactions are likely affecting the position of the excitation band. Unfortunately, we have examined no other examples of borates that contain a small electronegative cation in a matrix rich in larger electropositive species. Nevertheless, as a general rule, compounds rich in large electropositive elements are likely to produce lower-energy excitation maxima. These lower-energy maxima will be positioned well away from the exciting peak, 147 nm, of the plasma.

Following excitation of the host, energy must be transferred to the luminescent center for emission to occur. In materials exhibiting photoconductivity, the energy may be transferred from the host to the luminescent centers by the transport of electrons and holes. In other cases the undoped host may have its own luminescent centers composed of vacancies or molecular complexes. The energy is then transferred from such host luminescent centers to doped activators via resonant energy transfer. A typical example is  $\text{Eu}^{3+}:\text{YVO}_4$ , wherein the energy is transferred from a  $\text{VO}_4^{3+}$  group to the  $\text{Eu}^{3+}$  ion.<sup>3</sup> From a study of several  $\text{Eu}^{3+}$ -doped vanadates, Blasse proposed that the efficiency of the transfer process is governed by an exchange process and the value of the V-O-Eu angle.<sup>1,4</sup> Specifically, a linear interaction was found to result in the highest transfer efficiency, while an orthogonal interaction afforded the lowest transfer efficiency. This model is readily correlated to the predominant, shared  $\sigma$ -orbital overlap for the linear geometry vs. an orthogonal, zero interaction for a bent geometry (*cf.* Figure 4.2.)

We have attempted to determine the applicability of this model to host sensitization of borates by examining the correlation between transfer efficiency

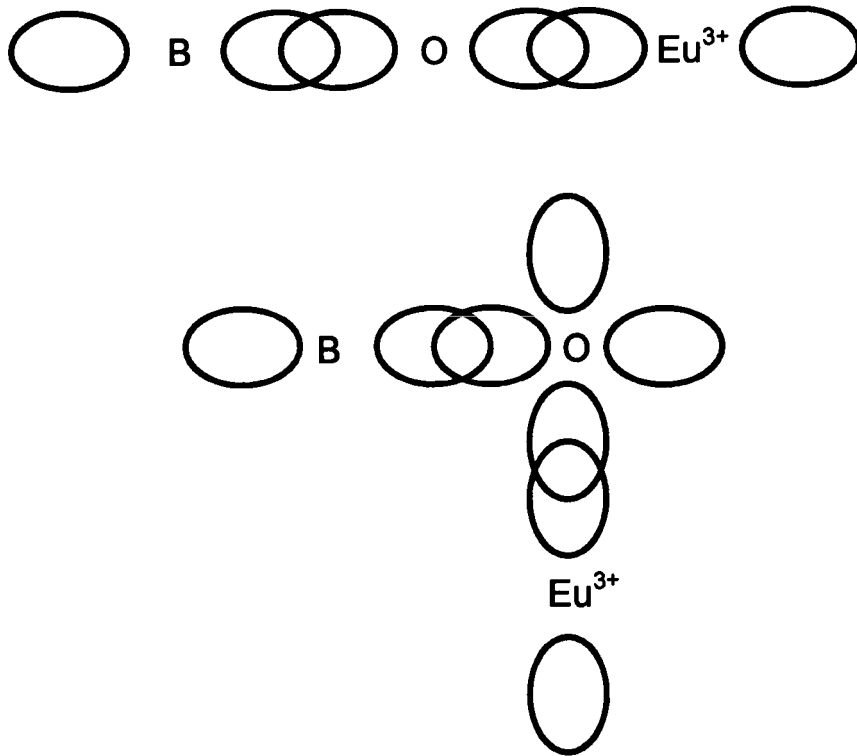


Figure 4.2.  $\sigma$ -interaction model for energy transfer a) linear interaction b) orthogonal interaction.

and B-O-Eu bond angles. Relative transfer efficiencies have been derived by using excitation spectra and crystal-structure data according to Equation 1.

Equation 1)

$$\frac{\text{VUV}}{\text{UV}} \approx \frac{\sigma_{\text{BO}_3} \rho_{\text{BO}_3} q_{\text{Eu}^{3+}} t}{\sigma_{\text{Eu}^{3+}} \rho_{\text{Eu}^{3+}} q_{\text{Eu}^{3+}}}$$

Here,  $\sigma$  is an absorption cross section,  $\rho$  is a density,  $q$  is the quantum efficiency for  $\text{Eu}^{3+}$  emission, and  $t$  is the transfer efficiency. VUV represents the maximum signal for  $\text{BO}_3$ -group excitation in the range 155-190 nm, and UV represents the maximum signal for direct  $\text{Eu}^{3+}$  excitation in the range 210-260 nm. The ratio  $\rho(\text{BO}_3)/\rho(\text{Eu}^{3+})$  is simply derived from each crystal structure as the number of

$\text{BO}_3$  groups attached to a given  $\text{Eu}^{3+}$  dopant site. In the analysis, all transfer efficiencies have been normalized to the characteristics of  $\text{Eu}:(\text{Y,Gd})\text{BO}_3$ . By setting  $t = 1$  for this material and measuring the ratio  $\text{VUV}/\text{UV}$  from the excitation spectrum, we can derive the ratio  $\sigma(\text{BO}_3)/\sigma(\text{Eu}^{3+})$ . This value then serves as a scale factor, since we assume that the relevant cross sections do not vary significantly among the various hosts in the study. So, by combining results from optical spectra and crystal-structure determinations, we can derive approximate, relative transfer efficiencies. These efficiencies are plotted vs. cosine weighted average B-O-Eu angles in Figure 4.3.

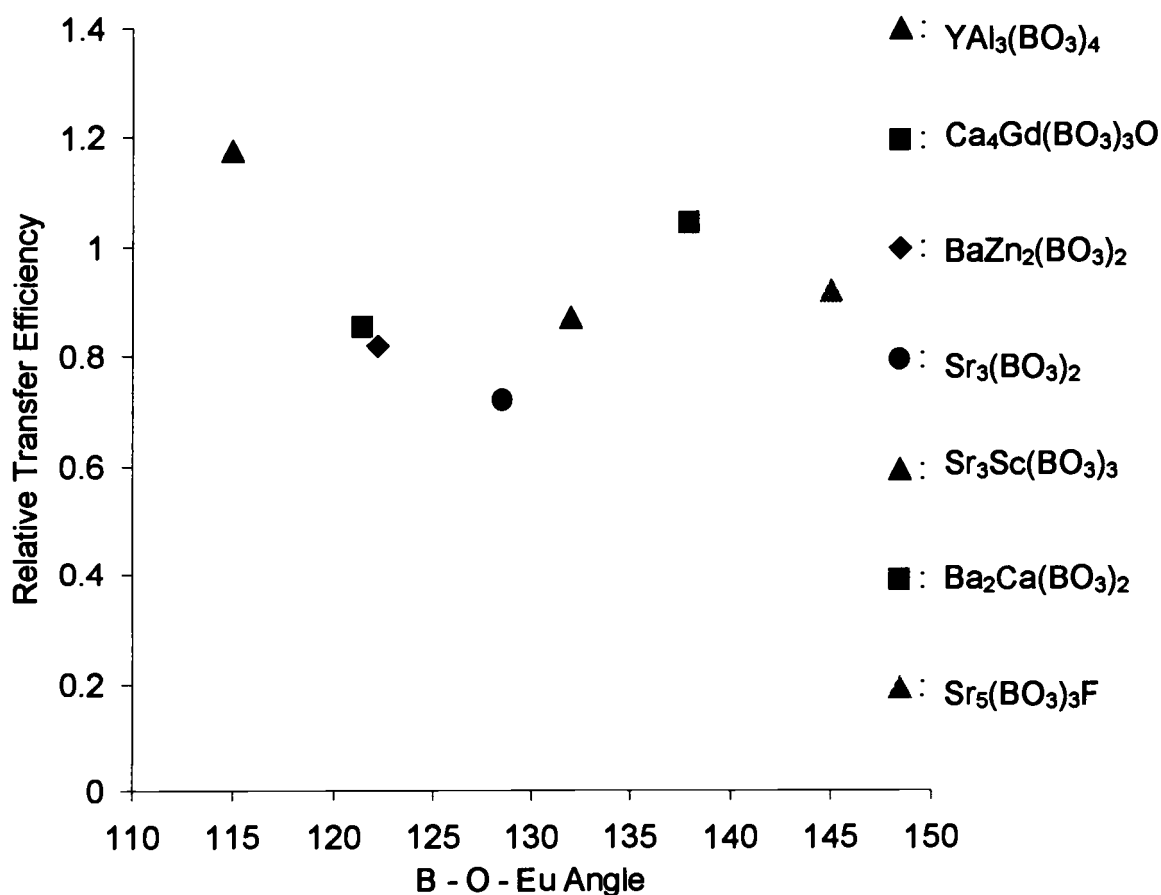


Figure 4.3. Relative transfer efficiency vs. cosine weighted average B-O-Eu angle.

Since the shared  $\sigma$  overlap varies as the cosine function, the resulting plot should yield a straight line if the proposed model of energy transfer is correct. There appears to be a modest trend of increasing transfer efficiencies with increasing B-O-Eu angle. The high, calculated efficiency for  $\text{YAl}_3(\text{BO}_3)_4$  is associated with the  $\text{AlO}_6$  groups which contribute to the VUV absorption. Of course, application of this model requires that the  $\text{BO}_3$  groups themselves be emitting species. Such emission may not be readily observed in many hosts as radiation absorbed by the  $\text{BO}_3$  groups should be readily transferred to the sublattice of associated host cations. To determine whether resonance energy transfer may be important in the operation of such materials, we have initiated a systematic study of the VUV luminescence characteristics of undoped hosts. We have recently identified a very strong UV emission at 250 nm from the undoped material  $\text{ScBO}_3$  (cf. Figure 4); the quantum efficiency is estimated to be above 60%. A similar, though longer wavelength (360 nm) broad-band emission, has been reported for the undoped oxide  $\text{Sc}_2\text{O}_3$  following X-ray excitation.<sup>5</sup> At the present time, we assume that the emission is associated with the  $\text{ScO}_6$  groups in the  $\text{ScBO}_3$  host. The optical transition is likely to be similar to the charge-transfer type processes for other d<sup>0</sup> transition-metal centers, e.g.,  $\text{ZrO}_6$  in  $\text{ZrP}_2\text{O}_7$ ,  $\text{VO}_4$  in  $\text{YVO}_4$ , and  $\text{WO}_4$  in  $\text{CaWO}_4$ .<sup>6</sup> We believe the presence of the stiff  $\text{BO}_3$  groups and the anisotropy of the  $\text{ScBO}_3$  structure contribute to the high-energy emission and the relatively small Stokes shift. Further studies are underway to identify additional compounds containing  $\text{Sc}^{3+}$  or other closed-shell electron species that may exhibit similar high-energy emission. Such materials having high quantum efficiencies may well be useful VUV-to-UV converters, allowing the development of new display schemes on the basis of readily available UV-excited phosphors.

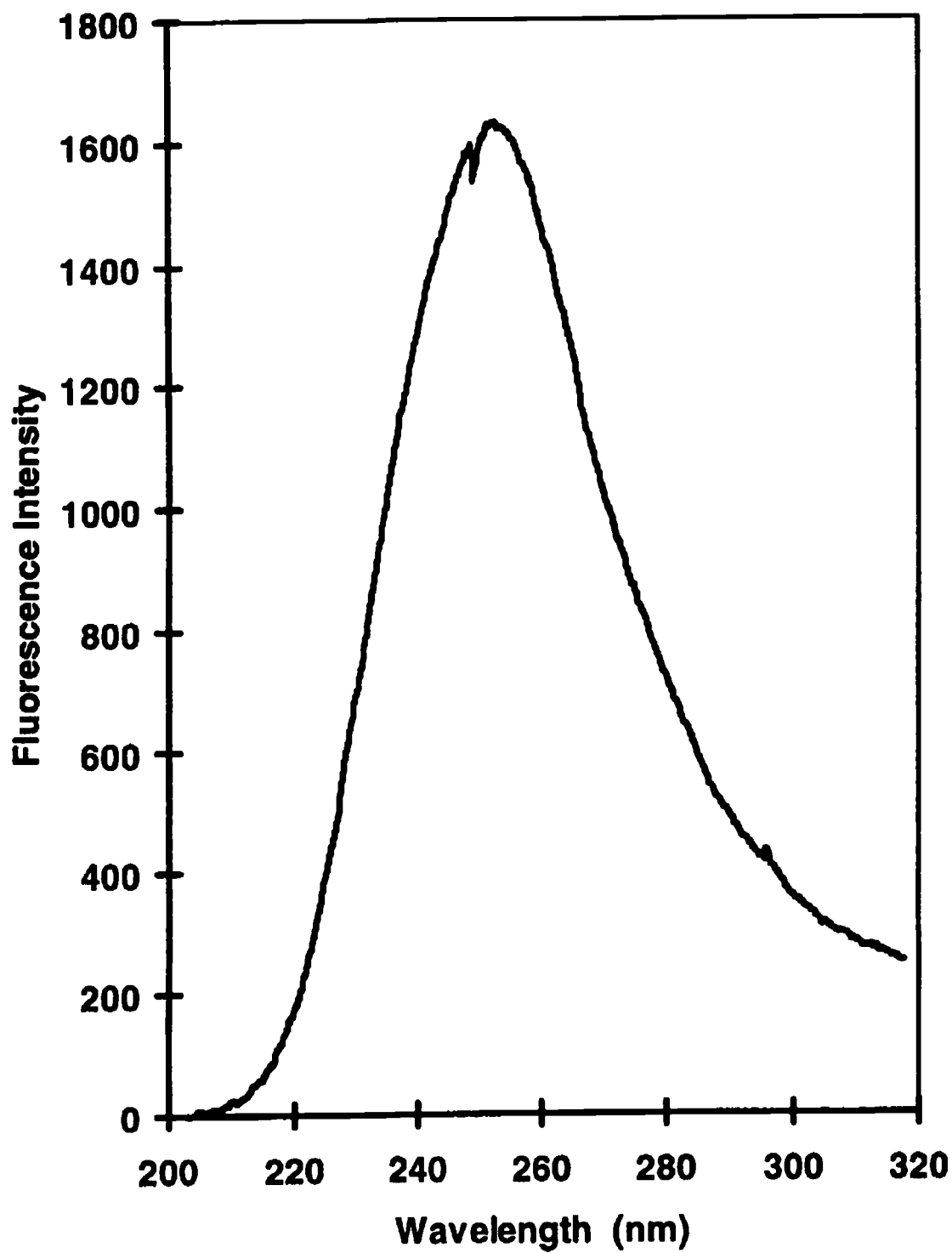


Figure 4.4. Emission spectrum of ScBO<sub>3</sub>.

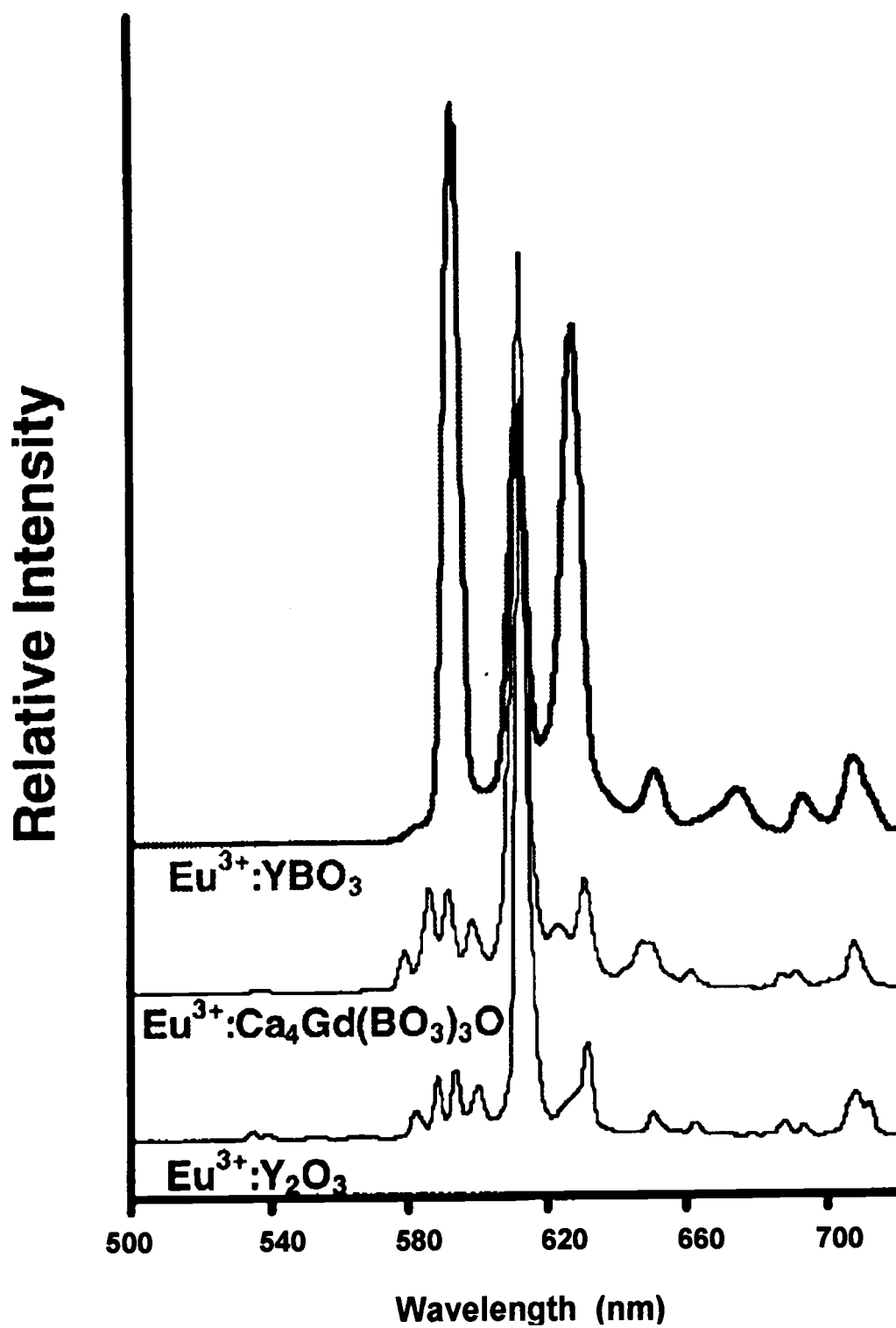
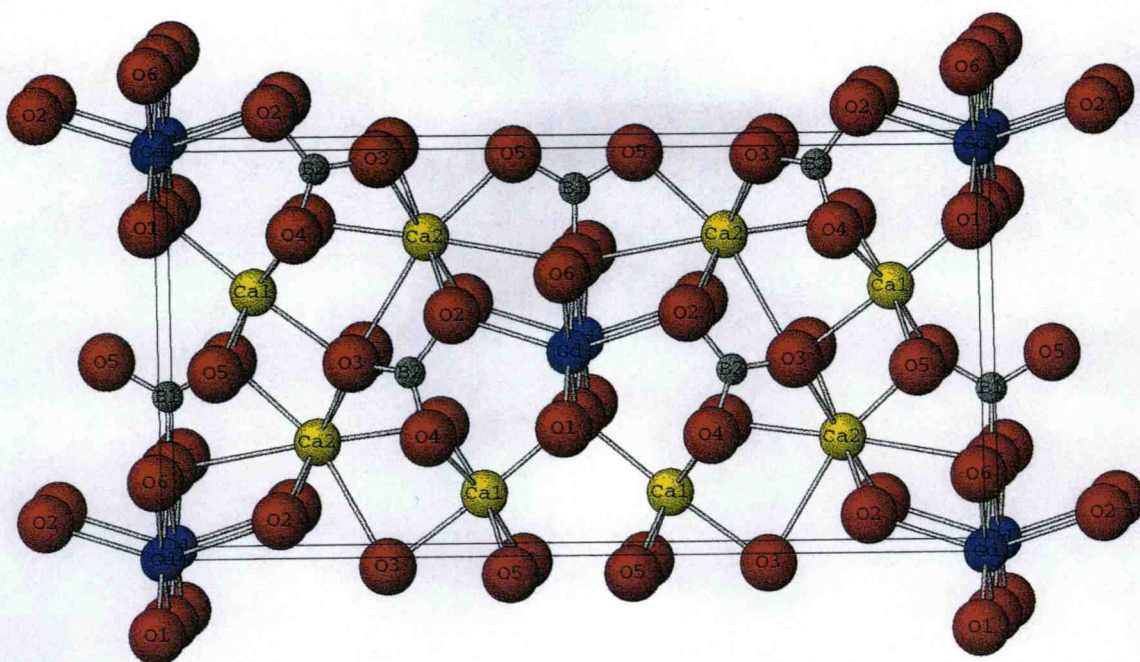


Figure 4.5. Emission spectra from Eu<sup>3+</sup>-doped oxides.

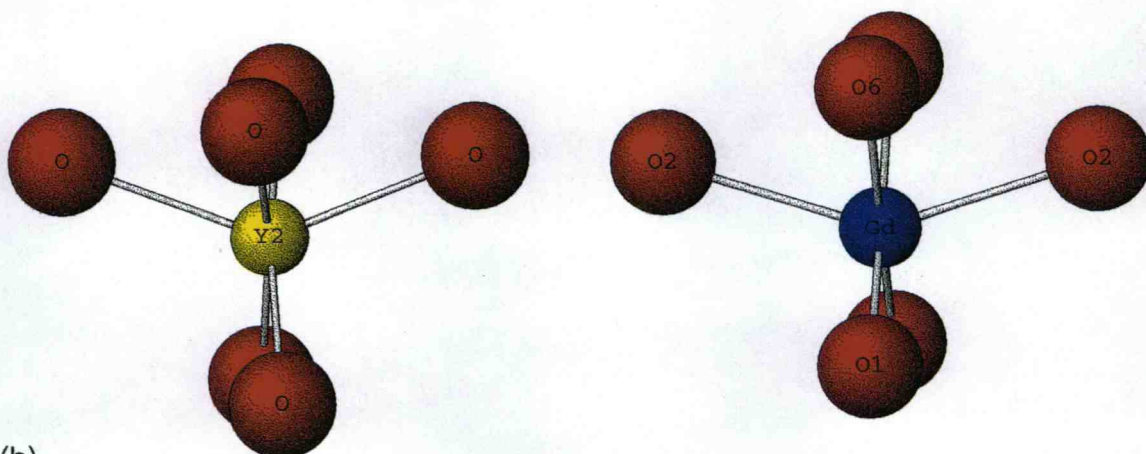


## Chromaticity

As noted earlier, the primary disadvantage of the material  $\text{Eu:}(\text{Y,Gd})\text{BO}_3$  is its poor chromaticity. This is readily apparent by considering the luminescence spectra in Figure 4.5, where the spectrum of  $\text{Eu:}(\text{Y,Gd})\text{BO}_3$  may be compared to that of  $\text{Eu:Y}_2\text{O}_3$ . The spectrum of the Y,Gd compound is dominated by the  $^5\text{D}_0 \rightarrow ^7\text{F}_1$  transition at 590 nm, limiting its saturation in the red at 611 nm. It is well known that saturated red luminescence and high quantum efficiencies for  $\text{Eu}^{3+}$  may be achieved by substituting the ion on an Y or Gd site surrounded by six O atoms in a distorted octahedral environment. We have been examining several such materials, and the compound  $\text{Eu:Ca}_4\text{Gd}(\text{BO}_3)_3\text{O}^7$  is one example. This material crystallizes in the monoclinic system and contains chains of edge-sharing  $\text{GdO}_6$  octahedra, Figure 4.6(a). As seen in Figure 4.(b), the  $\text{GdO}_6$  octahedron is distorted much like that of the  $\text{YO}_6$  octahedron in  $\text{Y}_2\text{O}_3$ , and their respective luminescence spectra are similar (cf. Figure 4.5.) The optimal brightness for  $\text{Eu:Ca}_4\text{Gd}(\text{BO}_3)_3\text{O}$  occurs at a 10 mol% doping level, corresponding to 60% of that observed for a commercial sample of  $\text{Eu}^{3+}:\text{Y}_2\text{O}_3$ . The brightness of the  $\text{Eu:Ca}_4\text{Gd}(\text{BO}_3)_3\text{O}$  samples has been found to change by less than 5% between 4.2 K and room temperature; the room-temperature luminescence lifetime is 1.8 ms. Considering these results, we assume that the quantum efficiency of the Eu-doped Ca,Gd compound is comparable to that of  $\text{Eu:Y}_2\text{O}_3$ . The lower brightness of the Ca,Gd material relative to  $\text{Eu:Y}_2\text{O}_3$  appears to result from a lower number density of doped  $\text{Eu}^{3+}$  ions. The number density,  $4.41 \times 10^{20} \text{ cm}^{-3}$ , of  $\text{Eu}^{3+}$  ions in the 10 mol% loading of  $\text{Eu}^{3+}$  in  $\text{Ca}_4\text{Gd}(\text{BO}_3)_3\text{O}$  corresponds to 50% of that,  $8.85 \times 10^{20} \text{ cm}^{-3}$ , for the 5 wt% loading of  $\text{Eu}_2\text{O}_3$  in the commercial sample of  $\text{Eu:Y}_2\text{O}_3$ ; the relative dopant densities are similar to the relative magnitudes of brightness. As such, the lower brightness of  $\text{Eu:Ca}_4\text{Gd}(\text{BO}_3)_3\text{O}$  relative to that of  $\text{Eu:Y}_2\text{O}_3$  is an intrinsic feature of the material resulting from the small number density of available dopant sites and the anisotropy in their connectivity. Higher brightness  $\text{Eu}^{3+}$  materials will likely only



(a)



(b)

Figure 4.6. (a) Unit-cell drawing of  $\text{Ca}_4\text{Gd}(\text{BO}_3)_3\text{O}$ , (b) left )  $\text{YO}_6$  octahedron in  $\text{Y}_2\text{O}_3$ , right )  $\text{GdO}_6$  octahedron in  $\text{Ca}_4\text{Gd}(\text{BO}_3)_3\text{O}$ .

be achieved in hosts containing highly concentrated, three-dimensionally dispersed dopant sites where concentration quenching can be limited.

## Summary

As a general rule,  $\text{BO}_3$ -group excitation maxima are expected to scale with the average electronegativity of the cations in a given host. A similar trend should be anticipated for other oxoanion compounds such as phosphates and silicates. The  $\sigma$ -overlap model for energy transfer may serve as a useful adjunct for the identification of efficient VUV-excited phosphors. Consideration of quantum efficiency, absorption characteristics, and chromaticity, however, should play a leading role in the development of new materials. The compound  $\text{ScBO}_3$  has been identified as an efficient VUV-to-UV converter. Such materials may provide new approaches to the development of efficient VUV excitation. Finally, due consideration should be given to dopant number densities when comparing relative magnitudes of brightness for related materials.

## Acknowledgments

Acknowledgment is made to the phosphor Technology Center of Excellence for support of this research. We wish to thank Professor Richard Meltzer, Delena Bell Gatch, and Kiwan Jiang of the University of Georgia for collection of the VUV spectra, and Professor Richard Meltzer for his collaboration on this project.

## References

---

1. Blasse G., *J. Chem. Phys.* 45, **1966**, 2356.
2. Cheng L. K., Bosenberg W., and Tang d. L., *J Cryst. Growth* 89, **1988**, 553; Eimerl D., Davis L., Velsko S., Graham E. K., and Zalkin A., *J Appl. Phys.* 62, **1987**, 1968; Chen C., Wu Y., Jiang A., Wu B., You G., Li R., and Lin S., *J Opt. Soc. Am. B* 6, **1989**, 616.
3. Palilla F., Levine A. K., and Rinkevics M., *J Electrochem. Soc.* 112, **1965**, 776.
4. Van Uitert L. G., Linares R. C., Soden R. R., and Ballman A. A., *J Chem. Phys.* 36, **1962**, 702.
5. Blasse G., and Brixner L. H., *Eur. J Solid State Inorg. Chem.* 28, **1991**, 767.
6. Blasse G., *Structure and Bonding* 42, **1980**, 1; Blasse G., *Inorg. Chim. Acta* 157, **1989**, 141.
7. Norrestam R., and Nygren M., *Chem. Mater.* 4, **1993**, 737; Dirksen G. J., and Blasse G., *J Alloys Compounds* 191, **1993**, 121; Ilyuknin A. B., Dzhurinskii B. F., *Zh Neorg. Khimii.* 38, **1993**, 917.

## CHAPTER 5

# THE STRUCTURE AND LUMINESCENCE PROPERTIES OF YTTRIUM MAGNESIUM PENTABORATE $\text{YMgB}_5\text{O}_{10}$

Gregory A. Peterson

(expanded version of manuscript entitled  $\text{YMgB}_5\text{O}_{10}$  submitted to  
*Acta Crystallogr., Sect. C* with Douglas Keszler and Alexandre Yokochi)

## Abstract

Yttrium magnesium pentaborate crystallizes in the monoclinic space group  $P2_1/n$  with cell parameters  $a = 8.530(1)$ ,  $b = 7.582(2)$ ,  $c = 9.373(2)$ , and  $\beta = 93.78(2)$ .  $YMgB_5O_{10}$  is isostructural to  $YCoB_5O_{10}$  and the family of lanthanide magnesium pentaborates  $LnMgB_5O_{10}$  ( $Ln = La, Ce, Pr, Nd, Sm, Eu, Gd, Tb, Dy, Ho,$  and  $Er.$ ) It is also one of the few known oxides containing a 10-coordinate Y atom. A concentration-quenching curve has been constructed for the solid solution  $Y_{1-x}Eu_xMgB_5O_{10}$  ( $0 < x \leq 1.$ ) Emission brightness is found to increase up to  $x = 0.75$ . The large value of  $x$  is consistent with the expected results for a one-dimensional energy-transfer process, which has been documented for many of the isostructural compounds.

## Introduction

$YMgB_5O_{10}$  was synthesized during an examination of the system  $Y_2O_3$ - $MgO$ - $B_2O_3$ . It is one member of the family of compounds  $LnMgB_5O_{10}$  where  $Ln$  = lanthanide.<sup>1</sup> Much work has been done on luminescence characterization and energy transfer on the family because of relatively high emission efficiencies and the presence of one-dimensional, zigzag chains of lanthanide polyhedra that extend through the structure.<sup>2,3,4</sup> In this contribution, we describe the crystal structure of  $YMgB_5O_{10}$  and the results of concentration-quenching and brightness measurements on the series  $Y_{1-x}Eu_xMgB_5O_{10}$  ( $0 < x \leq 1.$ )

## Materials and Methods

Powder samples of  $Y_{1-x}Eu_xMgB_5O_{10}$  ( $x = 0.01, 0.02, 0.05, 0.10, 0.25, 0.50, 0.75$ , and  $1$ ) were made by combining  $(1-x)$   $Y_2O_3$  (AESAR 99.9%),  $x$   $Eu_2O_3$  (ASEAR 99.99%),  $2$   $Mg(NO_3)_2 \cdot 6H_2O$  (AESAR 99.999%), and  $5.25$   $B_2O_3$  (ASEAR 99.98%). A series of grinding and heating steps were executed prior to a final anneal at  $1173$  K for  $4$  h. Irregular block-shaped crystals of  $YMgB_5O_{10}$  were obtained by melting the undoped powder in a Pt crucible at  $1373$  K for  $6$  h, cooling to  $1173$  K at  $18$  K  $h^{-1}$ , and then rapidly cooling to room temperature by switching off the power to the furnace. A crystal of approximate dimensions  $0.2 \times 0.1 \times 0.05$  mm was physically separated from the solidified melt and mounted on a glass fiber with epoxy for structure determination. All measurements were made on a Rigaku AFC6R diffractometer with graphite-monochromated Mo  $K\alpha$  radiation. Cell parameters and the orientation matrix for the data collection were obtained from a least squares refinement with 19 automatically-centered reflections in the range of  $20 < 2\theta < 38^\circ$ . Intensity data were collected over the range of indices  $-12 < h < 12$ ,  $-2 < k < 11$ ,  $-2 < l < 13$  by using an  $\omega$ - $2\theta$  scan technique to a maximum  $2\theta$  value of  $62^\circ$ . A total of 3101 general reflections were collected, and 1937 were observed ( $F_o^2 > 2\sigma(F_o^2)$ ) and unique. The structure was solved and refined by using SHELXS-97<sup>5</sup> and SHELXL-97.<sup>5</sup> Texsan<sup>6</sup> was used to apply psi-scan corrections to the raw data prior to generating the input data file for SHELXS. Final least-squares refinement on  $F_o^2$  resulted in the residuals  $R(F^2 > 2\sigma(F^2)) = 0.035$  and  $wR(F^2) = 0.104$ . The largest peak in the final difference electron-density map was 4.5% of an Y atom.

Luminescence data were collected in our laboratory. Excitation provided by an Oriel 300-W Xenon lamp was passed through a 50-cm water filter, focused onto the entrance slits of a Cary model-15 double prism monochromator, and subsequently focused onto the sample. Luminescence was collected at nearly a right angle to the excitation beam, dispersed through an Oriel 22500 1/8-m monochromator, and detected with a Hamatsu R636

photomultiplier tube. The signal was collected and amplified with a Keithley model 486 picoammeter and converted to a digital signal for computer acquisition. Spectrometer control and data acquisition were achieved with computer programs written in this laboratory. The excitation spectra were corrected by using sodium salicylate and rhodamine B as quantum counters. The emission spectra were corrected with a tungsten lamp that has been calibrated at Eppley Laboratories.

Concentration quenching for the solid solution  $Y_{1-x}Eu_xMgB_5O_{10}$  ( $x = 0.01, 0.02, 0.05, 0.10, 0.25, 0.50, 0.75$ , and 1) was determined by using the device pictured in Figure 5.1. This HKP brightness-measuring device was designed and manufactured at OSU for the purpose of making brightness measurements relative to standard materials. The sample excitation source is an Oriel model 6035 Hg/Ar calibration lamp, which operates on the basis of Hg emission line at 253.6 nm. The lamp housing is vented to remove ozone that is produced while the lamp is operating. An interference bandpass filter (2) allows the characteristic Hg emission at 253.6 nm to be passed onto the sample (3) while minimizing the background radiation from the lamp. The sample holder is keyed so that the sample is always horizontal, ensuring that the surface area of the powder and the placement of the sample in the device are always constant. A cutoff filter and neutral-density filter (4) are placed between the sample holder and the photomultiplier tube (PMT, 5). The cutoff filter absorbs the UV excitation energy up to the cutoff limit, and the neutral density filter attenuates and disperses the emission from the sample.

The PMT signal is a measurement of the photon flux from emission at all wavelengths greater than the cutoff limit. Thus, the PMT signal is the relative integrated emission for all of the  $Eu^{3+} {}^5D_0 \rightarrow {}^7F_n$  transitions ( $n = 1, 2, 3$ , and 4.) The PMT wavelength response is not important in this case, because the wavelengths of the emission transitions do not change among the samples. Standard analytical practices insure the minimization of effects from drift in lamp intensity and extraneous signals other than from the  $Eu^{3+}$  emission.<sup>7</sup>



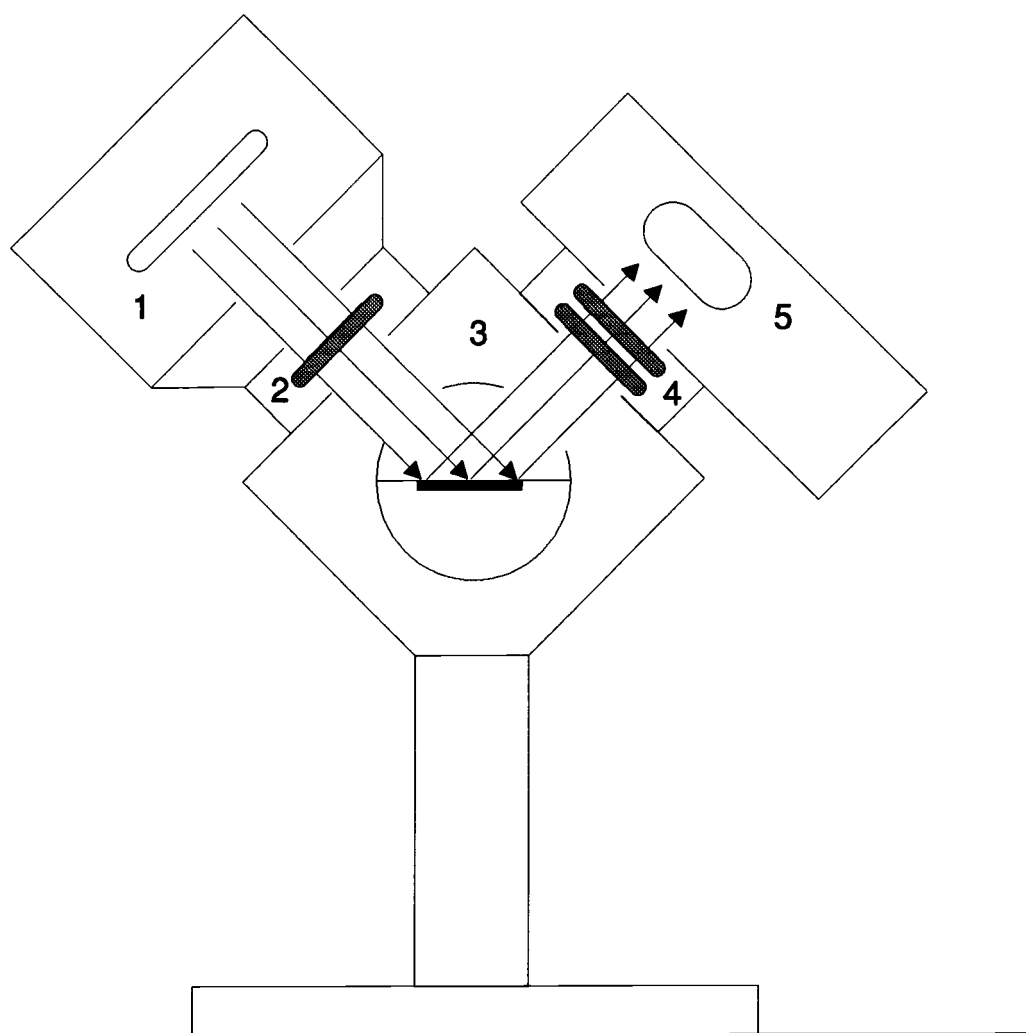


Figure 5.1. HKP Brightness Measuring Device. 1) mercury pen lamp used for excitation, 2) filter holder with 254 nm interference bandpass filter, 3) horizontally oriented powder-sample holder 4) filter holder with 500 nm cutoff filter and neutral-density filter, and 5) photomultiplier tube (PMT).

## Results and Discussion

Crystal data and experimental conditions are summarized in Table 5.1. Atomic coordinates and the isotropic displacement coefficients for the X-ray experiment are listed in Table 5.2. Selected interatomic distances and angles are summarized in Table 5.3. The unit-cell contents for  $\text{YMgB}_5\text{O}_{10}$  are illustrated in Figure 5.2. Figure 5.3 shows the 2-dimensional borate layer condensation as viewed along the  $[010]$  direction. Figure 5.4 illustrates how the intra- and inter-chain Y networks extend parallel to the  $b$  axis. The  $\text{Eu}^{3+}$  luminescence spectrum is found in Figure 5.5. The results of the concentration-quenching curve are illustrated in Figure 5.6.

Table 5.1. Crystal data and experimental conditions for  $\text{YMgB}_5\text{O}_{10}$ .

Diffractometer	Rigaku AFC6R
Radiation	0.70926 Å graphite monochromated Mo $K\alpha$
Formula wt., amu	327.27
Unit cell	Monoclinic
a, Å	8.530(1)
b, Å	7.582(2)
c, Å	9.373(2)
$\beta$ degrees	93.78(1)
V, Å <sup>3</sup>	604.9(2)
Space group	(#14) $P2_1/n$
Z	4
$D_{\text{calc}}$ , g cm <sup>-3</sup>	3.549
F(000)	624
Absorption coeff., $\mu$ cm <sup>-1</sup>	9.802
No. of unique data with $F_o^2 > 2\sigma F_o^2$	1937
$R[F2 > 2\sigma F_o^2]^*$	0.0350
$wR(F_o^2)^*$	0.1038

$$^*R = \Sigma(|F_o^2| - |F_c^2|) / \Sigma|F_o^2|; R_w = [\Sigma w(|F_o^2| - |F_c^2|)^2 / \Sigma w|F_o^2|^2]^{1/2}$$

Table 5.2. Atom positions and  $U_{eq}$  for  $YMgB_5O_{10}$ .

Atom	x	y	z	$U_{eq}^*$
Y	0.18524(5)	0.18601(5)	0.23923(4)	0.0063(1)
Mg	0.9007(2)	-0.0921(2)	0.3722(2)	0.0061(3)
O1	0.9637(3)	0.2919(4)	-0.2297(3)	0.0058(5)
O2	0.6822(3)	0.1505(4)	0.1362(3)	0.0059(5)
O3	0.5092(3)	-0.0904(4)	0.1978(3)	0.0066(5)
O4	0.6865(3)	0.0331(4)	0.3745(3)	0.0054(5)
O5	0.6808(3)	-0.1268(4)	0.0093(3)	0.0069(5)
O6	0.7440(3)	0.0520(4)	0.6268(3)	0.0070(5)
O7	0.5463(3)	0.2290(4)	0.5206(3)	0.0053(5)
O8	0.4945(3)	-0.3502(4)	0.0738(3)	0.0057(5)
O9	0.9160(3)	-0.0286(5)	0.1484(3)	0.0057(5)
O10	0.8245(3)	0.1084(4)	-0.0823(3)	0.0061(5)
B1	0.9817(5)	0.1740(6)	-0.1042(5)	0.0035(7)
B2	0.7768(5)	0.0319(6)	0.0560(5)	0.0039(8)
B3	0.5842(5)	0.0756(6)	0.2429(5)	0.0057(8)
B4	0.6611(5)	0.0996(6)	0.5070(5)	0.0056(8)
B5	0.5650(5)	-0.1888(6)	0.0893(5)	0.0056(7)

$$*U_{eq} = (1/3)\sum_i\sum_j U^{ij}a_i^T a_j.$$

Table 5.3. Selected bond distances and angles for  $\text{YMgB}_5\text{O}_{10}$ .

Atoms	Distance Å	Atoms	Degrees ( ° )
Y – Y intra-chain	3.9455(6)	O(1) – Y – O(5)	61.21(9)
Y – Y inter-chain	6.1957(6)	O(1) – Y – O(7)	121.4(1)
Y – O(1)	2.380(3)	O(1) – Y – O(9)	147.27(9)
Y – O(3)	2.471(3)	O(1) – Y – O(10)	57.04(9)
Y – O(5)	2.699(3)	O(3) – Y – O(9)	85.64(9)
Y – O(6)	2.319(3)	O(6) – Y – O(10)	68.6(1)
Y – O(6)	2.258(3)	O(1) – Mg – O(2)	62.6(1)
Y – O(7)	2.387(3)	O(1) – Mg – O(4)	140.0(1)
Y – O(8)	2.419(3)	O(1) – Mg – O(8)	118.7(1)
Y – O(9)	2.896(3)	O(1) – Mg – O(9)	62.17(1)
Y – O(10)	2.521(3)	O(4) – Mg – O(8)	87.6(1)
Y – O(10)	2.672(3)	O(8) – Mg – O(8)	89.3(1)
Mg – O(1)	2.370(3)	O(1) – B1 – O(9)	105.0(3)
Mg – O(2)	2.075(3)	O(1) – B1 – O(10)	105.6(3)
Mg – O(4)	2.060(3)	O(7) – B1 – O(9)	113.6(3)
Mg – O(8)	2.050(3)	O(2) – B2 – O(5)	109.6(3)
Mg – O(8)	2.088(3)	O(2) – B2 – O(9)	109.7(3)
Mg – O(9)	2.164(3)	O(9) – B2 – O(10)	112.0(3)
B1 – O(9)	1.482(5)	O(1) – B3 – O(2)	107.0(3)
B2 – O(2)	1.451(5)	O(2) – B3 – O(3)	113.3(3)
B2 – O(5)	1.504(5)	O(3) – B3 – O(4)	105.8(3)
B2 – O(9)	1.495(5)	O(1) – B3 – O(4)	112.2(3)
B3 – O(1)	1.472(5)	O(4) – B4 – O(6)	123.7(4)
B3 – O(2)	1.459(5)	O(4) – B4 – O(7)	119.6(4)
B4 – O(6)	1.337(5)	O(6) – B4 – O(7)	116.6(4)
B4 – O(7)	1.398(5)	O(3) – B5 – O(5)	121.3(4)
B5 – O(5)	1.362(5)	O(3) – B5 – O(8)	113.2(3)
B5 – O(8)	1.367(5)	O(5) – B5 – O(8)	125.4(4)

The contents of the unit cell are illustrated in Figure 5.2. The structure contains a 10-coordinate Y atom, a 6-coordinate Mg atom, and 3 and 4-coordinate B atoms. As seen in Figure 5.3, the distorted triangular and tetrahedral B-centered groups condense to form two-dimensional layers extending parallel to (101).

Y-O distances range from 2.258(3) to 2.896(3) Å; the average, 2.5(2) Å, is equivalent to the average 2.5(2) Å distance in the compound  $\text{YCoB}_5\text{O}_{10}$ .<sup>8</sup> The Y intra- and interchain distances are 3.945(1) and 6.196(1) Å, respectively. The zigzag chains of Y atoms that extend parallel to the b axis are easily seen in Figure 5.4.

The distorted octahedral site occupied by the Mg atom exhibits Mg-O distances ranging from 2.050(3) to 2.370(3) Å. The average Mg-O distance, 2.13(12) Å, is comparable to the 2.15(11) Å distance in the compound  $\text{LaMgB}_5\text{O}_{10}$ .<sup>1</sup>

The borate layers are comprised of three 4-coordinate B atoms (B1, B2, and B3) and two 3-coordinate B atoms (B4 and B5.) All B-O distances and O-B-O angles for the 3- and 4-coordinate B atoms are normal. The Y- and Mg-centered polyhedra share either edges or vertices with the condensed borate polyhedra.

### **Eu<sup>3+</sup> Luminescence**

Luminescence of the  $\text{Eu}^{3+}$  ion in a crystalline material is commonly associated with transitions from the excited state  $^5\text{D}_0$  to ground-state levels of the  $^7\text{F}_J$  manifold. In general, the more intense emission features are associated with the  $^5\text{D}_0 \rightarrow ^7\text{F}_1$  transition near 590 nm (orange) or the  $^5\text{D}_0 \rightarrow ^7\text{F}_2$  transition near 620 nm (red). Transitions of the type  $^5\text{D}_0 \rightarrow ^7\text{F}_2, ^7\text{F}_4, ^7\text{F}_6$ , follow the forced

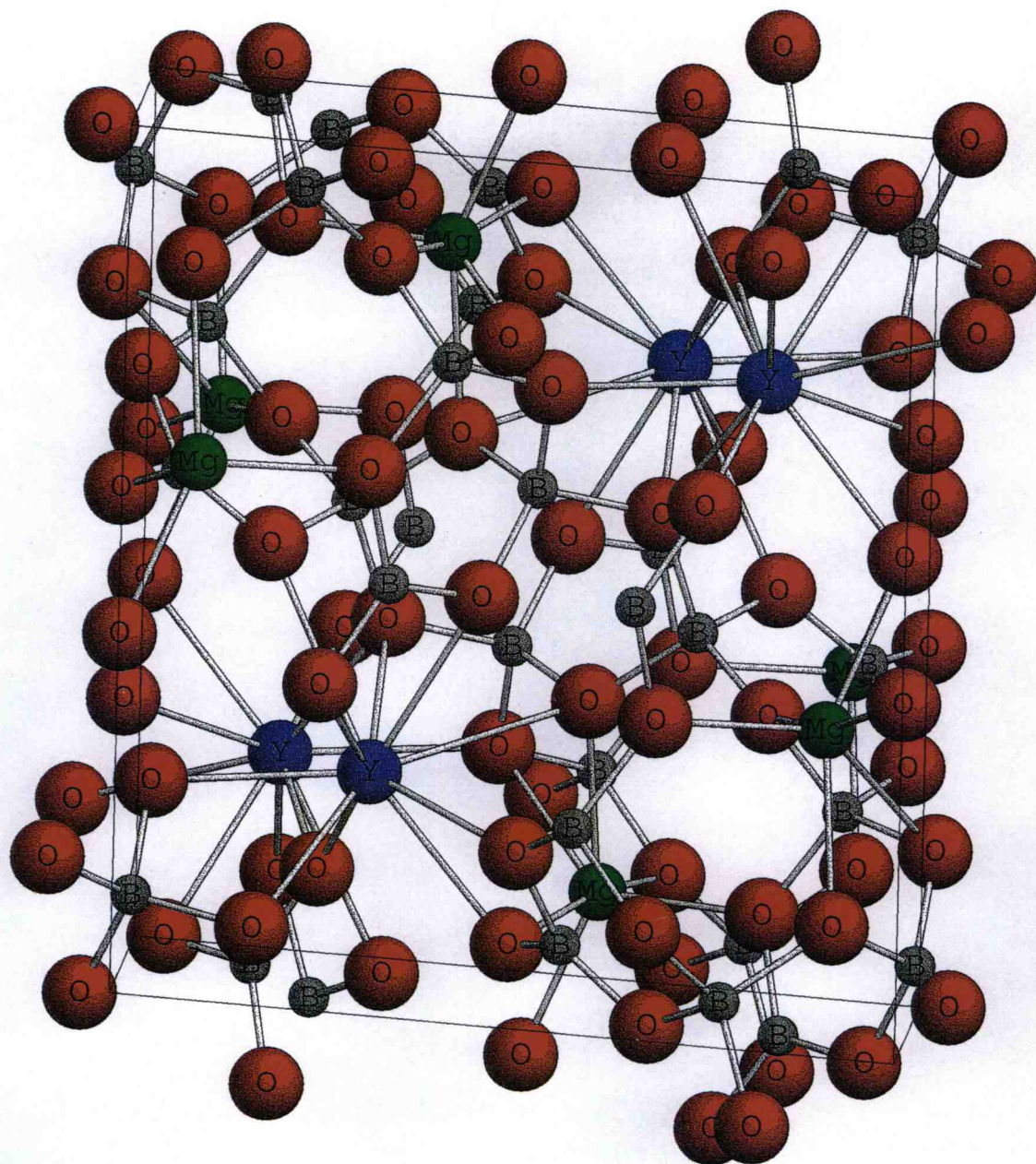


Figure 5.2. Unit-cell contents for  $\text{YMgB}_5\text{O}_{10}$  as viewed along  $[010]$ .



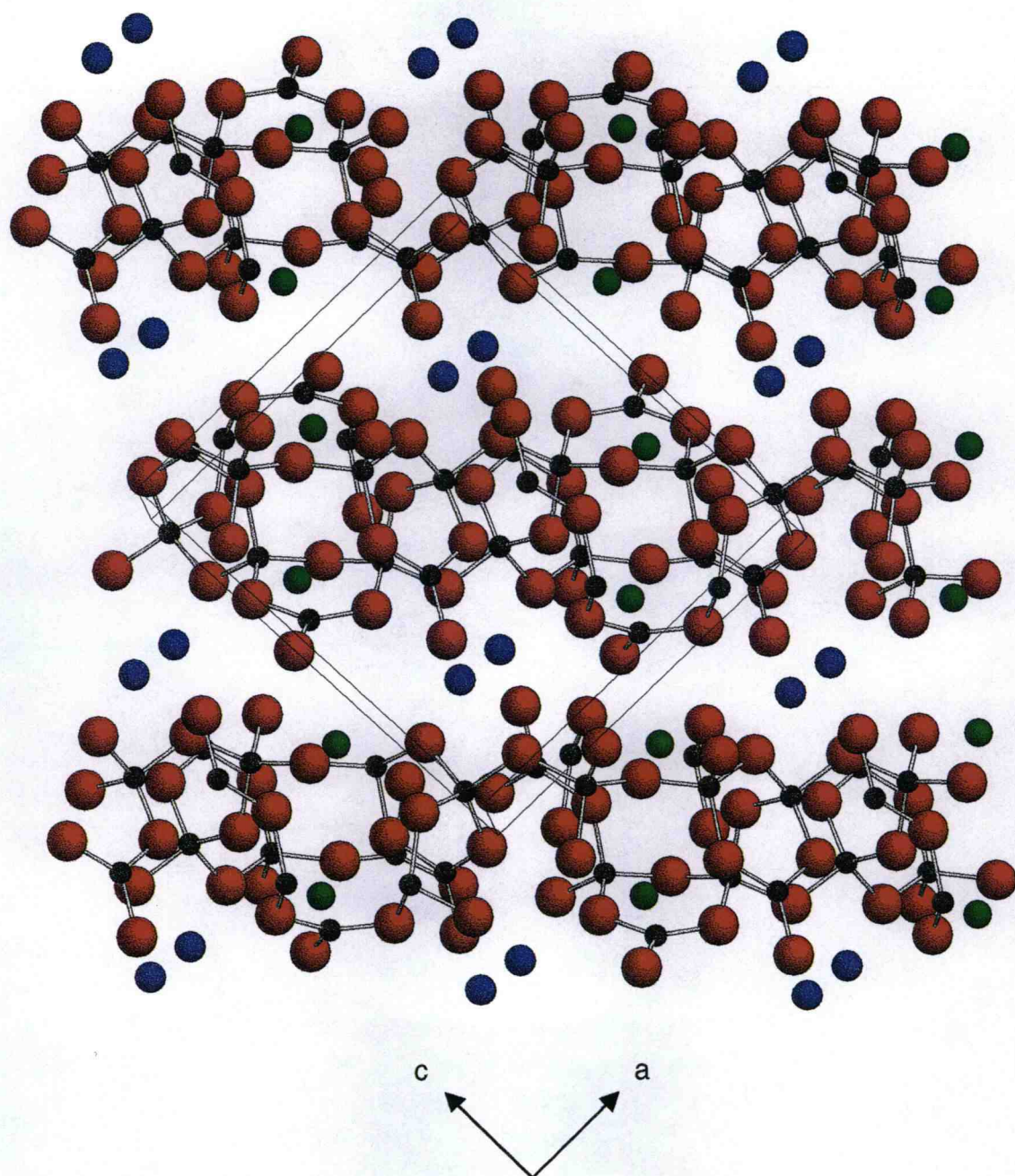


Figure 5.3. Two-dimensional borate layers as viewed along  $[010]$ .



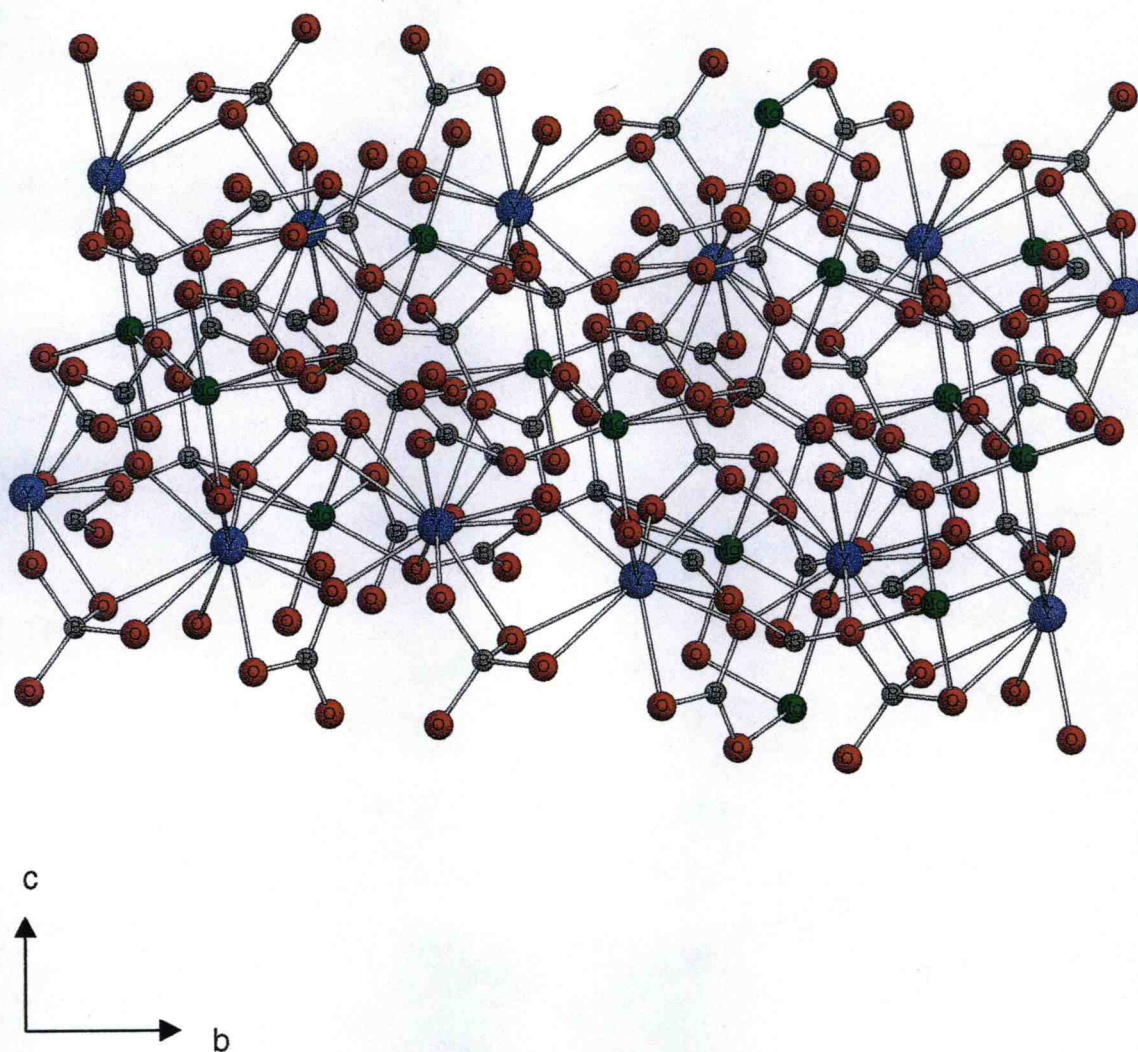


Figure 5.4. Zigzag chains of Y atoms extending parallel to the *b* axis. Inter-chain distance is 6.20 Å and intra-chain distances 3.95 Å.

electric-dipole selection rules, while transitions of the type,  $^5D_0 \rightarrow ^7F_1, ^7F_3, ^7F_5$ , follow the magnetic-dipole selection rules. If the  $\text{Eu}^{3+}$  ion occupies a site lacking a center of symmetry, the electric-dipole transitions are expected to predominate, and as noted above, the strongest of these is usually the  $J = 0 \rightarrow 2$  transition. In the spectrum of  $\text{Y}_{0.95}\text{Eu}_{0.05}\text{MgB}_5\text{O}_{10}$  (Figure 5.5), the most intense emission band corresponds to the  $J = 0 \rightarrow 2$  transition at 611 nm, a result that is consistent with the lack of a center of symmetry<sup>9</sup> for the 10-coordinate Y site.

The concentration-quenching curve for the  $\text{Y}_{1-x}\text{Eu}_x\text{MgB}_5\text{O}_{10}$  ( $0 < x \leq 1$ ) solid solution is shown in Figure 5.6. The brightness of each of the solid-solution compounds has been determined relative to a commercial  $\text{Eu}^{3+}:\text{Y}_2\text{O}_3$  phosphor;<sup>10</sup> hence, the composition  $\text{Y}_{0.25}\text{Eu}_{0.75}\text{MgB}_5\text{O}_{10}$  is, for example, only 50% as bright as the commercial material under 254 nm excitation. The relative PMT signal is plotted against the number density of  $\text{Eu}^{3+}$  cations. The data points in Figure 5.6 correspond to  $x = 0.01, 0.02, 0.05, 0.10, 0.25, 0.50, 0.75$ , and 1. Due to the weak oscillator strength of the parity forbidden  $4f^6$  transitions, the intensity of the  $\text{Eu}^{3+}$  emission is expected to have a linear dependence on concentration<sup>4</sup>. As expected for this compound, emission brightness increases to a relatively high value of  $x = 0.75$ . Beyond  $x = 0.75$ , a steep decrease in the emission brightness ensues. This behavior differs from that of many phosphors, where incorporation of small relative quantities of  $\text{Eu}^{3+}$  ( $< 10$  at.%) leads to considerable concentration quenching. The unusual concentration dependence in  $\text{Y}_{1-x}\text{Eu}_x\text{MgB}_5\text{O}_{10}$  is associated with the structure, specifically the one-dimensional chains of  $\text{YO}_{10}$  polyhedra. This chain structure dimensionally reduces the probability for energy migration among the doped  $\text{Eu}^{3+}$  cations.<sup>2</sup> A high probability for energy transfer has been shown to occur for some of the rare-earths such as  $\text{Tb}^{3+}$ ,  $\text{Eu}^{3+}$  and  $\text{Gd}^{3+}$ . Atoms such as  $\text{La}^{3+}$  and  $\text{Y}^{3+}$  do not show this phenomena, so that they can be used to isolate such atoms, one from the other, along the zigzag chain.

Energy transfer in the  $\text{LnMgB}_5\text{O}_{10}$  system is assumed to occur through two mechanisms. One-dimensional energy transfer is attributed to exchange

interactions between Ln atoms in the zigzag chains. This is possible because the relatively small distance between the intra-chain Ln atoms, which allow sufficient orbital overlap. Quasi one-dimensional energy transfer occurs when energy is transferred between the chains of the Ln polyhedra. Ln – Ln inter-chain energy transfer occurs through multi-polar interactions between chains where the distance is too great for exchange interactions. Thus, the probability of intra-chain energy transfer is much greater than the probability of inter-chain energy transfer. In a structure such as  $\text{Eu}^{3+}:\text{Y}_2\text{O}_3$ , however, there is greater probability for energy migration because of the three-dimensional condensation of the  $\text{YO}_6$  groups. We might expect that the signal would continue to increase to a maximum at  $x = 1.00$ , however, it has been shown that there are traps that quench the  $\text{Eu}^{3+}$  luminescence at high concentrations. One of these traps is thought to occur when  $\text{Eu}^{3+}$  is substituted onto the  $\text{Mg}^{2+}$  site.<sup>11</sup>

On an absolute scale, the loading of  $\text{Eu}^{3+}$  cations into the  $\text{YMgB}_5\text{O}_{10}$  structure prior to concentration quenching losses is also quite high. For the  $\text{Eu}^{3+}:\text{Y}_2\text{O}_3$  phosphor, the  $\text{Eu}^{3+}$  number density is approximately  $9.5 \times 10^{20} \text{ cm}^{-3}$ . For  $\text{Y}_{0.25}\text{Eu}_{0.75}\text{MgB}_5\text{O}_{10}$ , the number density is 30% greater at  $1.2 \times 10^{21} \text{ cm}^{-3}$ . Clearly the absorption strength at 254 nm, or the intrinsic radiative efficiency,<sup>12</sup> or both for the  $\text{Eu}^{3+}$  ion in the host  $\text{YMgB}_5\text{O}_{10}$  are not as great as those achieved for the  $\text{Eu}^{3+}$  ion in  $\text{Y}_2\text{O}_3$ .

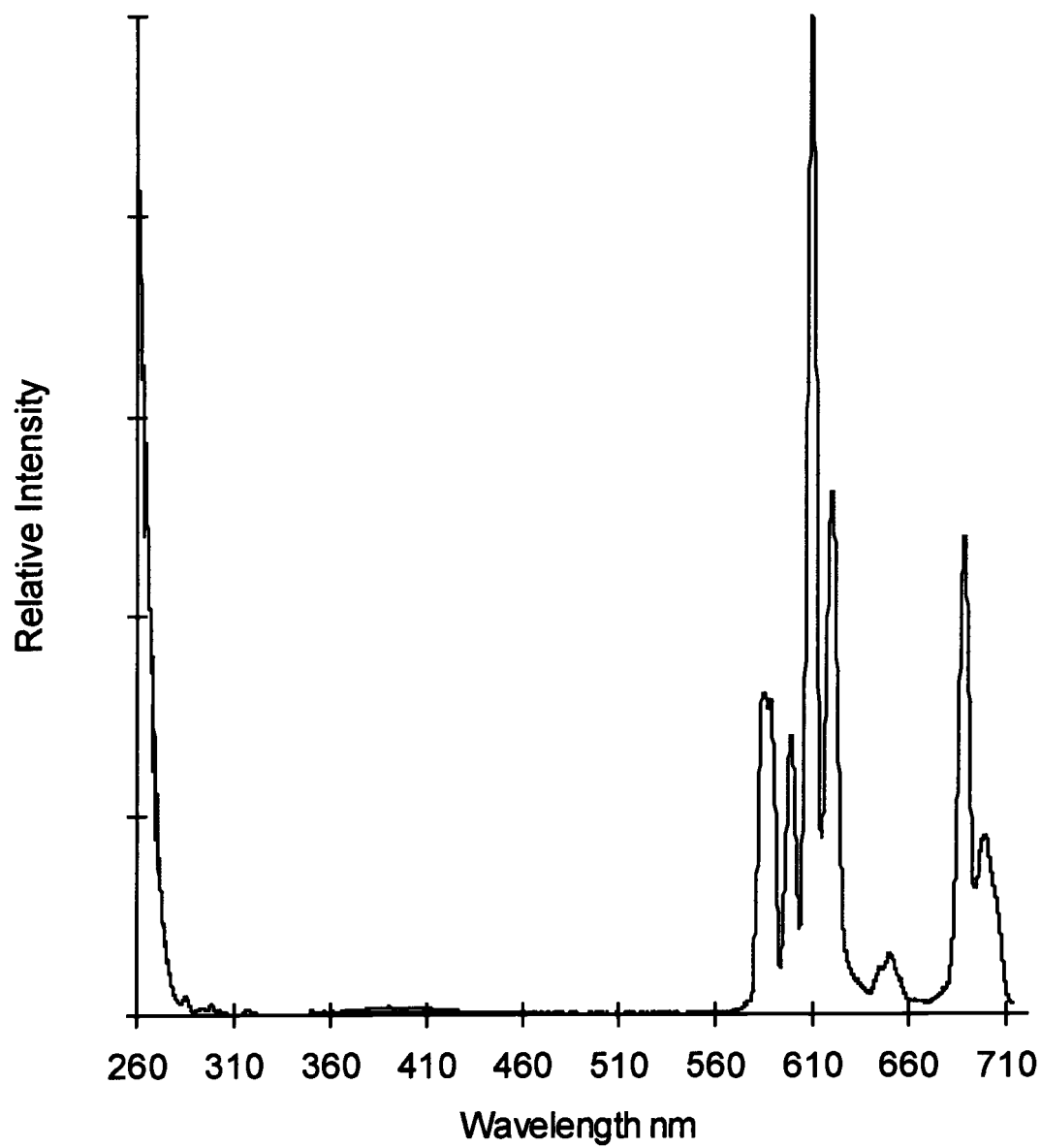


Figure 5.5. The luminescence spectrum of  $\text{Y}_{0.95}\text{Eu}_{0.05}\text{MgB}_5\text{O}_{10}$ .

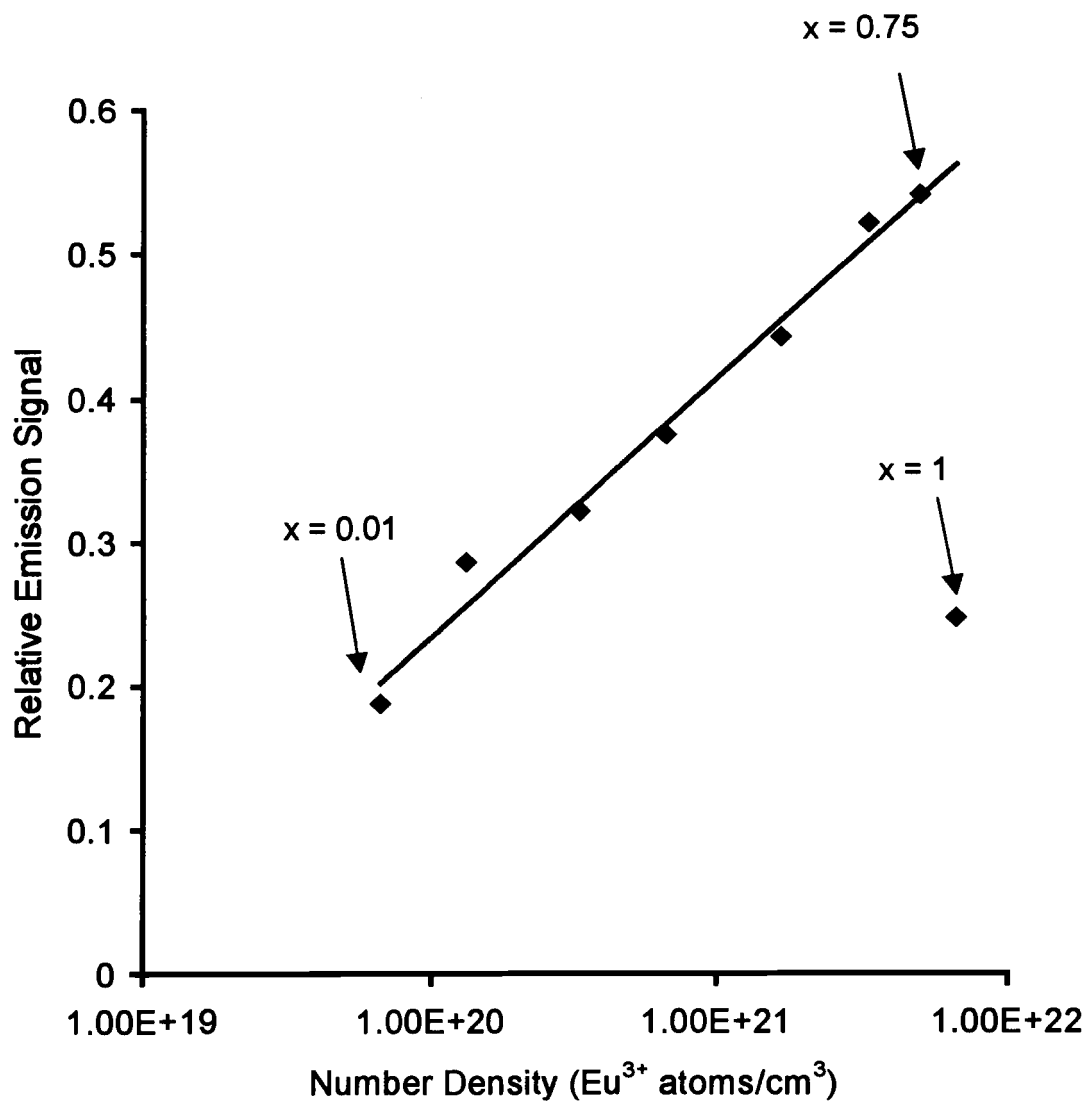


Figure 5.6. Emission signal vs.  $\text{Eu}^{3+}$  concentration in the series  $\text{Y}_{1-x}\text{Eu}_x\text{MgB}_5\text{O}_{10}$  ( $0 < x \leq 1.$ )

## Acknowledgments

Acknowledgment is made to the Phosphor Technology Center of Excellence for support of this research. We thank Ted Hinke for manufacturing the HKP brightness-measuring device.

## References

- 
1. Saubat B., Vlasse M., and Fouassier C., *J. Solid State Chem.*, **34**, **1980**, 271.
  2. Fouassier C., Saubat B., and Hagenmuller P., *J. Luminescence*, **23**, **1981**, 405.
  3. Saakes M., Leskela M., and Blasse G., *Mat. Res. Bull.*, **19**, **1984**, 83.
  4. Buijs M., and Blasse G., *J. Luminescence*, **34**, **1986**, 263.
  5. Sheldrick, G. M., Institut für Anorganische Chemie der Unniversitat, Gottingen, FRG.
  6. *Texsan for Windows*, Version 1.0 (1997).  
Molecular Structure Corporation, 3200A Research Forest Drive,  
The Woodlands, TX 77381, USA.
  7. Ingle J., Crouch S., *Spectrochemical Analysis*, **1988**, Prentice Hall
  8. Abdullaev G. K., Mamedov K. S., Dzhaferov G. G., and Aliev O. A., *Zhurnal Neorganicheskoi Khimii ZNOKA*, **25**, **1980**, 364.
  9. Blasse G., Kita A., *Solid State Luminescence, Theory, Materials and Devices*, Chapter 2, **1993**. Publisher
  10. Osram Sylvania Luminescent Material, Type 2342, Lot No. YCX472.
  11. van Schaik W., Blasse G., *J. Lumin.* **62**, **1994** 203.
  12. Blasse G., *J. Chem. Phys.*, **45**, **1966**, 2356.

## CHAPTER 6

### $\text{Ln}_4\text{BO}_7\text{F}$ , (Ln = Y, Dy, Ho, Er, Tm and Yb); STRUCTURE AND SELECTED OPTICAL PROPERTIES

Gregory A. Peterson and Douglas A. Keszler

To be submitted to Journal of Solid State Chemistry

## Abstract

The new family of compounds  $\text{Ln}_4\text{BO}_7\text{F}$  ( $\text{Ln} = \text{Y}, \text{Dy}, \text{Ho}, \text{Er}, \text{Tm}, \text{and Yb}$ ) has been synthesized, and the structure of the Y derivative has been determined by single-crystal X-ray diffraction methods.  $\text{Y}_4\text{BO}_7\text{F}$  crystallizes in the orthorhombic space group  $\text{Pnma}$  (No. 62) with four formula units in a cell of dimensions  $a = 11.316(2)$ ,  $b = 3.640(2)$ , and  $c = 16.384(3)$  Å.  $R = 0.036$ , and  $wR = 0.034$  for a least-squares refinement of 50 variables with 849 unique reflections. Dy, Ho, Er, Tm, and Yb powders have been synthesized, and unit-cell parameters have been refined from X-ray data. Excitation and emission spectra for  $\text{Tb}^{3+}$ - and  $\text{Eu}^{3+}$ -doped  $\text{Y}_4\text{BO}_7\text{F}$ ; concentration-quenching curves for  $\text{Tb}^{3+}$ - and  $\text{Eu}^{3+}$ -doped  $\text{Ln}_x\text{Y}_{4-x}\text{BO}_7\text{F}$  ( $0 < x \leq 0.5$ ); thermal-quenching data for  $\text{Eu}^{3+}_{0.1}\text{Y}_{3.9}\text{BO}_7\text{F}$ ; and VUV spectra of  $\text{Eu}^{3+}$ -doped  $(\text{Y},\text{Gd})\text{BO}_3$ ,  $\text{Y}_2\text{O}_3$ , and  $\text{Y}_4\text{BO}_7\text{F}$  are presented.

## Introduction

The new family of orthoborate oxide fluoride  $\text{Ln}_4\text{BO}_7\text{F}$  ( $\text{Ln} = \text{Y}, \text{Dy}, \text{Ho}, \text{Er}, \text{Tm}, \text{and Yb}$ ) has been discovered as part of a program on the development of vacuum-ultraviolet (VUV) excited  $\text{Eu}^{3+}$  phosphors. Such materials are of interest to replace  $\text{Eu}:(\text{Y},\text{Gd})\text{BO}_3$  in plasma display panels (PDPs) for HDTV applications.  $\text{Eu}:(\text{Y},\text{Gd})\text{BO}_3$  is an exceptionally bright, red-emitting phosphor under excitation at 147 nm from the Xe discharge in a PDP. Its absorption strength at 147 nm is derived from the presence of borate groups. The orientation of these groups in the structure also provides an efficient means for transferring excitation energy to the  $\text{Eu}^{3+}$  activator. The phosphor emission color, however, is not a true, saturated red. Instead, a significant emission near 590 nm imparts an orange color to the luminescence and this color is largely correlated to the approximate centrosymmetric character of the  $\text{Eu}^{3+}$  dopant site.



To improve the color of  $\text{Eu}^{3+}$  emission, while retaining absorption near 147 nm, we have examined various ternary and quaternary systems containing  $\text{Y}_2\text{O}_3$  and  $\text{B}_2\text{O}_3$  for new phases. In this contribution we describe the new material  $\text{Y}_4\text{BO}_7\text{F}$ , its derivatives, and its  $\text{Eu}^{3+}$  luminescence properties.

## Materials and Methods

Powder samples of  $\text{Ln}_4\text{BO}_7\text{F}$  ( $\text{Ln} = \text{Y, Dy, Ho, Er, Tm, and Yb}$ ) were made by combining the reagents in the molar ratios: 2  $\text{Ln}_2\text{O}_3$  (Stanford Materials, 99.99% or Alfa-Aesar, 99.99%,) 0.5  $\text{B}_2\text{O}_3$  (Alfa-Aesar, 99.98%,) 1.5  $\text{NH}_4\text{F} \cdot \frac{1}{2}\text{H}_2\text{O}$  (Alfa-Aesar, 99.99%,) and 0.2  $\text{Na}_2\text{CO}_3$  (GFS, 99.999%). A series of grinding and heating steps were executed prior to a final anneal at 1373 K for 4 h. Rod-shaped crystals of  $\text{Y}_4\text{BO}_7\text{F}$  were obtained by an evaporative flux method. A 4.3-g mixture of  $\text{YBO}_3$ :  $\text{KF}:\text{B}_2\text{O}_3$  - 47:48:5 wt % was contained in a 10-mL Pt crucible. The Pt crucible was centered in the hot zone of a vertical tube furnace, heated from 25 to 1573 K over an 8-h period, and held at 1573 K for 8 h. A flow of 4 %  $\text{H}_2(\text{g})$ : 96 %  $\text{Ar}(\text{g})$  directed from the bottom of the tube was used as a carrier gas to remove the more volatile KF throughout the heating and cooling cycle. Rod-shaped crystals that were 3–4 mm long with cross-sections of 0.3–1 mm were removed from the rim of the Pt crucible after the furnace had been cooled to room temperature.

A crystal of approximate dimensions 0.2 x 0.15 x 0.1 mm<sup>3</sup> was removed from the center section of a rod shaped crystal and mounted on a glass fiber with epoxy for structure determination. All measurements were made on a Rigaku AFC6R diffractometer with graphite-monochromated Mo  $\text{K}\alpha$  radiation. Cell parameters and the orientation matrix for the data collection were obtained from a least squares refinement with 19 automatically-centered reflections in the range of  $29 < 2\theta < 38^\circ$ . Intensity data were collected over the range of indices  $0 < h < 15$ ,  $-6 < k < 6$ , and  $0 < l < 28$  by using the  $\omega$ - $2\theta$  scan technique to  $2\theta_{\text{max}} = 75^\circ$ . A total of 3089 general reflections were collected, and 1558

were observed ( $F_o^2 > 3\sigma(F_o^2)$ ). The structure was solved by using the direct-methods and least-squares refinement programs included in the Texsan software package.<sup>1</sup> After a full-matrix refinement of the model with isotropic displacement coefficients on each atom, the data were corrected for absorption by using the program DIFABS.<sup>2</sup>  $R = 0.036$  and  $wR = 0.034$  from a least-squares refinement with 50 variables and 849 unique reflections. Anisotropic displacement coefficients were refined only for atoms Y1, Y2, and Y3. The largest peak in the final difference electron-density map is 6.6% of a Y atom, and it is located at a distance 1.5 Å from Y1.

Powder diffraction data for the homologous series of compounds were collected on a Siemens D-5000. Unit cell parameters were refined by using the least squares computer program POLSQ.<sup>3</sup>

Concentration quenching data for the solid solutions  $\text{Eu}_x\text{Y}_{4-x}\text{BO}_7\text{F}$  and  $\text{Tb}_x\text{Y}_{4-x}\text{BO}_7\text{F}$  ( $0 < x \leq 0.5$ ) were determined by using the brightness-measuring device described in Chapter 5. The brightness of the red  $\text{Eu}^{3+}$ -doped samples were determined relative to a commercial  $\text{Eu}:\text{Y}_2\text{O}_3$  phosphor,<sup>4</sup> and the green Tb-doped samples are determined relative to a commercial  $\text{Ce,Tb:MgAl}_{11}\text{O}_{19}$  phosphor.<sup>5</sup> Standard analytical practices insure the minimization of effects from drift in the lamp output and extraneous signals other than those from the  $\text{Eu}^{3+}$  and  $\text{Tb}^{3+}$  emission.<sup>6</sup>

The VUV excitation spectra for  $\text{Eu}^{3+}$ -doped  $(\text{Y,Gd})\text{BO}_3$ ,  $\text{Y}_2\text{O}_3$ , and  $\text{Y}_4\text{BO}_7\text{F}$  were collected at the University of Georgia as part of a cooperative effort on the development of plasma display technologies. UV-Vis luminescence data were also collected in our laboratory. Excitation provided by an Oriel 300-W Xenon lamp was passed through a 50-cm water filter, focused onto the entrance slits of a Cary model-15 double prism monochromator, and subsequently focused onto the sample. Luminescence was collected at nearly a right angle to the excitation beam, dispersed through an Oriel 22500 1/8-m monochromator, and detected with a Hamatsu R636 photomultiplier tube. The signal was collected and amplified with a Keithley model 486 picoammeter and converted to a digital signal for computer acquisition. Spectrometer control and data acquisition were

achieved with computer programs written in this laboratory. The excitation spectra were corrected by using sodium salicylate and rhodamine B as quantum counters. The emission spectra were corrected with a tungsten lamp that has been calibrated at Eppley Laboratories, Inc. Chromaticity coordinates are calculated from the corrected spectrum with a program written in our laboratory.<sup>7</sup>

The thermal quenching data were also collected in our laboratory. The sample was placed in a Cryo Industries (Model CRG-102) cryostat, and cooled to 80 K with N<sub>2</sub>(l). A Conductus LTC-10 temperature controller was used to regulate the temperature for collection of data at 10-K intervals up to room temperature.

## Results and Discussion

Crystal data and experimental conditions for the X-ray-experiment on Y<sub>4</sub>BO<sub>7</sub>F are summarized in Table 6.1, atomic parameters are listed in Table 6.2, and the contents of the unit cell are depicted in Figure 6.1. The structure contains four crystallographically distinct Y sites and one B site. Atoms Y1 and Y4 are coordinated by seven O atoms -atom Y2 by one F and six O atoms and atom Y3 by two F and 5 O atoms. These Y centered polyhedra share vertexes and edges to form a three-dimensional framework (Figure 6.2) with the 3-coordinate B atoms occupying channels that extend along the *b* axis. Considering these coordination environments, the structure is best summarized by the descriptive formula Y<sub>4</sub>(BO<sub>3</sub>)O<sub>4</sub>F.

The Y1-centered polyhedron can best be described as a monocapped octahedron with approximate S<sub>6</sub> symmetry. The six O atoms forming the distorted octahedron are positioned at 2.305(8) to 2.343(7) Å, (avg. = 2.32 Å) from the Y1 atom, while the O3 atom, which forms the cap, is located at 2.59 Å from the Y atom. The Y1-centered polyhedron shares edges with the Y2, Y3, and Y4 polyhedra through O4...O6, O3...O6, and O5...O7, respectively (Figure

6.1.) The Y2-centered polyhedron is a highly distorted monocapped octahedron with the F-atom cap extending from a face formed by two O2 atoms and one O6 atom. The Y2-centered polyhedron shares edges with the Y3 and Y4 polyhedra through O2...F, and O1...O2, respectively. The Y3-centered polyhedron can be described as a distorted tetragonal base-trigonal base polyhedron. The tetragonal base is formed by the atoms O2, O3, O5, and F, and the trigonal base by the O3, O6, and F atoms. The range of Y3-O and Y3-F distances is 2.222(7) to 2.372(5) Å, resulting in a polyhedron with approximately  $C_s$  symmetry. The Y4-centered polyhedron can best be described as a monocapped trigonal prism with the O1 atom resting above the rectangular face formed by two O1 and two O7 atoms.

Interatomic distances and angles are listed in Table 6.4. Y-O distances range from 2.195(8) to 2.587(9) Å. The average distance, 2.33(1) Å, may be compared to the 2.328-Å Y-O distance calculated on the basis of a seven-coordinate Y site.<sup>8</sup> The distances also scale well with those, 2.258(3) to 2.896(3) Å, for the ten-coordinate site in  $YMgB_5O_{10}$ ,<sup>9</sup> as well as those, 2.24 – 2.33 Å, for the two 6-coordinate Y sites in  $Y_2O_3$ .<sup>10</sup> The two Y-F distances, 2.273(4) and 2.546(7) Å, are similar to those, 2.28 and 2.54 Å, observed in  $YF_3$ .<sup>11</sup>

All B-O distances and O-B-O angles in the  $BO_3$  triangle are normal. The 3-coordinate F atom has two F-Y3 distances at 2.272(4) Å and one F-Y2 distance at 2.546(7) Å. Y2-F-Y3 and Y3-F-Y3 angles of 103 and 106°, respectively, are consistent with the description of the F environment as a distorted trigonal pyramid. Atoms O1, O2, O5, and O6 are 4-coordinate and bond only to Y, having surroundings that are best described as distorted tetrahedra. Atoms O3, O4, and O7 are each coordinated by three Y atoms and one B atom with the B atom forming the apex of an irregular trigonal pyramid.

Bond-valence calculations<sup>12</sup> have been done to corroborate the crystallographic assignment of F in the structure; results are summarized in Table 3.3. The calculated charge on the F atom is -0.92, while charges for all other atoms are near conventional integral values. Placement of O on the 3-

coordinate F site without significant changes to the coordination environment i.e., same bond distances, results in a calculated bond valence for O =  $-1.23$ . Calculated valences for F substituted onto the O1, O2, O5, and O6 sites are  $-1.64$ ,  $-1.65$ ,  $-1.32$ , and  $-1.39$ , respectively. While these results support the crystallographic assignment of the F-atom position, it is possible that an extensive disorder could occur with the F atoms statistically distributed across the F, O1, O2, O5, and O6 sites. This model, however, is inconsistent with the unique coordination geometry at the F-site.

Table 6.1. Crystal data and experimental conditions for  $Y_4BO_7F$ .

Diffractometer	Rigaku AFC6R
Radiation	0.70926 Å graphite monochromated Mo $K\alpha$
Formula wt., u	497.43
Unit cell	Orthorhombic
a, Å	11.312(1)
b, Å	3.6426(3)
c, Å	16.389(2)
V, Å <sup>3</sup>	675.31(2)
Space group	(#62) Pnma
Z	4
D <sub>calc</sub> , g cm <sup>-3</sup>	4.896
F(000)	904
Absorption coeff., $\mu$ cm <sup>-1</sup>	34.12
No. of unique data	1558
$F_o^2 > 3\sigma(F_o^2)$	
R(F <sub>o</sub> )*	0.036
wR(F <sub>o</sub> )*	0.034

$$*R = \sum(|F_o| - |F_c|) / \sum |F_o|; wR = [\sum w(|F_o| - |F_c|)^2 / \sum w |F_o|^2]^{1/2}$$

Table 6.2. Atom parameters for Y<sub>4</sub>BO<sub>7</sub>F.

Atom	x	y	z	B <sub>eq</sub> *
Y1	0.36718(9)	0.2500	0.23980(6)	0.11(2)
Y2	0.7817(1)	-0.2500	0.44544(7)	0.15(2)
Y3	0.6121(1)	-0.2500	0.13356(6)	0.14(2)
Y4	0.4147(1)	-0.2500	0.43255(6)	0.06(2)
B	0.602(1)	0.2500	0.3110(7)	0.2(2)
O1	0.5979(7)	-0.2500	0.4878(4)	0.1(1)
O2	0.7776(7)	0.2500	0.5214(4)	0.2(1)
O3	0.5946(8)	0.2500	0.2258(4)	0.4(1)
O4	0.7090(7)	0.2500	0.3492(5)	0.4(1)
O5	0.2998(7)	-0.2500	0.3147(5)	0.1(1)
O6	0.4133(8)	-0.2500	0.1588(4)	0.4(1)
O7	0.4953(7)	0.2500	0.3519(4)	0.2(1)
F	0.5628(6)	0.2500	0.0578(4)	0.5(1)

$$*B_{eq} = (8\pi^2/3)\sum_i\sum_j U_{ij}a_i a_j^* a_i a_j$$

Table 6.3. Bond valence calculations and results for Y<sub>4</sub>BO<sub>7</sub>F.

Atom	Calculated Charge	Atom	Calculated Charge
Y1	+2.86	O1	-2.25
Y2	+3.02	O2	-2.28
Y3	+3.07	O3	-1.88
Y4	+3.17	O4	-1.93
B	+2.90	O5	-1.80
F	-0.92	O6	-1.90
		O7	-2.06

Table 6.4. Selected interatomic distances (Å) and angles (°).

Atoms	Distance, Å	Atoms	Angle, °
Y(1)– O(3)	2.587(9)	O(3) – Y(1) – O(5)	111.9(2)
Y(1)– O(4)	2.305(8)	O(4) – Y(1) – O(5)	111.9(2)
Y(1)– O(5) × 2	2.323(5)	O(4) – Y(1) – O(7)	167.7(2)
Y(1)– O(6) × 2	2.314(5)	O(5) – Y(1) – O(6) × 2	173.7(3)
Y(1)– O(7)	2.343(8)	O(6) – Y(1) – O(7) × 2	108.0(2)
Y(2)– O(1)	2.195(8)	O(1) – Y(2) – O(2)	78.6(2)
Y(2)– O(2) × 2	2.205(4)	O(1) – Y(2) – O(6)	149.6(3)
Y(2)– O(4) × 2	2.542(6)	O(2) – Y(2) – O(4)	159.0(3)
Y(2)– O(6)	2.268(8)	F – Y(2) – O(2)	66.8(2)
Y(2)– F	2.546(7)	F – Y(2) – O(6)	95.1(3)
Y(3)– O(2)	2.222(8)	O(2) – Y(3) – O(3)	81.8(2)
Y(3)– O(3) × 2	2.372(5)	O(3) – Y(3) – O(5)	80.9(2)
Y(3)– O(5)	2.287(8)	F – Y(3) – O(3)	160.2(3)
Y(3)– O(6)	2.285(9)	F – Y(3) – O(5)	115.5(2)
Y(3)– F × 2	2.273(4)	F – Y(3) – O(6)	81.8(2)
Y(4)– O(1)	2.259(8)	O(1) – Y(4) – O(1)	108.4(3)
Y(4)– O(1) × 2	2.244(4)	O(1) – Y(4) – O(2)	75.6(2)
Y(4)– O(2)	2.303(8)	O(1) – Y(4) – O(5)	147.5(3)
Y(4)– O(5)	2.327(8)	O(2) – Y(4) – O(5)	75.2(3)
Y(4)– O(7) × 2	2.430(5)	O(5) – Y(1) – O(7)	76.0(2)
B – O(3)	1.40(1)	O(3) – B3 – O(4)	120(1)
B – O(4)	1.37(1)	O(3) – B3 – O(7)	115(1)
B – O(7)	1.37(1)	O(4) – B4 – O(7)	123.9(9)

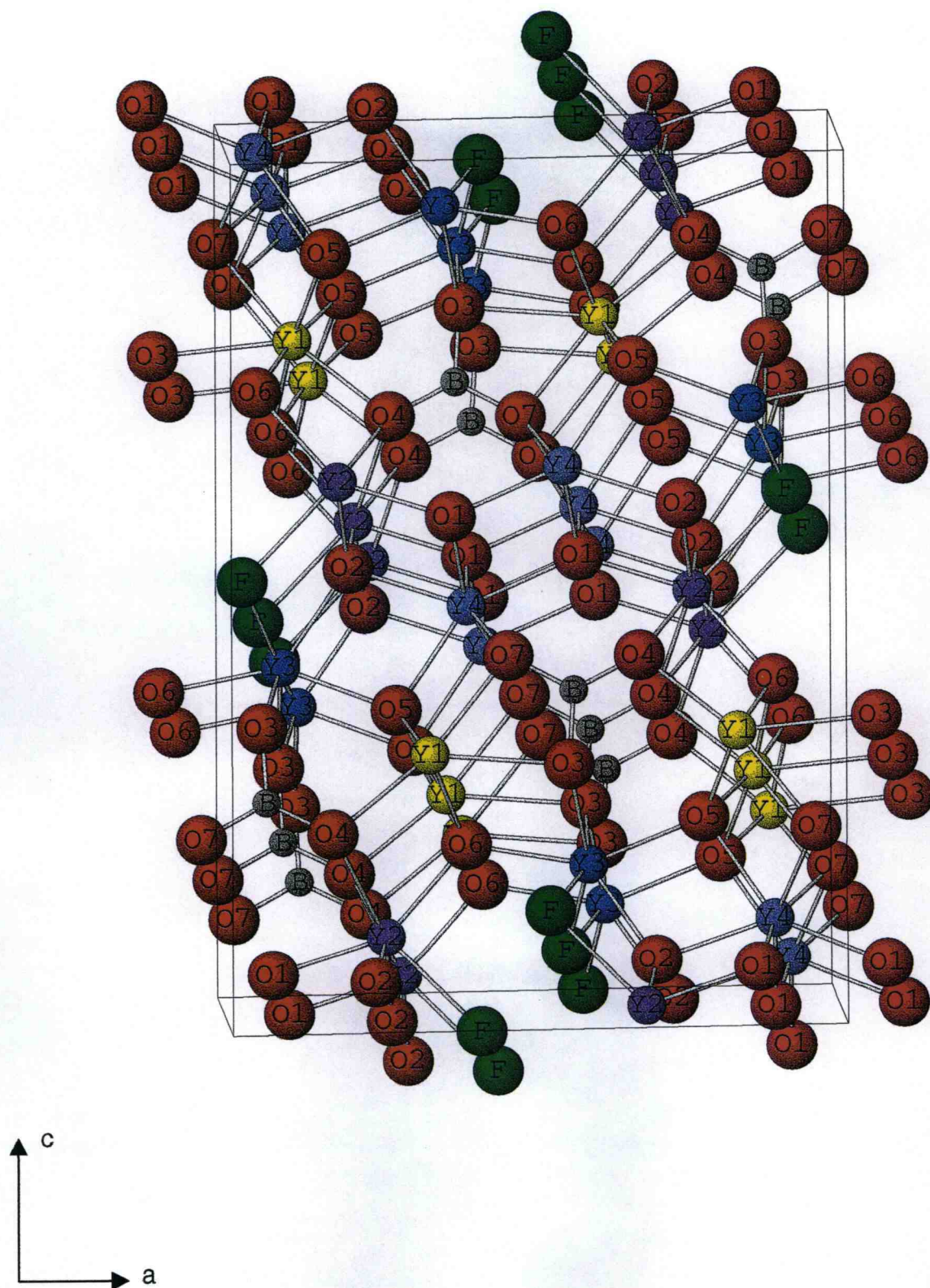


Figure 6.1. Unit-cell contents for  $\text{Y}_4\text{BO}_7\text{F}$ .



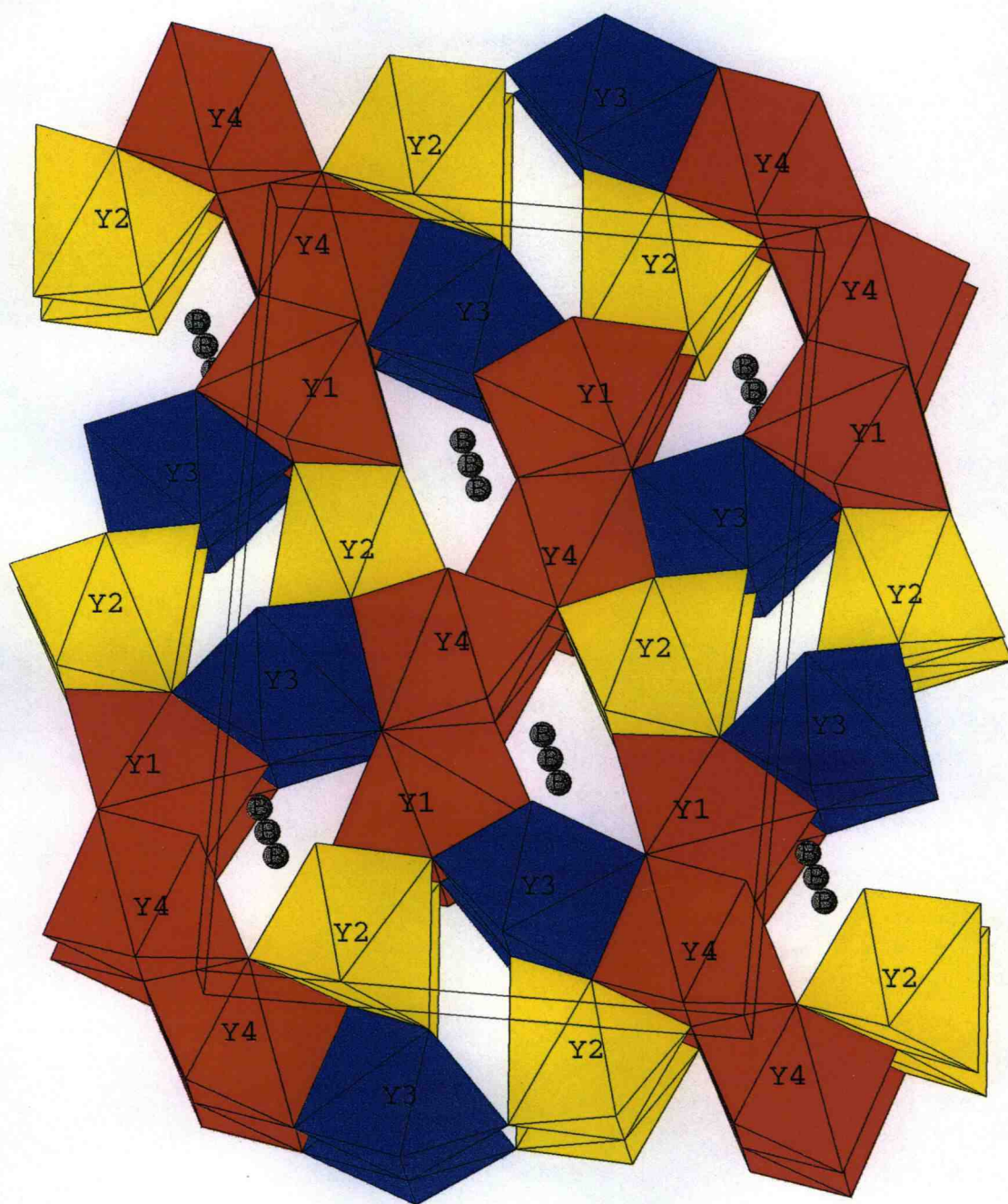


Figure 6.2. Y-centered Polyhedra.

As seen from Table 6.5 and Figure 6.3, each of the Ln derivatives in the range Dy-Yb exists in the orthorhombic structure type of the Y compound. Unit-cell volumes scale to the size of the Ln atom. Attempts to prepare Eu, Gd, and Tb derivatives resulted in the production of multi-phased powders that included the starting metal oxide,  $\text{LnBO}_3$ , and the  $\text{LnOF}$  phase. For the larger lanthanides (Ce – Sm,) no evidence for the existence of  $\text{Ln}_4(\text{BO}_3)\text{O}_4\text{F}$  was obtained; here, the X-ray diffraction patterns were dominated by the presence of  $\text{LnOF}$ .

Table 6.5. Cell data for  $\text{Ln}_4\text{BO}_7\text{F}$ .

Formula	a, Å	b, Å	c, Å	Volume Å <sup>3</sup>	Ln Crystal Radius <sup>13</sup> , Å
$\text{Dy}_4\text{BO}_7\text{F}$	11.3404(9)	3.6678(3)	16.495 (2)	686.1(2)	1.110
$\text{Y}_4\text{BO}_7\text{F}$	11.312(1)	3.6426(3)	16.389 (2)	675.3(2)	1.10
$\text{Ho}_4\text{BO}_7\text{F}$	11.318(1)	3.6448(3)	16.404 (2)	676.7(2)	1.098**
$\text{Er}_4\text{BO}_7\text{F}$	11.2799(7)	3.6215(2)	16.321(1)	666.7(2)	1.085
$\text{Tm}_4\text{BO}_7\text{F}$	11.225(1)	3.6011(3)	16.237 (2)	656.3(2)	1.075**
$\text{Yb}_4\text{BO}_7\text{F}$	11.188(1)	3.5800(4)	16.161 (2)	647.3(2)	1.065

\*\* average of 6- and 8-coordinate values.

## Spectroscopic Properties

Luminescence of the  $\text{Tb}^{3+}$  ion in a crystalline material is generally associated with transitions from the excited state  $^5\text{D}_4$  to ground-state levels of the  $^7\text{F}_j$  manifold, where  $j = 6, 5, 4$ , and  $3$ .<sup>14</sup> The  $^5\text{D}_4 \rightarrow ^7\text{F}_5$  transition is generally the stronger one, and its maximum is at 547 nm in the spectrum of  $\text{Tb}_{0.1}\text{Y}_{3.9}\text{BO}_7\text{F}$  (Figure 6.4.) Chromaticity coordinates  $x = 0.362$ , and  $y = 0.628$

compare well with  $x = .339$ , and  $y = 564$  for the phosphor  $\text{Tb:Y}_3(\text{Al,Ga})_5\text{O}_{12}$ .<sup>15</sup> The excitation spectrum consists of a broad absorption band that corresponds to the  $4f^8 \rightarrow 5d^1$  transition in  $\text{Tb}^{3+}$ .

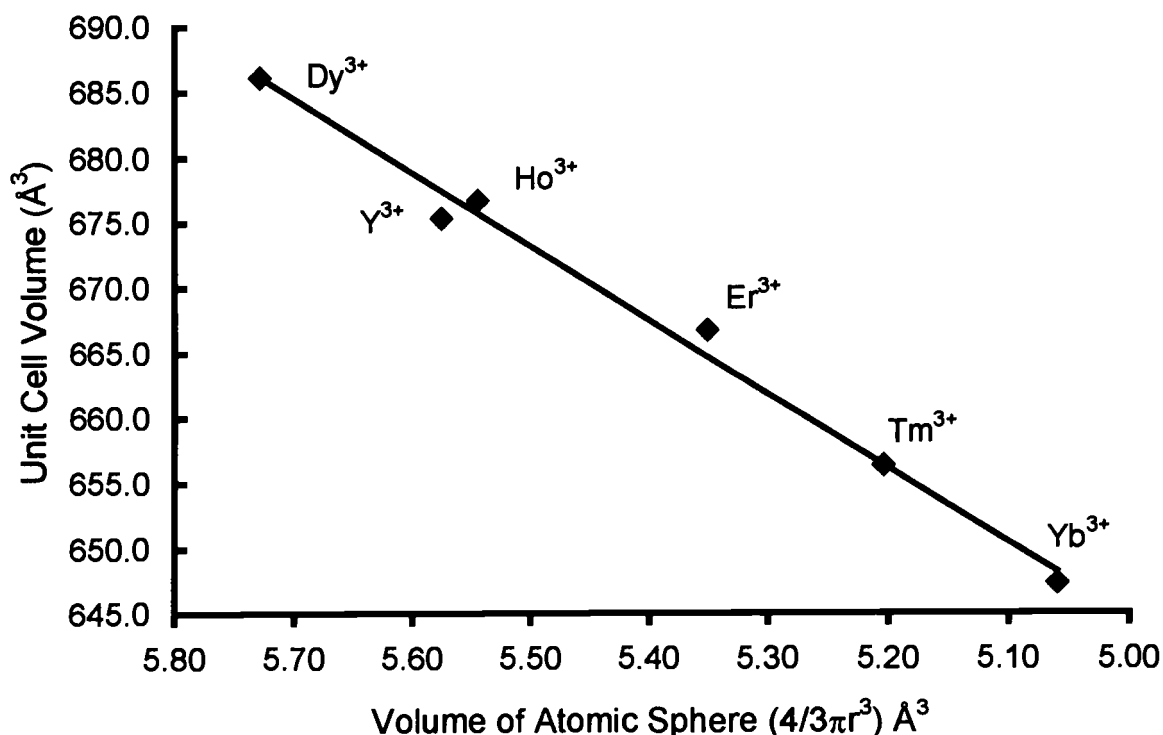


Figure 6.3. The relationship between the unit cell volume and the size of the atomic sphere.

Luminescence of the  $\text{Eu}^{3+}$  ion in a crystalline material is generally associated with transitions from the excited state  $^5\text{D}_0$  to ground-state levels of the  $^7\text{F}_J$  manifold. In general, the more intense emission features are associated with the  $^5\text{D}_0 \rightarrow ^7\text{F}_1$  transition near 590 nm (orange) or the  $^5\text{D}_0 \rightarrow ^7\text{F}_2$  transition near 620 nm (red). The transitions of the type,  $^5\text{D}_0 \rightarrow ^7\text{F}_2$ ,  $^7\text{F}_4$ ,  $^7\text{F}_6$ , follow the forced electric-dipole selection rules, while the transitions of the type,  $^5\text{D}_0 \rightarrow ^7\text{F}_1$ ,

${}^7F_3$ ,  ${}^7F_5$ , follow the magnetic-dipole selection rules. If the  $\text{Eu}^{3+}$  ion occupies a site lacking a center of symmetry, the electric-dipole transitions are expected to predominate, and as noted above, the strongest of these is usually the  $J = 0 \rightarrow 2$  transition. In the spectrum of  $\text{Eu}_{0.1}\text{Y}_{3.9}\text{BO}_7\text{F}$  (Figure 6.5), the most intense peak corresponds to the  $J = 0 \rightarrow 2$  transition at 612 nm, a result that is consistent with the lack of centers of symmetry for the four Y sites. The emission bands are inhomogeneously broadened because of the substitution of Eu on the four different Y sites. The chromaticity coordinates  $x = 0.645$  and  $y = 0.354$  compare well to the values  $x = 0.654$  and  $y = 0.346$  for the standard red phosphor  $\text{Eu}:\text{Y}_2\text{O}_3$ . The values also represent a deeper red color in comparison to the values  $x = 0.632$  and  $y = 0.368$  for  $\text{Eu}:(\text{Y},\text{Gd})\text{BO}_3$ .

Concentration quenching experiments were conducted for both  $\text{Eu}^{3+}$  and  $\text{Tb}^{3+}$ . Figure 6.4 is a plot of the relative brightness of a series of  $\text{Eu}^{3+}$  and  $\text{Tb}^{3+}$  substituted samples,  $\text{Y}_{4-x}\text{Eu}_x\text{BO}_7\text{F}$  and  $\text{Y}_{4-x}\text{Tb}_x\text{BO}_7\text{F}$  ( $x = 0.02, 0.05, 0.10, 0.20$  and  $0.50$ ). Samples with concentrations  $x \geq 0.50$  were not made with much success, since a lower solubility limit is observed with the larger lanthanides.

The results of the quenching experiments are comparable to those of  $\text{Eu}:\text{Y}_2\text{O}_3$ , a result that is not surprising when the structures of the two materials are compared. The  $\text{Y}_2\text{O}_3$  structure is a framework of Y-O-Y linkages, much like that of  $\text{Y}(\text{BO}_3)\text{O}_4\text{F}$ . As a result, the probabilities for energy migration should be similar for the two hosts.  $\text{Eu}_x:\text{Y}_{2-x}\text{O}_3$  showed that strong concentration quenching occurred at concentrations higher than  $x = 0.1$ ,<sup>4</sup> a consequence of energy migration over the three-dimensional Eu-O substructure to quenching impurities. Energy migration over  $\text{Tb}^{3+}$  sublattices has been shown to occur also,<sup>16</sup> so that a similar behavior is expected.

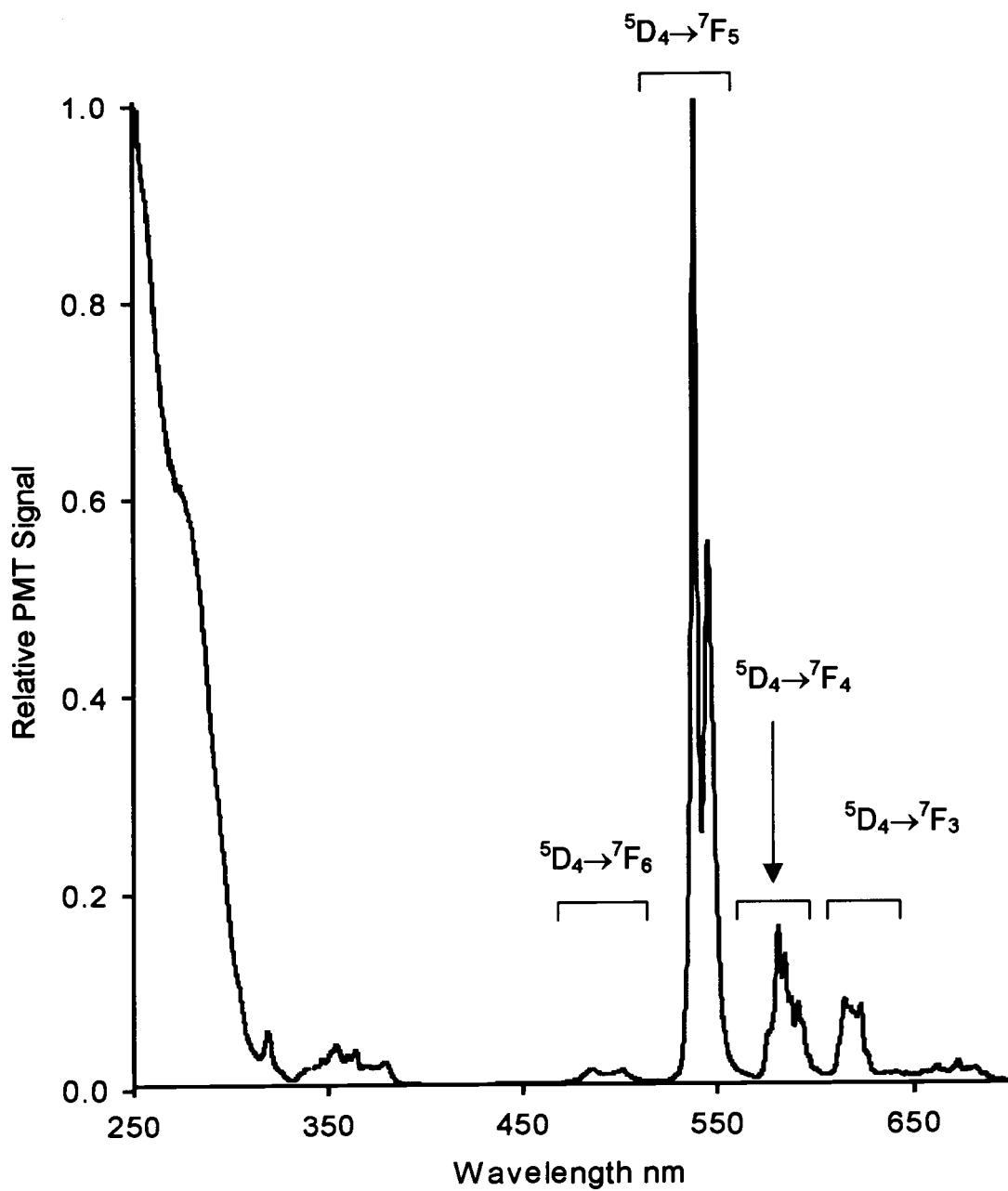


Figure 6.4. Excitation and emission spectra of  $\text{Tb}_{0.1}\text{Y}_{3.9}\text{BO}_7\text{F}$ ; emission  $\lambda_{\text{exc}} = 285 \text{ nm}$  excitation  $\lambda_{\text{em}} = 546 \text{ nm}$ .

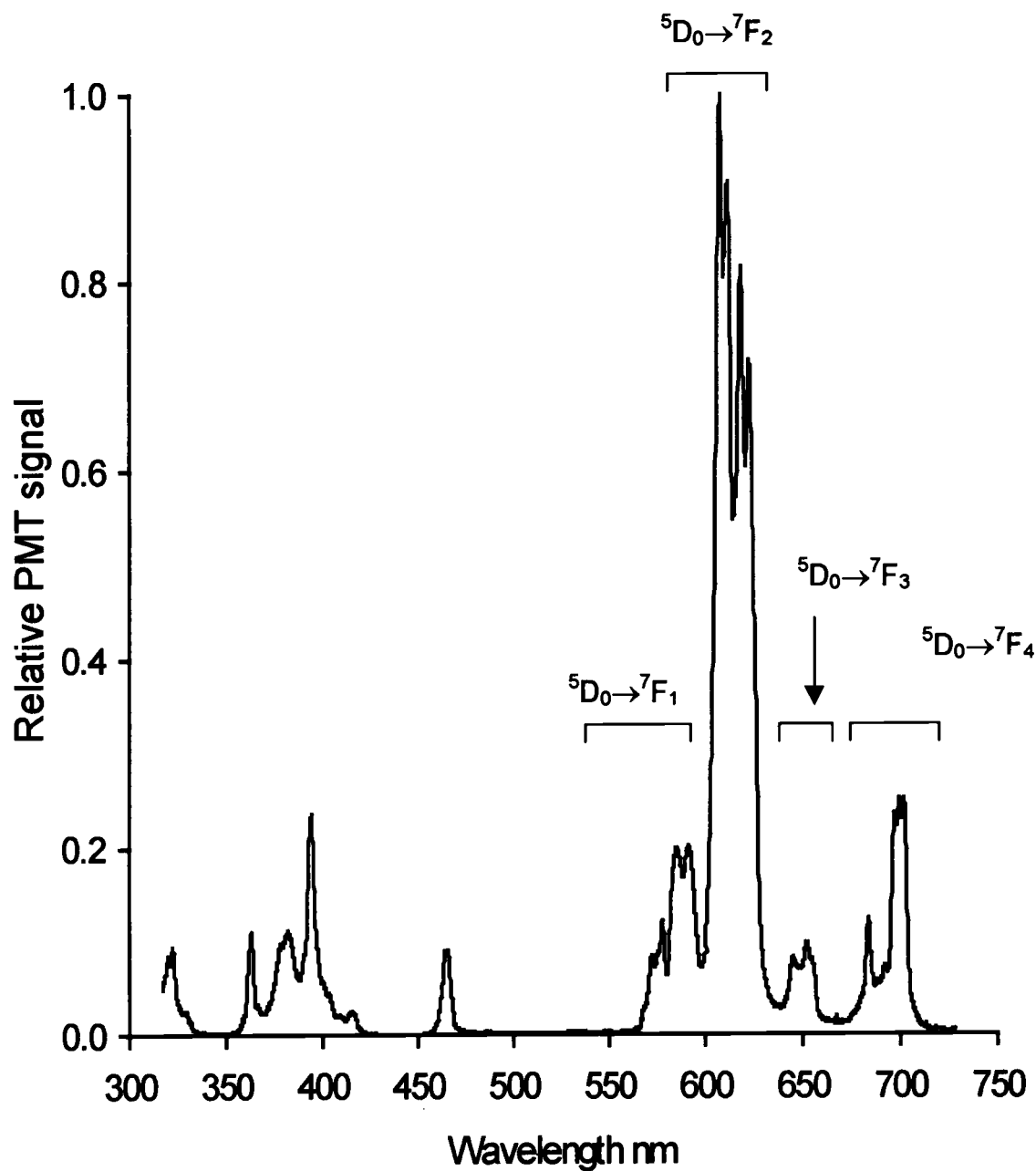


Figure 6.5. Excitation and emission spectra of  $\text{Eu}_{0.1}:\text{Y}_{3.9}\text{BO}_7\text{F}$   
 emission  $\lambda_{\text{exc}} = 276 \text{ nm}$  excitation  $\lambda_{\text{em}} = 612 \text{ nm}$ .

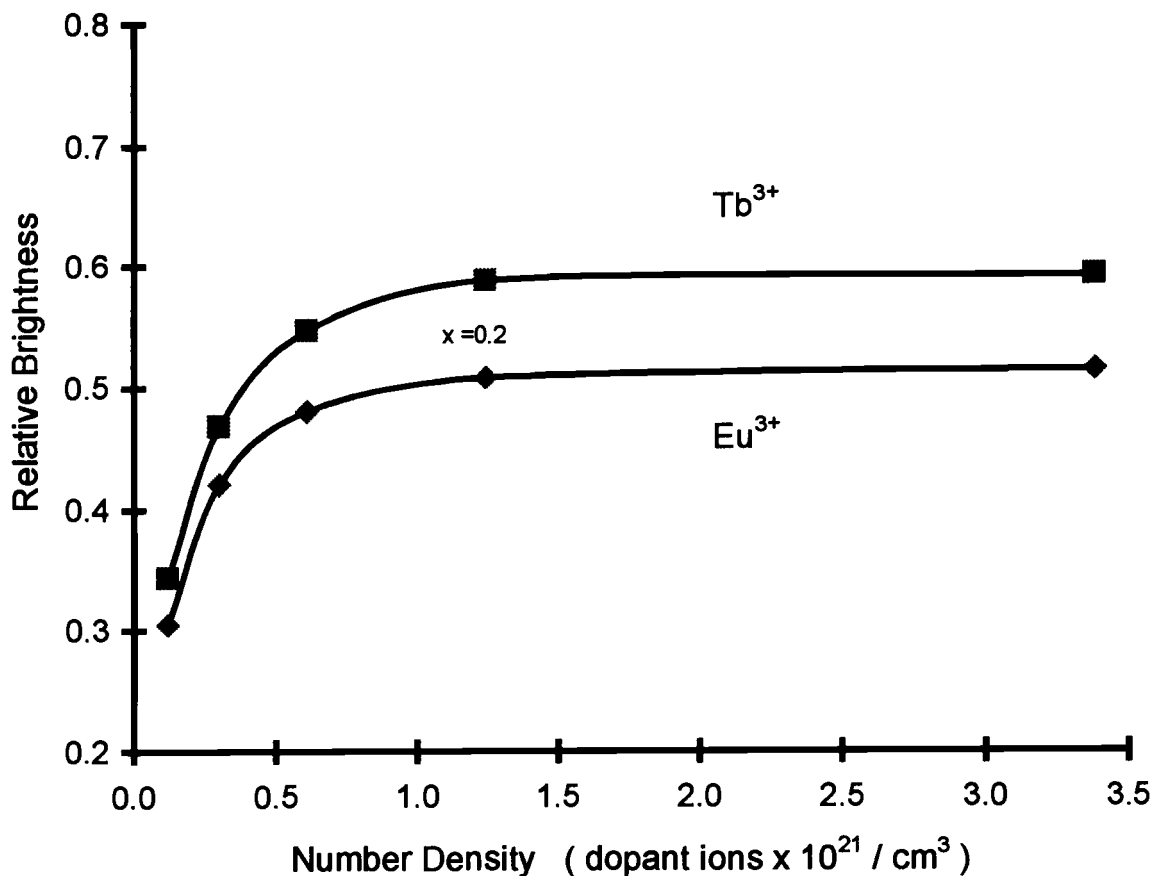


Figure 6.6. Concentration quenching of  $\text{Y}_{4-x}\text{Eu}_x\text{BO}_7\text{F}$  and  $\text{Y}_{4-x}\text{Tb}_x\text{BO}_7\text{F}$  ( $x = 0.02, 0.05, 0.10, 0.20$ , and  $0.50$ .)

Thermal-quenching measurements were made on  $\text{Eu}_{0.1}\text{Y}_{3.9}\text{BO}_7\text{F}$ , and the results are plotted in Figure 6.7. The relative brightness of the emission band at 612 nm is plotted as a function of temperature. The title compound shows a loss of 16% of its initial emission brightness as it is heated from 80 to 300 K, indicating nonradiative decay is limited in this host.

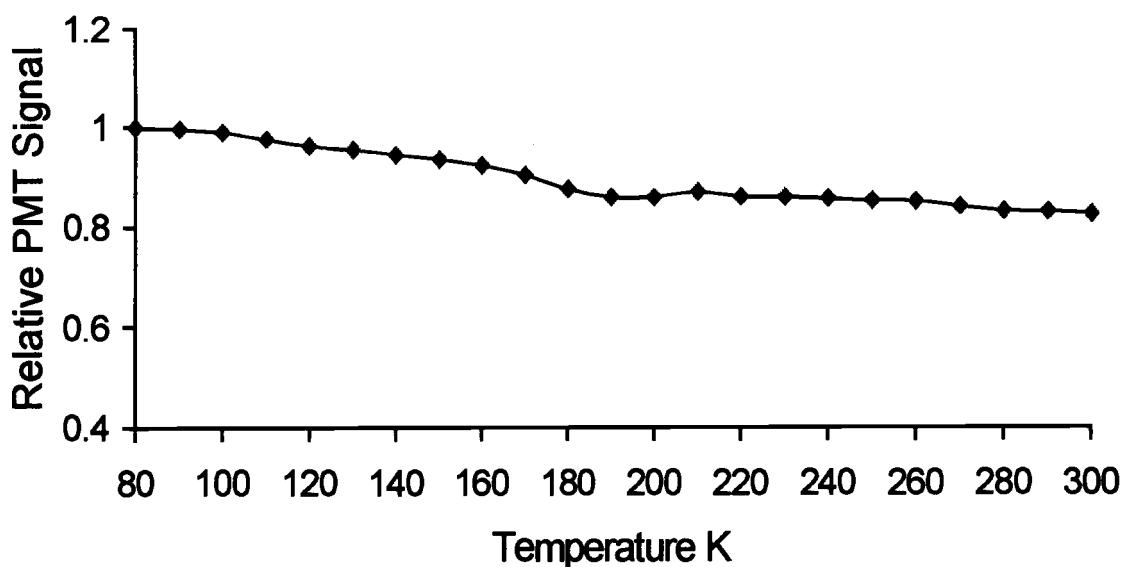


Figure 6.7. Temperature quenching in  $\text{Y}_{3.9}\text{Eu}_{0.1}\text{BO}_7\text{F}$ .

The VUV-excitation spectra for  $\text{Eu}^{3+}$ -doped  $(\text{Y,Gd})_1\text{BO}_3$ ,  $\text{Y}_2\text{O}_3$ , and  $\text{Y}_4\text{BO}_7\text{F}$  are compared in Figure 6.8. The broad bands can be assigned to either  $\text{O} \rightarrow \text{Eu}$  charge transfer (CT) or host absorption. The bands peaking near 210 nm in  $\text{Y}_2\text{O}_3$ , 220 nm in  $(\text{Y,Gd})\text{BO}_3$ , and 245 nm in  $\text{Y}_4\text{BO}_7\text{F}$  are associated with the  $\text{O} \rightarrow \text{Eu}$  excitation. The relationship between the energetic position of this band and the radiative efficiency of  $\text{Eu}^{3+}$  emission has been extensively discussed.<sup>2,4</sup> The longer wavelength observed for the  $\text{Eu}:\text{Y}_4\text{BO}_7\text{F}$  CT is consistent with the lower quantum efficiency of  $\text{Eu}^{3+}$ . In the borate materials, direct host excitation is expected to occur in the range of 140–180 nm as a result of  $\text{O} \rightarrow \text{B}$  charge transfer. Such a transition is clearly evident in the case of  $\text{Eu}:(\text{Y,Gd})\text{BO}_3$ , where the band extends from 130 to 170 nm. For  $\text{Eu}:\text{Y}_4\text{BO}_7\text{F}$ , this region of the spectrum is devoid of any reasonable absorption. The small peak near 195 nm is likely associated with host charge transfer of



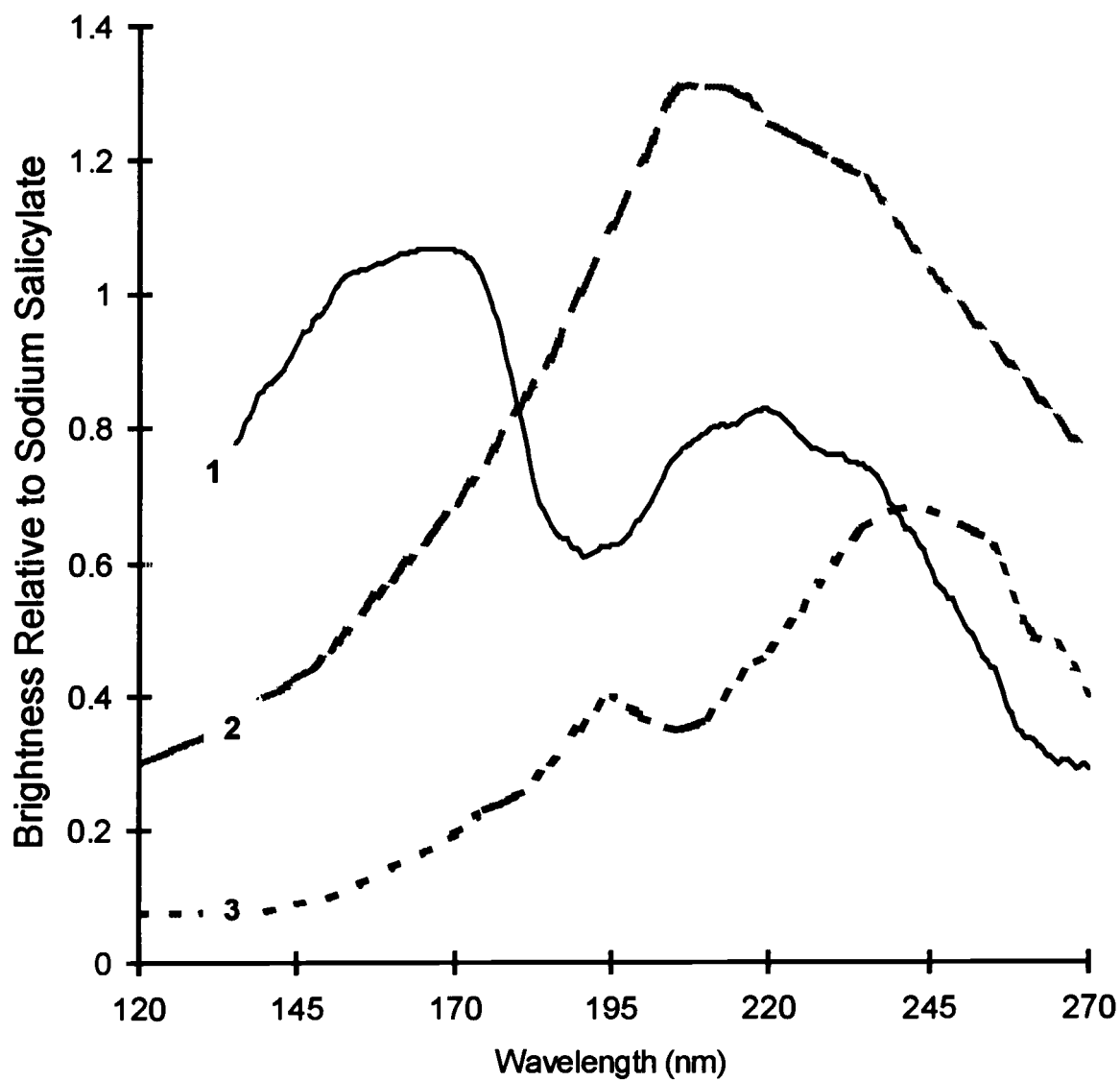


Figure 6.8. VUV excitation spectra for 1) Eu:(Y,Gd)BO<sub>3</sub>, 2)Eu:Y<sub>2</sub>O<sub>3</sub>, and 3) Eu:Y<sub>4</sub>BO<sub>7</sub>F.

the type  $O \rightarrow Y$ . In any event, the lack of significant excitation near 147 nm makes  $\text{Eu:Y}_4\text{BO}_7\text{F}$  of little utility for PDP applications, despite its improved color performance relative to that of  $\text{Eu:}(\text{Y,Gd})\text{BO}_3$ .

## Summary

The new family of compounds  $\text{Ln}_4\text{BO}_7\text{F}$  ( $\text{Ln} = \text{Y, Dy, Ho, Er, Tm, and Yb}$ ) has been synthesized. Chromaticity coordinates calculated from the emission spectra for  $\text{Tb}^{3+}$ - and  $\text{Eu}^{3+}$ -doped  $\text{Y}_4\text{BO}_7\text{F}$  reflect saturated green and red emission, respectively. Concentration-quenching curves for  $\text{Tb}^{3+}$ - and  $\text{Eu}^{3+}$ -doped  $\text{Ln}_x\text{Y}_{4-x}\text{BO}_7\text{F}$  ( $0 < x \leq 0.5$ ) resemble those determined for  $\text{Eu:Y}_2\text{O}_3$  resulting from the similarity in the structures. Thermal-quenching data for  $\text{Eu}^{3+}_{0.1}\text{Y}_{3.9}\text{BO}_7\text{F}$  indicates that nonradiative decay is limited in this host. VUV spectra of  $\text{Eu}^{3+}$ -doped  $(\text{Y,Gd})\text{BO}_3$ ,  $\text{Y}_2\text{O}_3$ , and  $\text{Y}_4\text{BO}_7\text{F}$  are presented. The lack of significant excitation near 147 nm makes  $\text{Eu:Y}_4\text{BO}_7\text{F}$  of little utility for PDP applications, despite its improved color performance relative to that of  $\text{Eu:}(\text{Y,Gd})\text{BO}_3$ .

## Acknowledgments

Acknowledgment is made to the Phosphor Technology Center of Excellence for support of this research. We wish to thank Professor Richard Meltzer for the VUV spectra.

## References

---

1. Texsan Structure Analysis Package, Molecular Structure Corp., MSC 3200A Research Forest Drive, The Woodlands, TX 77381
2. Walker N., Stuart D., *Acta Crystallogr. Sect. A* 39, **1983**, 158.
3. POLSQ: Least Squares Unit Cell Refinement, David Cahen, **1973**.
4. Osram Sylvania Luminescent Material, Type 2342, Lot No. YCX472.
5. Osram Sylvania Luminescent Material, Type 2291, Lot No. FJX439SI.
6. Ingle J., Crouch S., *Spectrochemical Analysis*.
7. Diaz, A, Quick Basic Program, Oregon State University, 26October, 1995
8. Brese N. E., O'Keeffe M., *Acta Cryst. B*47, **1991**, 192.
9. Peterson G. A., and Keszler D. A., Submitted to *Acta Crystallogr Sect.* 1999.
10. Maslen E. N., Streltsolv V. A., Ishizawan N., *Acta Crystallogr. Sect. B* 39, **1991**, 414.
11. Cheetham A. K., Norman N., *Acta Chemica Scandinavica Series A.* 28, **1974** 55.
12. Brese N. E., O'Keeffe M., *Acta Cryst. B*47, **1991**, 192.
13. Shannon R. D., *Acta Crystallogr. Sect. A* 32, **1976**, 751.
14. Verstegen J. M. P. J., *J. Electrochem. Soc.*, 121, **1974**, 1631.
15. Nichia Luminescent Material, Lot No. 1024-77GT.
16. Buijs M., van Vliet J. P. M., Blasse G., *J. Lumin.* 35, **1986**, 213.

## CHAPTER 7

### SYNTHESIS, CHARACTERIZATION AND LUMINESCENT PROPERTIES OF $\text{Li}_2\text{Ca}_8(\text{MO}_4)_3\text{F}_2$ (M = Si, Ge)

Gregory A. Peterson, Judith L. Kissick, Alexandre Yokochi,  
Annapoorna Akella, and Douglas A. Keszler

To be submitted to the Journal of Solid State Chemistry

## Abstract

The synthesis and characterization of two new isostructural materials  $\text{Li}_2\text{Ca}_6(\text{SiO}_4)_3\text{F}_2$  and  $\text{Li}_2\text{Ca}_6(\text{GeO}_4)_3\text{F}_2$  are reported. Single-crystal diffraction has been used to establish that both compounds crystallize in the trigonal space group  $R\bar{3}m(h)$ , for the germanate  $a = 7.3158(17)$  Å and  $c = 42.318(4)$  Å, and for the silicate  $a = 7.1560(10)$  Å and  $c = 41.533(8)$  Å. Fluoride analysis of  $\text{Li}_2\text{Ca}_6(\text{GeO}_4)_3\text{F}_2$  along with spectroscopic properties of  $\text{Nd}^{3+}$ - and  $\text{Yb}^{3+}$ -doped  $\text{Li}_2\text{Ca}_6(\text{GeO}_4)_3\text{F}_2$  will be discussed.

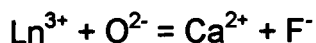
## Introduction

Important examples of commercially available oxoanion-halides include  $\text{Ca}_5(\text{PO}_4)_3\text{F/Cl:Mn}^{2+}, \text{Sb}^{3+}$ ,<sup>(1)</sup> which is used in fluorescent lighting applications,  $\text{BaCaBO}_3\text{F}$ , which has been suggested as a potential NLO material<sup>2</sup> and fluoroapatite  $\text{AE}_5(\text{PO}_4)_3\text{F}$  ( $\text{AE} = \text{Sr}$  or  $\text{Ca}$ ), which is a laser host material for ions such as  $\text{Ho}^{3+}$ ,<sup>(3)</sup>  $\text{Nd}^{3+}$ <sup>(3)</sup> and  $\text{Dy}^{3+}$ .<sup>(4)</sup>

The laser host material fluoroapatite or FAP has also been reported to provide a remarkably favorable crystal field environment for the  $\text{Yb}^{3+}$  laser ion compared with other oxide and fluoride host materials.<sup>5</sup> In a study of  $\text{Yb}^{3+}$  doping in a variety of laser host materials, including  $\text{LiYF}_4$ ,  $\text{SrF}_2$ ,  $\text{YAlO}_3$  and  $\text{Y}_3\text{Al}_5\text{O}_{12}$ ,  $\text{Yb}^{3+}:\text{Ca}_5(\text{PO}_4)_3\text{F}$  was shown to exhibit the most useful laser properties.<sup>6</sup> It shows strong, sharp absorption and emission lines, due to a favorable energy level structure, and is strongly  $\pi$  polarized, which the authors suggest may reduce amplified spontaneous emission losses. The structural analogue of this material,  $\text{Yb}^{3+}:\text{Sr}_5(\text{PO}_4)_3\text{F}$ , was subsequently reported to have similar properties to  $\text{Yb}^{3+}:\text{Ca}_5(\text{PO}_4)_3\text{F}$ .<sup>(7)</sup>

In Ca-FAP there are two crystallographically distinct Ca sites, Ca1, which is 9 coordinate  $\text{CaO}_9$  and Ca2, which is 7 coordinate  $\text{CaO}_6\text{F}$ . The presence of both F and O atoms in the Ca2 coordination sphere is a key factor. A number of

studies have been reported on the location of the  $\text{Ln}^{3+}$  ( $\text{Ln}^{3+} = \text{Nd}^{3+(8,9)}$ ,  $\text{La}^{3+}$ ,  $\text{Gd}^{3+}$ ,  $\text{Dy}^{3+(10,11)}$ ,  $\text{Ce}^{3+}$ ,  $\text{Pr}^{3+}$ ,  $\text{Er}^{3+}$ ,  $\text{Eu}^{3+}$ , and  $\text{Lu}^{3+ (11)}$ ) dopant ion within the crystal structure and all suggest that  $\text{Ln}^{3+}$  occupies the Ca2 site, through a charge compensation mechanism.



For every  $\text{Ln}^{3+}$  ion substituted on a  $\text{Ca}^{2+}$  site an associated F atom is replaced by an O atom. The new materials reported here,  $\text{Li}_2\text{Ca}_6(\text{SiO}_4)_3\text{F}_2$  and  $\text{Li}_2\text{Ca}_6(\text{GeO}_4)_3\text{F}_2$ , both contain two crystallographically distinct Ca sites that are 7 coordinate with both O and F atoms in the coordination sphere and are similar to the Ca2 site in Ca:FAP.

In this contribution, we describe the synthesis and structural characterization of the isostructural materials  $\text{Li}_2\text{Ca}_6(\text{SiO}_4)_3\text{F}_2$  and  $\text{Li}_2\text{Ca}_6(\text{GeO}_4)_3\text{F}_2$  and optical properties arising from the substitution of  $\text{Yb}^{3+}$  and  $\text{Nd}^{3+}$  in  $\text{Li}_2\text{Ca}_6(\text{GeO}_4)_3\text{F}_2$ .

## Materials and Methods

Crystal data and structural refinement data for  $\text{Li}_2\text{Ca}_6(\text{SiO}_4)_3\text{F}_2$  and  $\text{Li}_2\text{Ca}_6(\text{GeO}_4)_3\text{F}_2$  are shown in Table 7.1.

### ***$\text{Li}_x\text{Ca}_2\text{SiO}_4\text{F}_x$***

Single crystals of  $\text{Li}_2\text{Ca}_6(\text{SiO}_4)_3\text{F}_2$  were grown in a covered Pt crucible by melting a mixture of 51.5 wt%  $\text{CaCO}_3$  (99.95% Cerac), 15.5 wt%  $\text{SiO}_2$  (99.998% Alfa) and 33.0 wt%  $\text{LiF}$  (99.95% Cerac). The melt was heated at 1373 K for 16 h to ensure homogeneity, it was then cooled to room temperature at a rate of 0.07 K min<sup>-1</sup>. Numerous crystals formed in the crucible and a clear colorless block,

with approximate dimensions  $0.10 \times 0.10 \times 0.10 \text{ mm}^3$ , was physically separated from the matrix for analysis.

The crystal was mounted on a glass fiber and analyzed by using a Rigaku AFC6R X-ray diffractometer. Least squares refinement of 25 automatically centered reflections in the range  $30 \leq 2\theta \leq 36^\circ$  gave a trigonal unit cell  $a = 7.1560(10) \text{ \AA}$ , and  $c = 41.533(8) \text{ \AA}$ . Intensity data were collected at room temperature by using the  $\omega$ -scan technique with a rate  $= 4.0^\circ (\omega) \text{ min}^{-1}$ . The cell constants and Laue symmetry  $-3m1$  correspond to the trigonal system. Intensity data were collected over the range of indices  $0 \leq h \leq 10$ ,  $-10 \leq k \leq 10$ , and  $-58 \leq l \leq 58$ . From a total of 3841 measured reflections, 2533 were observed [ $F_o^2 > 3\sigma(F^2)$ ]. The intensities of three standard reflections were monitored throughout the data collection; average fluctuations were less than 0.5%.

Data were processed and the structure was solved using the Texsan crystallographic software package;<sup>12</sup> refinement was executed with by the WinGX software package.<sup>13</sup> The space group  $R-3m(h)$  has been chosen on the basis of a successful solution and refinement of the structure. The Ca and Si atoms were located by using the direct methods program SIR92.<sup>14</sup> The remaining atoms were placed from analysis of difference electron density maps. Full matrix, least-squares refinement with the program SHELXL<sup>15</sup> and anisotropic displacement coefficients on each atom resulted in the residuals  $R = 0.0460$  and  $wR = 0.1402$ . The largest peak in the final difference electron-density map corresponds to 4.5% of the Ca atom. Relevant crystallographic data and atomic parameters are listed in Table 7.2, and anisotropic displacement coefficients are summarized in Table 7.3.

### ***Li<sub>x</sub>Ca<sub>2</sub>GeO<sub>4</sub>F<sub>x</sub>***

Single crystals of  $\text{Li}_2\text{Ca}_6(\text{GeO}_4)_3\text{F}_2$  were grown in a covered Pt crucible by melting a mixture of 46.9 wt%  $\text{CaCO}_3$  (99.95% Cerac), 24.5 wt%  $\text{GeO}_2$  (99.998% Alfa) and 32.6 wt%  $\text{LiF}$  (99.95% Cerac). The melt was maintained at 1373 K for 16 h to ensure homogeneity; it was then cooled to room temperature

at a rate of  $0.07 \text{ K min}^{-1}$ . Numerous crystals formed in the crucible, and a clear colorless block, with approximate dimensions  $0.10 \times 0.15 \times 0.20 \text{ mm}^3$  was physically separated from the matrix for analysis.

The crystal was mounted on a glass fiber and analyzed by using a Rigaku AFC6R X-ray diffractometer. Least-squares refinement of 21 automatically centered reflections in the range  $30 \leq 2\theta \leq 40^\circ$  gave a trigonal unit cell  $a = 7.3158(17) \text{ \AA}$  and  $c = 42.318(4) \text{ \AA}$ . Intensity data were collected at room temperature by using the  $\omega$ -scan technique with a rate  $= 8.0^\circ (\omega) \text{ min}^{-1}$ . The cell constants and Laue symmetry  $-3m1$  correspond to the trigonal system. Intensity data were collected over the range of indices  $-10 \leq h \leq 10$ ,  $-10 \leq k \leq 10$ , and  $-59 \leq l \leq 59$ . From a total of 4176 measured reflections, 3354 were observed [ $F_o^2 > 3\sigma(F^2)$ ]. The intensities of three standard reflections were monitored throughout the data collection; average fluctuations were less than 0.3%.

Data were processed and corrected for absorption effects with PSI scans; the structure was solved by using the Texsan crystallographic software package,<sup>12</sup> and it was refined by using the WinGX software package.<sup>13</sup> The space group  $R\text{-}3m(h)$  has been chosen on the basis of a successful solution and refinement of the structure. The Ca and Ge atoms were located by using the direct methods program SIR92.<sup>14</sup> The remaining atoms were placed from analysis of difference electron-density maps. Final full-matrix, least-squares refinement on  $F^2$  with the program SHELXL<sup>15</sup> and anisotropic displacement coefficients on each atom resulted in the residuals  $R = 0.0249$  and  $wR = 0.0804$ . The largest peak in the final difference electron-density map corresponds to 0.9% of the Ge atom. Relevant crystallographic data and atomic parameters are listed in Table 7.4, and anisotropic displacement coefficients are summarized in Table 7.5.

Fluorine analysis was performed using a Corning fluoride selective electrode. Approximately 0.07g samples was dissolved in  $1\text{cm}^3$  conc.  $\text{HNO}_3$ , and made up to  $50 \text{ cm}^3$  with millipore water.  $50 \text{ cm}^3$  of FAD (Corning Fluoride Analysis Dilluent #478172), a buffer solution to ensure a pH of between 5 and 5.5, was then added. Fluoride ion concentration was obtained from a calibration



graph, plotted on semi logarithmic graph paper, for NaF standards (made up from Corning Calibration solution #478165, 0.1M) with concentrations between  $1 \times 10^{-5}$  M and  $1 \times 10^{-3}$  M.

### ***Doped Samples of $\text{Li}_x\text{Ca}_2\text{GeO}_4\text{F}_x$***

Powder samples of both  $\text{Yb}^{3+}$ - and  $\text{Nd}^{3+}$ - doped  $\text{Li}_x\text{Ca}_2\text{GeO}_4\text{F}_x$  were prepared by mixing stoichiometric amounts of  $\text{CaCO}_3$  (99.95% Cerac),  $\text{GeO}_2$  (99.998% Alfa Aesar),  $\text{LiF}$  (99.95% Cerac) and either  $\text{Yb}_2\text{O}_3$  (99.99%, Alfa Aesar) or  $\text{Nd}_2\text{O}_3$  (99.999%, Stanford). Samples with  $\text{Yb}^{3+}$  and  $\text{Nd}^{3+}$  concentrations between 0.5 and 10% then subjected to 2 heat treatments totaling 8 h at temperatures in the range 873 to 1073 K depending on the amount and type of dopant present. Products were analyzed by powder X-ray diffraction. All patterns obtained matched those generated from the results of the single-crystal study. No evidence for Nd or Yb oxide or fluoride impurities was found.

Luminescence data for  $\text{Nd}^{3+}$ - doped samples were collected in our laboratory. Excitation from an Oriel 300-W Xenon lamp was passed through a 50-cm water filter, focused onto the entrance slits of a Cary model-15 double prism monochromator, and subsequently directed onto the sample. Luminescence was collected at a right angle to the excitation beam, dispersed through an Oriel 22500 1/8-m monochromator with interchangeable gratings. A ruled grating blazed at 1000 nm (spectral resolution ca. 0.2 nm) was used for collecting the  $\text{Nd}^{3+}$  emission. A Hamatsu R1767 S-1 type PMT was cooled with dry ice for detection of the  $\text{Nd}^{3+}$  emission. The signal was collected and amplified with a Keithley model 486 picoammeter and converted to a digital signal for computer acquisition. Spectrometer control and data acquisition were achieved with computer programs written in this laboratory. The excitation spectra were corrected by using sodium salicylate and rhodamine B as quantum counters. The emission spectra were corrected with a tungsten lamp that has

Table 7.1. Crystal data and Structural Refinement parameters for  $\text{Li}_2\text{Ca}_6(\text{GeO}_4)_3\text{F}_2$  and  $\text{Li}_2\text{Ca}_6(\text{SiO}_4)_3\text{F}_2$ .

Empirical Formula	Ge <sub>3</sub> Ca <sub>6</sub> F <sub>2</sub> O <sub>12</sub> Li <sub>2</sub>	Si <sub>3</sub> Ca <sub>6</sub> F <sub>2</sub> O <sub>12</sub> Li <sub>2</sub>
Formula Weight, u	234.14	191.86
Temperature, K	293(2)	296(2)
Wavelength, Å	Mo K $\alpha$ , 0.71073	
Crystal System	Trigonal	
Space Group	R $\bar{3}$ m (#166)	
a, Å	7.3158(17)	7.1560(10)
b, Å	7.3158(17)	7.1560(10)
c, Å	42.318(4)	42.533(8)
Volume, Å <sup>3</sup>	1961.5(7)	1841.9(5)
Z	18	18
Density (Calculated), g cm <sup>-3</sup>	3.602	3.113
Absorption Coefficient, mm <sup>-1</sup>		2.987
F(000)	2034	1710
Crystal Size mm <sup>3</sup>	0.1 x 0.1 x 0.05	0.1 x 0.1 x 0.05
$\theta$ Range for Data Collection <sup>o</sup>	2.89 to 30.05	2.94 to 30
Index Ranges	-10 $\leq$ h $\leq$ 10	-10 $\leq$ h $\leq$ 10
	-10 $\leq$ k $\leq$ 10	-10 $\leq$ h $\leq$ 10
	-59 $\leq$ l $\leq$ 59	-58 $\leq$ h $\leq$ 58
Reflections Collected	4174	3841
Independent Reflections	789 [R <sub>int</sub> = 0.0515]	737 [R <sub>int</sub> = 0.0844]
Data/Parameters	789/62	737/59
Goodness-of-fit on F <sup>2</sup>	1.089	1.125
Final R indices [I > 2 $\sigma$ (I)]	R1 = 0.0249	R1 = 0.0460
	wR2 = 0.0804	wR2 = 0.1402
R indices (all data)	R1 = 0.0284	R1 = 0.0632
	wR2 = 0.0827	wR2 = 0.1508

$$R = \Sigma(|F_o|^2 - |F_c|^2) / \Sigma|F_o|^2 \quad wR = [\Sigma w(|F_o|^2 - |F_c|^2)^2 / \Sigma|F_o|^2]^{\frac{1}{2}}$$

Table 7.2. Atomic Coordinates and equivalent isotropic displacement parameters for  $\text{Li}_2\text{Ca}_6(\text{SiO}_4)_3\text{F}_2$ .

Atom	Position	x	y	z	U(eq)*
Si1	6c	2/3	1/3	0.03786(6)	0.007(1)
Si2	6c	1/3	2/3	0.08326(6)	0.008(1)
Si3	6c	2/3	1/3	0.15797(6)	0.0010(1)
Ca1	18h	0.1576(1)	0.3153(2)	0.03161(3)	0.018(1)
Ca2	18h	-0.16527(8)	0.16527(8)	0.10372(3)	0.014(1)
F1	6c	0	0	0.0667(1)	0.014(1)
F2	3a	0	0	0	0.011(2)
F3	3b	0	0	1/2	0.009(1)
O1	6c	0	0	0.1360(2)	0.014(1)
O2	6c	2/3	1/3	0.0776(2)	0.013(1)
O3	18h	-0.2080(3)	0.2080(3)	0.0257(1)	0.013(1)
O4	18h	0.5448(3)	0.4552(6)	0.1436(1)	0.016(1)
O5	18h	0.2069(3)	0.4138(6)	0.0936(1)	0.015(1)
O6	6c	1/3	2/3	0.0436(2)	0.020(2)
Li1**	18h	-0.1322(15)	0.1322(15)	0.4794(4)	0.050(4)

\* $U(\text{eq}) = (1/3)\sum_i \sum_j U^{ij} a_i^* a_j^*$  \*\*occupancy 0.6667

Table 7.3. Anisotropic displacement coefficients for  $\text{Li}_2\text{Ca}_6(\text{SiO}_4)_3\text{F}_2$ .

Atom	U11	U22	U33	U23	U12	U13
Si1	0.008(1)	0.008(1)	0.006(1)	0	0	0.004(1)
Si2	0.008(1)	0.008(1)	0.009(1)	0	0	0.004(1)
Si3	0.011(1)	0.011(1)	0.007(1)	0	0	0.006(1)
Ca1	0.018(1)	0.017(1)	0.018(1)	-0.002(1)	-0.001(1)	0.009(1)
Ca2	0.013(1)	0.013(1)	0.020(1)	0.000(1)	0.000(1)	0.008(1)
F1	0.015(2)	0.015(2)	0.012(2)	0	0	0.007(1)
F2	0.010(2)	0.010(2)	0.014(3)	0	0	0.005(1)
F3	0.008(2)	0.008(2)	0.011(3)	0	0	0.004(1)
O1	0.017(2)	0.017(2)	0.008(3)	0	0	0.009(1)
O2	0.014(2)	0.014(2)	0.010(3)	0	0	0.007(1)
O3	0.012(1)	0.012(1)	0.019(2)	-0.001(1)	0.001(1)	0.009(2)
O4	0.020(2)	0.020(2)	0.012(2)	0.001(1)	-0.001(1)	0.013(2)
O5	0.009(1)	0.007(2)	0.029(2)	0.004(2)	0.002(1)	0.004(1)
O6	0.025(2)	0.025(2)	0.010(3)	0	0	0.012(1)
Li1	0.050	0.050	0.050	-	-	-

Table 7.4. Atomic Coordinates and equivalent isotropic displacement parameters for  $\text{Li}_2\text{Ca}_6(\text{GeO}_4)_3\text{F}_2$ .

Atom	Position	x	y	z	U(eq)*
Ge1	6c	2/3	1/3	0.03815(1)	0.0062(2)
Ge2	6c	1/3	2/3	0.08266(1)	0.0078(2)
Ge3	6c	2/3	1/3	0.15794(1)	0.0112(2)
Ca1	18h	0.15404(5)	0.3081(1)	0.03127(2)	0.0095(2)
Ca2	18h	-0.16393(5)	0.16393(5)	0.10379(2)	0.0127(2)
F1	6c	0	0	0.06592(8)	0.0144(7)
F2	3a	0	0	0	0.0127(9)
F3	3b	0	0	0.5	0.016(1)
O1	6c	0	0	0.1340(1)	0.0123(8)
O2	6c	2/3	1/3	0.0799(1)	0.0128(8)
O3	18h	-0.2019(2)	0.2019(2)	0.02572(5)	0.0177(5)
O4	18h	0.5388(2)	0.4612(2)	0.14240(6)	0.0189(5)
O5	18h	0.1994(2)	0.3987(4)	0.09251(6)	0.0150(5)
O6	6c	1/3	2/3	0.0404(1)	0.0102(8)
Li1**	18h	-0.1272(8)	0.1272(8)	0.4798(3)	0.037(3)

\*U(eq) =  $(1/3)\sum_i\sum_j U^{ij}a_i^*a_j^*$  \*\*occupancy = 0.6667

Table 7.5. Anisotropic displacement coefficients for  $\text{Li}_2\text{Ca}_6(\text{GeO}_4)_3\text{F}_2$ .

Atom	U11	U22	U33	U23	U12	U13
Ge1	0.0069(2)	0.0069(2)	0.0048(3)	0	0	0.0034(1)
Ge2	0.0080(2)	0.0080(2)	0.0074(3)	0	0	0.0040(1)
Ge3	0.0147(2)	0.0147(2)	0.0041(3)	0	0	0.0074(1)
Ca1	0.0095(2)	0.0105(3)	0.0087(3)	-0.0007(2)	-0.0003(1)	0.0052(1)
Ca2	0.0127(3)	0.0127(3)	0.0142(3)	0.0004(1)	-0.0004(1)	0.0074(3)
F1	0.016(1)	0.016(1)	0.010(2)	0	0	0.0082(5)
F2	0.014(1)	0.014(1)	0.011(2)	0	0	0.0068(7)
F3	0.011(1)	0.011(1)	0.026(3)	0	0	0.0054(7)
O1	0.016(1)	0.016(1)	0.006(2)	0	0	0.0081(6)
O2	0.016(1)	0.016(1)	0.0056(2)	0	0	0.0082(6)
O3	0.0103(8)	0.0103(8)	0.017(2)	-0.0006(4)	0.0006(4)	0.0067(9)
O4	0.028(1)	0.028(1)	0.011(1)	0.0011(5)	-0.0011(5)	0.021(1)
O5	0.0104(8)	0.009(1)	0.025(1)	0.0046(9)	0.0023(5)	0.0043(5)
O6	0.013(1)	0.013(1)	0.005(2)	0	0	0.0064(6)
Li1	0.056(6)	0.0056(6)	0.029(6)	0.005(2)	-0.005(2)	0.052(7)

been calibrated at Eppley Laboratories, Inc. Data were plotted as relative emitted energy per constant energy interval, and peak positions were determined by fitting the spectra with Gaussian profiles for determination of the energy-level diagram pictured in Figure 7.7.

Data for the 2 mol%  $\text{Yb}^{3+}$  doped samples were collected at Ecole Nationale Supérieure de Chimie de Paris using a Ti:sapphire laser excitation source and a PbS detector with chopper and lock in amplifier.

## Results and Discussion

### *Crystal Structure of $\text{Li}_2\text{Ca}_6(\text{GeO}_4)_3\text{F}_2$*

Refinement of the single crystal data suggests that the LiF stoichiometry is 0.67. The three F sites within the unit cell are all fully occupied giving an overall stoichiometry of  $x = 0.67$  which corresponds to 12 F atoms within the unit cell. Further analysis of the electron density shows that there are no other possible sites within the unit cell for extra F ions to be located, as all excess electron density is located close to other atoms and is not of significant quantity to be a complete ion. This F stoichiometry means that for charge neutrality to be maintained within the material the Li site must be partially occupied. Isotropic refinement of this site gave an occupancy close to 0.67 and the occupancy was constrained to 2/3 occupancy for anisotropic refinement. Fluorine analysis on a number of samples gave fluoride ion concentrations ranging from 0.62 to 0.70 supporting the results of the single crystal refinement, that the F and consequently Li content is 0.67.

The crystal structure of  $\text{Li}_2\text{Ca}_6(\text{GeO}_4)_3\text{F}_2$  (Figure 7.1) can be viewed as a repeat of three compositionally equivalent layers, A, B, and C, which differ only in translation within the unit cell. With layer B related to layer A by  $(2/3, 1/3, 1/3)$  and layer C related to layer A by  $(1/3, 2/3, 2/3)$  – the equivalent positions of the space group. Each of these layers is composed of 6 formula units,

$\text{Li}_4\text{Ca}_{12}\text{Ge}_6\text{O}_{24}\text{F}_4$ , made up of three sub layers. Two of which are contain Ge1 and Ge2 centered  $\text{GeO}_4$  tetrahedra and  $\text{FCa}_6$  octahedra,  $\text{Ca}_6\text{Ge}_2\text{O}_8\text{F}_{1.5}$ . These sandwich the third layer, which contains  $\text{Li}_4\text{Ge}_2\text{O}_8\text{F}$ , and is made up of Ge3 orthosilicate groups and distorted  $\text{FLi}_6$  octahedra.

Viewing the unit cell down the c axis shows the high degree of threefold symmetry in the material. Figure 7.2 shows the symmetry requirements of the  $\text{GeO}_4$  tetrahedra and the  $\text{FCa}_6$  and  $\text{FLi}_6$  octahedra which all exhibit three fold symmetry.

The three crystallographically distinct Ge atoms are in 4 coordinate sites with symmetry  $\text{C}_{3v}$ . The Ge coordinates with the O in the coordination sphere to form  $\text{GeO}_4$  units that can be described as slightly distorted tetrahedra, which have been compressed along the threefold axis (parallel to the c axis). Each Ge atom is coordinated to three of one type of O atom, which form the face perpendicular to the 3-fold axis. These three O atoms have the same Ge-O distances and the O-Ge-O angles are equivalent. The fourth O atom forms a bond with the Ge that is aligned along the c axis. Ge1 is coordinated by three O3 atoms at a distance of 1.749(3) Å and one O2 at a distance of 1.751(4) Å, with O3-Ge1-O3 angles of 111.34(7) ° and O2-Ge1-O3 angles of 107.54(8) °. Ge2 is coordinated by three O5 atoms at a distance of 1.745(2) Å and one O6 atom at a distance of 1.786(4) Å, with O5-Ge2-O5 angles of 114.86(6) ° and O5-Ge2-O6 angles of 103.31(9) °. Ge3 is coordinated by three O4 atoms at a distance of 1.749(3) Å and one O1 at a distance of 1.751(4) Å, with O4-Ge3-O4 angles of 106.72(9) ° and O4-Ge3-O1 angles of 112.10(8) °. It is obvious from the differences between the observed O-Ge-O angles and the ideal tetrahedral angle of 109.5 °, that the Ge1- and Ge2-centered tetrahedra have been slightly compressed while the Ge3-centered tetrahedra has been stretched along the c axis. Calculated valences for all Ge atoms using the bond valence method are within 2 % of the ideal value.<sup>16</sup>

The two crystallographically distinct Ca sites are 7 coordinate with symmetry  $\text{C}_1$ , in which the Ca is associated with both O and F atoms (Figure 7.3.)



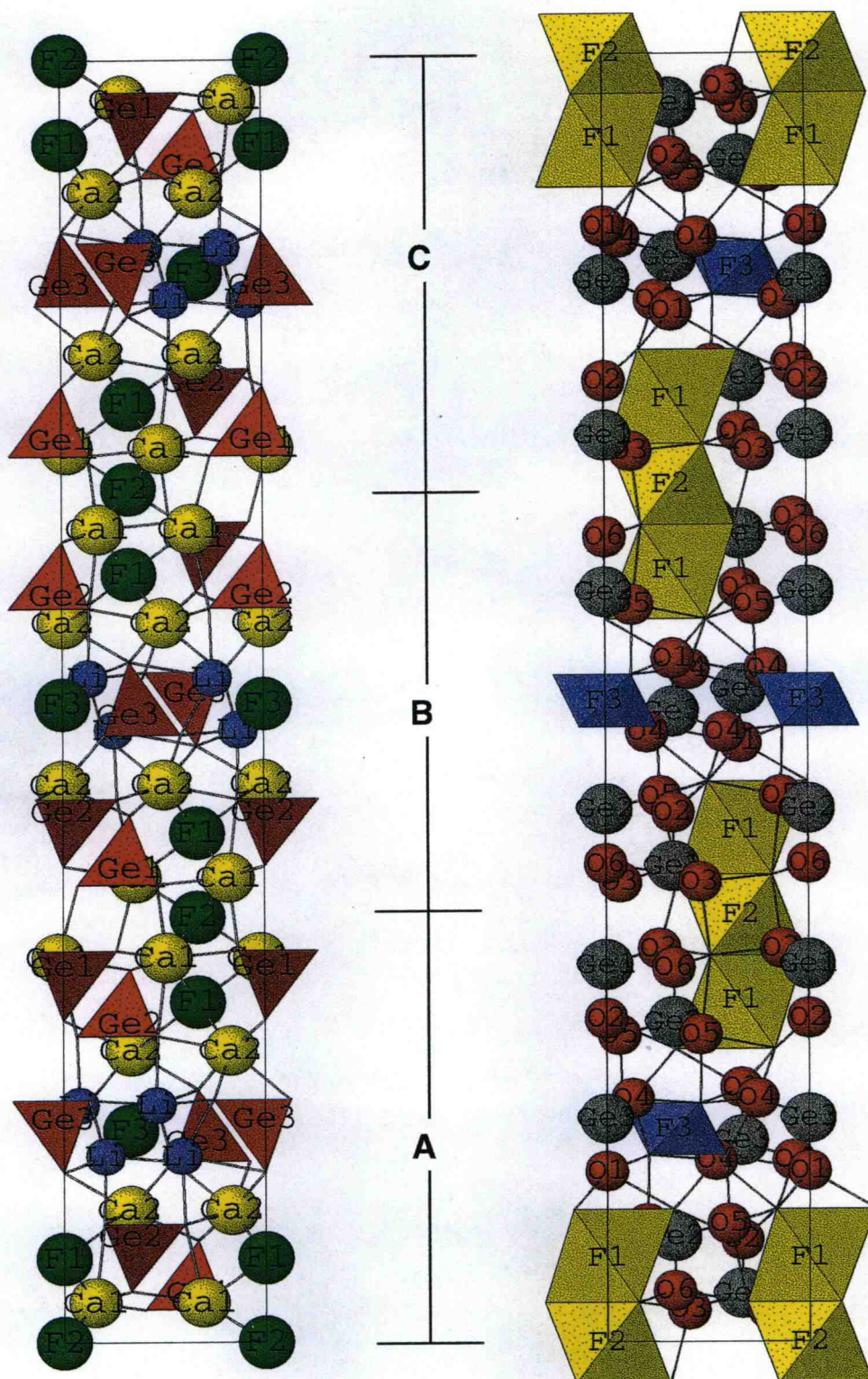


Figure 7.1. Unit-cell contents viewed along  $c$ . (a) Ge-centered tetrahedra plotted, (b) F-centered octahedra plotted.



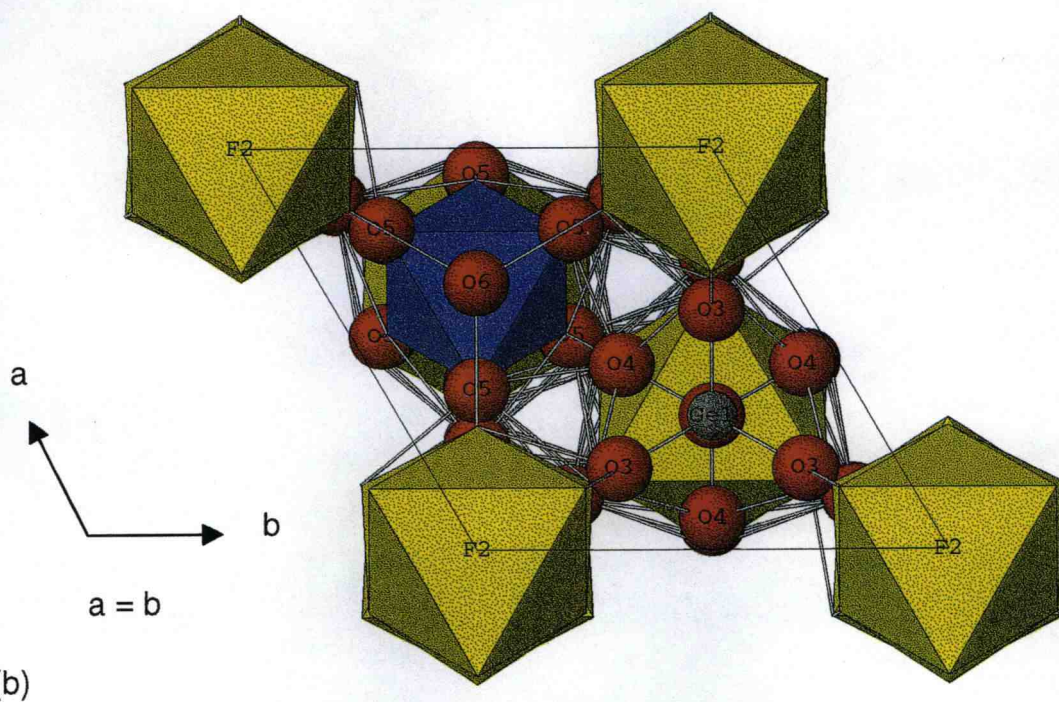
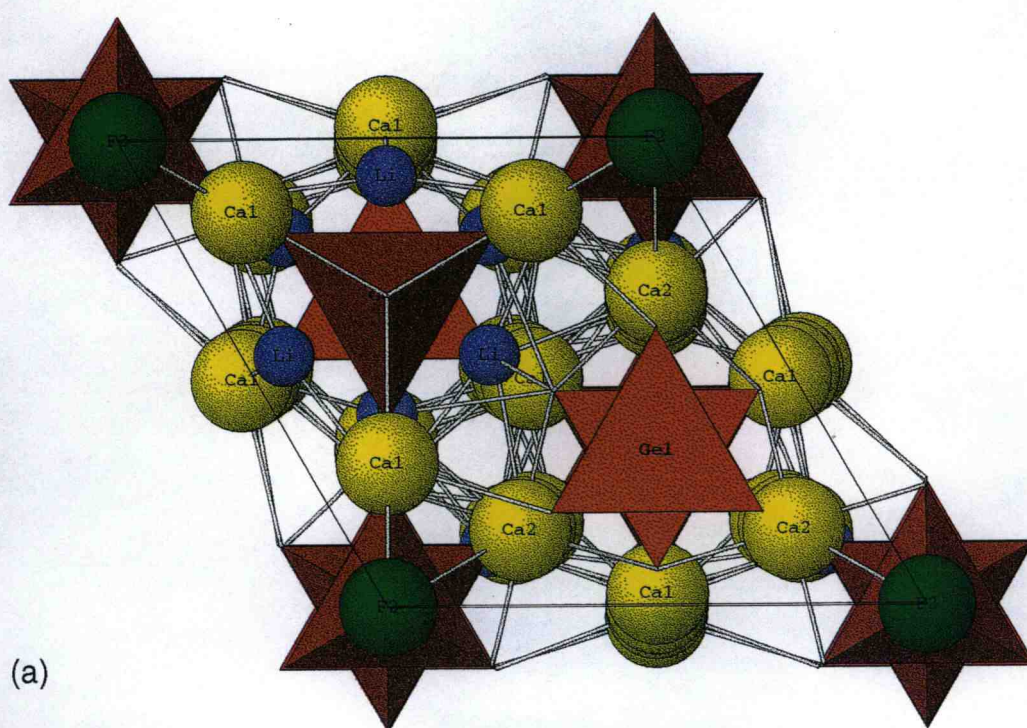


Figure 7.2. Unit-cell contents viewed down the  $c$  axis. a)  $\text{GeO}_4$  tetrahedra plotted, b) F-centered octahedra plotted;  $\text{FCa}_6$  = yellow and  $\text{FLi}_6$  = light blue.

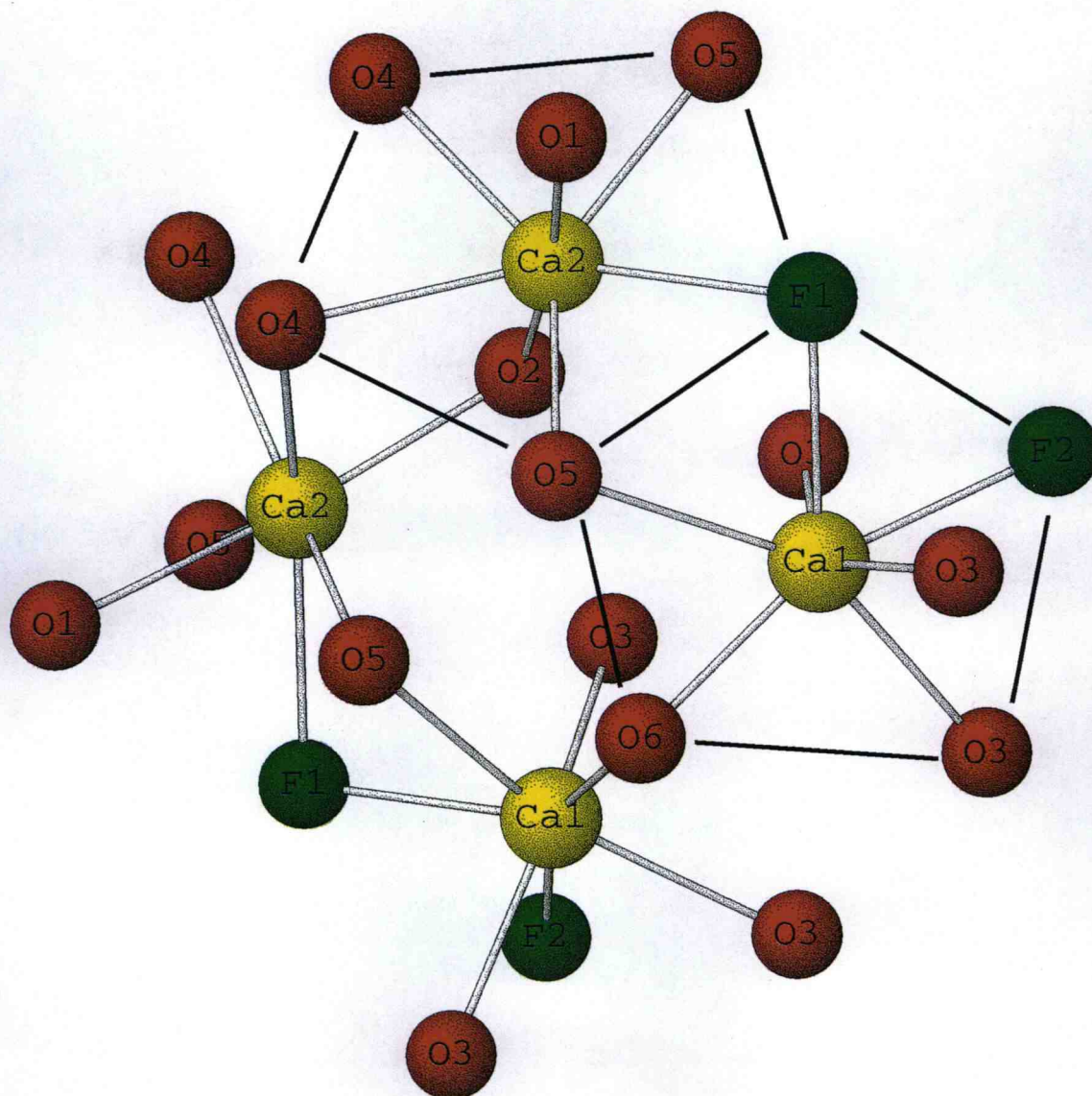


Figure 7.3. Ca-centered pentagonal-bipyramid polyhedra.

These sites can best be described as distorted pentagonal-bipyramids. F1, F2, O3, O5, and O6 form the pentagonal plane of atoms around Ca1. Two additional O3 atoms occupy the axial positions and have an O3-Ca1-O3 angle between them of  $144.34(9)^\circ$ . The pentagonal plane around Ca2 is formed by two-O4 atoms, two-O5 atoms, and one-F1 atom. An O1 atom and an O2 atom occupy the axial positions, with an O1-Ca2-O2 angle of  $173.6(2)^\circ$ . The Ca1-O distances range from 2.305(1) to 2.639(3) Å, and the Ca2-O distances range from 2.372(2) to 2.536(2) Å. The Ca-F distances range from 2.358(1) to 2.624(2) Å. Calculated valences using the bond valence method are +2.0(1) and +1.8(1) for Ca1 and Ca2, respectively.

The Li atom occupies a 6-coordinate site with  $C_1$  symmetry in which both O atoms from the surrounding  $\text{GeO}_4$  tetrahedra and an F3 atom are present in the coordination sphere as illustrated in Figure 7.4. The  $\text{LiO}_5\text{F}$  polyhedron is best described as a distorted octahedron containing four normal Li-O distances, which average 2.248(8) Å, one long Li-O distance at 2.66(1) Å and one Li-F distance, which is 1.83(1) Å. The Li-O distances are comparable to those reported for the 6-coordinate Li atom in  $\text{BaLiB}_9\text{O}_{15}$ <sup>17</sup> with two distances, 1.889(6) and 2.80(2) and the Li-F3 distance is comparable to the Li-F distance of 2.013 Å in  $\text{LiF}$ <sup>18</sup>. All O-Li-O and O-Li-F angles are reasonable for the distorted octahedron. The valence of the Li atom, from bond-valence methods, is +0.8(1)<sup>16</sup>. The Li atom sits on a special position and complete occupancy of this site would give 18 Li atoms within the unit cell. As mentioned previously, complete occupancy of the three F sites only gives 12 F atoms within the unit cell. In order to maintain charge neutrality within the unit cell it is only necessary for 2/3 of these sites to be occupied. Consequently the valence, calculated using the bond valence method, reported here is higher than expected, however, as Li is one of the lightest elements and the thermal displacement parameters are large, when compared to those of Ge, Ca, O, and F, this discrepancy is minor.

The three F sites are 6 coordinate and have  $D_{3h}$  symmetry (Figure 7.5.) The atoms F1 and F2 are coordinated by three-Ca1 and three-Ca2,



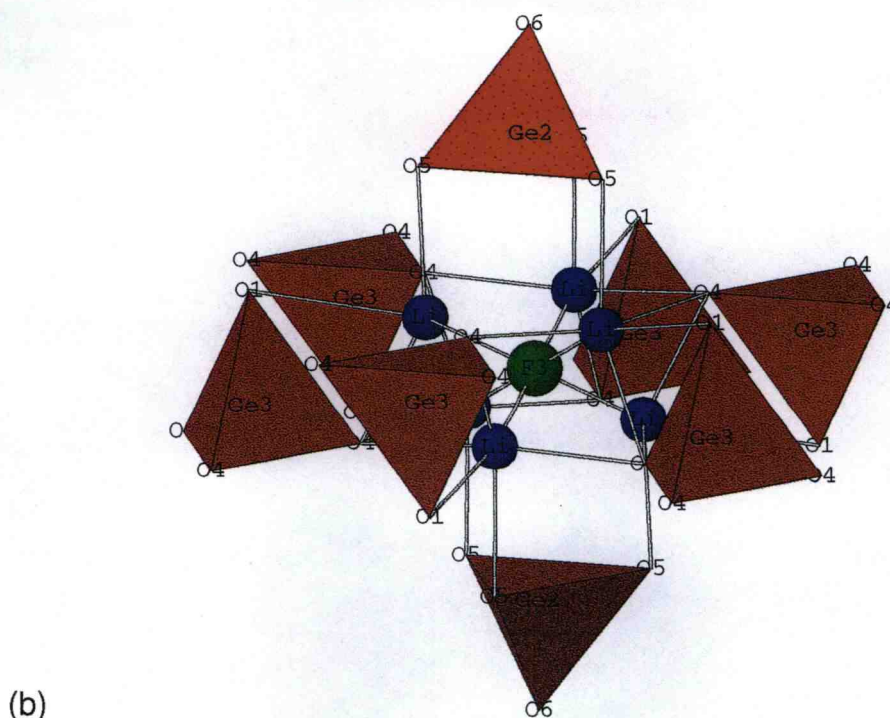
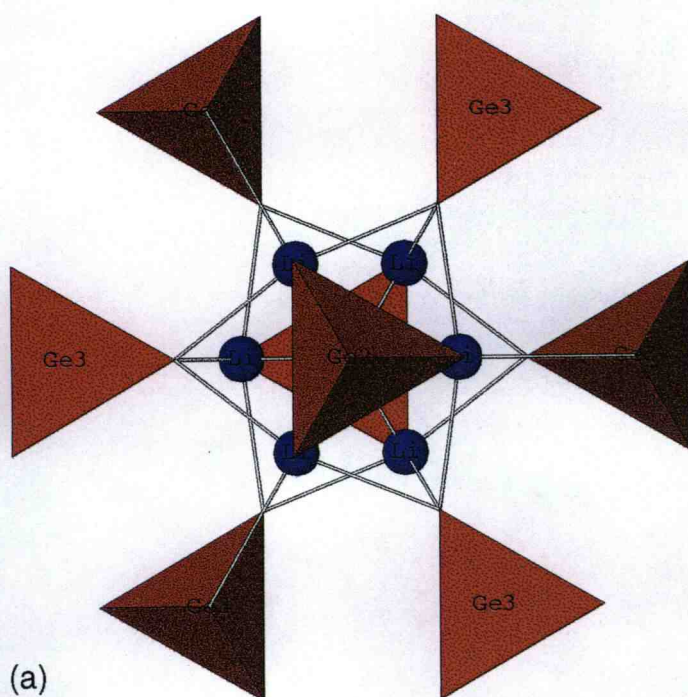


Figure 7.4.  $F3$ -centered,  $FLi_6$  octahedron with surrounding  $GeO_4$  tetrahedra. (a) viewed down  $c$ . (b)  $Ge$ -centered tetrahedra which alternate directions in the  $ab$  plane as they encompass the  $FLi_6$  octahedron.

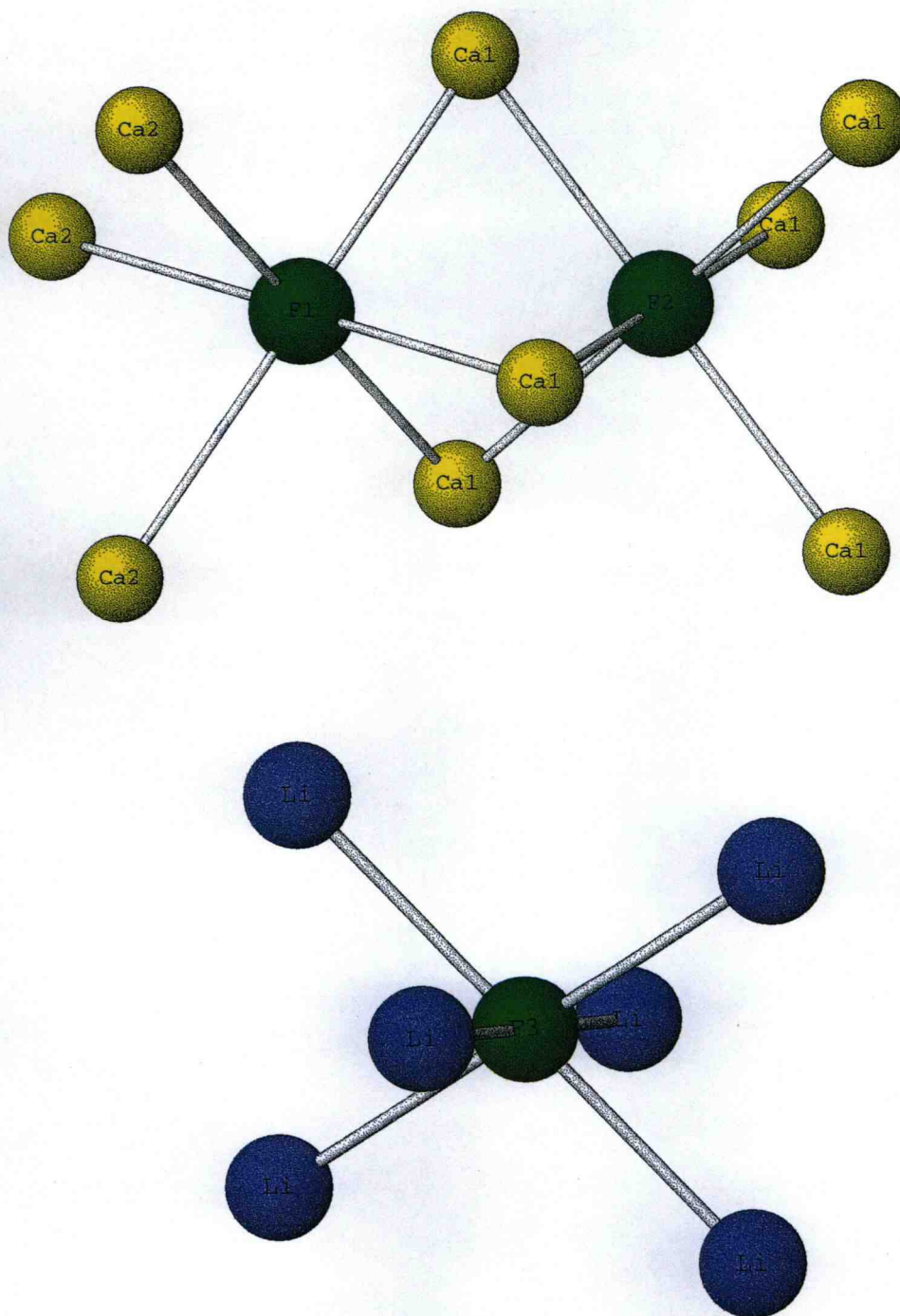


Figure 7.5. F-centered octahedral environments.

and six-Ca1 atoms respectively, and form nearly perfect  $\text{FCa}_6$  octahedra. The two  $\text{FCa}_6$  octahedra face share three-Ca1 atoms with F1-Ca1 distances of 2.441(2) Å, and F2-Ca1 distances of 2.3582(8) Å. The F1-centered  $\text{FCa}_6$  octahedron has three longer F1-Ca2 distances of 2.624(2) Å while the F2 centered  $\text{FCa}_6$  octahedron has three additional F2-Ca1 bonds. The F1 and F2 atoms both sit on the three-fold axes and the Ca1 and Ca2 atom faces are perpendicular to the three-fold symmetry axes in the structure. Consequently, the F1-centered octahedron has been stretched along its three-fold faces while the F2-centered octahedron has been compressed. The calculated valences for both the F1 and F2 atom using the bond valence method are  $-1.4(1)$  and  $-1.5(1)$  respectively. These values are significantly higher than the ideal value of  $-1$ . There are two possible explanations for this. First, that the F atoms are filling sites within the unit cell that force them to be closer to the surrounding Ca atoms than they would ideally like to be. This is demonstrated by the fact that the bond lengths are all slightly shorter than those expected for 6 coordinate F atoms, this in turn leads to a greater contribution to valence from the surrounding Ca atoms. The second is that the F sites are partially occupied by O atoms. For this to be the case and for charge neutrality to be maintained within the material, the calculated bond valence for the O atoms would have to show values significantly lower than the ideal value of  $-2$ . No evidence for this is found with the calculated bond valences for the O atoms being  $-2.0(1)$ ,  $-2.0(1)$ ,  $-2.0(1)$ ,  $-2.1(1)$ ,  $-1.8(1)$ , and  $-1.9(1)$  for O1, O2, O3, O4, and O5 respectively. The F3 atom is coordinated by 6 Li atoms to form a trigonal antiprism with F3-Li1 bond distances of 1.83(1) Å. The calculated valence of the F3 atom using the bond valence sum method is  $-1.1(1)$ . This is assuming a Li site occupancy of  $2/3$ , i.e. at any one time only 4 of the 6 Li atoms coordinated to the F3 atom is actually present.

The crystal structure of  $\text{Li}_2\text{Ca}_6(\text{SiO}_4)_3\text{F}_2$  is isostructural to that of  $\text{Li}_2\text{Ca}_6(\text{GeO}_4)_3\text{F}_2$  and the main structural features can be described in an identical manner. Bond lengths and angles for  $\text{Li}_2\text{Ca}_6(\text{SiO}_4)_3\text{F}_2$  and  $\text{Li}_2\text{Ca}_6(\text{GeO}_4)_3\text{F}_2$  are shown in Table 7.6 and 7.7, respectively.

Table 7.6. Distances and Angles for  $\text{Li}_2\text{Ca}_6(\text{SiO}_4)_3\text{F}_2$ .

Atoms		Distance (Å)	Atoms		Angle (°)
Si1 – O3	x3	1.634(4)	O3-Si1-O3	x3	110.9(2)
Si1 – O2		1.652(7)	O3-Si1-O1		108.3(2)
Si1 – O5	x3	1.624(4)	O5-Si2-O5	x3	113.3(2)
Si1 – O6		1.648(8)	O5-Si2-O6		105.3(2)
Si1 – O4	x3	1.623(4)	O4-Si3-O4	x3	107.4(2)
Si1 – O1		1.637(7)	O4-Si3-O1		111.5(2)
Ca1 – O3	x2	2.342(3)	O3-Ca1-O3		70.6(1)
Ca1 – O3		2.460(4)	O3-Ca1-O6		70.8(1)
Ca1 – O5		2.645(4)	O5-Ca1-O6		88.2(2)
Ca1 – O6		2.234(2)	O5-Ca1-F1		63.8(2)
Ca1 – F1		2.438(4)	O3-Ca1-F2		66.6(1)
Ca1 – F2		2.345(1)	F1-Ca1-F2		144.8(2)
Ca2 – O1		2.448(4)	O1-Ca2-O2		68.7(1)
Ca2 – O2		2.348(3)	O4-Ca2-O4		78.5(1)
Ca2 – O4	x2	2.494(3)	O4-Ca2-O5	x2	63.2(1)
Ca2 – O5	x2	2.387(3)	O1-Ca2-F1		70.1(2)
Ca2 – F1		2.561(4)	O5-Ca2-F1	x2	174.3(2)
Li – O1		2.52(2)	O1-Li1-O4		96.1(5)
Li – O4		2.06(2)	O4-Li1-O4		87.2(5)
Li – O4	x2	2.296(4)	O4-Li1-O4	x2	97.7(5)
Li – O5		2.18(2)	O4-Li1-O5		161.9(9)
Li – F3		1.85(2)	O4-Li1-O5	x2	162.8(9)
			O1-Li1-F3		153.4(1)



Table 7.6 Cont. Distances and Angles for  $\text{Li}_2\text{Ca}_6(\text{SiO}_4)_3\text{F}_2$ .

Atoms			Distance (Å)	Atoms			Angle (°)
F1-Ca1	x3		2.438(4)	Ca1-F1-Ca1	x3		87.9(2)
F1-Ca2	x3		2.561(4)	Ca2-F1-Ca2	x3		87.7(2)
				Ca1-F1-Ca2			92.2(3)
				Ca1-F1-Ca2			179.9(2)
F2-Ca1	x6		2.354(1)	Ca1-F2-Ca1			88.08(4)
				Ca1-F2-Ca1			91.92(4)
				Ca1-F2-Ca1			180.00(7)
F3-Li1	x6		1.85(2)	Li1-F3-Li1			79.7(7)
				Li1-F3-Li1			100.3(7)
				Li1-F3-Li1			180.0(1)
O1-Ca2	x3		2.448(4)	Ca2-O1-Ca2	x3		92.9(2)
O1-Li1	x3		2.53(1)	Li1-O1-Li1	x3		117.3(2)
O1-Si3			1.637(7)	Li1-O1-Si3	x3		80.5(4)
				Ca2-O1-Si3	x3		123.2(1)
O4-Li1	x2		2.296(4)	Ca2-O4-Ca2			92.7(1)
O4-Ca2	x2		2.494(3)	Ca2-O4-Si3	x2		93.9(2)
O4-Si3			1.623(4)	Ca2-O4-Li1	x2		132.3(1)
O5-Li1			2.18(2)	Ca2-O5-Ca2			96.0(1)
O5-Ca1			2.645(4)	Ca2-O5-Si2	x2		132.00(7)
O5-Ca2	x2		2.387(3)	Ca1-O5-Li1			164.8(5)
O5-Si2			1.624(4)				

Table 7.7. Distances and Angles for  $\text{Li}_2\text{Ca}_6(\text{GeO}_4)_3\text{F}_2$ .

Atoms		Distance (Å)	Atoms		Angle (°)
Ge1-O3	x3	1.747(2)	O3-Ge1-O3	x3	111.34(7)
Ge1-O2		1.751(4)	O3-Ge1-O1		107.54(8)
Ge2-O5	x3	1.745(2)	O5-Ge2-O5	x3	114.86(6)
Ge2-O6		1.786(4)	O5-Ge2-O6		103.31(9)
Ge3-O4	x3	1.749(3)	O4-Ge3-O4	x3	106.72(9)
Ge3-O1		1.751(4)	O4-Ge3-O1		112.10(8)
Ca1-O3	x2	2.327(2)	O3-Ca1-O3		144.34(9)
Ca1-O3		2.487(2)	O3-Ca1-O6		107.57(4)
Ca1-O5		2.639(3)	O5-Ca1-O6		67.77(11)
Ca1-O6		2.305(1)	O5-Ca1-F1		65.65(9)
Ca1-F1		2.441(2)	O3-Ca1-F2		72.79(5)
Ca1-F2		2.3582(8)	F1-Ca1-F2		71.05(7)
Ca2-O1		2.440(2)	O1-Ca2-O2		173.6(1)
Ca2-O2		2.372(2)	O4-Ca2-O4		67.3(1)
Ca2-O4	x2	2.535(2)	O4-Ca2-O5	x2	78.77(8)
Ca2-O5	x2	2.386(2)	O1-Ca2-F1		69.23(1)
Ca2-F1		2.624(2)	O5-Ca2-F1	x2	66.65(6)
Li-O1		2.66(1)	O1-Li1-O4		96.8(3)
Li-O4		2.13(1)	O4-Li1-O4		162.2(6)
Li-O4	x2	2.282(3)	O4-Li1-O4	x2	97.4(3)
Li1-O5		2.30(1)	O4-Li1-O5		150.1(5)
Li1-F3		1.83(1)	O4-Li1-O5	x2	86.0(3)
			O1-Li1-F3		163.4(7)

Table 7.7 Cont. Distances and Angles for  $\text{Li}_2\text{Ca}_6(\text{GeO}_4)_3\text{F}_2$ .

Atoms			Distance (Å)	Atoms			Angle (°)
F1-Ca1	x3		2.442(2)	Ca1-F1-Ca1	x3		87.7(1)
F1-Ca2	x3		2.624(1)	Ca2-F1-Ca2	x3		86.58(9)
				Ca1-F1-Ca2			92.89(2)
				Ca1-F1-Ca2			179.3(2)
F2-Ca1	x6		2.358(8)	Ca1-F2-Ca1			180.00(3)
				Ca1-F2-Ca1			91.58(2)
				Ca1-F2-Ca1			88.42(2)
F3-Li1	x6		1.83(1)	Li1-F3-Li1			180.000(2)
				Li1-F3-Li1			99.8(5)
				Li1-F3-Li1			80.2(5)
O1-Ca2	x3		2.440(2)	Ca2-O1-Ca2	x3		95.0(1)
O1-Li1	x3		2.66(1)	Li1-O1-Li1	x3		116.2(2)
O1-Ge3			1.751(4)	Li1-O1-Ge3	x3		78.6(3)
				Ca2-O1-Ge3	x3		121.63(8)
O4-Li1	x2		2.282(3)	Ca2-O4-Ca2			94.35(9)
O4-Ca2	x2		2.535(2)	Ca2-O4-Ge3	x2		92.43(8)
O4-Ge3			1.749(3)	Ca2-O4-Li1	x2		132.14(6)
O5-Li1			2.30(1)	Ca2-O5-Ca2			97.89(9)
O5-Ca1			2.639(3)	Ca2-O5-Ge2	x2		130.86(5)
O5-Ca2	x2		2.386(2)	Ca1-O5-Li1			169.6(3)
O5-Ge2			1.745(2)				

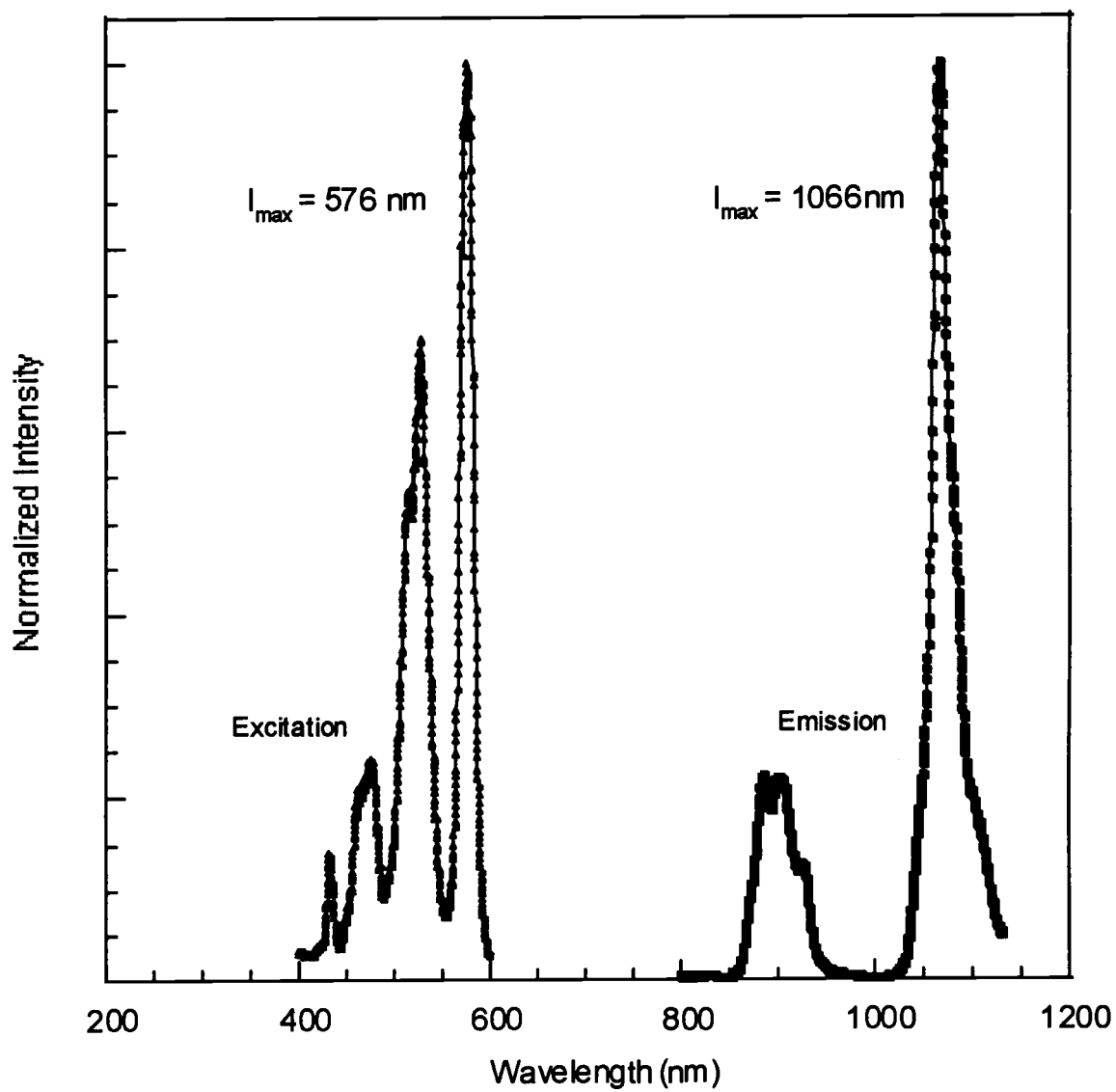
### ***Optical Properties of Nd<sup>3+</sup> and Yb<sup>3+</sup> doped Li<sub>2</sub>Ca<sub>6</sub>(GeO<sub>4</sub>)<sub>3</sub>F<sub>2</sub>***

The excitation and emission spectra collected on powder samples of Nd<sup>3+</sup> and Yb<sup>3+</sup> doped Li<sub>2</sub>Ca<sub>6</sub>(GeO<sub>4</sub>)<sub>3</sub>F<sub>2</sub> are shown in Figures 7.6 and 7.8 respectively. Substitution of Nd<sup>3+</sup> on the Ca<sup>2+</sup> sites has been discussed previously with reference made to the Nd<sup>3+</sup>-doped fluoroapatite mineral Ca<sub>5</sub>(PO<sub>4</sub>)<sub>3</sub>F<sup>19</sup> (FAP), which contains a Ca site that has a similar coordination sphere to the sites in the title compound; 6-coordinate to O and 1-coordinate to F. Nd<sup>3+</sup> is assumed to be statistically distributed on both Ca sites in Li<sub>2</sub>Ca<sub>6</sub>(GeO<sub>4</sub>)<sub>3</sub>F<sub>2</sub>, which results in inhomogeneous broadening of absorption and emission bands. The C<sub>1</sub> symmetry of the Ca sites results in a lifting of the degeneracy of the shielded f-orbital multiplets, thus the metastable <sup>4</sup>F<sub>3/2</sub> excited-state level and the <sup>4</sup>I<sub>j</sub> multiplets of the ground state manifold each split with 2J+1 degeneracy. Excited-state population from the <sup>4</sup>F<sub>3/2</sub> manifold is channeled into the doubly-degenerate levels of the <sup>4</sup>I<sub>j</sub> ground-state. These transitions give rise to luminescence that can terminate on eight <sup>4</sup>I<sub>15/2</sub> levels with emission at ca. 2000 nm, seven <sup>4</sup>I<sub>13/2</sub> levels with emission at ca. 1400 nm, six <sup>4</sup>I<sub>11/2</sub> levels with emission at ca. 1060 nm, and five <sup>4</sup>I<sub>9/2</sub> levels containing the ground state near 890 nm.

The 300 K luminescence spectrum of Nd<sub>0.02</sub>Li<sub>0.67</sub>Ca<sub>1.98</sub>GeO<sub>4.02</sub>F<sub>0.65</sub> is given in Figure 7.6, and an energy level diagram including the observed stark levels of the <sup>4</sup>F<sub>3/2</sub>→<sup>4</sup>I<sub>11/2</sub> and <sup>4</sup>F<sub>3/2</sub>→<sup>4</sup>I<sub>9/2</sub> transitions (Figure 7.7) has been constructed from the energy spectrum. The spectrum is dominated by two main features, emission from <sup>4</sup>F<sub>3/2</sub>→<sup>4</sup>I<sub>11/2</sub> and <sup>4</sup>F<sub>3/2</sub>→<sup>4</sup>I<sub>9/2</sub>, with their most intense peaks at 9380 and 11080 cm<sup>-1</sup> respectively. Within the excited state at 300 K, thermal population of both levels of the split, metastable <sup>4</sup>F<sub>3/2</sub> will occur, giving rise to luminescence from both levels. The intensity of these transitions is dictated by dipole-selection rules, the fractional population of the excited state levels as determined by the partition function, and nonradiative pathways. The energy separation of the <sup>4</sup>F<sub>3/2</sub> excited-state levels could not be determined from the data collected. The energy-level diagram shows only four of five levels predicted for

the  $^4F_{3/2} \rightarrow ^4I_{9/2}$  transitions with a total energy separation of  $660 \text{ cm}^{-1}$ , and only four of six  $^4F_{3/2} \rightarrow ^4I_{11/2}$  transitions with an energy separation of  $380 \text{ cm}^{-1}$ . These values are comparable to those of Nd:FAP, for which all stark levels have been observed, and for which with energy separation between the highest and lowest  $^4I_{9/2}$  and  $^4I_{11/2}$ , is  $708$  and  $606 \text{ cm}^{-1}$ , respectively. The lowest energy level of the  $^4F_{3/2}$  manifold in Nd:FAP is at  $11314 \text{ cm}^{-1}$ , as compared to the lowest level at  $11435 \text{ cm}^{-1}$  in  $\text{Nd}_{0.02}\text{Li}_{0.67}\text{Ca}_{1.98}\text{GeO}_{4.02}\text{F}_{0.65}$ . The approximate positions of the  $^4I_{13/2}$  and  $^4I_{15/2}$  reported in the energy level diagram are the average energy of the seven and eight stark levels reported for Nd:FAP, respectively. The excitation spectrum of  $\text{Nd}_{0.02}\text{Li}_{0.67}\text{Ca}_{1.98}\text{GeO}_{4.02}\text{F}_{0.65}$  (Figure 7.6) is comprised of transitions to closely spaced excited-state levels which may include the  $^2G_j$ ,  $^4G_j$ ,  $^2K_j$ ,  $^2D_j$  and  $^2P_j$  manifolds.

The distinct peak in the  $\text{Yb}^{3+}$  data is due to an absorption maximum at  $980 \text{ nm}$ , which corresponds to excitation of the material (Figure 7.8). Other peaks observed have not been successfully resolved, and this has been attributed to the fact that the data were collected on powder samples. Peak fitting of the unresolved background has been performed and suggests that 4 other distinct peaks are present, with maxima at  $937 \text{ nm}$ ,  $1006 \text{ nm}$ ,  $1044 \text{ nm}$  and  $1072 \text{ nm}$ . It is hoped that boules of  $\text{Yb}^{3+}$  doped  $\text{Li}_2\text{Ca}_6(\text{GeO}_4)_3\text{F}_2$  can be grown and that data collected on single crystal samples will give a clearer picture of the excitation and emission peaks.



7.6. Excitation and emission spectrum for  $\text{Nd}_{0.02}\text{Li}_{0.67}\text{Ca}_{1.98}\text{GeO}_{4.02}\text{F}_{0.65}$

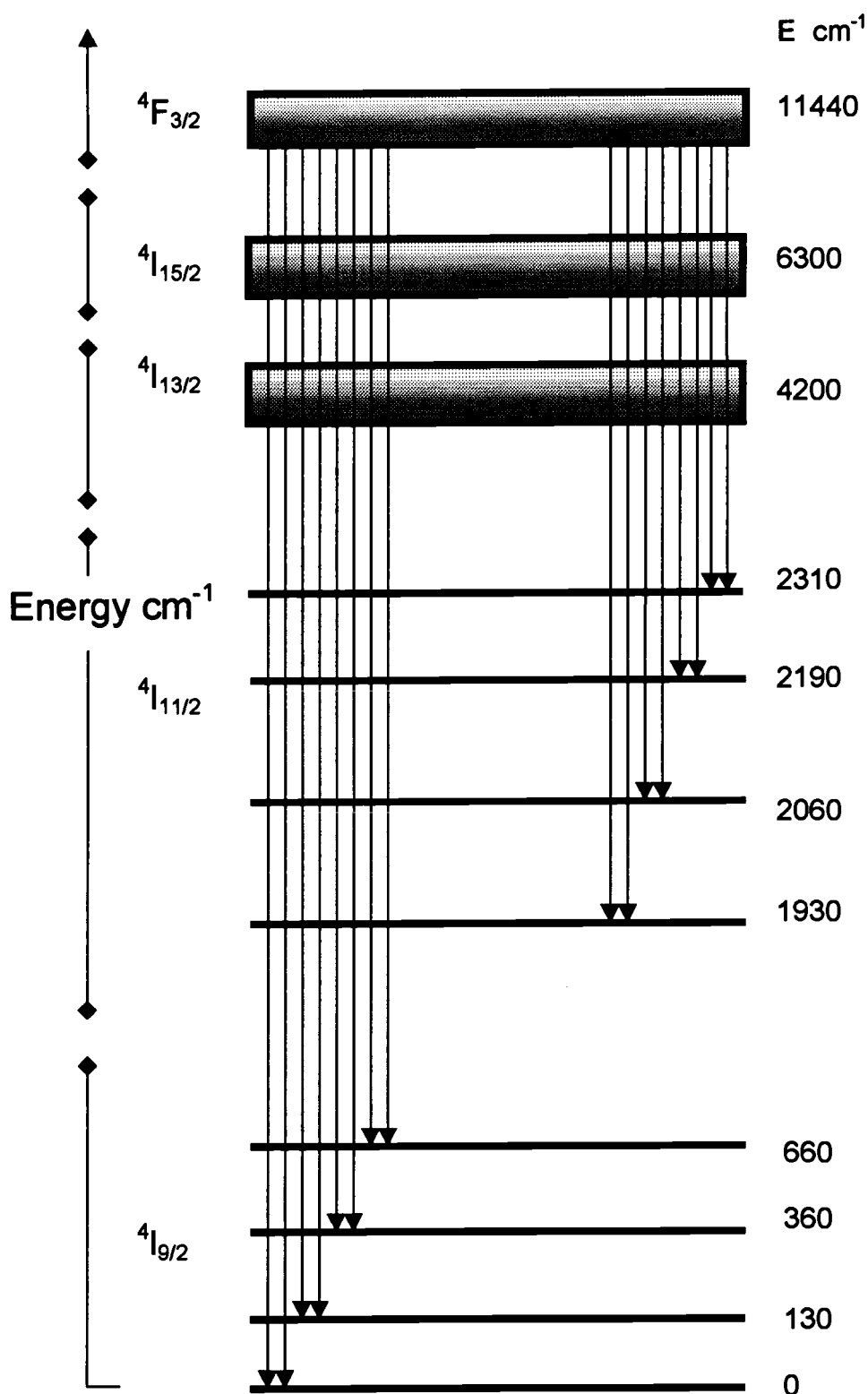


Figure 7.7. Energy-diagram with stark levels for  $\text{Nd}_{0.02}\text{Li}_{0.67}\text{Ca}_{1.98}\text{Ge}_{0.42}\text{F}_{0.65}$ .

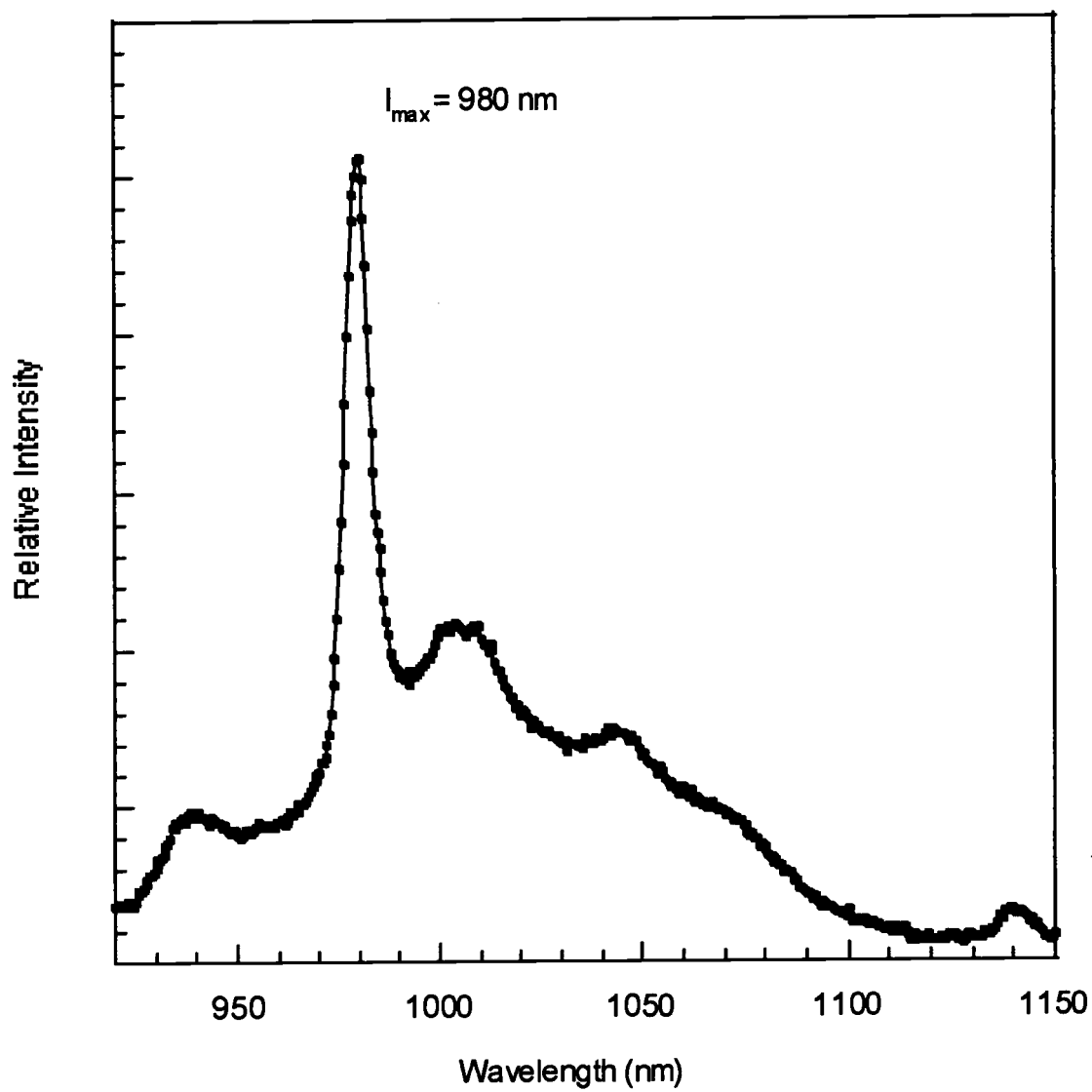


Figure 7.8. Emission spectrum for  $\text{Yb}_{0.02}\text{Li}_{0.67}\text{Ca}_{1.98}\text{GeO}_{4.02}\text{F}_{0.65}$



## Summary

In this paper we report the synthesis and characterization of the new materials  $\text{Li}_2\text{Ca}_6(\text{SiO}_4)_3\text{F}_2$  and  $\text{Li}_2\text{Ca}_6(\text{GeO}_4)_3\text{F}_2$ . Both crystallize in the space group  $R\text{-}3\text{m(h)}$ , and they are isostructural. The structure consists of three compositionally equivalent layers, A, B, and C, which differ only in translation within the unit cell, that are repeated throughout the three dimensional array.

Powder samples of  $\text{Li}_2\text{Ca}_6(\text{GeO}_4)_3\text{F}_2$  have been successfully doped with both  $\text{Nd}^{3+}$  and  $\text{Yb}^{3+}$ . Analysis of optical properties reveals that the material has similar optical properties to those of Ca-FAP.

An important advantage of  $\text{Li}_2\text{Ca}_6(\text{GeO}_4)_3\text{F}_2$  is that its melting point is comparatively low. Crystals were grown at a temperature of 1325 K, significantly lower than the temperatures used to grow commonly used laser crystals, such as YAG and sapphire which both have melting temperatures in excess of 2173 K. If the optical properties are optimised this could be a significant advantage in the processing of new laser crystals.

## Acknowledgments

Acknowledgment is made to the National Science Foundation for support of this research.

## References

- 
1. Welker T., J. Lumin. 48/49, **1991**, 49.
  2. Akella A., Ph.D. Thesis, Oregon State University, 1994.
  3. Kaminskii A.A., Laser Crystals, Springer Verlag 1990.

- 
4. Gruber J.B., Zandi B. and Merkle L., *J. Appl Phys.* **83**(2), **1998**, 1009.
  5. DeLoach L.D., Payne S.A., Smith L.K., Kway W.L. and Krupke W.F., *J. Opt. Soc. Am. B* **11**(2) (1994) 269.
  6. DeLoach L.D., Payne S.A., Chase L.L., Smith L.K., Kway W.L. and Krupke W.F., *IEEE J. Quantum Electron.*, **29**(4) (1993) 1179.
  7. Payne S. A., Beach R.J., Bibeau C., Ebberts C. A., Emmanuel M. A., Honea E. C., Marshall C. D., Page R. H., Schaffers K. I., Skidmore J. A., Sutton S. B., Krupke W. F., *IEEE J. Sci. Top. Quantum Electron.*, **3**(1) (1997) 71.
  8. Mackie P.E. and Young R.A., *J. Appl. Cryst.* **6** (1973) 26.
  9. Fleet M.E. and Pan Y-M., *J. Solid St. Chem.* **112** (1994) 78.
  10. Fleet M.E. and Pan Y-M., *Am. Mineral.* **80** (1995) 329.
  11. Fleet M.E. and Pan Y-M., *Am. Mineral.* **82** (1997) 870.
  12. TEXSAN, Structure analysis package, Molecular Structure Corporation, MSC 3200A, Research Forest Drive, The Woodlands, TX 77381. (199?).
  13. WinGX, a windows program for crystal structure analysis. L.J. Farrugia, university of Glasgow (1998).
  14. SIR92, a program for crystal solution. Altomare A., Cascarano G., and Giacorazzo C., and Guagliardi A. *J. Appl Crystallogr.* **26** (1993) 345
  15. SHELX97, programs for crystal structure analysis (relase 97-2) Sheldrick G.M. Institut für Anorganische Chemie der Universität, Tammanstrasse 4, D-3400, Göttingen, Germany. (1998)
  16. Brese N.E. and O'Keefe M. *Acta Cryst.* **B47** (1991) 192.
  17. Akella A., Tu J. M., Keszler D. A., *Inorg. Chem.*
  18. Recher K., Wallrafen F., and Dupre K., *Naturwissenschaften* **75** (1988) 156.
  19. Kaminskii A. A., *Laser Crystals, Their Physics and Properties*, 2nd ed., 1990, Springer-Verlag

## CHAPTER 8

### STRUCTURE OF $\text{Sr}_4\text{Ge}_2\text{O}_7\text{F}_2$ AND SELECTED LUMINESCENCE PROPERTIES

Gregory. A. Peterson, Annapoorna Akella,  
and Douglas A. Keszler

## Abstract

The structure and selected luminescent properties of the germanate fluoride  $\text{Sr}_4\text{Ge}_2\text{O}_7\text{F}_2$  are described. Crystal data: FW = 645.65 u, monoclinic,  $P2_1/c$  (#14),  $a = 8.024(1)$ ,  $b = 11.224(1)$ ,  $c = 11.547(2)$  Å,  $\beta = 109.79(1)^\circ$ ,  $V = 978.6(3)$  Å<sup>3</sup>,  $Z = 2$ ,  $R = 0.046$ ,  $wR = 0.051$ . The structure contains four crystallographically distinct Sr atoms that are coordinated by a combination of 6, 7, or 8 O and F atoms. The Ge atoms are bound by 4 O atoms at the corners of distorted tetrahedra; pairs of Ge atoms share one O atom to form a pyrogermanate group. Powders doped with  $\text{Pb}^{2+}$ ,  $\text{Tb}^{3+}$ , and  $\text{Eu}^{3+}$  exhibit UV, green, and red emission, respectively.

## Introduction

The compounds  $\text{Ca}_{2.275}\text{GeO}_4(\text{O}_{0.45}\text{F}_{0.55})$ ,<sup>1</sup>  $\text{Mg}_{28}\text{Ge}_{7.55}\text{O}_{32}\text{F}_{15.04}$ ,<sup>2</sup> and  $\text{KMg}_{2.5}\text{Ge}_4\text{O}_{18}\text{F}_2$ <sup>3</sup> are the only reported examples of alkaline-earth germanate fluorides that have been structurally characterized. Among the corresponding family of silicate fluorides, structures have been reported for  $\text{Sr}_2\text{LiSiO}_4\text{F}$ ,<sup>4</sup>  $\text{Ca}_2\text{Mg}_5\text{Si}_8\text{O}_{22}\text{F}_2$ ,<sup>5</sup> and  $\text{Ca}_4\text{Si}_2\text{O}_7\text{F}_2$ .<sup>6</sup> Because of the potential to realize highly anisotropic crystal fields in such materials, we have been interested in the synthesis and study of new examples as luminescent hosts. In general, related oxoanion halides have found widespread interest and use as phosphors, e.g.,  $\text{Sb,Mn:Ca}_5(\text{PO}_4)_3\text{F}$ , and laser materials, e.g.,  $\text{Yb:Sr}_5(\text{PO}_4)_3\text{F}$ .<sup>7</sup>

In this contribution, we describe the crystal structure of the material  $\text{Sr}_4\text{Ge}_2\text{O}_7\text{F}_2$ , which has been found to be isostructural to the mineral cuspidine,  $\text{Ca}_4\text{Si}_2\text{O}_7\text{F}_2$ . Luminescent properties of samples doped with  $\text{Pb}^{2+}$ ,  $\text{Eu}^{3+}$ , and  $\text{Tb}^{3+}$  ions are also described.

## Materials and Methods

A sample of  $\text{Sr}_4\text{Ge}_2\text{O}_7\text{F}_2$  was prepared by heating the molar quantities of 3  $\text{SrCO}_3$  (AESAR, 99.9%), 2  $\text{GeO}_2$  (ALFA, 99.98%), and 1  $\text{SrF}_2$  (AESAR, 99.9%) in an atmosphere of Ar. A crystal was obtained by slowly cooling this melted material in a Pt crucible from 1223 to 873 K at 6 K/h, and then rapidly cooling at 50 K/h to room temperature. A colorless, transparent crystal of dimensions  $0.10 \times 0.12 \times 0.10$  mm was selected and mounted on a glass fiber with epoxy for structure determination. All measurements were made at 296 K on a Rigaku AFC6R diffractometer with graphite-monochromated  $\text{Mo K}\alpha$  radiation. Cell constants and the orientation matrix for data collection were obtained from a least-squares refinement with 19 automatically centered reflections in the range  $30 \leq 2\theta \leq 36^\circ$ . The cell constants correspond to a monoclinic cell; Laue symmetry  $2/m$  was determined on the diffractometer. Intensity data were collected over the range of indices  $0 \leq h \leq 12$ ,  $0 \leq k \leq 18$ ,  $-18 \leq l \leq 18$  by using the  $\omega$ -scan technique to a maximum  $2\theta$  value of  $70^\circ$ , and from 4592 measured reflections, a total of 2489 were observed [ $F_o^2 \geq 3\sigma F_o^2$ ]. The intensities of three representative reflections measured after every block of 200 data varied by an average of 2% during the collection.

The structure was solved by using the *TEXSAN* crystallographic software package.<sup>8</sup> The crystal was found to form in the centrosymmetric space group  $P2_1/c$ . The positions of the Sr and Ge atoms were derived from the direct methods program *SHELXS*,<sup>9</sup> while the remaining atoms O and F were located from difference electron density maps. After a full-matrix, least-squares refinement of the model with isotropic displacement coefficients on each atom, an absorption correction was applied by using the program *DIFABS*<sup>10</sup> (transmission factors = 0.80 -1.47). The data were averaged ( $R_{\text{int}} = 0.054$ ), and the model was refined with anisotropic displacement coefficients on each atom except for O2 and O3. Standard neutral atom scattering factors were used.<sup>11</sup> Final least-squares refinement resulted in the residuals  $R = 0.046$  and  $wR = 0.051$ . The largest peak in the final difference electron-density map

corresponds to 0.88% of the Sr atom. Crystal data are outlined in Table 1, and atomic positional and thermal parameters are listed in Table 2.

The luminescence measurements were performed on powder samples that were produced by using  $\text{NH}_4\text{F} \cdot \frac{1}{2}\text{H}_2\text{O}$  as the source of F. Stoichiometric quantities of  $\text{SrCO}_3$  (AESAR 99.99%),  $\text{GeO}_2$  (AESAR 99.999%),  $\text{NH}_4\text{F} \cdot \frac{1}{2}\text{H}_2\text{O}$  (AESAR 99.9975%),  $\text{Na}_2\text{CO}_3$  (GFS 99.999%),  $\text{PbO}$  (AESAR 99.99+%),  $\text{Eu}_2\text{O}_3$  (Stanford Materials 99.995%),  $\text{Tb}_4\text{O}_7$  (AESAR 99.99%), were mixed to produce the compounds  $\text{Sr}_{3.95}\text{Pb}_{0.05}\text{Ge}_2\text{O}_7\text{F}_2$ ,  $\text{Sr}_{3.94}\text{Eu}_{0.03}\text{Na}_{0.03}\text{Ge}_2\text{O}_7\text{F}_2$ , and  $\text{Sr}_{3.90}\text{Tb}_{0.05}\text{Na}_{0.05}\text{Ge}_2\text{O}_7\text{F}_2$ . The samples were heated in covered alumina crucibles for 30 min at 923 K. They were cooled, ground, and reheated, 20 min at 1273 K, 20 min at 1323 K, and 4 h at 1323 K. Phase formation was verified by analysis of X-ray diffraction patterns from a Philips diffractometer.

Steady state, room-temperature luminescence spectra were obtained on a computer-controlled right angle spectrometer. Excitation from an Oriel 300-W Xenon lamp was passed through a 50-cm water filter, focused onto the entrance slits of a Cary model-15 double prism monochromator, and subsequently directed onto the sample. Luminescence was collected at a near-right angle to excitation, dispersed through an Oriel 22500 1/8-m monochromator, and detected with a Hamamatsu R636 photomultiplier tube. The signal was collected and amplified with a Keithley model 486 picoammeter then converted to a digital signal for computer acquisition. Spectrometer control and data acquisition were achieved with computer programs written in this laboratory. The excitation spectra were corrected by using sodium salicylate and rhodamine B as quantum counters over the appropriate wavelength ranges. The emission spectra were corrected with a tungsten lamp that has been calibrated at Eppley Laboratories, Inc.

Table 8.1. Crystal data and experimental conditions for  $\text{Sr}_4\text{Ge}_2\text{O}_7\text{F}_2$ .

Parameter	Data
Diffractometer	Rigaku AFC6R
Radiation	graphite monochromated Mo $K\alpha$
$\lambda$ , Å	0.70926
Formula wt., u	645.65
Unit cell	Monoclinic
a, Å	8.024(1)
b, Å	11.224(1)
c, Å	11.547(2)
$\beta$ , °	109.79(1)
V, Å <sup>3</sup>	978.6(3)
Space group	(#14) $P2_1/c$
Z	4
$D_{\text{calc}}$ , g cm <sup>-3</sup>	4.382
F(000)	1160
$\mu$ , cm <sup>-1</sup>	270.26
No. of unique data	2489
$F_o^2 > 3\sigma(F_o^2)$	
R( $F_o$ )*	0.046
wR( $F_o$ )*	0.051

$$*R = \sum (|F_o| - |F_c|) / \sum |F_o| ; wR = [ \sum w(|F_o| - |F_c|)^2 / \sum w |F_o|^2 ]^{1/2}$$

Table 8.2. Atom positions and Beq for Sr<sub>4</sub>Ge<sub>2</sub>O<sub>7</sub>F<sub>2</sub>.

Atom	x	y	z	B <sub>eq</sub> *
Sr1	0.4690(1)	0.08110(7)	0.68322(7)	0.34(2)
Sr2	0.3365(1)	-0.13231(7)	0.91678(8)	0.46(3)
Sr3	0.8310(1)	-0.13400(7)	0.92273(7)	0.36(3)
Sr4	-0.0289(1)	0.09323(7)	0.69941(7)	0.36(2)
Ge1	0.1530(1)	-0.19424(9)	0.62417(8)	0.30(3)
Ge2	0.2730(1)	0.19652(9)	0.36749(8)	0.37(3)
F1	0.0750(7)	-0.0069(5)	0.9011(4)	0.5(2)
F2	0.5738(8)	-0.0005(5)	0.8974(5)	0.8(2)
O1	0.2721(9)	0.2142(6)	0.7461(5)	0.6(2)
O2	0.7211(9)	0.2157(6)	0.7567(6)	0.6(1)
O3	0.200(1)	-0.0488(6)	0.6683(6)	1.0(1)
O4	0.1350(1)	-0.2673(6)	0.9750(6)	0.8(2)
O5	0.9358(9)	-0.2662(6)	0.1232(6)	0.8(2)
O6	0.4084(9)	0.2366(6)	0.5121(6)	0.7(2)
O7	0.720(1)	-0.0498(6)	0.6750(7)	0.9(2)

$$*B_{eq} = (8\pi^2/3)\sum_i\sum_j U_{ij}a_i a_j^* a_i a_j$$



## Results and Discussions

A view of the contents of the unit cell is given in Figure 8.1. The structure contains four types of Sr atoms one 6-coordinate, two 7-coordinate, and one 8-coordinate; and two crystallographically distinct 4-coordinate Ge atoms. The Sr-centered polyhedra share edges and vertices to form a three-dimensional framework (Figure 8.2) that contains distorted tetrahedral interstices occupied by the Ge atoms. As indicated by the stoichiometry, the Ge-centered tetrahedra share corners to form  $\text{Ge}_2\text{O}_7$  groups.

Atom Sr1 is bound by one each of atoms O1, O2, O3, O6, O7, and F2 in a distorted octahedral geometry. Atom Sr2 is bound by one each of atoms O2, O3, O4, O6, and F1 and two F2 atoms in an environment best described as a distorted monocapped octahedron. Atom Sr3 is bound to one each of atoms O1, O4, O5, O6, O7, and F2 and two F1 atoms in an environment best described as a distorted dodecahedron. The Sr4 atom is bonded to one each of atoms O1, O2, O3, O4, O5, O7, and F1 in a distorted monocapped octahedral geometry. The Sr1 atom shares edges O1...O3 and O2...O7 with Sr4 atoms, edges O2...O6 and O3...F2 and vertex F2 with Sr2 atoms, and edges O1...O6 and O7...F2 with Sr3 atoms to give seven Sr atoms about the Sr1-centered octahedron; there is no O or F atom directly bridging the Sr1 atoms themselves. In addition to its shared elements with atom Sr1, atom Sr2 shares an F2...F2 edge with another Sr2 atom, edges O4...F1, O6...F2, and F1...F2 with Sr3 atoms, and edges O2...O4 and O3...F1 with Sr4 atoms. The remaining connections among the Sr-centered polyhedra involve edges O1...O4, O5...F1, and O7...F1 between the Sr3 and Sr4 atoms.

Selected interatomic distances and angles are listed in Table 8.3. The average Sr1-O distance is  $2.51 \pm 0.06$  Å, which compares to the Sr-O distance of 2.53 Å for a 6-coordinate Sr atom and Shannon radii.<sup>12</sup> The average Sr2-O distance is  $2.57 \pm 0.19$  Å, and the average Sr4-O distance is  $2.60 \pm 0.11$  Å, which compare, respectively, to the average Sr-O distance of  $2.64 \pm 0.08$  for a 7-coordinate Sr atom in  $\text{Sr}_2\text{ScLiB}_4\text{O}_{10}$ <sup>13</sup> and 2.59 Å from crystal radii. The

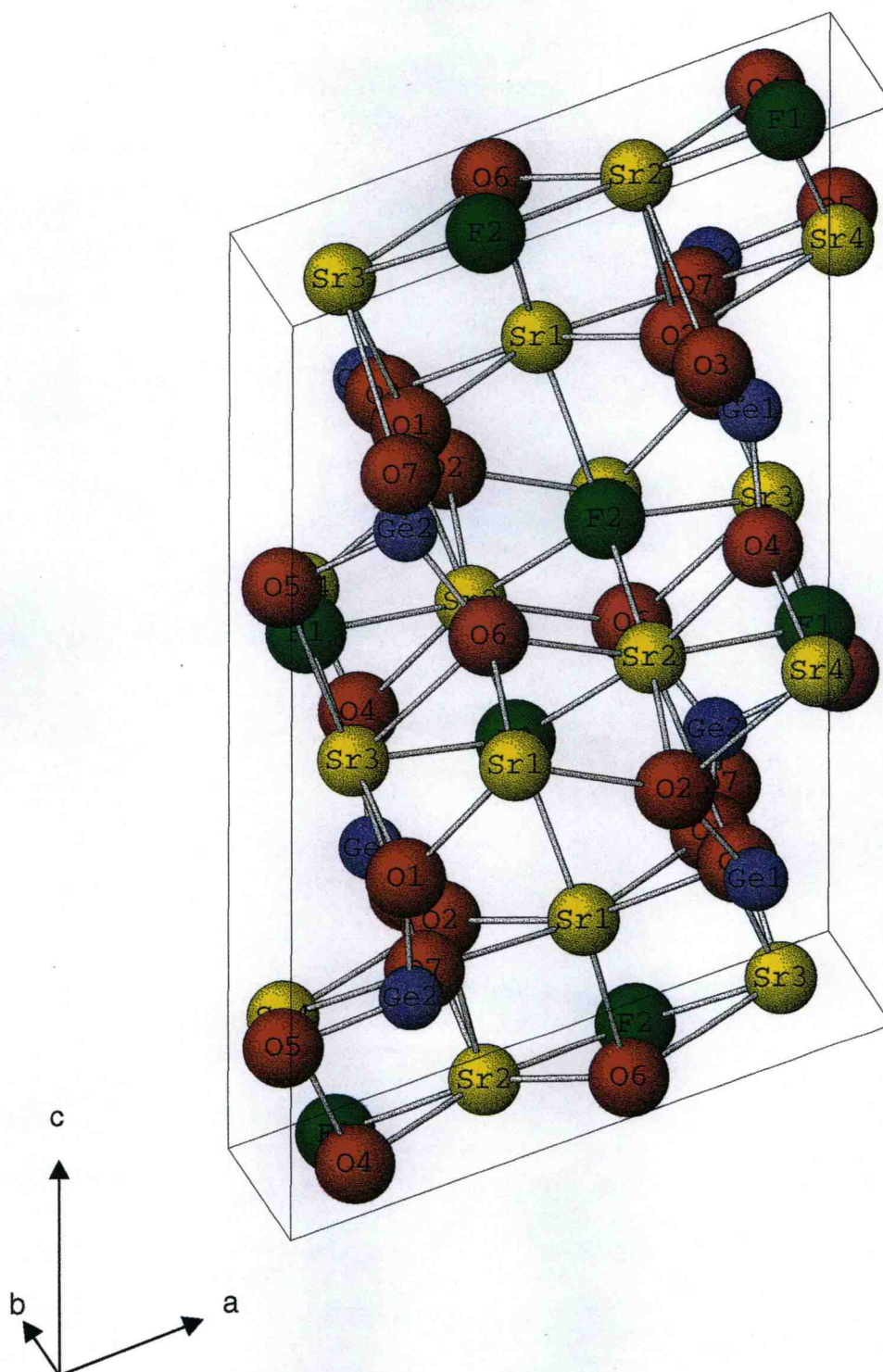


Figure 8.1. Unit-cell diagram of  $\text{Sr}_4\text{Ge}_2\text{O}_7\text{F}_2$ ; view is along the  $b$  axis.



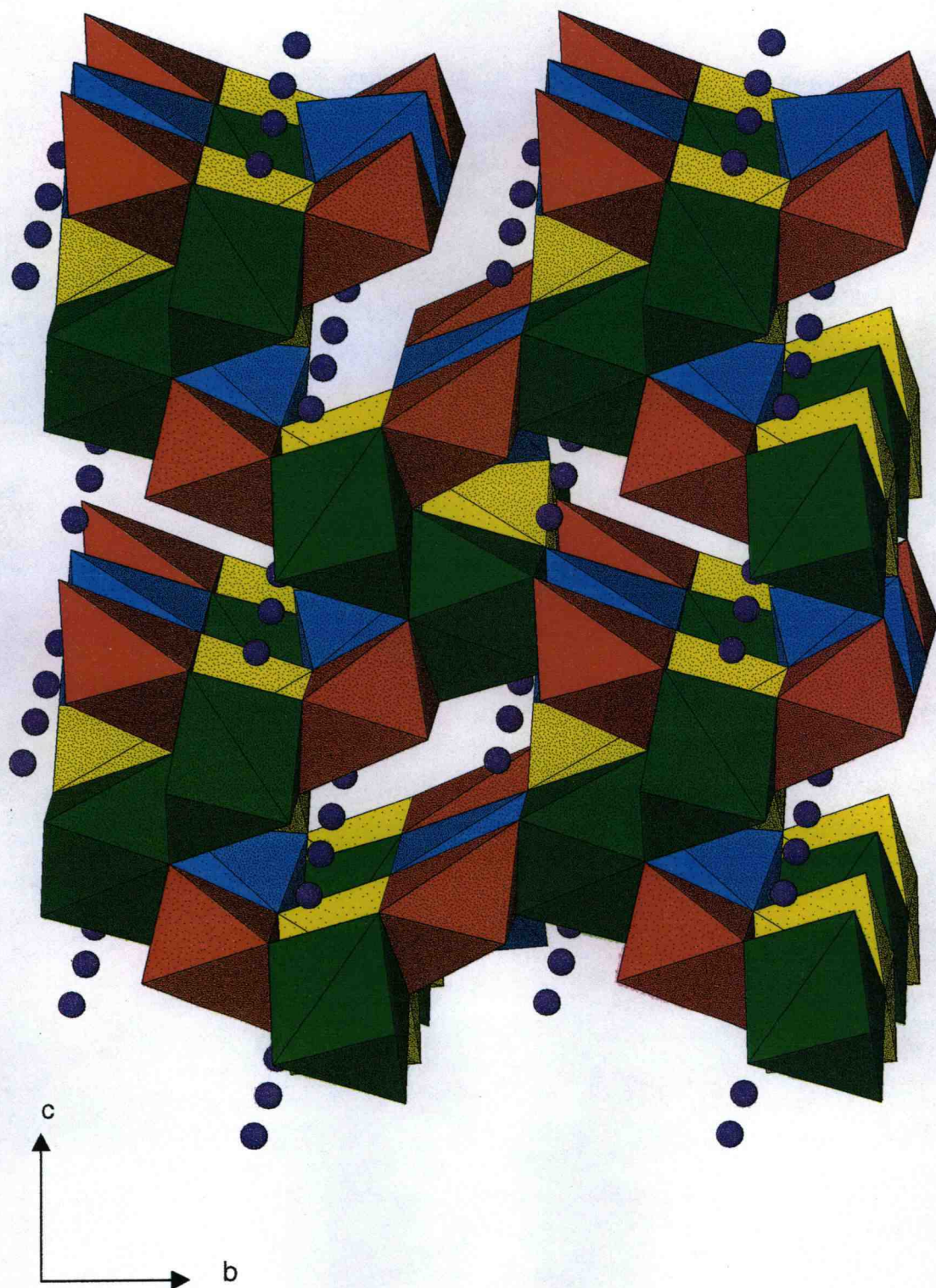


Figure 8.2. Framework resulting from condensation of Sr Polyhedra. Small, circles represent Ge atoms.

Table 8.3. Selected interatomic distances (Å) and bond angles (°).

Atoms	Distance(Å)	Atoms	Angles ( °)
Sr (1)– O(1)	2.587(7)	O(1) – Sr(1) – O(2)	93.4(2)
Sr (1)– O(2)	2.305(8)	O(1) – Sr(1) – O(3)	75.7(2)
Sr (1)– O(3)	2.323(8)	O(1) – Sr(1) – O(6)	80.9(2)
Sr (1)– O(6)	2.314(7)	O(1) – Sr(1) – O(7)	165.2(2)
Sr (1)– O(7)	2.343(8)	O(6) – Sr(1) – O(7)	108.3(2)
Sr (1)– F(2)	2.195(6)	F(2) – Sr(1) – O(2)	85.6(5)
Sr (2)– O(2)	2.546(7)	O(2) – Sr(2) – O(3)	61.6(2)
Sr (2)– O(3)	2.864(8)	O(2) – Sr(2) – O(4)	81.0(2)
Sr (2)– O(4)	2.474(8)	O(3) – Sr(2) – O(4)	114.2(2)
Sr (2)– O(6)	2.416(8)	O(3) – Sr(2) – O(6)	122.2(2)
Sr (2)– F(1)	2.476(6)	F(1) – Sr(2) – O(2)	113.3(2)
Sr (2)– F(2)	2.479(7)	F(1) – Sr(2) – F(2)	107.8(2)
Sr (2)– F(2)	2.506(6)	F(2) – Sr(2) – O(6)	79.0(2)
Sr (3)– O(1)	2.516(7)	O(1) – Sr(3) – O(4)	80.7(2)
Sr (3)– O(4)	2.753(8)	O(1) – Sr(3) – O(5)	102.7(2)
Sr (3)– O(5)	2.635(8)	O(4) – Sr(3) – O(5)	60.3(2)
Sr (3)– O(6)	2.709(7)	O(4) – Sr(3) – O(7)	110.7(2)
Sr (3)– O(7)	2.850(8)	O(5) – Sr(3) – O(6)	60.0(2)
Sr (3)– F(1)	2.510(6)	F(1) – Sr(3) – O(1)	112.0(5)
Sr (3)– F(1)	2.487(6)	F(1) – Sr(3) – F(1)	72.1(2)
Sr (3)– F(2)	1.495(7)	F(1) – Sr(3) – F(2)	107.0(2)

Table 8.3(Cont'd). Selected Interatomic Distances (Å) and Bond Angles ( ° )

Atoms	Distance(Å)	Atoms	Angles ( ° )
Sr (4)– O(1)	2.664(7)	O(1) – Sr(4) – O(2)	113.1(2)
Sr (4)– O(2)	2.695(8)	O(1) – Sr(4) – O(3)	72.5(2)
Sr (4)– O(3)	2.539(8)	O(1) – Sr(4) – O(4)	83.4(2)
Sr (4)– O(4)	2.466(8)	O(1) – Sr(4) – O(5)	59.2(2)
Sr (4)– O(5)	2.742(8)	O(5) – Sr(4) – O(7)	122.8(2)
Sr (4)– O(7)	2.510(8)	F(1) – Sr(4) – O(1)	92.5(2)
Sr (4)– F(1)	2.459(8)	F(1) – Sr(4) – O(2)	92.7(2)
Ge (1)– O(2)	1.728(8)	O(2) – Ge(1) – O(3)	108.4(4)
Ge (1)– O(3)	1.712(8)	O(2) – Ge(1) – O(4)	118.5(4)
Ge (1)– O(4)	1.727(7)	O(2) – Ge(1) – O(5)	99.7(3)
Ge (1)– O(5)	1.799(8)	O(3) – Ge(1) – O(5)	110.3(4)
Ge (2)– O(1)	1.727(7)	O(1) – Ge(2) – O(5)	100.1(3)
Ge (2)– O(5)	1.759(8)	O(1) – Ge(2) – O(6)	117.2(3)
Ge (2)– O(6)	1.722(7)	O(5) – Ge(2) – O(7)	100.4(4)
Ge (2)– O(7)	1.730(8)	O(6) – Ge(2) – O(7)	117.6(4)

average Sr3-O distance is  $2.69 \pm 0.12$  Å, which compares well to a Sr-O distance of  $2.67 \pm 0.17$  for 8-coordinate Sr atoms in  $\text{SrKB}_5\text{O}_9$ <sup>14</sup> and 2.64 Å obtained from crystal radii. The Sr-F distances fall in the narrow range of 2.459(6) - 2.506(6) Å. All of these distances are statistically equivalent.

The Ge1 atom is connected to one each of atoms O2, O3, O4, and O5, and the Ge2 atom is bonded to one each of atoms O1, O5, O6, and O7, in each case forming slightly distorted tetrahedra. Atom O5 serves as the common vertex between these polyhedra. The average Ge1-O bond distance is  $1.74 \pm 0.04$  Å, and the average Ge2-O bond distance is  $1.73 \pm 0.02$  Å; each compares, for example, to the Ge-O distance of 1.79 Å in  $\text{SrGeO}_3$ .<sup>15</sup> All O-Ge-O angles deviate from the tetrahedral value by less than  $10^\circ$ . The bridging angle, Ge1-O5-Ge2 =  $151.6(4)^\circ$ , may be compared to the angle Si-O-Si =  $144^\circ$  in  $\alpha$ -quartz.<sup>16</sup> Variations in M-O-M angles of this type have been previously considered.<sup>17</sup> We note that the pyrogermanate group adopts a nearly eclipsed geometry.

All O atoms are 4-coordinate and best described as distorted tetrahedra. Atoms O1, O2, O3, O4, O6, and O7 are each coordinated by three Sr atoms and one Ge atom. Atom O5 is coordinated by two Sr, and two Ge atoms.

The bond-valence method<sup>18,19</sup> was used to calculate the valences of all the atoms in the structure. Each F atom has a valence within 10 % of the standard integral value, indicating that they have been correctly identified in the structure analysis. All of the other atoms have calculated valences within 5 % of standard integral values, except for atoms O3 and O7 where valences of 1.8 and 1.8, respectively, indicate lack of bonding electron density, and atom O5 where the valence of 2.3 indicates a slight excess of bonding electron density.

### ***Pb<sup>2+</sup> Luminescence***

The emission wavelength of the  $\text{Pb}^{2+}$  ion is strongly dependent on the nature of the phosphor host as it can vary from ultraviolet to red.<sup>20</sup> In the spectrum of

$\text{Sr}_{3.95}\text{Pb}_{0.05}\text{Ge}_2\text{O}_7\text{F}_2$  (Figure 8.4), the emission wavelength for the  $(^3\text{P}_1) ^3\text{P}_0 \rightarrow ^1\text{S}_0$  transition is centered at 367 nm. The breadth of the emission band arises from the strong vibrational-electronic coupling as well as a contribution from the slightly higher energy  $^3\text{P}_1$ , which is thermally populated at the dopant concentration and temperature of this experiment. The Stokes shift is ca. 8800  $\text{cm}^{-1}$ , a value consistent with a  $6s^2$  ion such as  $\text{Pb}^{2+}$  on a Sr site.<sup>21</sup> Such large Stokes shifts are associated with large relaxation of the  $^3\text{P}$  excited state, which is expected on the basis of the large and irregular coordination of the anions around the Sr sites. Similar results have been noted for the isoelectronic species,  $\text{Bi}^{3+}$ .<sup>22</sup> The broad excitation bands centered at 248 and 273 nm are assigned as  $^1\text{S}_0 \rightarrow ^3\text{P}_{0,1}$ . Assignment of the excited state-levels is made difficult since the description of the multi-electron levels of the  $6s^2$  configuration are situated somewhere between the LS- and jj-coupling schemes.<sup>21</sup>

### ***Eu<sup>3+</sup> Luminescence***

At the concentrations utilized here, luminescence of the  $\text{Eu}^{3+}$  ion in a crystalline material is generally associated with transitions from the excited state  $^5\text{D}_0$  to ground-state levels of the  $^7\text{F}_J$  manifold. In general, the more intense emission features are associated with the  $^5\text{D}_0 \rightarrow ^7\text{F}_1$  transition near 590 nm (orange) or the  $^5\text{D}_0 \rightarrow ^7\text{F}_2$  transition near 610 nm (red). The transitions  $^5\text{D}_0 \rightarrow ^7\text{F}_2, ^7\text{F}_4, ^7\text{F}_6$  follow forced electric-dipole selection rules, while the transitions of the type,  $^5\text{D}_0 \rightarrow ^7\text{F}_1, ^7\text{F}_3, ^7\text{F}_5$  follow magnetic-dipole selection rules. If the  $\text{Eu}^{3+}$  ion occupies a site lacking a center of symmetry, the electric-dipole transitions are expected to predominate, and as noted above, the strongest of these is usually the  $J = 0 \rightarrow 2$  transition. In the spectrum of  $\text{Sr}_{3.94}\text{Eu}_{0.03}\text{Na}_{0.03}\text{Ge}_2\text{O}_7\text{F}_2$  (Figure 8.4), we observe the most intense peak corresponding to the  $J = 0 \rightarrow 2$  transition at 611 nm, a result that is consistent with the lack of a center of symmetry for the four  $\text{Sr}^{2+}$  sites. The emission bands are inhomogeneously broadened because of the substitution of  $\text{Eu}^{3+}$  on multiple  $\text{Sr}^{2+}$  sites. The

chromaticity coordinates  $x = 0.642$  and  $y = 0.358$ , compare well to the values  $x = 0.654$  and  $y = 0.346$  for the standard red phosphor  $\text{Eu:Y}_2\text{O}_3$ .

### ***Tb<sup>3+</sup> Luminescence***

Luminescence of the  $\text{Tb}^{3+}$  ion in a crystalline material is generally associated with transitions from the excited state  $^5\text{D}_4$  to ground-state levels of the  $^7\text{F}_j$  manifold, where  $j = 6, 5, 4$ , and  $3$ .<sup>23</sup> The  $^5\text{D}_4 \rightarrow ^7\text{F}_5$  transition is generally the strongest line, and its maximum is at 547 nm in the spectrum of (Figure 8.5.) The transitions at 416, 439, and 460 nm originate from the  $^5\text{D}_3 \rightarrow ^7\text{F}_j$  transitions that are normally quenched by either cross relaxation or exchange mechanisms in more concentrated  $\text{Tb}^{3+}$  systems.<sup>24</sup> The excitation spectrum consists of a strong, broad absorption band that corresponds to the  $4f^8 \rightarrow 5d^1$  transition in  $\text{Tb}^{3+}$ . Chromaticity coordinates,  $x = 0.269$ , and  $y = 0.451$ , were calculated from the spectrum. The values reflect the contribution of the  $^5\text{D}_3 \rightarrow ^7\text{F}_j$  transitions that emit in the blue portion of the spectrum.

### **Summary**

The structure and selected luminescent properties of  $\text{Sr}_4\text{Ge}_2\text{O}_7\text{F}_2$  are described. The large asymmetric Sr sites provide an ideal environment for  $\text{S}^2$  ions such as  $\text{Pb}^{2+}$  and  $\text{Bi}^{2+}$ , resulting in a large Stokes shift, and comparatively large splitting of the excited state  $^3\text{P}$  levels. The chromaticity coordinates of  $\text{Eu:Sr}_4\text{Ge}_2\text{O}_7\text{F}_2$  reflect a suitable emission color when compared to  $\text{Eu:Y}_2\text{O}_3$ . The chromaticity coordinates of  $\text{Tb:Sr}_4\text{Ge}_2\text{O}_7\text{F}_2$  have a strong blue component, reflecting the  $^5\text{D}_3 \rightarrow ^7\text{F}_j$  transitions that are present in the spectrum.



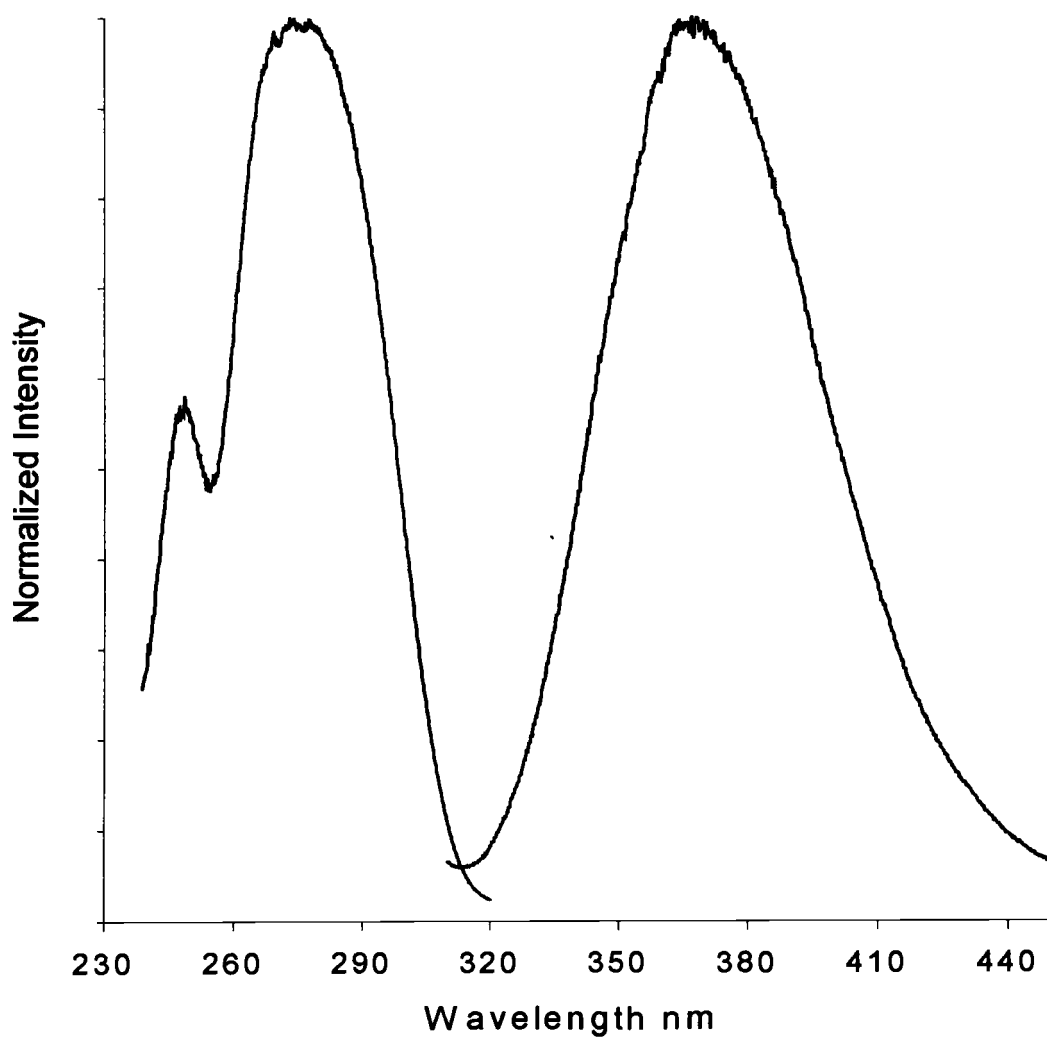


Figure 8.3. Excitation and emission spectrum of  $\text{Sr}_{3.95}\text{Pb}_{0.05}\text{Ge}_2\text{O}_7\text{F}_2$  at 298 K ( $\lambda_{\text{exc}} = 294$  nm for emission and  $\lambda_{\text{em}} = 368$  nm for excitation).

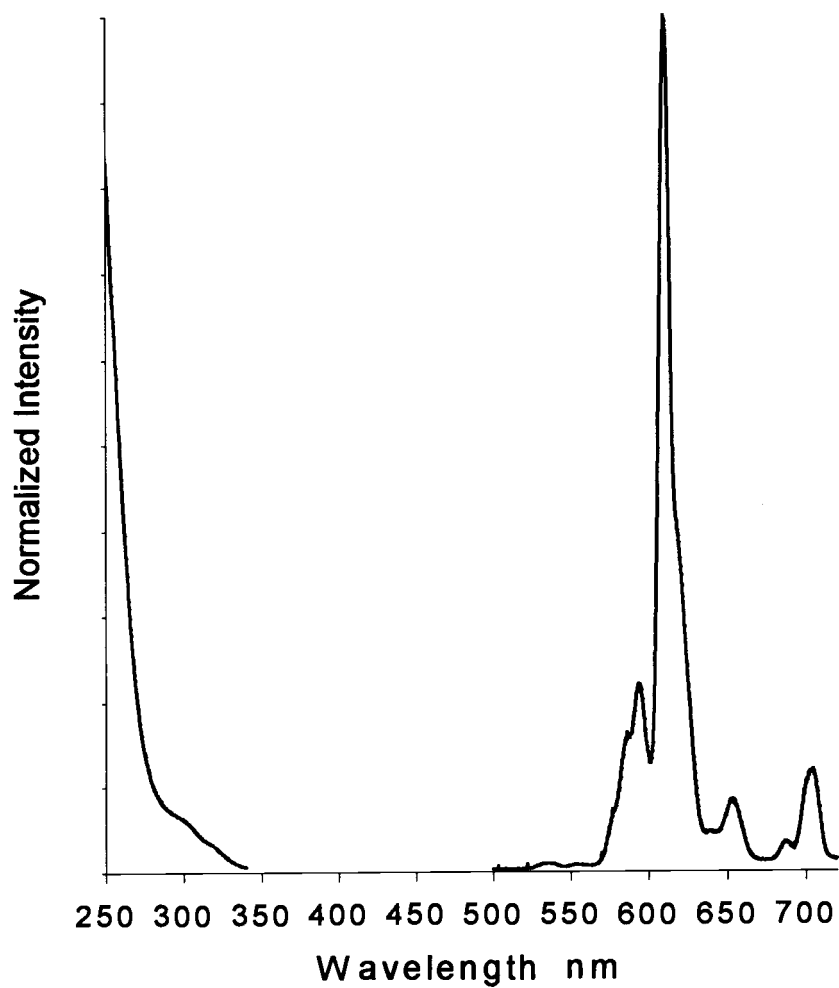


Figure 8.4. Excitation and emission spectrum of  $\text{Sr}_{3.95}\text{Eu}_{0.03}\text{Na}_{0.03}\text{Ge}_2\text{O}_7\text{F}_2$  at 298 K ( $\lambda_{\text{exc}} = 260$  nm for emission and  $\lambda_{\text{em}} = 611$  nm for excitation).

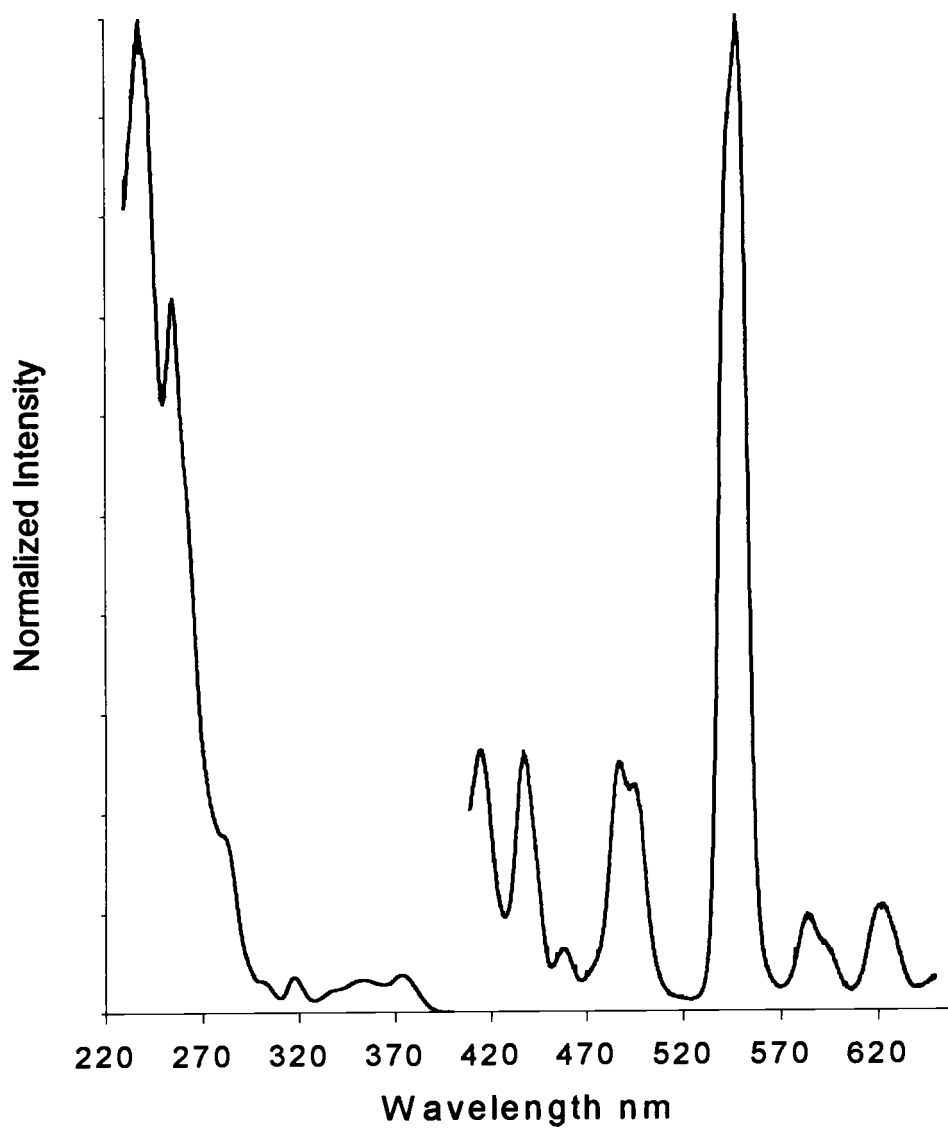


Figure 8.5. Excitation and emission spectrum of  $\text{Sr}_{3.90}\text{Tb}_{0.05}\text{Na}_{0.05}\text{Ge}_2\text{O}_7\text{F}_2$  at 298 K (  $\lambda_{\text{exc}}$  = 264 nm for emission and  $\lambda_{\text{em}}$  = 548 nm for excitation).

## Acknowledgments.

This research was supported by the US National Science Foundation, Solid-State Chemistry Program. Acknowledgment is made to the Donors of The Petroleum Research Fund, administered by the American Chemical Society, for partial support of the work.

## References

1. Nishi, F.; Takeuchi, Y. *Acta Crystallogr., Sect. C* **40**, **1984**, 730.
2. Bless, P.W.; Dreele R.B. von, Kostiner E, Hughes R.E. *J. Solid State Chem.* **4**, **1972**, 262.
3. Toraya, H.; Iwai, S.; Marumo, F.; Hirao, M. *Z. Kristallogr.* **148**, **1978**, 65.
4. Akella, A.; Keszler, D. A. *Chem. Mater.* **7**, **1995**, 1299.
5. Cameron, M.; Gibbs G. V. *Am. Mineral.* **58**, **1973**, 879.
6. Smirnova, R. F.; Rumanova, I. M.; Belov N. V. *Zap. Vsesoy. Mineralog. Obschch.* **84**, **1955**, 159.
7. Marshall, C. D.; Smith, L. K.; Beach, R. J.; Emanuel, M. A.; Schaffers, K. I.; Skidmore, J.; Payne, S. A.; Chai, B. T. *IEEE J. Quantum Electron.* **32**, **1996**, 650.
8. TEXSAN: Single Crystal Structure Analysis Software, Version 5.0 **1989**, Molecular Structure Corp., The Woodlands, TX, 77381.
9. Sheldrick, G. SHELXS86. In *Crystallographic Computing 3*; Sheldrick, G.; Kruger, C.; Goddard, R.; Eds.; Oxford University Press: New York, 1985; p 175.
10. Walker, N.; Stuart, D. *Acta Crystallogr., Sect. A* **39**, **1983**, 158.
11. *International Tables for X-ray Crystallography*, Kynoch Press: Birmingham, England, **1974**, Vol. IV.

- 
12. Shannon, R. D. *Acta Crystallogr., Sect. A* 32, **1976**, 751.
  13. Thompson, P. D.; Keszler, D. A. *Solid State Ionics* 32/33, **1989**, 521.
  14. Tu, J., Keszler, D. A. *Acta Crystallogr., Sect. C*, in press.
  15. Nadezhina, T. N.; Pobedimskaya, E. A.; Ilyukhin, V.V.; Belov, N. V. *Sov. Phys. Crystallogr.* 26, **1981**, 168.
  16. Levien, L., Prewitt, C. T., Weidner, D. *Am. Mineral.* 65, **1980**, 920.
  17. Gibbs, G. V.; Meagher, E. P.; Newton, M. D.; Swanson, D. K.; *Structure and Bonding in Crystals, Volume I*, O'Keeffe, M. and Navrotsky, A., Eds., Academic Press: New York, 1981, p. 195.
  18. Schlager, M.; Hoppe, R. Z. *Anorg. Allg. Chem.* 619, **1993**, 976.
  19. O'Keeffe, M.; Hansen, S. *J. Am. Chem. Soc.* 110, **1988**, 1506.
  20. Meijerink A., Jetten H., and Blasse G., *J. Solid State Chem.* 76, **1988**, 115.
  21. Timmermans C. W. M., and Blasse G., *J. Solid State Chem.* 52, **1984**, 222.
  22. Blasse G., *Prog. Solid State Chem.* 18, **1988**, 79.
  23. Verstegen J. M. P. J., *J. Electrochem. Soc.*, 121, **1974**, 1631.
  24. Berdowski P. A. M., Lammers M. J. J., Blasse G., *Chem. Phys. Letters*, 113, **1985**, 387.

## CHAPTER 9

### CONCLUSION

The focus of the seven main chapters of this thesis was to find and characterize new solid-state materials for potential optical applications. Structure-property relationships determined from existing optical materials provided a starting point for the search for new solid-state compounds. While it is possible to use these relationships to envision new solid-state compounds, and to write out interesting chemical formulas, it is not possible to predict whether these compounds will be thermodynamically stable, and if they exist, their structure type. A new, solid-state compound may contain a suitable chemical composition for the substitution of a particular dopant ion, yet lack a crystal/electronic structure that provides the desired optical properties, and vice-versa. Throughout the seven chapters, we try to exploit what is known about existing materials in our search for new compounds with improved optical properties.

While certain guidelines may apply, it is difficult to predict with any certainty whether a new solid-state borate compound will form in a noncentrosymmetric space group, a desirable property for nonlinear optical (NLO) applications, whether it will melt congruently, or what the borate structural motif may be, based on a given formula. A good example of this uncertainty is realized in the compound  $\text{YBO}_3$ , which could potentially possess an orthoborate ( $\text{BO}_3$ ) phase which is related to calcite at low temperatures, and a rhombohedral phase containing a  $\text{B}_3\text{O}_9$  ring system at higher temperatures.

The borate-groups structural motif and orientation in the noncentrosymmetric compounds  $\text{CeSc}_3(\text{BO}_3)_4$  (CSB) and  $\text{NaLiB}_4\text{O}_7$  are highlighted in Chapters 2 and 3, respectively. CSB forms in both a high-temperature centrosymmetric  $\text{C2/c}$  phase and a low-temperature noncentrosymmetric  $\text{R32}$  phase. Stoichiometric, trigonal crystals of the  $\text{R32}$  phase, which possess the desired NLO properties, can be grown by using a high-temperature solution growth, where formation of the lower temperature phase is favored. Incorporation of additional Li into the  $\text{NaLiB}_4\text{O}_7$  structure to give a stoichiometry of  $\text{Na}_{0.55}\text{Li}_{1.45}\text{B}_4\text{O}_7$  results in a phase change from a face-centered orthorhombic structure to a body-centered tetragonal structure, a modest change that may allow tunability of the NLO properties.

The study of fundamental structure-property relationships of VUV-excited phosphors is found in Chapter 4, and Chapters 5 and 6 highlight the structural and optical characterization of two Y- and B-containing compounds that were produced in a search for  $\text{Eu}^{3+}$ -substituted, red plasma display panel (PDP) phosphors. The compound  $\text{Eu}:\text{Y}_2\text{O}_3$  contains small noncentrosymmetric six-coordinate Y sites, and it is an efficient UV-excited  $\text{Eu}^{3+}$ -doped phosphor with the  $\text{Eu}^{3+}$ -activator possessing a quantum efficiency close to unity.  $\text{Eu}^{3+}:(\text{YGd})\text{BO}_3$  contains borate groups that are responsible for strong absorption of the Xe-plasma discharge, a requirement necessary for an efficient PDP phosphor. The ternary phase diagrams that were studied in Chapters 5 and 6 resulted in the isolation of two interesting Y- and B-containing optical materials,  $\text{YMgB}_5\text{O}_{10}$  and  $\text{Y}_4\text{BO}_7\text{F}$ . VUV spectra for  $\text{Eu}^{3+}:\text{YMgB}_5\text{O}_{10}$  and  $\text{Eu}^{3+}:\text{Y}_4\text{BO}_7\text{F}$  were collected and analyzed. Both compounds absorbed poorly in the VUV portion of the spectrum close to the Xe emission (147 nm), however, both compounds provided noncentrosymmetric Y-sites for  $\text{Eu}^{3+}$ -substitution, producing relatively efficient red-saturated luminescence when excited by UV light.

The crystallographic similarity of the Ca sites in  $\text{Li}_2\text{Ca}_6(\text{GeO}_4)_3\text{F}_2$  to the Sr sites in  $\text{Sr}_5(\text{PO}_4)_3\text{F}$ , and the highly anisotropic crystal field produced in both materials due to the interaction between the highly ionic, F-containing alkaline-

earth sites and the highly covalent  $\text{GeO}_4$ -groups, make the oxoanion-fluoride compounds in Chapter 7 of much interest for  $\text{Yb}^{3+}$ -doped laser materials. The Stark levels of the ground state of the  $\text{Yb}^{3+}$  ion are forced far enough apart in materials with highly anisotropic crystal fields, that efficient, pseudo three-level lasing can be achieved by using the upper ground state level as a terminal laser level. There are only a small number of Ge- and Si-containing alkaline-earth oxoanion-fluoride compounds found in the literature. New materials with slightly different structures may reveal new structure-property relationships specific to the nature of the  $\text{Yb}^{3+}$  ion. Compounds containing the cations Ca, Sr, Ba, Al, Ga, Si, Ge, P and As would be a good place for future work in searching for new oxoanion-fluoride compositions, with crystallographic features that may enhance the splitting of the  $\text{Yb}^{3+}$  ground state.



## BIBLIOGRAPHY

Abdullaev G. K., Mamedov K. S., Dzhaferov G. G., and Aliev O. A., *Zhurnal Neorganicheskoi Khimii ZNOKA*, 25, **1980**, 364.

Aka G., Viegas N., Telsseire B., Kahn-Harari A. and Godard J., *J. Mater. Chem*, 5(4), **1995**, 583.

Akella A., Ph.D. Thesis, Oregon State University, **1994**.

Akella A., Tu J. M., Keszler D. A., *Inorg. Chem.*

Akella A., Keszler D. A., *Chem. Mater.* 7, **1995**, 1299.

Berdowski P. A. M., Lammers M. J. J., Blasse G., *Chem. Phys. Letters*, 113, **1985**, 387.

Blasse G., *J. Chem Phys.* 45, No 7, **1966**, 2356.

Blasse G., Kita A., *Solid State Luminescence, Theory, Materials and Devices*, Chapter 2, **1993**. Publisher

Blasse G., Grabmaier B. C., *Luminescent Materials*, Springer Verlag, Berlin Germany, **1994**.

Blasse G., and Brixner L. H., *Eur. J Solid State Inorg. Chem.* 28, **1991**, 767.

Blasse G., *Structure and Bonding* 42, **1980**, 1.

Blasse G., *Inorg. Chim. Acta* 157, **1989**, 141.

Blasse G., and Brill A., *J. Chem. Phys.*, 47(12), **1967**, 5139.

Blasse G., *Prog. Solid State Chem.* 18, **1988**, 79.

Bless P.W., von Dreele R.B., Kostiner E., Hughes R.E. *J. Solid State Chem.* 4, **1972**, 262.

Bordui P. F. and Fejer M. M., *Annu. Rev. Mater. Sci.*, 23, **1993**, 321.

Brese N. E., and O'Keeffe M., *Acta Crystallogr. Sect. B* 47, **1991**, 192.

Buijs M., and Blasse G., *J. Luminescence*, 34, **1986**, 263.

## BIBLIOGRAPHY (Continued)

- Buijs M., Meyerink A., Blasse G., *J. Lumin.* 37, **1987**, 9.
- Buijs M., van Vliet J. P. M., Blasse G., *J. Lumin.* 35, **1986**, 213.
- Cameron M., Gibbs G. V., *Am. Mineral.* 58, **1973**, 879.
- Chadeyron G., Mahiou R., El-Ghozzi M., Arbus A., Zambon D., Cousseins J. C., *J. Lumin.* 72-74, **1997**, 564.
- Chadeyron G., Mahiou R., El-Ghozzi M., Arbus A., Cousseins J. C., *J. Solid State Chem.*, 128, **1997**, 261.
- Chani V. I., et. al., *J. Crystal Growth*, 133, **1993**, 173.
- Chani V. I., et. al., *J. Crystal Growth*, 133, **1993**, 181.
- Cheetham A. K., Norman N., *Acta Chemica Scandinavica Series A.* 28, **1974** 55.
- Chen C., Wang Y., Xia Y., Wu B., Tang D., Wu K., Wenrong Z., Yu L. and Mei L., *J. Appl. Phys.*, 77(6), **1995**, 2268.
- Chen C., Wang Y., Xia Y., Wu B., Tang D., Wu K., Wenrong Z., Yu L., and Mei L., *J. Appl. Phys.* 77 (6), **1995**, 2268.
- Chen C., Wu Y., Jiang A., Wu B., You G., Li R., and Lin S., *J Opt. Soc. Am. B* 6, **1989**, 616.
- Chen C., Wu Y., Li R., *J. Crystal Growth*, 99, **1990**, 790.
- Cheng L. K., Bosenberg W., and Tang d. L., *J Cryst. Growth* 89, **1988**, 553.
- DeLoach L.D., Payne S.A., Chase L.L., Smith L.K., Kway W.L. and Krupke W.F., *IEEE J. Quantum Electron.*, 29(4) **1993**, 1179.
- DeLocah L.D., Payne S.A., Smith L.K., Kway W.L. and Krupke W.F., *J. Opt. Soc. Am. B* 11(2), **1994** 269.
- Diaz, A, Quick Basic Program, Oregon State University, October 26, **1995**.
- Dirksen G. J., and Blasse G., *J Alloys Compounds* 191, **1993**, 121.
- Eimerl D., Davis L., Velsko S., Graham E. K., and Zalkin A., *J Appl. Phys.* 62, **1987**, 1968.

## BIBLIOGRAPHY (Continued)

- Fan S.-J., Shen G.-S., Wang W., Li J.-L. and Le X.-H., *J. Crystal Growth*, **99**, **1990**, 811.
- Fleet M.E. and Pan Y.-M., *J. Solid St. Chem.* **112**, **1994**, 78.
- Fleet M.E. and Pan Y.-M., *Am. Mineral.* **80**, **1995**, 329.
- Fleet M.E. and Pan Y.-M., *Am. Mineral.* **82**, **1997**, 870.
- Fouassier C., Saubat B., and Hagenmuller P., *J. Luminescence*, **23**, **1981**, 405.
- Gibbs G. V., Meagher E. P., Newton M. D., Swanson D. K., *Structure and Bonding in Crystals, Volume I*, O'Keeffe, M. and Navrotsky, A., Eds., Academic Press: New York, 1981, p. 195.
- Gruber J.B., Zandi B. and Merkle L., *J. Appl. Phys.* **83**(2) **1998**, 1009.
- Henderson B., and Imbush G. B., *Optical Spectroscopy of Inorganic Solids*, Clarendon Press, Oxford UK, **1989**.
- Huber G., Jensen T., Meyn J. P., *IEEE J. Quantum Electronics*, **30**, **1994**, 913.
- Ilyuknin A. B., Dzhurinskii B. F., *Zh Neorg. Khimii.* **38**, **1993**, 917.
- Ingle J., Crouch S., *Spectrochemical Analysis*, **1988**, Prentice-Hall.
- Itoh K., Marumo F. and Kuwano Y., *J. Crystal Growth*, **106**, **1990**, 728.
- Kaminskii A. A., *Laser Crystals, Their Physics and Properties*, 2nd ed., **1990**, Springer-Verlag
- Kato K., *IEEE J. Quantum Electron.* **22**(7), **1986**, 1013.
- Kellendonk F., van den Belt T., Blasse G., *J. Chem. Phys.*, **76**(3), **1982**, 1194.
- Koike J., Kojima T., Toyonaga R., Kagami A., Hase T., and Inaho S., *J. Electrochem. Soc.* **126**, **1979**, 1008.
- Krogh-Moe, *Acta Crystallogr. Sect. B*, **24**, **1968**, 179.
- Krogh-Moe, *Acta Crystallogr. Sect. B*, **28**, **1972**, 3089.
- Kurtz S. W., Perry T. T., *J. Appl. Phys.* **39**, **1968**, 3798.

## BIBLIOGRAPHY (Continued)

Kuz'micheva G., Rybakov V., Kuz'min O., Kutovoi S., Abstract found at <http://krystal.karlov.mff.cuni.cz/ecm/abstract/c/5/620.htm> 4/23/99.

Levien, L., Prewitt, C. T., Weidner, D. *Am. Mineral.* 65, **1980**, 920.

Mackie P.E. and Young R.A., *J. Appl. Cryst.* 6, **1973**, 26.

Marshall, C. D., Smith, L. K., Beach, R. J., Emanuel, M. A., Schaffers, K. I., Skidmore, J., Payne, S. A., Chai, B. T., *IEEE J. Quantum Electron.* 32, **1996**, 650.

Maslen E. N., Streltsolv V. A., Ishizawan N., *Acta Crystallogr. Sect. B* 39, **1991**, 414.

Meijerink A., Jetten H., and Blasse G., *J. Solid State Chem.* 76, **1988**, 115.

Meyn J-P., Jensen T., Huber G., *IEEE J. Quantum Electron.* 30(4), **1994**, 913.

Mishra K. C., Berkowitz J. K., Johnson K. H., Schmidt P. C., *Phys. Rev. B* 45(19), **1992**, 10902.

Mori Y., Kuroda I., Nakajima S., Sasaki T. and Nakai S., *Appl. Phys. Lett.*, 67(13), **1995**, 1818.

Nadezhina T. N., Pobedimskaya E. A., Ilyukhin V.V., Belov N. V., *Sov. Phys. Crystallogr.* 26, **1981**, 168.

Nishi F., Takeuchi Y., *Acta Crystallogr., Sect. C* 40, **1984**, 730.

Norrestam R., and Nygren M., *Chem. Mater.* 4, **1993**, 737.

Norrestam R., *Arkiv foer Kemi*, 29, **1968**, 343.

O'Keeffe, M.; Hansen, S. *J. Am. Chem. Soc.* 110, **1988**, 1506.

Osram Sylvania Luminescent Material, Type 2291, Lot No. FJX439SI.

Osram Sylvania Luminescent Material, Type 2342, Lot No. YCX472.

Ostroumov V., Petermann K., Huber G., Ageev A. A., Kutovoj S., Kuzmin O., Panyutin V., Pfeifer E., Hinz A., *J. Lumin.* 72-74., **1997**, 826.

## BIBLIOGRAPHY (Continued)

Palilla F., Levine A. K., and Rinkevics M., *J Electrochem. Soc.* 112, **1965**, 776.

Payne S. A., Beach R.J., Bibeau C., Ebberts C. A., Emmanuel M. A., Honea E. C., Marshall C. D., Page R. H., Schaffers K. I., Skidmore J. A., Sutton S. B., Krupke W. F., *IEEE J. Sci. Top. Quantum Electron.*, 3(1), 1997, 71.

Peterson G. A., and Keszler D. A., Submitted to *Acta Crystallogr Sect. C*, **1999**.

Petrov V., Rotermund F., Noack F., R. Komatsu, Sugawara T., and Uda S., *J. Applied Physics*, 84(11), **1998**, 5887.

POLSQ: Least Squares Unit Cell Refinement, David Cahen, **1973**.

Recher K., Wallrafen F., and Dupre K., *Naturwissenschaften*, 75, **1988**, 156.

Reynolds T. A., Thesis, Oregon State University, 1992.

Reynolds T. A., Keszler D. A., Gruber J. B., Zhandi B., *Submitted to J. Lumin.*, **1999**.

Saakes M., Leskela M., and Blasse G., *Mat. Res. Bull.*, 19, **1984**, 83.

Saubat B., Vlasse M., and Fouassier C., *J. Solid State Chem.*, 34, **1980**, 271.

Schlager M., Hoppe R. Z., *Anorg. Allg. Chem.* 619, **1993**, 976.

Shannon R. D., *Acta Crystallogr. Sect. A* 32, **1976**, 751.

Sheldrick, G. M., Institut für Anorganische Chemie der Universität, Göttingen, FRG.

Sheldrick, G. M., *In crystallographic Computing 3*; Sheldrick G.M., Kruger C., and Goddard R., Eds.; Oxford Univ Press, Oxford U.K., 1985, 175.

SHELX97, programs for crystal structure analysis (release 97-2) Sheldrick G.M. Institut für Anorganische Chemie der Universität, Tammanstrasse 4, D-3400, Göttingen, Germany. 1998.

SIR92, a program for crystal solution. Altomare A., Cascarano G., and Giacorazzo C., and Guagliardi A. *J. Appl Crystallogr.* 26, **1993**, 345.

Smirnova R. F., Rumanova I. M., Belov N. V., *Zap. Vsesoy. Mineralog. Obschch.* 84, **1955**, 159.

## BIBLIOGRAPHY (Continued)

Sun H., Keszler D. A., *Acta Cryst. Sect. C* **44**, **1988**, 1505.

TEXSAN for Windows, Version 1.04 (1997).

TEXSAN: Structure Analysis Package, Molecular Structure Corp., MSC (3200A, Research Forest Drive, The Woodlands, TX 77381) International Tables for X-ray Crystallography, Vol. IV. Birmingham: Kynoch Press, **1974**.

TEXSAN: Single Crystal Structure Analysis Software, Version 5.0 **1989**, Molecular Structure Corp., The Woodlands, TX, 77381.

Thompson P. D., Keszler D. A., *Solid State Ionics* **32/33**, **1989**, 521.

Timmermans C. W. M., and Blasse G., *J. Solid State Chem.* **52**, **1984**, 222.

Toraya H., Iwai S., Marumo F., Hirao, M., *Z. Kristallogr.* **148**, **1978**, 65.

Tu J., Keszler D. A., *Inorganic Chem.*, **35**, **1996**, 463.

Tu J-M. and Keszler D. A., *Mater. Res. Bull.*, **30**(2), **1995** 209.

Tu, J., Keszler, D. A. *Acta Crystallogr., Sect. C*, in press.

van Schaik W., Blasse G., *Chem Mater.* **4**, **1992**, 410.

van Schaik W., Blasse G., *J. Lumin.* **62**, **1994** 203.

Van Uitert L. G., Linares R. C., Soden R. R., and Ballman A. A., *J Chem. Phys.* **36**, **1962**, 702.

Verstegen J. M. P. J., *J. Electrochem. Soc.*, **121**, **1974**, 1631.

Voronkov A. A., Pyatenko Y. A., *Kristallografiya* **12**, **1967**, 258.

Walker N., Stuart D., *Acta Crystallogr. Sect. A* **39**, **1983**, 158.

Welker T., *J. Lumin.* **48/49**, **1991**, 49.

## BIBLIOGRAPHY (Continued)

WinGX, a windows program for crystal structure analysis. L.J. Farrugia, University of Glasgow, **1998**.

Yvon K., Jeitschko W., Parthe E., *J. Appl. Crystallogr.* **10**, **1977**, 73.

## CURRICULUM VITAE

**Gregory Allen Peterson**

Department of Chemistry, Gilbert Hall 153  
Oregon State University  
Corvallis, OR 97330

### Education

PhD. Materials Chemistry, Oregon State University, June 1999  
B.S. Chemistry, Seattle University, June 1988

### Publications

G. A. Peterson, T. A. Reynolds and D. A. Keszler, "Trigonal Huntite Borate  $\text{CeSc}_3(\text{BO}_3)_4$  (CSB)," manuscript in preparation for submission to the Journal of Solid-State Chemistry.

G. A. Peterson, Jun-Ming Tu and D. A. Keszler, "The Noncentrosymmetric Alkali Metal Borate  $\text{NaLiB}_4\text{O}_7$ ," manuscript in preparation for submission to the Journal of Solid-State Chemistry.

G. A. Peterson, S. K. Crossno, D. A. Keszler, R. Meltzer, D. Bell-Gatch and K. Jiang, "Structure-Property Relationships of VUV-Excited Phosphors," manuscript in preparation for submission to the Society for Information Display.

G. A. Peterson, D. A. Keszler and Alexandre Yokochi, " $\text{YMgB}_5\text{O}_{10}$ ," submitted to the Acta Crystallographica.

G. A. Peterson and D. A. Keszler, " $\text{Ln}_4\text{BO}_7\text{F}$ , (Ln = Y, Dy, Ho, Er, Tm and Yb); Structure and Selected Optical Properties," manuscript in preparation for submission to the Journal of Solid-State Chemistry.

G. A. Peterson, J. L. Kissick, A. Yokochi, A. Akella and D. A. Keszler, "Synthesis, Characterization and Luminescent Properties of  $\text{Li}_2\text{Ca}_6(\text{MO}_4)_3\text{F}_2$  (M = Si, Ge)," manuscript in preparation for submission to the Journal of Solid-State Chemistry.

G. A. Peterson, A. Akella and D. A. Keszler, "Structure of  $\text{Sr}_4\text{Ge}_2\text{O}_7\text{F}_2$  and Selected Luminescence Properties," manuscript in preparation for submission to the Journal of Solid-State Chemistry.



Reynolds, T. A., D. Keszler, G. Peterson, 'A New Family of Optical Materials For High-Power Optical Frequency Conversion,' Final Report to the United States Air Force on Contract No. F33615-98-C-5437, From ReyTech Corporation, Bend, OR 97702, March, 1999.

Reynolds, T. A., D. Keszler, G. Peterson, G. Gruber, B. Zandi, "Highly Efficient Solid-State Crystals for Lasers and Nonlinear Optics,' Phase I Final Report to the National Science Foundation on grant No. 9760642, From ReyTech Corporation, Bend, OR 97702, January, 1999.

Reynolds, T. A., D. Keszler, G. Peterson, 'A New Family of Optical Materials For High-Power Optical Frequency Conversion,' Second Bimonthly Report to the United States Air Force on Contract No. F33615-98-C-5437, From ReyTech Corporation, Bend, OR 97702, October, 1998.

Reynolds, T. A., D. Keszler, G. Peterson, 'A New Family of Optical Materials For High-Power Optical Frequency Conversion,' First Bimonthly Report 1 to the United States Air Force on Contract No. F33615-98-C-5437, From ReyTech Corporation, Bend, OR 97702, August, 1998.

## **Conferences**

*A New Family of Lanthanide Borate Fluorides*, Gregory A. Peterson and Douglas A. Keszler, 53<sup>rd</sup> Northwest Regional Meeting of the American Chemical Society, June 17-20, 1998, USA

*Structure-Property Relationships of VUV-Excited Phosphors*, Douglas A. Keszler and Gregory A. Peterson, 2<sup>nd</sup> International Conference on the Science and Technology of Display Phosphors, November 18-20, 1996, USA

*A Fundamental Study of VUV Host Sensitized Luminescence*, Gregory A. Peterson and Douglas A. Keszler, 51<sup>st</sup> Northwest Regional Meeting of the American Chemical Society, June 19-22, 1998, USA